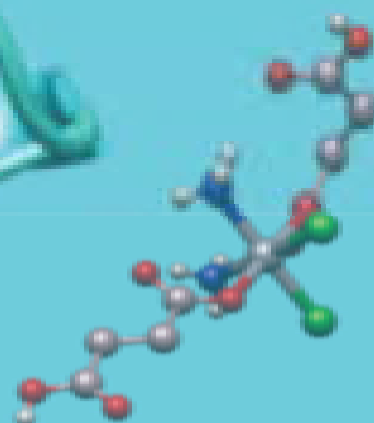
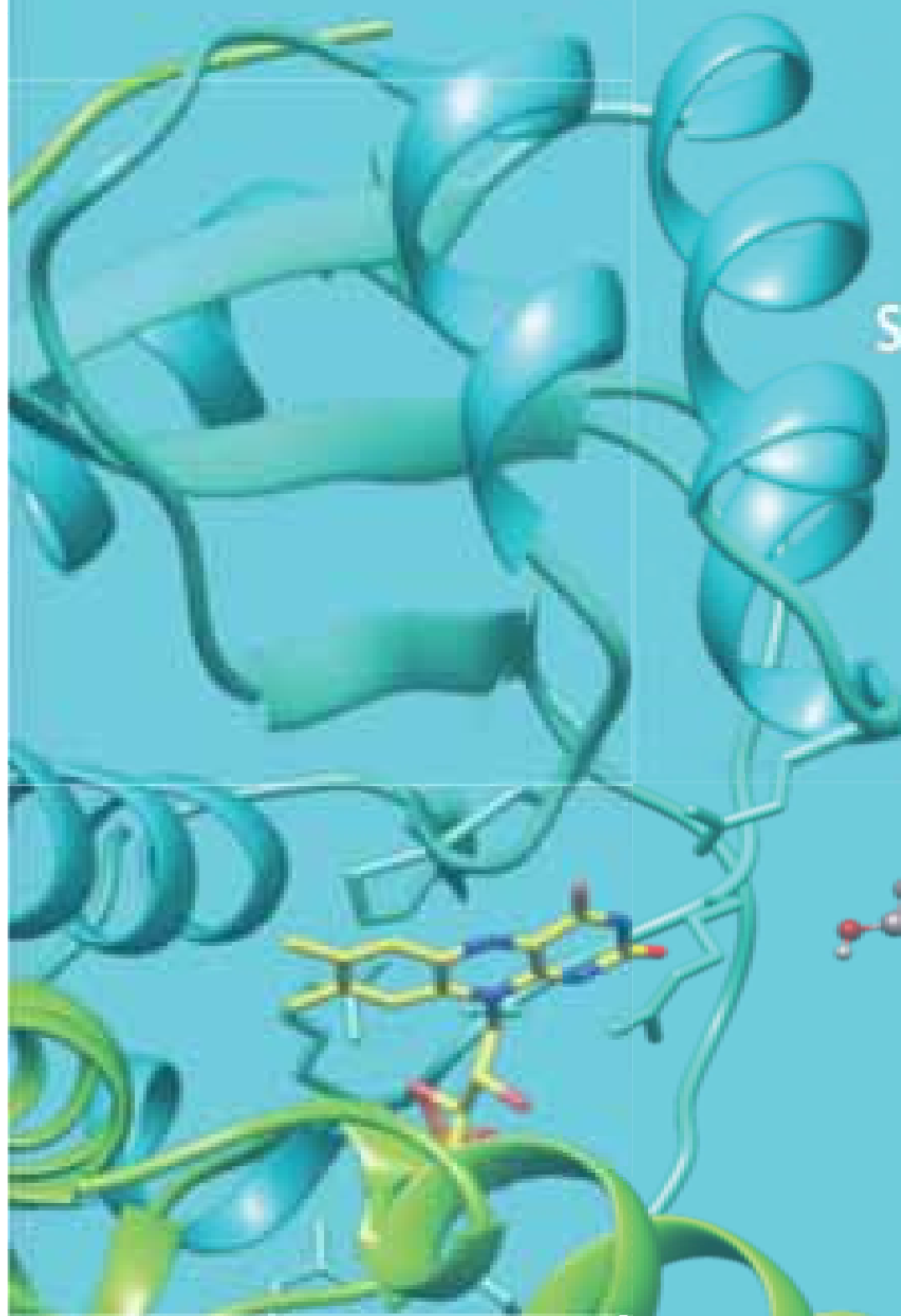


# Bioorthogonal Photocatalytic Activation of Metal-Based Anticancer Agents

Silvia Alonso  
de Castro



UPV EHU



UPV EHU





Universidad  
del País Vasco

Euskal Herriko  
Unibertsitatea

# Bioorthogonal Photocatalytic Activation Of Metal-Based Anticancer Agents

**Doctoral Thesis**

Silvia Alonso de Castro

**Thesis Supervisor**

Prof. Luca Salassa

**Donostia, 2018**





# **Bioorthogonal Photocatalytic Activation of Metal-Based Anticancer Agents**

PhD Thesis

**SILVIA ALONSO DE CASTRO**

Donostia, 2018

**Thesis Supervisor:** Prof. Luca Salassa

**University Tutor:** Prof. Isabel Goñi



## ***Funding Agencies***

This thesis was economically supported by the Spanish Ministry of Economy and Competitiveness (grant CTQ2012-39315, CTQ2016-80844-R and BES-2013-065642) and the European COST Actions CM1105 and CM1403. Moreover, the EEBB-I-17-12445 fellowship funded my stay in the laboratory of Prof. Walter Berger at the Medical University of Vienna (Austria).





# ***Table of contents***

<b>Resumen</b>	iii
<b>Summary</b>	ix
<b>Chapter 1</b> <b>Platinum(IV) anticancer complexes meet flavins: an overview on their chemistry and photochemistry</b>	
<b>1a</b> <b>Platinum(IV) complexes as photoactivatable anticancer prodrugs</b>	
1.1. Platinum complexes	5
1.2. Photoactivatable Pt <sup>IV</sup> prodrugs	10
1.3. Strategies for the enhanced photoactivation of Pt(IV) prodrugs	19
1.4. References	24
<b>1b</b> <b>Flavins and flavoproteins</b>	
1.1. Introduction	29
1.2. References	36
<b>Chapter 2</b> <b>Bioorthogonal catalysis in drug design</b>	
2.1. Introduction	41
2.2. Catalytic metallodrugs targeting biomolecules	42
2.3. Bioorthogonal metal-based catalysis towards extracellular substrates	51
2.4. A new approach – outlook	57
2.5. References	58
<b>Chapter 3</b> <b>Riboflavin as bioorthogonal photocatalyst for the activation of a Pt<sup>IV</sup> prodrug</b>	
3.1. Introduction	65
3.2. Results and Discussion	66
3.3. Conclusions	75

3.4.	Experimental Section	76
3.5.	References	78
<b>Chapter 4</b>	<b>Biological activity of Pt<sup>IV</sup> prodrugs triggered by riboflavin-mediated bioorthogonal photocatalysis</b>	
4.1.	Introduction	83
4.2.	Results and Discussion	86
4.3.	Conclusions	96
4.4.	Experimental Section	97
4.5.	References	100
<b>Chapter 5</b>	<b>Bioorthogonal Catalytic Activation Of Pt And Ru Anticancer Complexes By FAD And Flavoproteins</b>	
5.1.	Introduction	107
5.2.	Results and Discussion	108
5.3.	Conclusions	115
5.4.	Experimental details	116
5.5.	References	121
	<b>Conclusions</b>	125
	<b>Chapter 3 Supporting Information</b>	129
	<b>Chapter 4 Supporting Information</b>	163
	<b>Chapter 5 Supporting Information</b>	181
	<b>Acknowledgements</b>	227
	<b>Curriculum Vitae</b>	229

## **Resumen**

La terapia fotodinámica (Photodynamic Therapy, PDT) es un tratamiento contra el cáncer y otras enfermedades clínicamente aprobado que emplea luz para activar a un fotosensibilizador y generar oxígeno singlete y otras especies de oxígeno reactivas (reactive oxygen species, ROS) capaces de inducir la muerte celular. Desde un punto de vista químico, la eficacia de esta fototerapia se ve limitada por la falta de oxígeno disponible en tumores, los cuales son generalmente hipóxicos. Por tanto, los profármacos anticancerígenos con metales que son fotoactivables han surgido como una fotoquimioterapia alternativa que no depende de la presencia de oxígeno, debido a sus propiedades fotoquímicas únicas.

Entre los diferentes tipos de compuestos fotoactivables, los complejos antitumorales de Pt<sup>IV</sup> se han estudiado extensamente como posibles profármacos y tienen un papel relevante en las prácticas preclínicas. Normalmente, los compuestos de Pt<sup>IV</sup> experimentan su fotoreducción para generar especies citotóxicas de Pt<sup>II</sup> (e.g. cisplatin) cuando han sido irradiados con luz UV, una característica que potencialmente podría reducir los efectos secundarios que se producen con quimioterapias sistémicas.

Sin embargo, ciertas limitaciones fotoquímicas están íntimamente relacionadas a esta clase de compuestos y es necesario corregirlas para avanzar en su aplicación. Por ejemplo, la profundidad de la penetración de luz en el tejido necesita mejorarse desplazando hacia el rojo del espectro la longitud de onda de excitación utilizada para activar los complejos de Pt<sup>IV</sup>. Esta cuestión es una tarea complicada ya que normalmente causa una reducción en la eficiencia fotoquímica.

La riboflavina, la vitamina B2, es una biomolécula exógena esencial para nuestro metabolismo. La riboflavina se convierte rápidamente en flavín mononucleótido (FMN) y flavín adenín dinucleótido (FAD) intracelularmente. FMN y más frecuentemente FAD se une a cientos de existentes apo-flavoenzimas. Las flavinas y flavoenzimas han promovido un enorme interés en investigación debido a su rol clave en funciones catalíticas biológicas y su localización.

En mi tesis, he combinado conceptos sobre catálisis junto con las destacadas propiedades fotofísicas y fotoquímicas de las flavinas para abordar las limitaciones de la fotoquimioterapia con metales. Estas limitaciones están asociadas con las pobres propiedades de absorción de los complejos metálicos, especialmente los compuestos de Pt<sup>IV</sup>. Los complejos metálicos son típicamente considerados como catalizadores, los cuales convierten sustratos en compuestos más valiosos, mientras que aquí, empleo de manera poco convencional las flavinas como fotocatalizadores para activar profármacos con metales que actúan como sustratos. Esta aplicación sin precedentes consigue la activación fotocatalítica de los complejos de Pt<sup>IV</sup> y Ru<sup>II</sup>-areno con gran eficiencia y selectividad, incluso en ambiente biológico.

La presente tesis está dividida en dos partes principales, los dos primeros capítulos definen el contexto de la investigación desarrollada en mi trabajo, mientras que del capítulo tres al cinco se describe el trabajo experimental que he llevado a cabo durante los cuatro años de mi beca de doctorado.

**Capítulo 1** destaca los principales componentes empleados en la aplicación fototerapéutica con metales estudiada en esta tesis. En este capítulo, en primer lugar describo las ventajas y limitaciones de los profármacos de platino en la terapia contra el cáncer, en concreto centrándome en agentes fotoactivables. A continuación, presento las propiedades fotoquímicas y fotofísicas de las flavinas y flavoproteínas elegidas, destacando algunas de sus aplicaciones clave.

**Capítulo 2** contextualiza la aplicabilidad de metalofármacos catalíticos en entornos biológicamente relevantes y para terapia contra el cáncer. Diferentes estrategias dirigidas a dianas terapéuticas han sido descritas en este campo emergente. Por una parte se incluyen en esta área los metalofármacos que interaccionan con biomoléculas intracelulares, al mismo tiempo que también se describen los metalofármacos que son capaces de producir *in situ* agentes anticancerígenos a partir de sustratos extracelulares.

**Capítulo 3** describe el descubrimiento de una nueva reacción bioortogonal, que consiste en la activación fotocatalítica de profármacos anticancerígenos de Pt<sup>IV</sup> mediante el fotosensitizador biológico riboflavina (vitamina B2). La riboflavina bajo irradiación de luz a 460 nm consigue la eficiente conversión fotocatalítica de Pt<sup>IV</sup> en especies de Pt<sup>II</sup> en entornos biológicos induciendo resultados citotóxicos comparables a los del cisplatino. Las bajas dosis de luz junto con los altos número de recambio fotocatalíticos hacen de este sistema una estrategia atractiva para ampliar la acción antineoplásica de los agentes quimioterapéuticos con metales con control espacio-temporal.

*“Riboflavin As Bioorthogonal Photocatalyst For The Activation Of A Pt<sup>IV</sup> Prodrug”*

*Alonso-de Castro, S.; Ruggiero, E.; Ruiz-de-Angulo, A.; Rezabal, E.; Mareque-Rivas, J.C.; Lopez, X.; López-Gallego, F. and Salassa, L. Chem. Sci., 2017, 8, 4616–4625.*

**Capítulo 4** investiga el mecanismo biológico a través del cual la riboflavina activa fotocatalíticamente dos profármacos de Pt<sup>IV</sup> que inducen la muerte celular en diversas líneas de células cancerígenas. La combinación de administrar riboflavina y los profármacos de Pt<sup>IV</sup> al ser irradiados muestra un efecto sinérgico entre la terapia fotodinámica y fotoquimioterapia en el tratamiento de las células Capan-1 (cáncer pancreático) dentro de las diferentes líneas celulares evaluadas. Además, obteniendo una ruta diferente de muerte celular comparada con la obtenida en los controles con cisplatino. Parte de este trabajo ha sido llevado a cabo durante 4 meses de estancia en el grupo de Dr. Walter Berger en la Medical University of Vienna.

*“Biological activity of Pt<sup>IV</sup> prodrugs triggered by riboflavin-mediated bioorthogonal photocatalysis”*

*Alonso-de Castro, S.; Terenzi, A.; Hager, S.; Englinger, B.; Faraone, A.; Galanski, M.; Keppler, B. K.; Berger, W. and Salassa, L. Sci. Rep. 2018, Submitted.*

**Capítulo 5** explora la capacidad de FAD (flavín adenín dinucleótido), FMN (flavín mononucleótido), y cuatro flavoproteínas para actuar como fotocatalizadores poco convencionales para la conversión de complejos anticancerígenos de Pt<sup>IV</sup> y Ru<sup>II</sup> en sus especies potencialmente tóxicas. Las flavoproteínas evaluadas son capaces de convertir los sustratos metálicos con diferentes velocidades dependiendo de la accesibilidad y la carga de la superficie del centro activo de la flavina. Una de las flavoproteínas probadas (NOX: NADH oxidasa de *Thermus thermophilus*), en presencia de NADH (forma reducida de la coenzima nicotinamida adenín dinucleótido), cataliza la activación de Pt<sup>IV</sup> en la oscuridad también, indicando por primera vez que las flavoproteínas pueden contribuir al inicio de la actividad de los agentes quimioterapéuticos de Pt<sup>IV</sup>.

*“Bioorthogonal Catalytic Activation of Platinum and Ruthenium Anticancer Complexes by FAD and Flavoproteins”*

*Alonso-de Castro, S.; Cortajarena, A.; López-Gallego, F. and Salassa, L. Angew. Chem. Int. Ed. 2018, 57, 3143–3147 (VIP, Very Important Paper)*

*Inside cover: Angew. Chem. Int. Ed. 12/2018*

*Highlighted in Chemistry Views*

Además del trabajo mencionado anteriormente, durante mi doctorado también he contribuido en el desarrollo de otros proyectos de investigación y en la preparación de artículos de revisión. Estas actividades no están incluidas en esta tesis, aunque han sido instrumentales para obtener más conocimiento en las áreas de compuestos de coordinación fotoactivables, nanomateriales de conversión ascendente y agentes de

MRI (resonancia magnética de imagen). Como resultado de mi Implicación en estos proyectos, he contribuido a la preparación de 4 artículos publicados en revistas internacionales revisadas por pares y 1 artículo de divulgación.

*“Polyurethane Based Organic Macromolecular Contrast Agent (PU-ORCA) For Magnetic Resonance Imaging”*

*Garmendia, S.; Mantione, D.; Alonso-de Castro, S.; Jehanno, C.; Lezama, L.; Hedrick, J. L.; Mecerreyes, D.; Salassa, L. and Sardon, H. Polym. Chem., 2017, 8, 2693–2701.*

*“Upconverting Nanoparticles For The Near Infrared Photoactivation Of Transition Metal Complexes: New Opportunities And Challenges In Medicinal Inorganic Photochemistry”*

*Ruggiero, E.; Alonso-de Castro, S.; Habtemariam, A. and Salassa, L. Dalton Trans., 2016, 45, 13012–13020.*

*“Photorelease of Pyridyl Esters in Organometallic Ru(II) Arene Complexes”*

*Habtemariam, A.; Garino, C.; Ruggiero, E.; Alonso-de Castro, S.; Mareque-Rivas, J.C. and Salassa, L. Molecules, 2015, 20, 7276–7291.*

*“Nuevos Materiales de Conversión Ascendente para Fotoquimioterapia con Complejos de Metales de Transición”*

*Alonso-de Castro, S.; Ruggiero, E. and Salassa, L. CIC Network Ciencia y Tecnología, 2015, 15, 40.*

*“The Photochemistry of Transition Metal Complexes and Its Application in Biology and Medicine”*

*Ruggiero, E.; Alonso-de Castro, S.; Habtemariam, A. and Salassa, L. Struct. Bond., 2014, 165, 69–108.*



## ***Summary***

Photodynamic Therapy (PDT) is a clinically approved treatment for cancer and other diseases that employs light to activate a photosensitizer and generate singlet oxygen and other reactive oxygen species (ROS) able to induce cell death. From a chemical point of view, the efficacy of this phototherapy approach is limited by the lack of oxygen available in tumours, which are generally hypoxic. Hence, light-activatable metal-based anticancer prodrugs have emerged as an alternative oxygen-independent photochemotherapy, owing to their unique photochemical properties.

Among the various classes of photoactivatable compounds, Pt<sup>IV</sup> antitumour agents are intensively studied as prodrug candidates and have a relevant role in preclinical practice. They typically undergo photoreduction into cytotoxic Pt<sup>II</sup> species (e.g. cisplatin) when irradiated with UV light, a feature that may potentially help reducing side-effects of systemic chemotherapies.

Nevertheless, an intimately related photochemical feature for this class of compounds need to be improved for advancing their use towards application. Tissue penetration needs to be enhanced by red-shifting excitation wavelengths employed to activate Pt<sup>IV</sup> complexes, a challenging task that often causes dramatic reductions in terms of photochemical efficiency.

Riboflavin, vitamin B2, is an essential exogenous biomolecule for our metabolism. Riboflavin is rapidly converted into flavin mononucleotide (FMN) and flavin adenine dinucleotide (FAD) intracellularly. FMN and more frequently FAD bind hundreds of the existing apo-flavoenzymes. These flavins and flavin dependent-enzymes have motivated an enormous interest in research due to their key role in biological catalytic functions and localization.

In my thesis, I have combined catalysis concepts and the outstanding photophysical and photochemical features of flavins to address the limitations of metal-based photochemotherapy associated with the poor absorption properties of metal complexes, particularly of Pt<sup>IV</sup> compounds. Metal complexes are typically regarded as catalysts which convert organic substrates in more valuable compounds, whereas

here, I unconventionally employ flavins as photocatalysts to activate metal-based prodrugs which act as substrates. This unprecedented approach achieves photocatalytic activation of Pt<sup>IV</sup> and Ru<sup>II</sup>-arene complexes with high efficiency and remarkable selectivity, even in the biological environment.

This thesis manuscript is divided in two main parts, the first two chapters define the framework of the research developed in my work, while chapter three to five report on the experimental work that I have carried out in the four years of my Ph.D. fellowship.

**Chapter 1** outlines the main components employed in the metal-based phototherapeutic approach studied in this thesis. In this chapter, I first describe the advantages and limitations of platinum prodrugs in cancer therapy, in particular focusing on photoactivatable agents. Then, I present the photochemical and photophysical properties of flavins and selected flavoproteins, highlighting some of their key application.

**Chapter 2** contextualizes the applicability of catalytic metallodrugs in biological relevant environments and for cancer therapy. Different targeting strategies have been reported in this emerging field, including metallodrugs that react with biomolecules and organometallic catalysts that are able to produce in situ anticancer agents from extracellular substrates.

**Chapter 3** describes the discovery of a new bioorthogonal reaction, that is the photocatalytic activation of Pt<sup>IV</sup> anticancer prodrugs by the biological photosensitizer riboflavin (vitamin B2). Riboflavin under 460-nm light irradiation achieves efficient photocatalytic conversion of Pt<sup>IV</sup> into Pt<sup>II</sup> species in biological environment inducing comparable cytotoxic results to cisplatin. Low light doses used and high photocatalytic turnovers make this system an attractive strategy to amplify the antineoplastic action of metal-based chemotherapeutics with spatio-temporal control.

*“Riboflavin As Bioorthogonal Photocatalyst For The Activation Of A Pt<sup>IV</sup> Prodrug”*

*Alonso-de Castro, S.; Ruggiero, E.; Ruiz-de-Angulo, A.; Rezabal, E.; Mareque-Rivas, J.C.; Lopez, X.; López-Gallego, F. and Salassa, L. Chem. Sci., 2017, 8, 4616–4625.*

**Chapter 4** investigates the biological mechanism through which riboflavin-photocatalytic activation of two Pt<sup>IV</sup> prodrugs induces cell death in a number of cancer cell lines. Among the different cell lines tested, the combination of riboflavin and Pt<sup>IV</sup> prodrugs shows a synergistic effect between photodynamic therapy and photochemotherapy in the treatment of Capan-1 cells (pancreatic cancer), obtaining a different cell death pathway compared to cisplatin. Part of this work has been carried out during a 4-months stay in the group of Dr. Walter Berger at the Medical University of Vienna.

*“Biological activity of Pt<sup>IV</sup> prodrugs triggered by riboflavin-mediated bioorthogonal photocatalysis”*

*Alonso-de Castro, S.; Terenzi, A.; Hager, S.; Englinger, B.; Faraone, A.; Galanski, M.; Keppler, B. K.; Berger, W. and Salassa, L. Sci. Rep. 2018, Submitted.*

**Chapter 5** explores the capability of FAD (flavin adenine dinucleotide), FMN (flavin mononucleotide), and four flavoproteins to act as unconventional photocatalysts for the conversion of Pt<sup>IV</sup> and Ru<sup>II</sup> anticancer complexes into their potentially toxic species. The flavoproteins tested are capable to convert the metal substrates with different rates depending on the pocket accessibility and surface charge of the flavin binding pocket. One of the flavoproteins tested (NOX: NADH oxidase from *Thermus thermophilus*), in the presence of NADH (reduced form of the coenzyme nicotinamide adenine dinucleotide), catalyses Pt<sup>IV</sup> activation in the dark as well, indicating for the

first time that flavoenzymes may contribute to initiating the activity of Pt<sup>IV</sup> chemotherapeutic agents.

*“Bioorthogonal Catalytic Activation of Platinum and Ruthenium Anticancer Complexes by FAD and Flavoproteins”*

*Alonso-de Castro, S.; L. Cortajarena, A.; López-Gallego, F. and Salassa, L. Angew. Chem. Int. Ed. 2018, 57, 3143–3147 (VIP, Very Important Paper)*

*Inside cover: Angew. Chem. Int. Ed. 12/2018*

*Highlighted in Chemistry Views*

In addition to the aforementioned work, during my Ph.D. I have also contributed to the development of other research projects and to the preparation of review articles. These activities are not included in this thesis, yet they were instrumental in obtaining more insights in the areas of photoactivatable coordination compounds, upconversion nanomaterials and MRI (magnetic resonance imaging) agents. As a result of my involvement, I contributed to the preparation of 4 articles published in international peer-reviewed journals and 1 outreach journal article.

*“Polyurethane Based Organic Macromolecular Contrast Agent (PU-ORCA) For Magnetic Resonance Imaging”*

*Garmendia, S.; Mantione, D.; Alonso-de Castro, S.; Jehanno, C.; Lezama, L.; Hedrick, J. L.; Mecerreyes, D.; Salassa, L. and Sardon, H. Polym. Chem., 2017, 8, 2693–2701.*

*“Upconverting Nanoparticles For The Near Infrared Photoactivation Of Transition Metal Complexes: New Opportunities And Challenges In Medicinal Inorganic Photochemistry”*

*Ruggiero, E.; Alonso-de Castro, S.; Habtemariam, A. and Salassa, L. Dalton Trans., 2016, 45, 13012–13020.*

*“Photorelease of Pyridyl Esters in Organometallic Ru(II) Arene Complexes”*

*Habtemariam, A.; Garino, C.; Ruggiero, E.; Alonso-de Castro, S.; Mareque-Rivas, J.C. and Salassa, L. Molecules, 2015, 20, 7276–7291.*

*“Nuevos Materiales de Conversión Ascendente para Fotoquimioterapia con Complejos de Metales de Transición”*

*Alonso-de Castro, S.; Ruggiero, E. and Salassa, L. CIC Network Ciencia y Tecnología, 2015, 15, 40.*

*“The Photochemistry of Transition Metal Complexes and Its Application in Biology and Medicine”*

*Ruggiero, E.; Alonso-de Castro, S.; Habtemariam, A. and Salassa, L. Struct. Bond., 2014, 165, 69–108.*



# 1

**Platinum(IV) anticancer complexes  
meet flavins: an overview on their  
chemistry and photochemistry**





# 1a

**Platinum(IV) Complexes as  
Photoactivatable  
Anticancer Prodrugs**



## 1.1 Platinum complexes

Platinum complexes are essential in the panel of chemotherapy treatments. With the discovery in 1965 by Barnett Rosenberg that cisplatin (cis-diamminedichloridoplatinum) caused cell division arrest in *Escherichia coli* (*E. coli*) via an electrolysis experiment,<sup>1</sup> medicinal inorganic chemistry became an emerging field. Later in 1978, cisplatin was the first Pt<sup>II</sup> complex approved for cancer treatment by the Food and Drug Administration (FDA). Since then, other seven Pt<sup>II</sup> compounds obtained the approval in clinics worldwide (carboplatin and oxaliplatin) or in selected countries (nedaplatin, lobaplatin, heptaplatin, miriplatin and dicycloplatin) (Figure 1).<sup>2,3</sup>

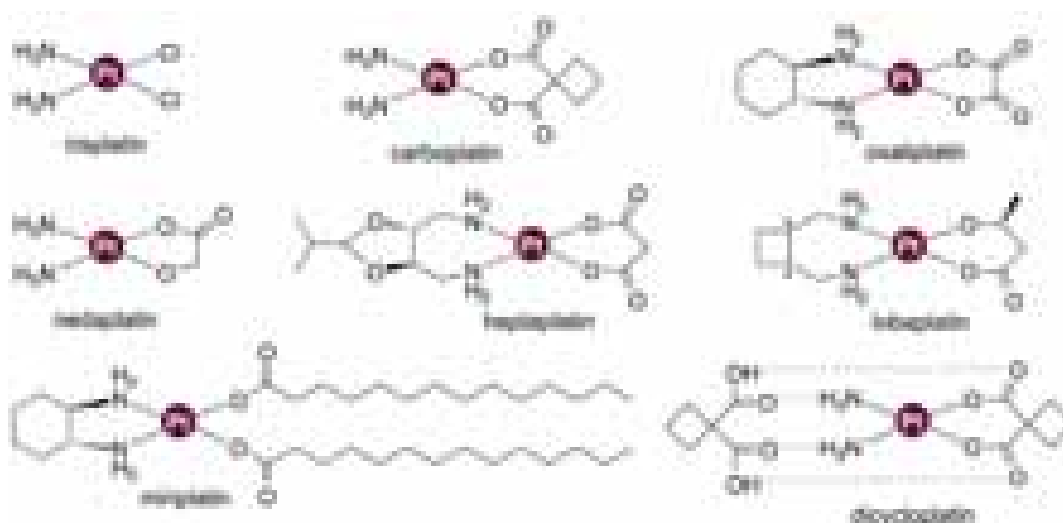


**Figure 1.** Schematic structures of clinically approved Pt<sup>II</sup> drugs.

As a consequence of the impact produced by cisplatin discovery, other metal complexes have also been studied for anticancer purposes; for example ruthenium, cobalt, rhodium, iridium and gold. Among non-platinum compounds, it is important to highlight that the Ru<sup>III</sup> complexes NAMI-A and KP1019 (where NAMI-A = (ImH)[*trans*-RuCl<sub>4</sub>(dmsO-S)(Im)], Im = imidazole; and KP1019 = (IndH)[*trans*-RuCl<sub>4</sub>(Ind)<sub>2</sub>], Ind = indazole) reached clinical trials. In the case of NAMI-A, owing to the long Ru body retention time observed in Phase I, NAMI-A was combined with Gemcitabine in Phase I/II studies and declared “insufficiently effective for further use”. On the other hand, the relatively low solubility of KP1019 did not allow further dose escalation in Phase I.

## Chapter 1a

Therefore, another Phase I study was performed with the more soluble sodium derivative Na[*trans*-RuCl<sub>4</sub>(Ind)<sub>2</sub>] (KP1339). Very recently, the Phase I results in the US showed KP1339 to be suitable for combination therapies. Despite having modest anticancer activity, this agent allows controlling the disease progression by avoiding the proliferation of malignant cells.<sup>4</sup>

This chapter will focus on selected aspects of the enormous Pt medicinal chemistry, arbitrarily excluding anticancer agents based on other metals. The choice is necessary in light of the literature vastness field and for the nature of the research work performed during the thesis.

The mechanism by which the classical platinum drugs exert their anticancer effect has been investigated during decades. Square planar Pt<sup>II</sup> complexes are generally accepted to act as prodrugs per se. They contain two carrier ligands and two leaving ligands (Figure 2). The latter are exchanged inside cells to later interact with DNA strands via interstrand or intrastrand interactions, ultimately causing cell death. For instance, the CBDCA (cyclobutane dicarboxylate) chelating ligand bestows lower reactivity and slower DNA binding kinetics to carboplatin with respect to cisplatin, despite the two complexes form similar final reaction products. In addition, carboplatin shows alternative mechanisms of action, as well as other Pt complexes, which help overcoming cisplatin drug resistance.<sup>5</sup>

Notwithstanding the good survival rates of patients treated with Pt<sup>II</sup> drugs (e.g. the use of cisplatin exceeds 95% cure rate survival for testicular cancer),<sup>6</sup> systemic toxicity is associated to these metal-based therapies causing several side effects in patients (Figure 2).<sup>7</sup>

Because of the need to tackle the clinical problems of Pt<sup>II</sup> drugs, an increased interest of the scientific community focused on the investigation of Pt<sup>IV</sup> complexes, which display higher stability and hydrolytic inertness. In general, Pt<sup>IV</sup> agents do not undergo fast hydrolysis in biological environments and reduce subsequent unspecific toxicity. This family of octahedral compounds incorporates axial ligands (Figure 2) into their chemical structure, which help modulating solubility parameters and biological effects in cells, as well as adding vectors for targeting specifically cancer cells.<sup>7</sup>

Octahedral Pt<sup>IV</sup> complexes act as prodrugs of Pt<sup>II</sup> agents. They require an additional step of activation in which they undergo reductive elimination of ligands. This reaction is typically triggered inside cells by intracellular reducing agents (e.g. glutathione (GSH) or ascorbic acid) which are able to reduce inert Pt<sup>IV</sup> ions into their Pt<sup>II</sup> analogues. Subsequently, these form reactive aqua species that give DNA adducts and consequently induce cell death (Figure 2).<sup>3</sup> Much of the research carried out on Pt<sup>IV</sup> complexes has consisted in improving the pharmacological profiles of Pt drugs, elucidating the details of the Pt<sup>IV</sup> → Pt<sup>II</sup> activation and its biological effects, obtaining promising toxicity profiles *in vitro*, and overcoming drug resistance caused by previous treatments.

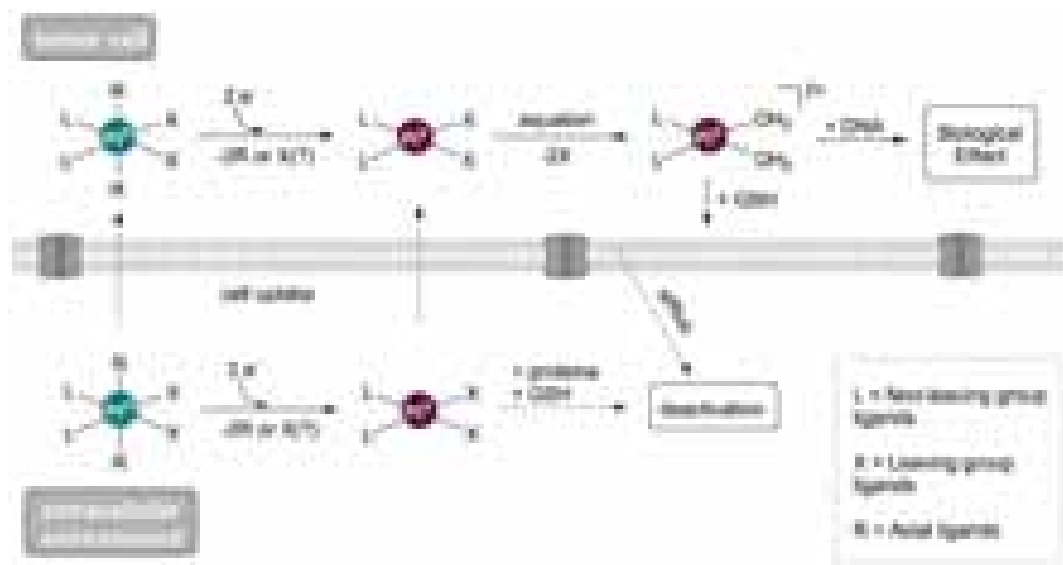


**Figure 2.** Schematic representation of the mechanism of activation of Pt<sup>IV</sup> prodrugs and their biological action in cells. Scheme adapted from reference 3.

Insights in the mechanism by which these octahedral Pt<sup>IV</sup> complexes are converted into square planar Pt<sup>II</sup> derivatives are essential for the rational design and enhancement of metal prodrug features. These processes are complex to elucidate and strictly depend on the type of ligands and their spatial distribution around the metal center. Nevertheless, compared to Pt<sup>II</sup> agents, administration of inert Pt<sup>IV</sup> complexes is typically resulting in an increased circulation lifetime in the blood due to reduced reactions with plasma proteins.<sup>8</sup> In particular, a way to increase this circulation lifetime consists in the bioconjugation of a Pt<sup>IV</sup> complex with human serum albumin protein (HSA) which also

enhances the tumor accumulation due to the EPR (enhanced permeability retention) effect *in vivo*.<sup>9</sup> The reduction potentials of Pt<sup>IV</sup> complexes should be considered since these prodrugs will be activated inside the cancer cells and not in the bloodstream. The biological GSH and ascorbic acid are both present at lower concentrations in blood plasma (900 and 50–150  $\mu\text{M}$  respectively) and in higher concentrations in the cells (approximately 2 and 1 mM respectively). Experimental studies have proposed several mechanisms for the reductive elimination reaction of Pt<sup>IV</sup> complexes, such as outer sphere reactions, inner sphere mechanisms and Pt<sup>II</sup> catalyzed reaction schemes.<sup>8,10</sup> Inner sphere reactions involve the interaction between a reductant and the metal complex. The capacity of Pt-coordinated ligands to interact (e.g. via H-bonding, electrostatic or  $\pi$ - $\pi$  stacking interactions) with the reductant governs dramatically the electron transfer efficiency. On the other hand, outer sphere reductions are less efficient and normally involve Pt<sup>III</sup> intermediates with one electron reductions. For example, the *trans* orientated chlorido ligands in the Pt<sup>IV</sup> complex JM576 provides a reduction via the formation of an inner sphere pathway for electron transfer which is three orders of magnitude faster than its *cis* chloride isomer JM216. This instead follows an outer sphere electron transfer generating different Pt<sup>II</sup> product (Figure 3).<sup>8,10</sup>

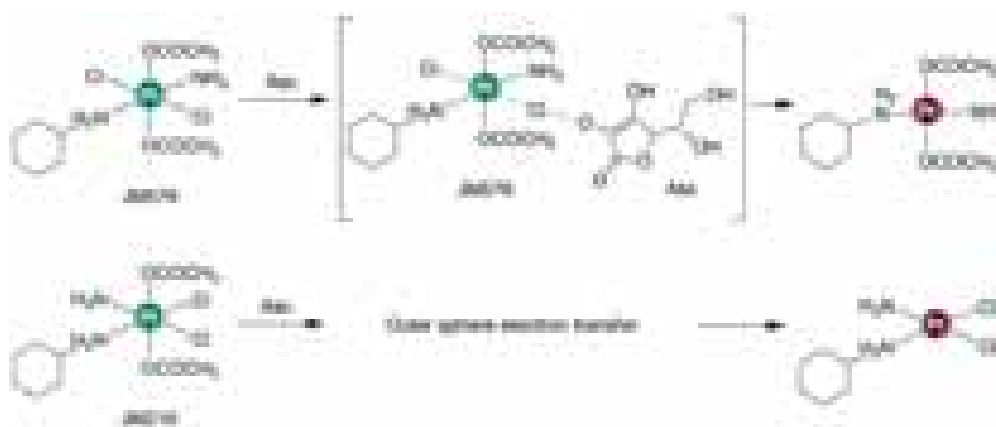


**Figure 3.** Reduction reaction for two different Pt<sup>IV</sup> isomers: (above) Fast reduction for JM576 with *trans* chlorido ligands forming a chloride bridge between the ascorbate and the metal center; (below) slower reduction of the *cis* isomer through an outer sphere mechanism. Figure reproduced from reference 8.

Many of the pharmacologically promising Pt<sup>IV</sup> prodrugs incorporate two axial carboxylato ligands which reduce the capacity of the complex to form bridging

moieties for electron transfer, and consequently lower their reduction potentials compared to chloride analogues.

Several Pt<sup>IV</sup> prodrugs have undergone clinical trials. Representative examples are Ormaplatin, Iproplatin, Satraplatin and LA-12 (Figure 4). Ormaplatin, also known as tetraplatin or tetrachloro (*trans*-1,2-diaminocyclohexane)platinum(IV), is rapidly reduced to dichloro (*trans*-1,2-diaminocyclohexane)platinum(II) in tissue culture medium ( $t_{1/2} = 5\text{--}15$  min). The complex finished Phase I studies and its toxicity is thought to arise from fast reduction to the active Pt<sup>II</sup> form because of the presence of the chloride axial ligands.<sup>7</sup> Encouraging results have also been obtained for the Pt<sup>IV</sup> complex iproplatin, also known as JM9, CHIP, or *cis*-dichlorobis(isopropylamine)*trans*-dihydroxyplatinum(IV). Iproplatin is less prone to reduction and deactivation by biological reducing agents than ormaplatin, due to the presence of hydroxide axial ligands instead of chlorides, which confer higher reduction potential. This slower deactivation allows an easier distribution of the complex throughout the body. Another remarkable feature of iproplatin is its very high water solubility (44.1 mM), which allows simpler formulation and administration. Iproplatin reached Phase II in combination with carboplatin for breast cancer. Satraplatin, *trans,cis,cis*-bis(acetato)amminecyclohexylaminedichloroplatinum(IV) (Figure 4), was the first platinum agent reported to have oral activity. This complex was rationally designed with suitable lipophilicity and stability for oral administration. Satraplatin is in Phase III in combination with prednisone for prostate cancer treatment and in Phase I for solid tumors including brain tumors in children and young adults. A Phase I clinical trial was also carried out with LA-12, a derivative of satraplatin in which the cyclohexylamine is replaced with adamantylamine (Figure 4).<sup>7</sup>

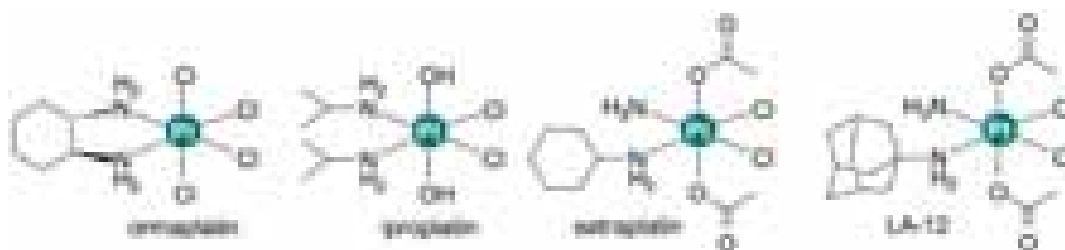


**Figure 4.** Chemical structures of Pt<sup>IV</sup> agents that have undergone clinical trials.

Pt<sup>IV</sup> prodrugs have to be approved for clinical use yet, although some offer the promise of increased efficacy and reduced side effects. Nonetheless, researchers have further developed the Pt<sup>IV</sup> prodrug strategy<sup>3,7,10,11</sup> exploiting the axial ligand to provide the desired biological properties such as lipophilicity, redox stability, cancer-cell targeting, orthogonal or complementary bioactivity, and improved cellular uptake. The design of the axial ligands has been instrumental to load Pt<sup>IV</sup> complexes onto a great variety of nanoparticles and other delivery systems.<sup>7</sup>

An alternative and promising strategy to improve Pt<sup>IV</sup> application has been the use of light for the Pt<sup>IV</sup> activation, which is the main focus of this thesis.

## **1.2 Photoactivatable Pt<sup>IV</sup> prodrugs**

The use of light as external stimuli has been extensively investigated in drug delivery and theranostics. This approach is minimally invasive and allows spatio-temporal control of the biological activity of the therapeutic agents, avoiding systemic side effects. Currently, photodynamic therapy (PDT) is the most important clinically employed light-triggered treatment.

PDT is a powerful procedure for the cure of non-malignant diseases and tumors (e.g. skin, head, neck, lung, pancreas, esophagus, bladder, prostate and neoplasms). PDT drugs are photosensitizers whose typical structure is based on tetrapyrrole macrocycles with highly conjugated electron systems that allow efficient visible light absorption (Figure 5). Upon visible light-excitation, the photosensitizer generates a triplet excited state able to react with <sup>3</sup>O<sub>2</sub> (Type II reaction) or other biomolecules (Type I reaction) to finally produce cytotoxic <sup>1</sup>O<sub>2</sub> and reactive oxygen species (ROS) (Figure 5).





**Figure 5.** Chemical structure of the photosensitizer Photofrin and PDT mechanism of action.

It is worth highlighting that each single PDT component separately is non-toxic per se, but their simultaneous combination produces cell death.<sup>12</sup>  $^1\text{O}_2$  and ROS can directly damage cells and/or vasculature, and induce inflammatory and immune responses.<sup>13</sup> In addition, ROS produced by photosensitizers can not only induce tumor cell apoptosis directly, but also disrupt the cytomembrane and endolysosomes. This may be helpful for combinatory treatments of PDT and chemotherapy because it could prevent that chemotherapeutic drugs are pumped out from the cell by P-glycoproteins or being degraded by enzymes.<sup>14</sup> Transition metal compounds also play a key role in PDT. A representative example is the Ru polypyridyl complex named TLD-1433, which has entered into clinical trials as a novel PDT photosensitizer for the treatment of non-muscle-invasive bladder cancer.<sup>15</sup> Furthermore, the Pd-based PDT agent TOOKAD (tetrahydroporphyrin) for prostate adenocarcinoma treatment has recently been clinically approved in Latin America.<sup>16</sup>

Fostered by the success of PDT in cancer treatment,<sup>12</sup> light-activation strategies are being currently applied to overcome systemic drawbacks observed for traditional metal-based chemotherapy. In photochemotherapy (or photoactivated chemotherapy), light is used to control spatio-temporally the generation of metal-based drugs and their cytotoxic effects.<sup>17</sup> This approach requires complexes to be non-toxic and stable in the dark under physiological conditions, but at the same time they need to be capable of generating cytotoxic metal-based species which target key functions in cells upon light activation. The investigation of novel photoactivatable metal-based prodrugs could potentially lead to overcome limitations coming from both

PDT and chemotherapy. For instance, PDT oxygen dependency limits the effectiveness of the treatment since many tumors are hypoxic and O<sub>2</sub> concentration progressively decreases during application of the therapy.<sup>18</sup> On the other hand, light activation of prodrugs may help preventing the unspecific toxic effects associated with chemotherapy, which provoke severe side effects and limit drug administration.

Among all the classes of photoactivatable metal-based prodrugs, this chapter will focus on Pt<sup>IV</sup> complexes. This family of compounds has particularly poor absorption properties and strongly needs new activation approaches to advance their use towards preclinical settings. Nevertheless, the capacity of Pt<sup>IV</sup> photoactivatable complexes to be converted into clinically approved Pt<sup>II</sup> drugs, whose anticancer profiles is well known and studied, may overall ease their advance towards the clinics.

The photochemical and photophysical processes of low spin octahedral d<sup>6</sup> metal complexes, in which Pt<sup>IV</sup> complexes are included, are governed by a variety of excited states (Figure 6). These are generated upon absorption of light and subsequent promotion of one electron to higher-energy unoccupied orbitals. The corresponding electronic transitions are generally defined:

- *Metal centered (MC) transitions*: These are orbitally (Laporte)-forbidden transitions with weak absorptions. Typically antibonding orbitals are populated, therefore the excited states generated often lead to bond lengthening and favor ligand substitution.
- *Charge-transfer (CT) transitions*: They include metal-to-ligand (MLCT), ligand-to-metal (LMCT) or to-solvent (TS) transitions. These have higher intensity and can lead to redox reactions (e.g. metal reduction and radical generation).
- *Ligand-centered (LC) transitions*: These generally are often seen in large delocalized systems and involve  $\pi$ - $\pi^*$  excited states.



**Figure 6.** Simplified orbital and excited-state diagram for a  $d^6$  metal complex with octahedral coordination (strong crystal field is assumed). Small double colored arrows represent the electron involved in each electronic transition. When in the singlet state they are spin-down, or in the triplet state they are spin-up. Schematic representation reproduced from reference 17.

Time-resolved optical techniques and computational methods have often been employed to characterize the excited states involved in the photoactivation of metal complexes.<sup>17</sup> In the case of  $Pt^{IV}$  photoactivatable anticancer agents, Density Functional Theory (DFT) calculations have highlighted that MC and LMCT states are responsible for their photochemical behavior and for the generation of  $Pt^{IV}$  and  $Pt^{II}$  photoproducts, which often are dissimilar than the ones obtained by direct chemical reduction of the complexes.<sup>19,20</sup>

In addition to the discovery of cisplatin biological activity, Barnett Rosenberg was also the first to report in 1967 that light activation of  $Pt^{IV}$  compounds produced cytotoxic species which affected bacterial growth in *E. coli*.<sup>21</sup> Thirty years later Bednarski and coworkers were the first in the middle and late 1990s to investigate the photochemistry, DNA-binding, and antiproliferative properties of the photoproducts originated from iodido  $Pt^{IV}$  diamine complexes. The photoactivation of these complexes primarily involves redox processes, but ligand substitution and isomerization could commonly occur.<sup>22,23</sup> The first generation of derivatives,

represented by *cis,trans*-[Pt(en)(I)<sub>2</sub>(OAc)<sub>2</sub>] (**1**) (where OAc = OCOCH<sub>3</sub> and en = H<sub>2</sub>NCH<sub>2</sub>CH<sub>2</sub>NH<sub>2</sub>) (Figure 7), reacts to visible light by binding irreversibly to DNA and forming adducts with 5'-GMP (guanosine 5'-monophosphate, used to model DNA binding) in the same manner as the Pt<sup>II</sup> complex [Pt(en)Cl<sub>2</sub>]. Furthermore, the photolysis products are cytotoxic in TCCSUP human bladder cancer cells. However, these complexes are too reactive towards biological thiols (e.g., GSH), which rapidly reduce (30 min) them to cytotoxic Pt<sup>II</sup> species in the dark, thus making them unsuitable as effective prodrugs.<sup>23,24</sup>

The second generation of photoactivatable Pt<sup>IV</sup> complexes includes the diazido-Pt<sup>IV</sup> complexes developed by Sadler and Bednarski. Representative examples are the *cis,trans*-[Pt(en)(N<sub>3</sub>)<sub>2</sub>(OH)<sub>2</sub>] (**2**) and *cis,trans,cis*-[Pt(N<sub>3</sub>)<sub>2</sub>(OH)<sub>2</sub>(NH<sub>3</sub>)<sub>2</sub>] (**3**) (Figure 7). Light irradiation at 366 nm converts both complexes into cytotoxic species that effectively induce cancer cell death by affecting their nuclei. Photoproducts are shown to bind irreversibly to DNA and form similar products with DNA and 5'-GMP as their corresponding Pt<sup>II</sup> complexes with released azido ligands. However, differently from iodide Pt<sup>IV</sup> complexes, azido Pt<sup>IV</sup> complexes are stable towards GSH reduction and binding, which greatly decreases their dark cytotoxicity. These early studies showed that photoactivatable azido Pt<sup>IV</sup> antitumor agents are promising candidates for new drug development.<sup>24</sup>

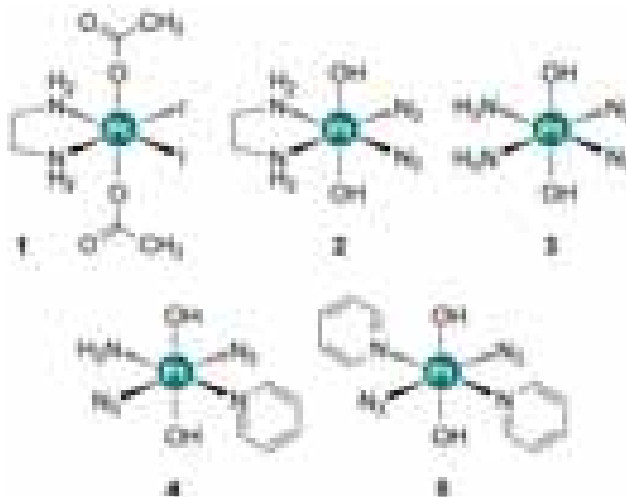


**Figure 7.** Schematic representation of the photoactivatable Pt<sup>IV</sup> complexes: *trans,cis*-[Pt(OAc)<sub>2</sub>I<sub>2</sub>(en)] (**1**), *cis,trans*-[Pt(en)(N<sub>3</sub>)<sub>2</sub>(OH)<sub>2</sub>] (**2**), *cis,trans,cis*-[Pt(N<sub>3</sub>)<sub>2</sub>(OH)<sub>2</sub>(NH<sub>3</sub>)<sub>2</sub>] (**3**), *trans,trans,trans*-[Pt(N<sub>3</sub>)<sub>2</sub>(OH)<sub>2</sub>(py)(NH<sub>3</sub>)] (**4**) and *trans,trans,trans*-[Pt(N<sub>3</sub>)<sub>2</sub>(OH)<sub>2</sub>(py)<sub>2</sub>] (**5**).

The complex *trans,trans,trans*-[Pt(N<sub>3</sub>)<sub>2</sub>(OH)<sub>2</sub>(py)(NH<sub>3</sub>)] (**4**)<sup>25</sup> (Figure 7) was evaluated toward several human cancer cells. <sup>14</sup>N NMR studies demonstrated that NH<sub>3</sub>, N<sub>2</sub>, and azide are released from **4** upon photoactivation, besides Pt-based species. The average IC<sub>50</sub> values obtained after 30 minutes of UVA light irradiation (0.12 mW/cm<sup>2</sup>) was 55 ± 28 μM. Notably, under visible light irradiation (420 nm) the complex is also effective (1.17 J/cm<sup>2</sup>). Remarkably, **4** showed antitumor activity *in vivo* in nude mice. Blue light (100 J/cm<sup>2</sup> at 420 nm) was delivered through the skin for 30 minutes, followed by a second irradiation 6 hours later (total dose of approx. 200 J/cm<sup>2</sup>). Survival of 2 mice of 7 treated with **4** and light was obtained after 35 days, while no survival was reached for control experiments.

Sadler and coworkers also reported on the biological activity of *trans,trans,trans*-[Pt(N<sub>3</sub>)<sub>2</sub>(OH)<sub>2</sub>(py)<sub>2</sub>] (**5**) (Figure 7)<sup>26</sup>, which was a potent phototoxic agent under 365-nm irradiation towards human several cancer cell lines such as keratinocytes (HaCaT), parental (A2780) and cisplatin resistant (A2780CIS) ovarian carcinoma, oesophageal adenocarcinoma (OE19), and hepatoma (HepG2) cells. Irradiation with a low-dose (5 J/cm<sup>2</sup>) of visible light (420 nm) provides for HaCaT cells a cytotoxic activity 10 times higher than cisplatin, and a phototoxic index (PI) greater than 22. In OE19 cells, the IC<sub>50</sub> value is 8.4 μM and PI also >25 when irradiated with visible light. The presence of pyridine ligands is crucial for the biological activity of the photoproducts. Pyridines remain coordinated to the platinum center upon irradiation, avoiding the typical condensation and fragmentation of cell nuclei caused by cisplatin.

More recent efforts in the development of photoactivatable Pt<sup>IV</sup> prodrugs aimed at improving cell uptake and cancer cell targeting. In 2014, the group of Sadler exhaustively evaluated the lipophilicity of ten photoactivatable Pt<sup>IV</sup> diazido prodrugs of formula *trans,trans,trans*-[Pt(N<sub>3</sub>)<sub>2</sub>(OH)<sub>2</sub>(R)(R')] (where R and R' are NH<sub>3</sub>, methylamine, ethylamine, pyridine, 2-picoline, 3-picoline or thiazole), among which complexes **4** and **5**, in order to correlate lipophilicity with anticancer activity. Lipophilicity is an important feature in the design of drug because it plays a key role in the passive influx of drug molecules into cells. The lipophilicity of the Pt<sup>IV</sup> diazido complexes investigated show a linear dependence based on this hydrophobic nature of the coordinated ligands. However, *in vitro* results show no correlation between lipophilicity and

intracellular accumulation of platinum, probably suggesting the involvement of active transport and favored influx of selected structures. Furthermore, no correlation between platinum accumulation and photocytotoxicity was observed in A2780 cancer cells, implying that the type of intracellular damage induced by these complexes, rather than their abundance, plays a key role in their cytotoxic effect.<sup>27</sup>

Adding targeting capability to Pt<sup>IV</sup> complexes was the following step in the design of more effective prodrug candidates. In 2015, Marchán and coworkers reported a new anticancer agent by conjugating a Pt<sup>IV</sup> diazido complex to a cyclic RGD-containing peptide (**6**). This targeting moiety is selectively recognized by  $\alpha_v\beta_3$  and  $\alpha_v\beta_5$  integrins (Figure 8) in order to increase selectivity for cancer cells.<sup>28</sup> Upon visible light irradiation (420 nm, 5 J cm<sup>-2</sup>), phototoxicity was induced preferentially in SK-MEL-28 melanoma cancer cells, which overexpress  $\alpha_v\beta_3$  integrin compared to control DU-145 human prostate cancer cells. This clearly indicates that peptide conjugation had a positive effect on the intracellular accumulation of the photoactivatable Pt<sup>IV</sup> prodrug. Notably, platinum accumulation in SK-MEL-28 cells after exposure to conjugate was higher (about 2.8-fold) than in control DU-145 cells. The intracellular accumulation of the conjugate in MBAMD-468 (breast carcinoma cell line) was also higher than in DU-145 cells (about 3.6-fold) despite the very low expression of  $\alpha_v\beta_3$  integrin in the breast carcinoma cell line. These results suggest that the internalization of the Pt–c(RGDfK) conjugate mediated by  $\alpha_v\beta_5$  integrin occurs as well. Additionally, the phototoxicity of **6** in SK-MEL-28 (IC<sub>50</sub> = 19.5  $\mu$ M) was similar to that of the parent succinylated complex (IC<sub>50</sub> = 15.5  $\mu$ M).

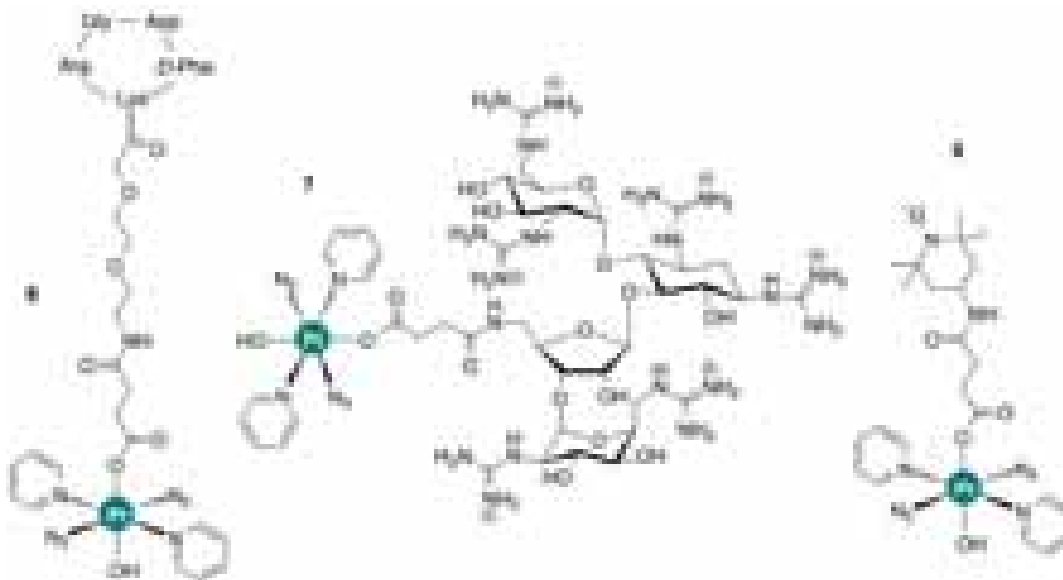


**Figure 8.** *Trans,trans,trans*-[Pt(N<sub>3</sub>)<sub>2</sub>(OH)<sub>2</sub>(py)<sub>2</sub>] conjugated with a cyclic peptide containing the RGD sequence (–Arg–Gly–Asp–) (**6**); *trans,trans,trans*-[Pt(N<sub>3</sub>)<sub>2</sub>(OH)(succ)(py)<sub>2</sub>] (succ = succinylate, py = pyridine), has been conjugated to guanidinoneomycin (**7**); and *trans,trans,trans*-[Pt(N<sub>3</sub>)<sub>2</sub>(Py)<sub>2</sub>(OH)(succinate)] conjugated with TEMPO (**8**).

Sadler and Marchán also conjugated a photoactivated Pt<sup>IV</sup> diazido complex to guanidinoneomycin (**7**) (Figure 8), a known RNA-binding ligand able to transport large bioactive cargos into cells in a selective and proteoglycan-dependent manner.<sup>29</sup> The aim of using this polycationic compound as targeting ligand is to promote the intracellular accumulation of the phototoxic Pt<sup>IV</sup> prodrug in cancer cells. Under visible-light irradiation ( $\lambda_{\text{max}}= 420 \text{ nm}$ ,  $5 \text{ J cm}^{-2}$ ), **7** can potentially promote platination of RNA over DNA what may lead to chemotherapeutic agents with a novel mechanism of action. Cellular uptake studies showed that guanidinoneomycin conjugation improves the intracellular accumulation of the Pt<sup>IV</sup> agent in two cancer cell lines, and particularly in SK-MEL-28 cells. Notably, the higher phototoxicity of the conjugate in SK-MEL-28 cells than in DU-145 cells suggests a degree of selectivity towards the malignant melanoma cell line. Moreover, it was demonstrated that the photoactivation of the Pt–guanidinoneomycin conjugate in the presence of 5'-GMP lead to the formation of *trans*-[Pt(N<sub>3</sub>)(py)<sub>2</sub>(5'-GMP)]<sup>+</sup>, as does the parent Pt<sup>IV</sup> complex.

Adopting a similar synthetic strategy, a stable free radical TEMPO (2,2,6,6-tetramethylpiperidine-1-oxyl) was incorporated in the axial position of *trans,trans,trans*-[Pt(N<sub>3</sub>)<sub>2</sub>(Py)<sub>2</sub>(OH)(succinate)] (**8**) (Figure 8).<sup>30</sup> Upon 420-nm light excitation, the reduction in LMCT band was monitored in aqueous solution by UV-Vis and EPR (Electron paramagnetic spectroscopy). Results indicated that the complex undergoes loss of an azido ligand and/or electron transfer from the azido ligands to the Pt<sup>IV</sup> center, resulting in the formation of azidyl radicals and Pt<sup>IV/II</sup> species. The photocytotoxicity of **8** (50 mW at 465 nm for 1 h) increases by 1.2 times against A2780 ovarian cancer cells compared with its parent analogue. The biological action was ascribed to the attack on DNA by the Pt<sup>II</sup> photoproducts as well as to the activity of the reactive azidyl radicals and antioxidant properties of the TEMPO ligand.

In 2017, the Sadler group described a new strategy to design hydrogels that can deliver photoactivatable Pt<sup>IV</sup> anticancer complexes to cancer cells.<sup>31</sup> Incorporation of *trans,trans,trans*-[Pt(N<sub>3</sub>)<sub>2</sub>(Py)<sub>2</sub>(OH)(succinate)] coupled with dopamine (**9**) into the non-toxic G<sub>4</sub>K<sup>+</sup>B hydrogel, a G-quadruplex formed by guanosine-borate units (Figure 9) dramatically increases its photocytotoxic potency toward cisplatin-resistant human ovarian cancer cells (cisplatin-resistant A2780Cis). The **9**-G<sub>4</sub>K<sup>+</sup>B hydrogel displays activity against A2780Cis in the dark (IC<sub>50</sub> = 16 μM), but is significantly more potent (IC<sub>50</sub> = 3 μM) upon irradiation (1 h, 465 nm, 50 mW) with a PI of 5.6. In order to evaluate the cytotoxic selectivity between cancer and healthy cells, the same conditions employed for A2780Cis cells were applied to MRC-5 normal lung fibroblasts. Both **9** and **9**-G<sub>4</sub>K<sup>+</sup>B hydrogels are nontoxic toward MRC-5 (IC<sub>50</sub> > 50 μM) giving a photocytotoxicity selectivity factor (ratio of the activity between normal and cancer cells) of >18 for the **9**-G<sub>4</sub>K<sup>+</sup>B hydrogel. This result is an early indication of the possibility of reducing unwanted side effects by the use of hydrogels as a delivery strategy.



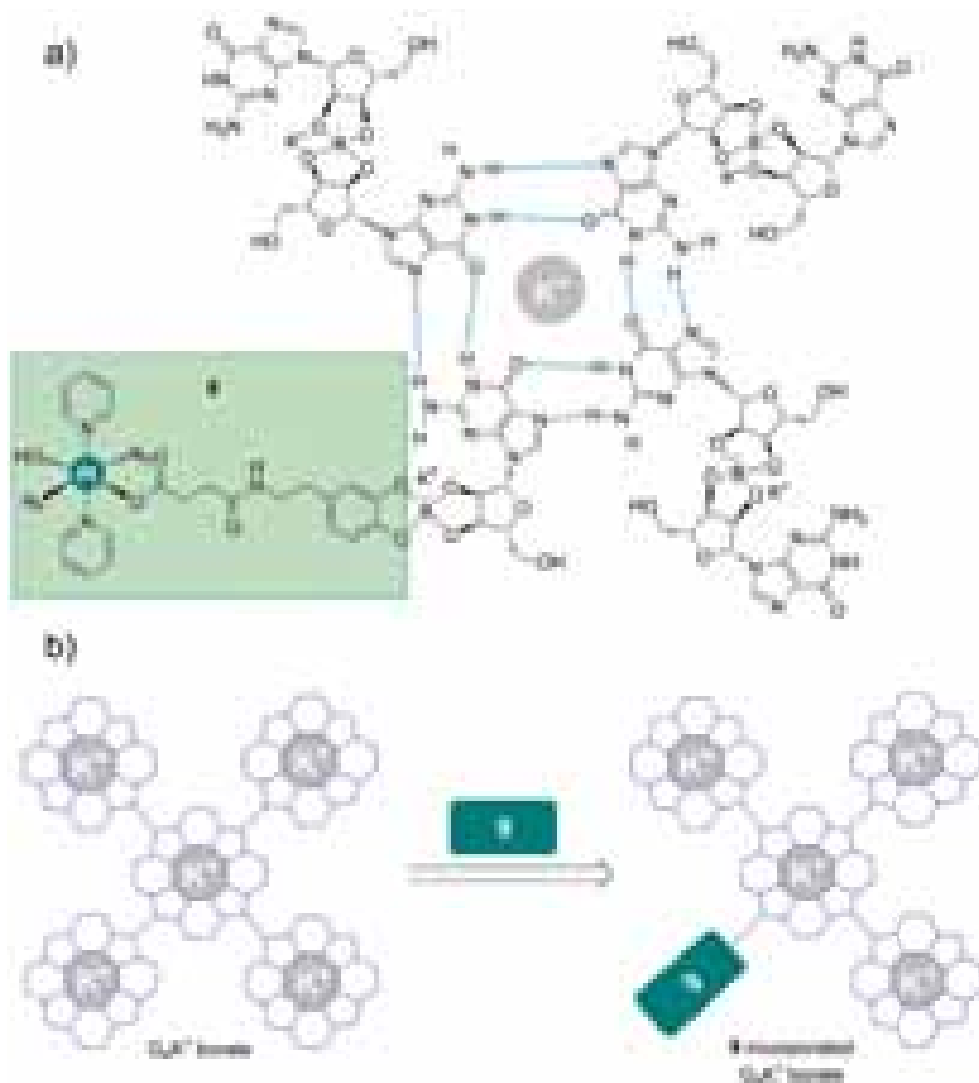


**Figure 9.** a) Complex **9** obtained reacting dopamine hydrochloride with *trans,trans,trans*-[Pt(N<sub>3</sub>)<sub>2</sub>(Py)<sub>2</sub>(OH)(succinate)] and its structural interaction with guanosin-borate G<sub>4</sub> quadruplex; b) Schematic incorporation of **9** into G<sub>4</sub>K<sup>+</sup> borate hydrogel.

### ***1.3 Strategies for the enhanced photoactivation of Pt<sup>IV</sup> prodrugs***

Photoactivatable Pt<sup>IV</sup> anticancer prodrugs generally suffer from poor absorption profiles. Therefore, complementary strategies to delivery cytotoxic Pt<sup>II</sup> species at convenient excitation wavelengths have been explored. Following an approach earlier devised for Ru complexes by Alessio and coworkers,<sup>32</sup> metal complexes were

conjugated with porphyrins which absorb light in the red part of the visible, acting as antennas. Conjugates of this type, behave both as PDT and photochemotherapy agents due to the presence of the metal complex. This is the case of tetraplatinated porphyrins described by the group of Spingler,<sup>33</sup> whose conjugates can interact with DNA by both intercalation and platinum binding modes. Other delivery systems are based on biocompatible nanomaterials, such as inorganic or polymeric nanoparticles, that serve as vehicles for the photoactivatable anticancer drugs.<sup>11</sup>

New emerging approaches permit the transport and delivery of Pt<sup>IV</sup> prodrugs as well as their photoactivation by using light-irradiation wavelengths in the therapeutic window (600 – 1000 nm). In addition, they can act as a theranostic agent by combining therapeutic and multimodal imaging capabilities.

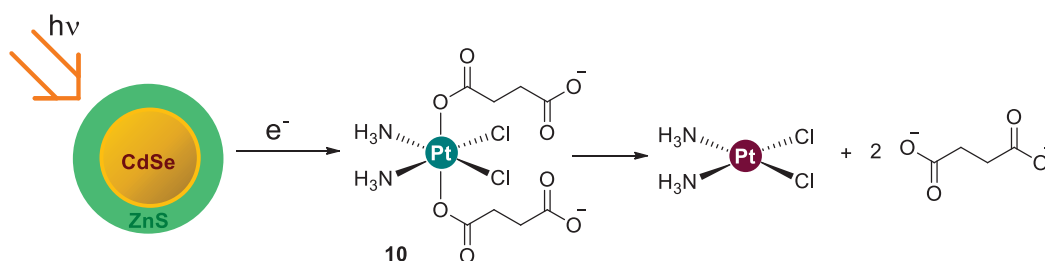


**Figure 10.** Schematic representation of the QDs photoactivation of **10** upon visible light irradiation (630 nm).

Mareque and coworkers demonstrated that core-shell CdSe–ZnS quantum dots (QDs) efficiently photoactivate a series of Pt<sup>IV</sup> complexes via ET (electron transfer) using visible light up to 630 nm, a wavelength currently in use for clinical PDT.<sup>19,34,35</sup> The two Pt<sup>IV</sup> complexes studied were [PtCl<sub>4</sub>(bpy)] (bpy = 2,2'-bipyridine) and *cis,cis,trans*-[Pt(NH<sub>3</sub>)<sub>2</sub>Cl<sub>2</sub>(O<sub>2</sub>CCH<sub>2</sub>CH<sub>2</sub>CO<sub>2</sub>H)<sub>2</sub>] (**10**) (Figure 10). After 1 h in the presence of QD, around 2000–2200 molecules of Pt<sup>II</sup> were generated per QD using low power visible laser light in the case of [PtCl<sub>4</sub>(bpy)].<sup>34</sup> Concerns regarding the toxicity of these systems exist, however no significant toxicity was found when employing micellar QDs loaded with **10** at concentrations required to photogenerate cisplatin. Additionally, the authors demonstrated the capability of micellar QD formulations to be radiolabelled with the *fac*-[<sup>99m</sup>Tc(OH<sub>2</sub>)<sub>3</sub>(CO)<sub>3</sub>]<sup>+</sup> complex, and therefore their capability to be used as theranostic agents for imaging (SPECT and optical imaging) as well as for photochemotherapy.<sup>35</sup>

Upconverting nanoparticles (UCNPs) are also a promising multimodal tool for the activation of metal-based prodrugs. This type of nanomaterials is typically composed by an inorganic host lattice (i.e. NaYF<sub>4</sub>, NaGdF<sub>4</sub>, NaLuF<sub>4</sub>, KYF<sub>4</sub>), activator ions (Er<sup>3+</sup>, Tm<sup>3+</sup>, Ho<sup>3+</sup>) and sensitizer ions (i.e. Yb<sup>3+</sup>). Upon near infrared (NIR) light excitation, these lanthanide-doped UCNPs undergo an anti-Stokes process which converts the absorbed low-energy NIR (980 or 808nm) light into UV and visible photons. The upconverted emission has been used to photoactivate the NO-releasing Roussin's Black Salt<sup>36</sup> and also to promote the ligand photodissociation of Ru polypyridyl complexes.<sup>37</sup> UCNPs have also shown promising properties as optical, MRI, and PET/SPECT imaging probes integrating suitable features for theranostics.<sup>38</sup>

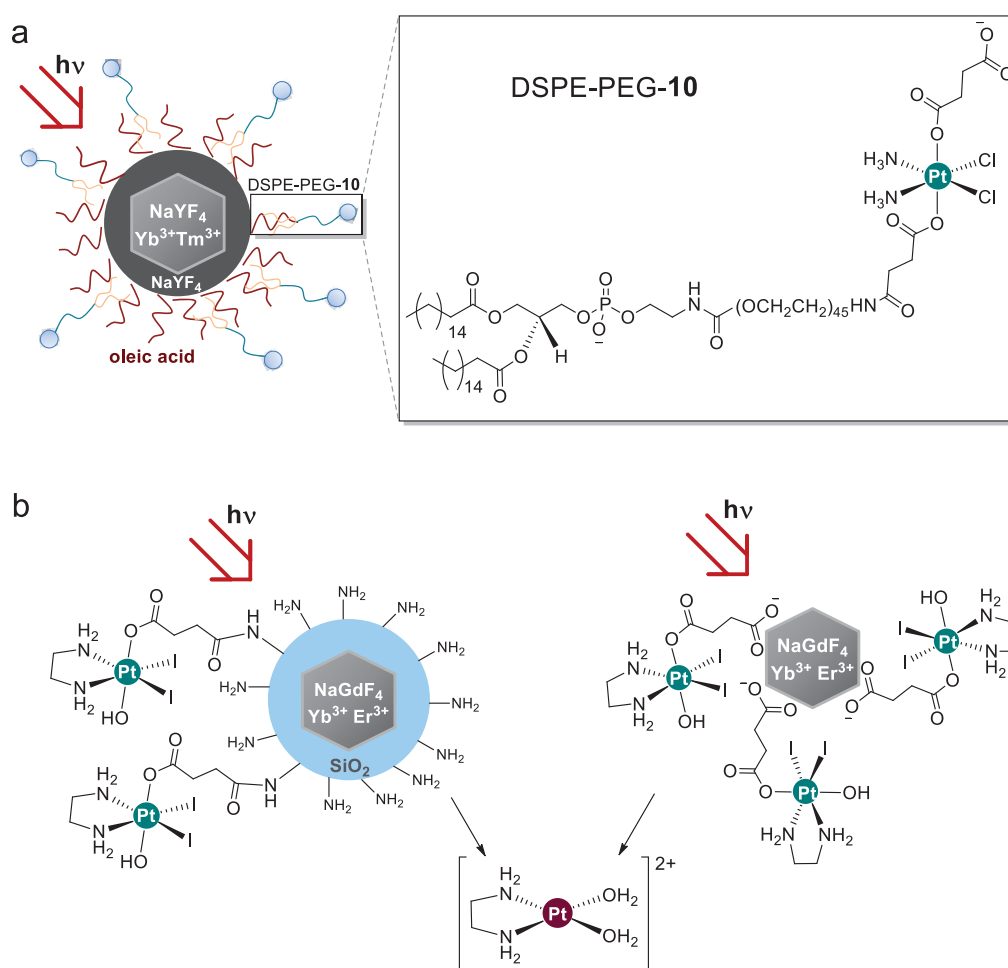


**Figure 11. a)** core-shell upconversion nanoparticles (UCNP) decorated with conjugated DSPE-PEG and complex **10**; **b) i:** *cis,trans*-[Pt(en)(I)<sub>2</sub>(O<sub>2</sub>CCH<sub>2</sub>CH<sub>2</sub>CO<sub>2</sub>H)(OH)] (where en = ethylenediamine) covalently linked to silica-coated UCNPs and **ii:** *cis,trans*-[Pt(en)(I)<sub>2</sub>(O<sub>2</sub>CCH<sub>2</sub>CH<sub>2</sub>CO<sub>2</sub>)(OH)]<sup>-</sup> electrostatically anchored to UCNP. Both UCNP nanoconstructs released the photoproduct [Pt(H<sub>2</sub>O)<sub>2</sub>(en)]<sup>2+</sup>.

## Chapter 1a

Our group reported the photoactivation of the Pt<sup>IV</sup> complex *cis,cis,trans*-[Pt(NH<sub>3</sub>)<sub>2</sub>(Cl)<sub>2</sub>(O<sub>2</sub>CCH<sub>2</sub>CH<sub>2</sub>CO<sub>2</sub>H)<sub>2</sub>] (**10**) by near infrared light (980 nm) using NaYF<sub>4</sub>:Yb<sup>3+</sup>/Tm<sup>3+</sup>@NaYF<sub>4</sub> core-shell upconversion nanoparticles (UCNPs) (Figure 11a).<sup>39</sup> The cisplatin precursor was coupled with the biocompatible PEGylated phospholipid DSPE-PEG(2000)-NH<sub>2</sub> (DSPE-PEG-**10**) (Figure 11a), affording a promising strategy to decorate the surface of the nanoparticles. This hybrid photoactivatable nanomaterials was capable of releasing Pt<sup>II</sup> species upon NIR light excitation ( $\lambda_{\text{exc}} = 980 \text{ nm}$ ,  $7.3 \text{ W} \cdot \text{cm}^{-2}$ ). <sup>1</sup>H NMR confirmed the release of the axial succinate ligands after 3.5 h of 980-nm irradiation and XPS indicated that UCNPs decorated with DSPE-PEG-**10** fully converted Pt<sup>IV</sup> into Pt<sup>II</sup> at the end of the photoreaction.

Bednarski *et al.* applied the use of UCNPs for the photoactivation of diiodido-Pt<sup>IV</sup> complexes at 980 nm.<sup>40</sup> Two different approaches were employed for loading the Pt<sup>IV</sup> complexes on the UCNPs (Yb,Er- and Yb,Tm-doped  $\beta$ -NaGdF<sub>4</sub>): (i) covalent attachment of the Pt<sup>IV</sup> complex via amide bonds on the silica-coated surface of the UCNPs; and (ii) electrostatic interactions between the UCNPs surface and diiodido-Pt<sup>IV</sup> carboxylato complexes (Figure 11b).

*In vitro* results on human leukemia HL60 cells indicated a substantial increase in cytotoxicity when both modified Pt<sup>IV</sup>-UCNPs are combined with five rounds of 30 min NIR light irradiation (980 nm,  $1.2 \text{ W/cm}^2$ ) compared to dark controls. However, NIR light alone also has a significant cytotoxic effect, 70 % reduction in cell vitality, at the same time exposure. The activated products are able to platinate calf thymus DNA. The main drawback of the systems developed by Bednarski was the limited stability of the diiodido- Pt<sup>IV</sup> complexes on the UCNP surface, where only 20% of the Pt loaded on the surface of both UCNP nanoconstructs did not undergo reduction as measured by XPS.

UCNP-based hybrid nanomaterials have the potential to overcome the poor absorption properties of metal complexes in the visible. The low toxicity (both *in vitro* and *in vivo*) of UCNPs with respect to other nanomaterials and their multimodal imaging capability are key advantages to exploit for novel applications in nanomedicine. Despite photoactivation reactions were accomplished employing these UCNP systems, there is

still need for significant improvements in the upconversion yield and optimization of the surface functionalization. This is mandatory in order to decrease the power density employed, and achieve safe application of NIR light sources *in vitro* and future *in vivo* studies.

## 1.4 References

- 1 B. Rosenberg, L. Vancamp and T. Krigas, *Nature*, 1965, **205**, 698–699.
- 2 U. Ndagi, N. Mhlongo and M. E. Soliman, *Drug Des. Dev. Ther.*, 2017, **11**, 599–616.
- 3 H. P. Varbanov, M. A. Jakupec, A. Roller, F. Jensen, M. Galanski and B. K. Keppler, *J. Med. Chem.*, 2013, **56**, 330–344.
- 4 E. Alessio and L. Messori, in *Metallo-drugs: Development and Action of Anticancer Agents*, De Gruyter, Berlin, Boston, 2018, vol. 18. Chapter 5.
- 5 S. Dasari and P. B. Tchounwou, *Eur. J. Pharmacol.*, 2014, **740**, 364–378.
- 6 W. Ansell and J. Shamash, *Int. J. Urol. Nurs.*, 2008, **2**, 103–112.
- 7 T. C. Johnstone, K. Suntharalingam, and S. J. Lippard, *Chem. Rev.*, 2016, **116**, 3436–3486.
- 8 E. Wexselblatt and D. Gibson, *J. Inorg. Biochem.*, 2012, **117**, 220–229.
- 9 J. Mayr, P. Heffeter, D. Groza, L. Galvez, G. Koellensperger, A. Roller, B. Alte, M. Haider, W. Berger, C. R. Kowol and B. K. Keppler, *Chem. Sci.*, 2017, **8**, 2241–2250.
- 10 D. Gibson, *Dalton Trans.*, 2016, **45**, 12983–12991.
- 11 V. Venkatesh and P. J. Sadler, in *Metallo-Drugs: Development and Action of Anticancer Agents*, De Gruyter, Berlin, Boston, 2018, vol. 18. Chapter 3.
- 12 P. Agostinis, K. Berg, K. A. Cengel, T. H. Foster, A. W. Girotti, S. O. Gollnick, S. M. Hahn, M. R. Hamblin, A. Juzeniene, D. Kessel, M. Korbelik, J. Moan, P. Mroz, D. Nowis, J. Piette, B. C. Wilson and J. Golab, *CA-Cancer J. Clin.*, 2011, **61**, 250–281.
- 13 D. van Straten, V. Mashayekhi, H. de Bruijn, S. Oliveira, D. Robinson, D. van Straten, V. Mashayekhi, H. S. de Bruijn, S. Oliveira and D. J. Robinson, *Cancers*, 2017, **9**, 19.
- 14 J. Yao, J. Feng and J. Chen, *Asian J. Pharm.*, 2016, **11**, 585–595.
- 15 Health Canada Approves Clinical Trial Application for Anti-Cancer Drug, <http://theralase.com/pressrelease/health-canada-approves-clinical-trial-application-anti-cancer-drug/>

- 16 TOOKAD® Soluble, Approved for Prostate Cancer Therapy in Mexico, <http://www.yedarnd.com/articles/tookad%C2%AE-soluble-approved-prostate-cancer-therapy-mexico>
- 17 N. J. Farrer, L. Salassa and P. J. Sadler, *Dalton Trans.*, 2009, **48**, 10690–10701.
- 18 N. Ahmad and H. Mukhtar, in *Methods in Enzymology*, Academic Press, 2000, vol. 319, pp. 342–358.
- 19 I. Infante, J. M. Azpiroz, N. G. Blanco, E. Ruggiero, J. M. Ugalde, J. C. Mareque-Rivas and L. Salassa, *J. Phys. Chem. C*, 2014, **118**, 8712–8721.
- 20 C. Garino and L. Salassa, *Philos. T. R. Soc. A*, 2013, **371**, 20120134–20120134.
- 21 B. Rosenberg, L. V. Camp, E. B. Grimley and A. J. Thomson, *J. Biol. Chem.*, 1967, **242**, 1347–1352.
- 22 N. A. Kratochwil, P. J. Bednarski, H. Mrozek, A. Vogler and J. K. Nagle, *Anti-cancer Drug Des.*, 1996, **11**, 155–171.
- 23 N. A. Kratochwil, M. Zabel, K.-J. Range and P. J. Bednarski, *J. Med. Chem.*, 1996, **39**, 2499–2507.
- 24 P. J. Bednarski and F. S. M. and P. J. Sadler, *Anti-cancer Agent Me.*, 2007, **7**, 75–93.
- 25 A. F. Westendorf, J. A. Woods, K. Korpis, N. J. Farrer, L. Salassa, K. Robinson, V. Appleyard, K. Murray, R. Grünert, A. M. Thompson, P. J. Sadler and P. J. Bednarski, *Mol. Cancer Ther.*, 2012, **11**, 1894–1904.
- 26 N. J. Farrer, J. A. Woods, L. Salassa, Y. Zhao, K. S. Robinson, G. Clarkson, F. S. Mackay and P. J. Sadler, *Angew. Chem. Int. Ed.*, 2010, **49**, 8905–8908.
- 27 A. M. Pizarro, R. J. McQuitty, F. S. Mackay, Y. Zhao, J. A. Woods and P. J. Sadler, *ChemMedChem*, 2014, **9**, 1169–1175.
- 28 A. Gandioso, E. Shaili, A. Massaguer, G. Artigas, A. González-Cantó, J. A. Woods, P. J. Sadler and V. Marchán, *Chem. Commun.*, 2015, **51**, 9169–9172.
- 29 E. Shaili, M. Fernández-Giménez, S. Rodríguez-Astor, A. Gandioso, L. Sandín, C. García-Vélez, A. Massaguer, G. J. Clarkson, J. A. Woods, P. J. Sadler and V. Marchán, *Chem. Eur. J.*, 2015, **21**, 18474–18486.
- 30 V. Venkatesh, C. J. Wedge, I. Romero-Canelón, A. Habtemariam and P. J. Sadler, *Dalton Trans.*, 2016, **45**, 13034–13037.

## Chapter 1a

- 31 V. Venkatesh, N. K. Mishra, I. Romero-Canelón, R. R. Vernooij, H. Shi, J. P. C. Coverdale, A. Habtemariam, S. Verma and P. J. Sadler, *J. Am. Chem. Soc.*, 2017, **139**, 5656–5659.
- 32 T. Gianferrara, A. Bergamo, I. Bratsos, B. Milani, C. Spagnul, G. Sava and E. Alessio, *J. Med. Chem.*, 2010, **53**, 4678–4690.
- 33 A. Naik, R. Rubbiani, G. Gasser and B. Spingler, *Angew. Chem. Int. Ed.*, 2014, **53**, 6938–6941.
- 34 N. G. Blanco, C. R. Maldonado and J. C. Mareque-Rivas, *Chem. Commun.*, 2009, **35**, 5257–5259.
- 35 C. R. Maldonado, N. Gómez-Blanco, M. Jauregui-Osoro, V. G. Brunton, L. Yate and J. C. Mareque-Rivas, *Chem. Commun.*, 2013, **49**, 3985–3987.
- 36 P. T. Burks, J. V. Garcia, R. GonzalezIrias, J. T. Tillman, M. Niu, A. A. Mikhailovsky, J. Zhang, F. Zhang, and P. C. Ford, *J. Am. Chem. Soc.*, 2013, **135**, 18145–18152.
- 37 E. Ruggiero, S. Alonso-de Castro, A. Habtemariam and L. Salassa, *Dalton Trans.*, 2016, **45**, 13012–13020.
- 38 J. Zhou, Q. Liu, W. Feng, Y. Sun, and F. Li, *Chem. Rev.*, 2015, **115**, 395–465.
- 39 E. Ruggiero, J. Hernández-Gil, J. C. Mareque-Rivas and L. Salassa, *Chem. Commun.*, 2015, **51**, 2091–2094.
- 40 S. Perfahl, M. M. Natile, H. S. Mohamad, C. A. Helm, C. Schulzke, G. Natile and P. J. Bednarski, *Mol. Pharm.*, 2016, **13**, 2346–2362.



# 1b

## Flavins and Flavoproteins



## 1.1 Introduction

Flavin (from Latin *flavus*, "yellow") is the term commonly used to define a family of yellow-colored compounds containing the basic structure 7,8-dimethyl-10-alkyl isoalloxazine. Riboflavin (Rf), also known as vitamin B<sub>2</sub>, is an essential component of living organisms and the precursor of all biologically relevant flavins.<sup>1</sup>

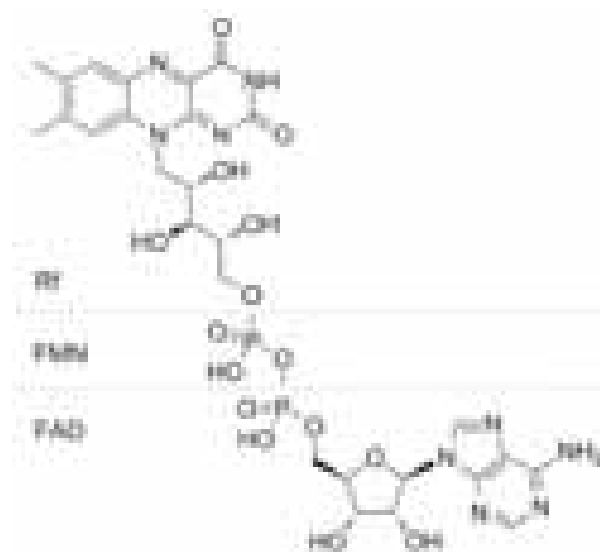


**Figure 1.** Chemical structures of riboflavin (Rf), flavin mononucleotide (FMN), and flavin adenine dinucleotide (FAD).

As such, Rf is an important component of our diet, found in nutrients such as milk, eggs, cereals and grains, some meats, and green vegetables. Upon ingestion, Rf is diversely distributed in tissues, but little is present as free Rf. Once internalized into cells, the majority of riboflavin is found as flavin adenine dinucleotide (FAD), and in smaller amounts as flavin mononucleotide (FMN) (Figure 1).<sup>1</sup>

These flavin cofactors have the ability to participate in one and two electron transfer processes. Flavins exist in three forms depending on their redox state and pH: oxidized, one-electron reduced (semiquinone) and two-electron reduced (Figure 2). Therefore, flavins are very versatile being able to transfer single electrons, hydrogen atoms and hydride ions.<sup>2</sup>

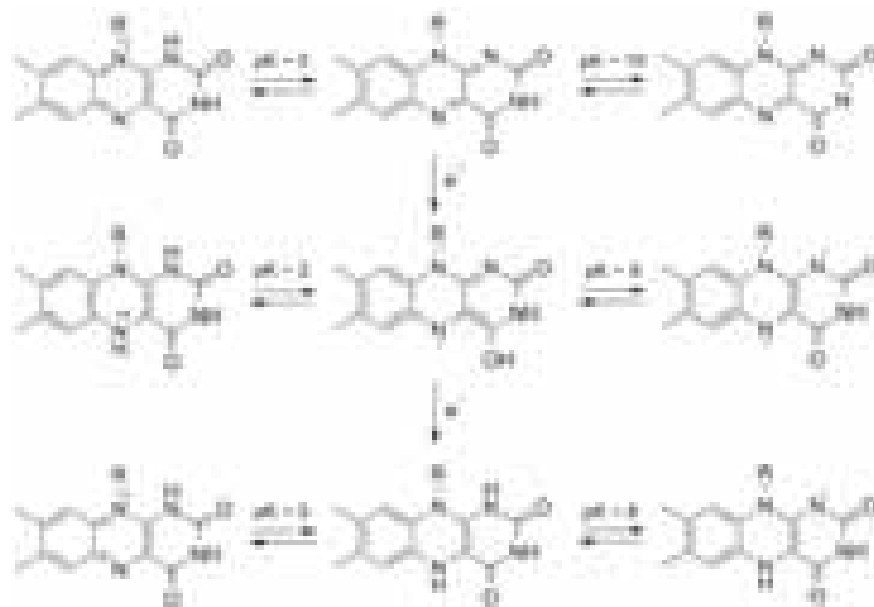


**Figure 2.** Redox and acid-base equilibria of flavins.

At physiological pH, the redox potential of free flavins is around  $E_m = -200$  mV ( $-219$  mV for FAD,  $-205$  mV for FMN, and  $-200$  mV for Rf). These values vary significantly (approx. from  $-400$  mV to  $+60$  mV) in flavin-containing proteins (flavoproteins) because of the protein environment. The proximity of aminoacidic residues with a positive charge may generally produce an increase of the flavin redox potential, while, a negative charge or a hydrophobic environment would reduce it.<sup>3</sup> Furthermore, studies where the target residue of covalently bound FAD in flavoenzymes is mutated, suggest that the covalent interaction would contribute to increase the oxidative power of the flavin.<sup>4</sup>

Oxidized flavins present good absorption (molar absorptivities  $> 10^4$   $M^{-1}cm^{-1}$ ) in the UV and visible part of the spectrum, displaying four peaks at 445, 375, 265 and 220 nm which all correspond to  $\pi \rightarrow \pi^*$  transitions. When flavins are photoexcited, the intersystem crossing from the singlet to their triplet state is generally efficient. The quantum yields for the triplet formation of Rf and FMN are high, 0.375 and 0.225 respectively. On the contrary, in the case of FAD, the triplet quantum yield is very low due to efficient radiationless decay to the ground state caused by stacking between the isoalloxazine and adenine moieties.<sup>5</sup> The neutral forms of flavins exhibit an intense

yellow-green fluorescence at around 520 nm while their anions and cations are non-fluorescent. The fluorescence quantum yield of Rf in water is 0.28 (pH 7).

Despite flavins are thermostable, they are sensitive to light excitation and have a tendency to photodecompose. In particular, Rf is highly sensitive to UV and visible light undergoing intramolecular photoreductions between the isoalloxazine ring and ribityl side chain, which acts as electron donor in the absence of external reducing agents. Several photoproducts are obtained via oxidation and further fragmentation of the side chain, including cyclodehydroriboflavin (CDRF), formylmethylflavin (FMF), lumichrome (LC), lumiflavin (LF) and carboxymethylflavin (CMF), (Figure 3). Except for lumichrome (LC), the photoproducts show absorption and emission properties similar to Rf. If further oxidized, they are totally decomposed and converted into 2,3-butanedione. However, the Rf photostability can be increased by alkylating the ribityl side chain, such as in the 2',3',4',5'-tetrabutyl ester of Rf.<sup>1</sup>

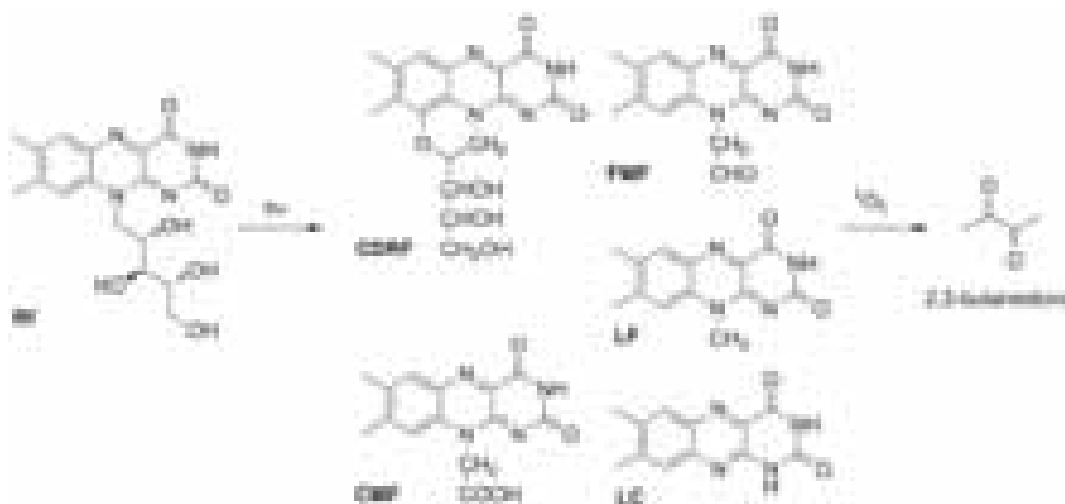


**Figure 3.** Photodegradation products of Rf in the presence of light and O<sub>2</sub>.

Apart from intramolecular reduction, addition and alkylation reactions upon light exposure, Rf can also carry out intermolecular photoreactions.<sup>6</sup> A great variety of photocatalytic processes have been developed using Rf as catalyst and organic substrates. For example, a decarboxylative fluorination of aliphatic carboxylic acids was described by Ye and coworkers.<sup>7</sup> Modified Rfs were used by the group of Cibulka to perform photocatalytic energy transfer [2+2] cycloadditions<sup>8</sup> and stereoselective

## Chapter 1b

photocatalytic esterification of various acids and alcohols.<sup>9</sup> Inspired by Nature's (Z) to (E) photoisomerization of retinal (vitamin A aldehyde), Gilmour and coworkers demonstrated in 2015 the reversed photoisomerization from (E) to (Z) by using Rf and modulating retinal substrate.<sup>10</sup>

Wolf *et al.* described a strategy for the enhancement of the reduction potential of riboflavin tetraacetate by coordinating scandium triflate. This coordinated compound enabled the challenging photocatalytic C–H oxidation of electron-deficient alkylbenzenes and benzyl alcohols.<sup>11</sup> Same photocatalysis was afforded by coordinating the tetraacetate riboflavin with biomimetic non-heme iron complexes.<sup>12</sup> Rf has been reported to photocatalytically perform the direct conversion from biaryl carboxylic acids without the need of substrate pre-functionalization into benzocoumarins. This photoproduct is a coumarin derivative, which has recently emerged as an interesting fluorophore in the bioimaging research.<sup>13</sup>

Another remarkable example of the bearing of Rf is its use as a photocatalyst/photosensitizer in the Mirasol Pathogen Reduction Technology System (Terumo BCT). In this process used to treat both platelet and plasma for blood transfusions, Rf inactivates significant levels of viruses and bacteria upon UV light irradiation.<sup>14</sup> The relevance of this technology is based on its straight forward applicability, the low cost of Rf and the absence of metal additives.

Flavins are present in multiple organisms. In particular, the human genome contains 90 genes encoding for flavin-dependent proteins.<sup>15</sup> Flavoenzymes can catalyze highly diverse reactions, such as oxidation and reduction, monooxygenation, dehydrogenation, and halogenation. However, more than 90% of the flavoproteins are oxidoreductases. Their essential and versatile role in most organisms, make flavoproteins a potential pharmacological target.<sup>16</sup>

Flavoenzymes have also been reported to perform artificial reactions, such as using the modified transient reactive flavin methylene iminium cofactor in enzymes which performs the nucleotide methylation and subsequent nucleotide activation.<sup>17</sup> Another example is the use of the enzyme flavocytochrome c3 (fcc3) to carry out fuel-forming in an artificial photosynthesis reaction. In cells, this enzyme catalyzes hydrogenation

across a C=C double bond (e.g. fumarate to succinate).<sup>18</sup> The versatility of flavin catalysts to adapt to variety of substrates has opened tremendous opportunities in the fields of biocatalysis and organocatalysis.

In this chapter, I briefly describe four selected flavoproteins among others, because these have played an important role in my doctorate project:

NADH oxidase (NOX from *Thermus thermophilus*) catalytically produces reactive oxygen species (ROS) by reducing molecular oxygen to superoxide and hydrogen peroxide in many cellular compartments. The structure of this homodimeric enzyme (22.78 KDa per subunit) consists of a central 4-stranded antiparallel beta-sheets covered by helices, a more flexible domain formed by two helices, and a C-terminal excursion connecting the subunits. The flavin moieties (FAD or FMN) at the active site are easily accessible and are located in a deep open cleft between the subunits.<sup>19</sup>

This flavoprotein is industrially utilized for the *in situ* cofactor regeneration of NADH.<sup>20,21</sup>

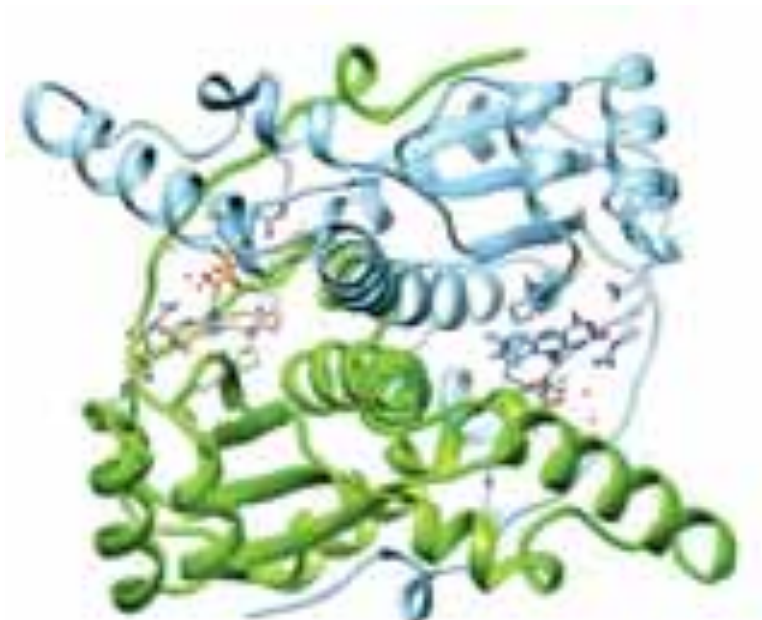


**Figure 4.** Crystal structure of the two subunits of NOX (NADH oxidase from *Thermus thermophilus*) with FMN cofactors using PDB ID 1NOX.

Glucose oxidase (GOX from *Aspergillus niger*) is a flavin-dependent oxidoreductase enzyme composed of two identical 80-kDa subunits with two FAD co-factors

bound. This enzyme catalyzes the oxidation by molecular oxygen of beta-D-glucose to D-glucono- $\delta$ -lactone and hydrogen peroxide. GOX is produced naturally in some fungi and insects, where the hydrogen peroxide generated by the enzyme acts as an anti-bacterial and anti-fungal agent. GOX is an industrially important enzyme used in various applications such as glucose-based enzymatic biosensors and biofuel cells due to its high intrinsic specificity and selectivity for glucose. Recently, its biocatalytic properties have been combined with nanotechnology for biosensor applications.<sup>21</sup>

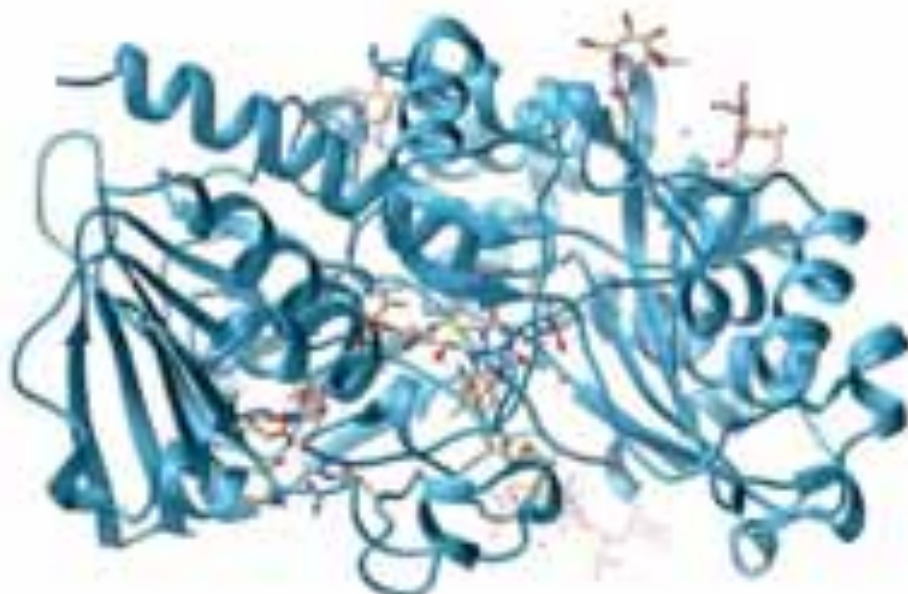


**Figure 5.** Crystal structure of GOX (Glucose oxidase from *Aspergillus niger*) with FAD cofactor using PDB ID 1CF3.

Glutathione reductase (GR from *S. cerevisiae*) is a dimeric flavo-oxidoreductase (118 kDa) involved in the cytoplasmic and mitochondrial redox regulatory systems. GR catalyzes the reduction of glutathione disulfide (GSSG) to the sulfhydryl form glutathione (GSH), using NADPH (nicotinamide adenine dinucleotide phosphate) as electron donor and FAD as coenzyme. GSH is a critical molecule in the cellular management of oxidative stress and in maintaining the reducing environment of the cell.



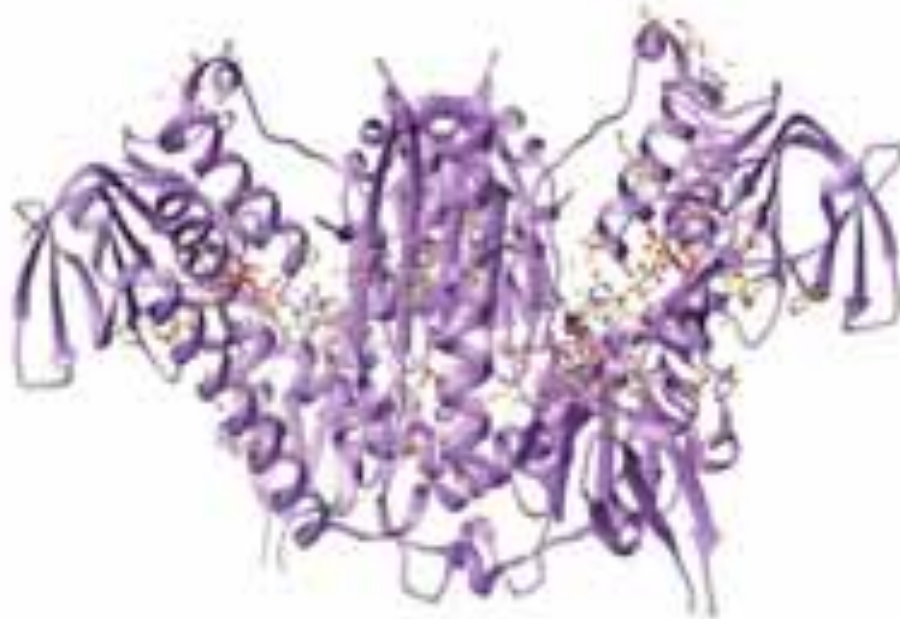


**Figure 6.** Crystal structure of GR (Glutathione reductase from *S. cerevisiae*) with FAD cofactor using PDB ID 2HQM.

miniSOG (for mini Singlet Oxygen Generator) is a fluorescent flavoprotein engineered from *Arabidopsis* phototropin 2 which contains 106 amino acids and FMN (14 kDa).<sup>22</sup> Fluorescent proteins derived from light, oxygen, or voltage (LOV) domains offer advantages as photosensitizers and fluorescent probes due to their small size (advantageous in protein fusions) and efficacy under anaerobic conditions.<sup>23</sup> Upon light excitation, miniSOG has been reported to photosensitize  $^1\text{O}_2$  ( $\Phi = 0.47 \pm 0.05$ ) practically to the same extent as free FMN.<sup>22</sup> However, miniSOG not only produces  $^1\text{O}_2$ , but also undergoes alternative type-I mechanisms involving radical species, in which the photooxidation of substrate anthracene-9,10-dipropionic acid (ADPA) is produced.<sup>24</sup> These findings show that miniSOG might be a potential tool as oxygen-independent fluorescent reporters.

Very recently, MiniSOG has been engineered to form fluorescent flavoprotein heterodimers (~26kDa) with phiLOV2.1, the most photostable flavoprotein known to date. These heterodimers endure photodegradation significantly, as well as combining properties required for appropriate imaging tools such as the photostable fluorescence, ROS photosensitization and/or 3,3'-diaminobenzidine (DAB) photo-oxidation.<sup>25</sup>



**Figure 7.** Crystal structure of miniSOG (mini Singlet Oxygen Generator) with FMN cofactor using PDB ID: 4EET.

## 1.2 References

- 1 A. M. Edwards, in *Flavins*, 2006, pp. 1–11.
- 2 P. F. Heelis, *Chem. Soc. Rev.*, 1982, **11**, 15–39.
- 3 O. Dym and D. Eisenberg, *Protein Sci.*, 2001, **10**, 1712–1728.
- 4 M. W. Fraaije, R. H. H. van den Heuvel, W. J. H. van Berkel and A. Mattevi, *J. Biol. Chem.*, 1999, **274**, 35514–35520.
- 5 S. D. M. Islam, T. Susdorf, A. Penzkofer and P. Hegemann, *Chem. Phys.*, 2003, **295**, 137–149.
- 6 I. Ahmad and F. H. M. Vaid, in *Flavins*, 2006, pp. 13–40.
- 7 X. Wu, C. Meng, X. Yuan, X. Jia, X. Qian and J. Ye, *Chem. Commun.*, 2015, **51**, 11864–11867.
- 8 V. Mojr, E. Svobodová, K. Straková, T. Neveselý, J. Chudoba, H. Dvořáková and R. Cibulka, *Chem. Commun.*, 2015, **51**, 12036–12039.
- 9 M. März, J. Chudoba, M. Kohout and R. Cibulka, *Org. Biomol. Chem.*, 2017, **15**, 1970–1975.
- 10 J. B. Metternich and R. Gilmour, *J. Am. Chem. Soc.*, 2015, **137**, 11254–11257.
- 11 B. Mühldorf and R. Wolf, *Chem. Commun.*, 2015, **51**, 8425–8428.
- 12 B. Mühldorf and R. Wolf, *Angew. Chem. Int. Ed.*, 2015, **55**, 427–430.
- 13 T. Morack, J. B. Metternich and R. Gilmour, *Org. Lett.*, 2018, **20**, 1316–1319.
- 14 J. M. Mundt, L. Rouse, J. Van den Bossche and R. P. Goodrich, *Photochem. Photobiol.*, 2014, **90**, 957–964.
- 15 W.-D. Lienhart, V. Gudipati and P. Macheroux, *Arch. Biochem. Biophys.*, 2013, **535**, 150–162.
- 16 E. Jortzik, L. Wang, J. Ma and K. Becker, in *Flavins and Flavoproteins*, Humana Press, New York, NY, 2014, pp. 113–157.
- 17 C. Bou-Nader, D. Cornu, V. Guerineau, T. Fogeron, M. Fontecave and D. Hamdane, *Angew. Chem. Int. Ed.*, 2017, **129**, 12697–12701.

## Chapter 1b

- 18 A. Bachmeier, B. J. Murphy and F. A. Armstrong, *J. Am. Chem. Soc.*, 2014, **136**, 12876–12879.
- 19 H. J. Hecht, H. Erdmann, H. J. Park, M. Sprinzl and R. D. Schmid, *Nat. Struct. Mol. Biol.*, 1995, **2**, 1109–1114.
- 20 J. Rocha-Martín, D. Vega, J. M. Bolivar, C. A. Godoy, A. Hidalgo, J. Berenguer, J. M. Guisán and F. López-Gallego, *BMC Biotechnol.*, 2011, **11**, 101.
- 21 P. Grunwald, *Biocatalysis and Nanotechnology*, CRC Press, 2017.
- 22 X. Shu, V. Lev-Ram, T. J. Deerinck, Y. Qi, E. B. Ramko, M. W. Davidson, Y. Jin, M. H. Ellisman and R. Y. Tsien, *PLOS Biol.*, 2011, **9**, e1001041.
- 23 A. M. Buckley, J. Petersen, A. J. Roe, G. R. Douce and J. M. Christie, *Curr. Opin. Chem. Biol.*, 2015, **27**, 39–45.
- 24 R. Ruiz-González, A. L. Cortajarena, S. H. Mejías, M. Agut, S. Nonell and C. Flors, *J. Am. Chem. Soc.*, 2013, **135**, 9564–9567.
- 25 A. Rodríguez-Pulido, J. Torra, S. H. Mejías, A. L. Cortajarena, R. Ruiz-González, S. Nonell and C. Flors, *ChemPhotoChem*, 2018, **2**, 571–574.

# 2

## **Bioorthogonal Catalysis in Drug Design**



## 2.1 Introduction

Nature has developed efficient and selective enzymes to perform a myriad of biological functions. Enzymes often employ metals and have inspired chemists in the design of abiotic catalytic processes, which are carried out by coordination or organometallic compounds and occur in complex biological environments. Accordingly, chemical activation and catalytic amplification can be harnessed to efficiently produce in cells bioactive species able to diagnose or cure diseases. Catalysis requires administration of low doses of metals to achieve desired biological effects, potentially diminishing metal toxicity in biological environments. Additionally, different mechanisms of action are normally associated to catalytic drugs, which can in principle help avoiding drug resistances. Yet, performing efficient and selective abiotic catalysis in biological environments is a challenging task because catalysts need to survive and perform in extreme complex habitats, where high concentrations of biomolecules and reactive chemical species can easily interfere and deactivate the whole catalytic process.

In this context, metal-based catalysis has merged with bioorthogonal chemistry to originate bioorthogonal catalysis, a young and thriving field, which has delivered new chemistry concepts and scientific breakthroughs. Bioorthogonal reactions are chemical modifications that can be performed within living biological systems, such as cultured mammalian cells or even complex organisms (e.g. zebrafish or mice) without interfering with their host biochemistry. The term bioorthogonal was coined 15-years ago by Bertozzi to describe the use of Staudinger ligation reactions for the selective modification of glycoproteins with biochemical and biophysical tags.<sup>1,2</sup>

The groups of Mascareñas and Do published this year two excellent review articles<sup>3,4</sup> which summarise the best achievements of bioorthogonal catalysis, specifically highlighting the key role played by organometallic chemistry. The labelling of proteins and membranes with fluorescent dyes (e.g. rhodamine)<sup>5,6</sup> is historically the first scientific achievement of bioorthogonal catalysis. However, a significant portion of the systems developed more recently in the field focuses on the deprotection reactions of allyl and propargyl groups from profluorescent dyes; a proof of concept strategy for demonstrating that catalysis takes place *in vitro* and *in vivo*.<sup>3</sup>

Metal-based catalytic processes specifically devised for therapy are still a minority. This introductory chapter will look at this latter aspect in particular. Herein, I organise an overview of the key concepts introduced in drug development by the combination of catalysis, bioorthogonal chemistry and metallodrug design. Although originated from a different perspective, there is a relatively small number of metallodrugs designed to work as enzyme mimics for the cleavage or modification of targeted biomolecules. They are also part of this specific field and share drug design concepts that are worth including in the chapter. Figure 1 is a schematic representation of the general strategies that have been employed to introduce catalysis in the development of novel drugs.

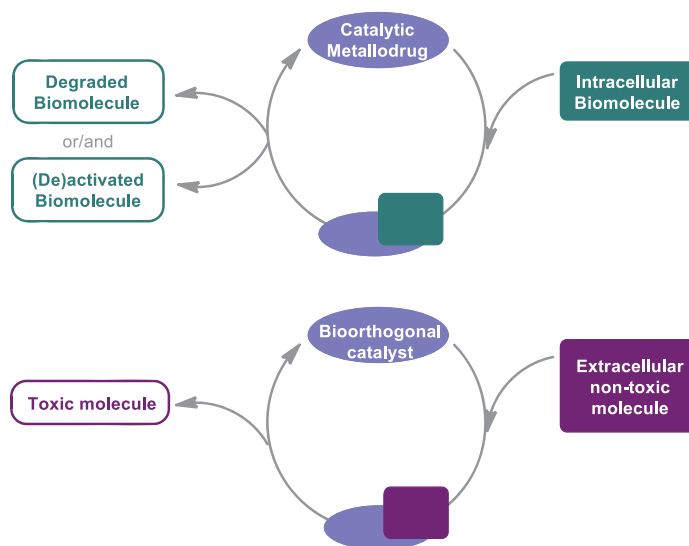


**Figure 1.** Schematic representation of the two main strategies adopted for the design of metallodrugs and bioorthogonal catalysts.

## 2.2 Catalytic metallodrugs targeting biomolecules

Cells depend on fundamental biomolecules such as DNA, RNA and proteins among others, which carry out processes indispensable for their functioning and survival. Catalysis approaches and catalytic metallodrugs have been developed to target and disrupt several of these essential biochemical entities for therapy purposes. The degradation of biomacromolecules (proteins, sugars, lipids and nucleic acids) and the perturbation of the redox balance in cells are the two key approaches explored for the



design of metallodrugs capable of inducing (cancer) cell death through a catalytic mechanism.

### ***Degradation of biomolecules***

Catalytic metallodrugs can exert therapeutic activity by targeting peptides and proteins and favouring their degradation and fragmentation via hydrolysis and oxidation reactions.

The first catalytic metallodrugs capable of cleaving enzymes and shutting down their activity date back to the 90s. The phenanthroline Cu<sup>II</sup> derivative (**1**, Figure 2), for instance, catalyzes the hydrolytic cleavage of carbonic anhydrase enzymes, specifically acting within their active site upon addition of a reducing agent.<sup>7</sup> Analogously, Fe<sup>III</sup> and Cu<sup>II</sup>-containing EDTA-biotin conjugates (**2**, Figure 2) were developed to catalytically produce the oxidative cleavage of streptavidin (a protein with extraordinary high affinity to biotin), selectively when this is in close proximity to its biotin (vitamin B7) binding site.<sup>8</sup>

[Co<sup>III</sup>(cyclen)(OH<sub>2</sub>)<sub>2</sub>]<sup>3+</sup> (**3**, Figure 2) is a peptide-cleaving catalyst that selectively cuts the enzyme peptide deformylase. The complex **3** is described as a potential antibiotic agent since this metalloenzyme is essential for bacterial growth.<sup>9</sup> Suh et al. employed **3** for the hydrolysis (at 310 K and pH 7.4) of amyloids,<sup>10–13</sup> which are insoluble aggregates of peptides or proteins formed in diseases such as Alzheimer's, Parkinson's and Type II diabetes.

A series of metal-based drugs (Cu<sup>II</sup>, Ni<sup>II</sup>, Fe<sup>III</sup> and Co<sup>II</sup>) were prepared using the so-called ATCUN motifs, metal-binding tripeptides present in the N-terminus of several naturally occurring proteins (Figure 2). Among these, the Cu<sup>II</sup> complex **4a**, coordinating as ligand lisinopril, the inhibitor of angiotensin-converting enzyme (ACE), demonstrated the capacity to catalytically cleave ACE, with potential implication in the treatment of hypertension and heart failure.<sup>14</sup>

## Chapter 2

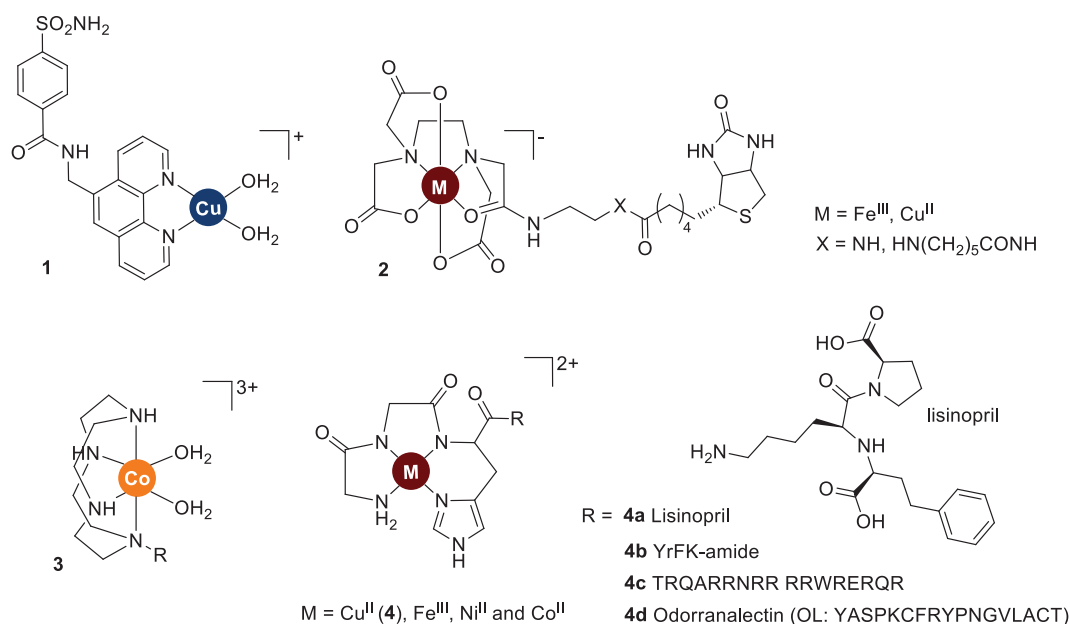


**Figure 2.** Chemical structures of catalytic metallodrugs and ligands employed in the degradation of biomolecules.

Cowan and coworkers redirected the use of ATCUN ligands to the catalytic cleavage of RNA, a process which normally occurs under oxidative stress. They designed a  $\text{Cu}^{\text{II}}$  ATCUN catalytic metallodrug (**4b**, Figure 2) to target hepatitis C via inactivation of its RNA.<sup>15,16</sup> The same group also described that a  $\text{Cu}^{\text{II}}$  ATCUN complexes with a Rev targeting peptide (a cell-penetrating peptide derived from the HIV-1 Rev protein) (**4c**, Figure 2) was able to recognize and catalytically cleave HIV1 RNA in *E. Coli* and in mammalian Jurkat cells.<sup>17,18</sup>

The Cowan group also designed artificial fucosidases (type of glycosidases) based on a Cu ATCUN motif incorporated into a fucose-selective binding domain (**4d**, Figure 2). These exhibit selective carbohydrate cleavage reactivity toward L-fucose over D-glucose.

This synthetic metalloprotein selectively cleaves fucose from the H2-antigen saccharide, enabling in such a way the efficient removal of this antigen from the red blood cells (erythrocytes). The rare Bombay blood type lacks this H2 antigen, which makes extremely difficult finding compatible blood for such patients that would need transfusions. Therefore, the application of this artificial glycosidases on regular human type-O blood with the H2-antigen converts such abundant blood type into a potential blood substitute for patients bearing the rare Bombay blood type.<sup>19</sup> This strategy may

also be applied for the selective degradation of other carbohydrates relevant in other sugar-dependent diseases.

Other examples of metal complexes containing ligands targeting specific peptides and RNA have been reported and reviewed elsewhere.<sup>20–24</sup>

### ***Redox imbalance***

Cells maintain a delicate redox balance by fine-tuning the concentration of oxidizing and reducing agents. This balance can be disrupted by oxidative and reductive stresses, which trigger a mismatch between reactive oxygen species (ROS) and/or reactive nitrogen species (RNS) and intracellular antioxidants. As a result, the structure of biomolecules such as DNA, lipids and proteins may be damaged, and the normal functioning of the cell altered.<sup>25</sup> The redox conditions of cells are crucial in the regulation of gene expression and some signalling pathways. Thus, the modulation of the redox equilibria in cells is an attractive strategy to which applying metal-based catalysts for therapy.

Photodynamic therapy (PDT) is a prototypical example of catalysis-based therapeutic approach that affects the cell redox balance. This clinically approved treatment relies on the photoinduced catalytic production of  $^1\text{O}_2$  and ROS in tumors. Despite several PDT agents have been approved for clinical use,<sup>26</sup> there is an emerging interest in extending the use to transition metal complexes as PDT agents. Metal complexes can be tailored to achieve optimal stability and biodistribution properties and can display relatively intense absorptions in the visible region, and good two-photon absorption cross-sections which enable two-photon excitation with highly-penetrating NIR light.<sup>27</sup> Examples of ROS generating catalysts for PDT include Ru,<sup>28–30</sup> Rh,<sup>31</sup> Ln,<sup>32,33</sup> Tb<sup>34</sup> complexes.<sup>35</sup> Few have emerged as promising PDT agents and are currently under clinical trials including motexafin lutetium (Antrin),<sup>36</sup> tin ethyl etiopurpurin (Purlytin),<sup>37</sup> and the polypyridil Ru complex TLD1433 which has completed clinical trials phase I in 2017.<sup>30</sup>

The enzyme superoxide dismutase (SOD) and its catalytic antioxidant activity have also been investigated in clinical trials for the treatment of age-related macular

## Chapter 2

degeneration.<sup>38</sup> SOD is an endogenous and first-line-of-defense enzyme that eliminates the superoxide anion  $O_2^-$  by catalyzing its dismutation into  $O_2$  and  $H_2O_2$ .<sup>39</sup> If superoxide is not regulated, causes many types of cell damage. Analogously,  $H_2O_2$  is also damaging but it is degraded by other enzymes such as catalase.

Two  $Mn^{II}$  MRI contrast agents (Figure 3), Mangafodipir (MnDPDP) and Calmangafodipir ( $Ca_4Mn(DPDP)_5$ ), have shown activity as SOD analogues. The last is in phase II clinical trials for the treatment of metastatic colorectal cancer.<sup>40,41</sup> A great number of other SOD mimicking complexes have been developed over the years stimulated by these clinical results.<sup>42</sup> Among others, the M40403 (Figure 3) manganese containing superoxide dismutase mimetic is undergoing clinical trials for the treatment of metastatic melanoma and renal carcinoma.<sup>43</sup>

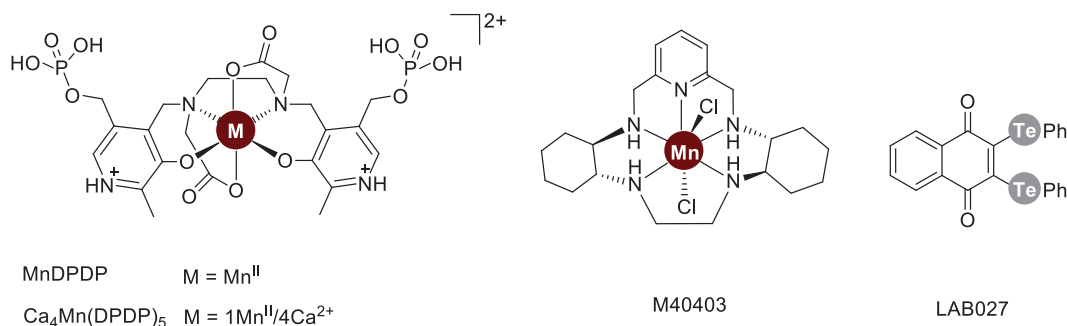


**Figure 3.** Chemical structures of manganese SOD analogues and organotelluride LAB027.

Differently from the previous manganese SOD analogues, the LAB027 derivative associates a quinone core along with two tellurium metalloid centers. The organotelluride redox catalyst is a prototypical member of the 'sensor/effector' family. LAB027 is able to recognize a particular intracellular state of cells, e.g. oxidative stress, and selectively kill the cells that are in such a state. In particular, LAB027 was found to amplify the level of ROS in human HT29 and murine CT26 colon cancer cells generating a lethal oxidative burst. LAB027 was demonstrated to be a potential drug to treat colon cancer, either alone or in combination with oxaliplatin, through a mechanism that involves mainly necrosis.<sup>44</sup>

Thiol groups significantly contribute to preserve the folding and stability of proteins and enzymes. Moreover, thiols also control the redox homeostasis of cells.<sup>45</sup> Glutathione (GSH) is the most important, non-enzymatic antioxidant component together with the nicotinamide adenine dinucleotide phosphate NADPH/NADP<sup>+</sup> couple.<sup>46</sup> GSH is a cysteine-containing tripeptide ( $\gamma$ -L-Glu-L-Cys-Gly), which can be oxidized to glutathione disulfide (GSSG) preventing cellular damage by ROS and RNS.

Sadler and coworkers reported half-sandwich Ru<sup>II</sup> arene complexes coordinating a  $\sigma$ -donor/ $\pi$ -acceptor phenylazopyridine ligand, which confers remarkable inertness toward ligand substitution. In phosphate buffer, the Ru<sup>II</sup> catalyst **5a** and **5b** (1% loading) (Figure 4) oxidized 10 mM GSH efficiently over 24 h, achieving turnover numbers (TON) of 37 and 46, and turnover frequencies (TOF) of 0.30 h<sup>-1</sup> and 0.37 h<sup>-1</sup> respectively. Complexes **5a** and **5b** as well as their *p*-cymene analogues were highly cytotoxic to A2780 human ovarian and the A549 human lung cancer cell lines with IC<sub>50</sub> values of 2–6  $\mu$ M, due to the catalytic reduction in the intracellular GSH concentration.<sup>47</sup>

In addition to redox balance, GSH is responsible for other cellular processes such as detoxification, i.e. conversion of endogeneous and exogeneous toxins into GS-X adducts.<sup>48,49</sup> Ru<sup>II</sup> complexes containing redox-active *o*-phenylenediamine chelating ligands with the formula  $[(\eta^6\text{-arene})\text{Ru}(\textit{o}\text{-phenylenediamine})\text{Cl}]^+$  (arene = *p*-cymene (**6**), hexamethylbenzene or biphenyl) (Figure 4) undergo ligand oxidation producing their *o*-benzoquinonediimine. Interestingly, the benzoquinone complexes can be reduced by the tripeptide GSH but readily undergo reoxidation in air.<sup>50</sup> Nevertheless, this family of Ru<sup>II</sup> complexes show no anticancer effect in lung and ovarian cancer cells (IC<sub>50</sub>>100  $\mu$ M), probably due to the low catalytic efficiency or because of the reoxidation by oxygen.<sup>50</sup>

Recently, Therrien and coworkers demonstrated that two thiolate-bridged Ru<sup>II</sup> arene dimers  $[(\eta^6\text{-arene})_2\text{Ru}_2(\text{SR})_3]^+$  (**7**) and  $[(\eta^6\text{-arene})_2\text{Ru}_2(\text{SR})_2\text{Cl}_2]$  (**8**) (where R includes more than 20 different substituents with variable lipophilicity) (Figure 4) were able to perform catalytic GSH oxidation under physiological conditions. These dimers showed anticancer activity against several cancer cell lines, including cisplatin-resistant ones.

Unfortunately, cytotoxicity results do not correlate with the the catalytic oxidation of GSH determined by NMR. A possible explanation concerning this discrepancy may be found in the different environmental conditions in which the study of the catalytic oxidation is performed, i.e. NMR tubes and not in the presence of live cells. Nevertheless, the catalytic GSH oxidation activity of **7** and **8** cannot be completely ruled out, since the cytotoxicity correlates well with lipophilicity what significantly influences the quantity of Ru uptaken in cells and consequently the effect in the GSH activity.<sup>51,52</sup>

The Ru<sup>II</sup> cage complex  $[(p\text{-cym})_6\text{Ru}_6(2,4,6\text{-tri(pyridine-4-yl)1,3,5-triazine})_2(1,4\text{-benzoquinonato})_3]^{6+}$  (**9**, Figure 4) and its naphthoquinonato analogue are normally synthesized to transport cytotoxic molecules into cancer cells.

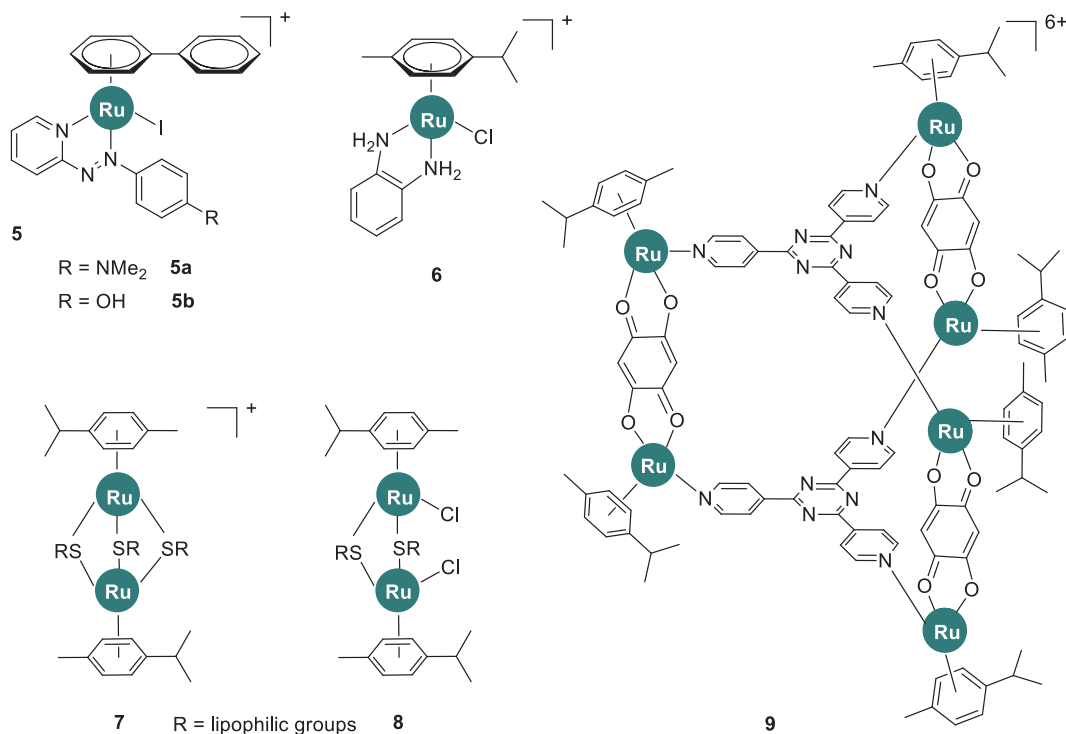


**Figure 4.** Chemical structures of Ru<sup>II</sup> metallodrug catalysts employed in the oxidation of thiols.

However, their capability to catalytically oxidize GSH to GSSH was also demonstrated. The presence of the histidine imidazole group, and the basic amino groups of lysine and arginine were shown to break the hexanuclear structure of **9** and coordinate to the p-cymene Ru<sup>II</sup> unit generating stable adducts.<sup>53,54</sup> In competitive studies, **9** showed to preferentially react to amino groups, while simultaneously oxidizing ascorbic acid,

cystein and GSH to dehydroascorbic acid, cystine, and GSSG, respectively. As a consequence of its oxidizing power, this precatalyst displayed good cytotoxicity profile ( $IC_{50} = 23 \mu\text{M}$ ) against A2780 cancer cells.

The abovementioned studies regarding the catalytic oxidations of thiols have shown promising results, yet the systems discussed lack specificity and can react with other sulphur-containing molecules. Nonetheless, their partial preference for GSH is encouraging for the design of a new generation of catalytic metallodrugs.

Transfer hydrogenation reactions are reduction processes in which a catalyst is able to transfer a hydride ion from a donor to a molecule containing a double bond. In biological relevant conditions, these reductions can be carried out in aqueous solutions using sodium formate as hydride source.<sup>55</sup> Such mild electron donor allows hydride transfer to biomolecules such as nicotinamide adenine dinucleotide (NADH/NAD<sup>+</sup>) or pyruvate. Importantly, cancer cells have a high metabolic rate in which high levels of oxidizing species are generated. This makes cancer cells more sensitive to changes in redox homeostasis, and therefore variation of the NAD<sup>+</sup>/NADH balance can provide an effective strategy to devise new therapies.

Early examples of application of this strategy concerned the development of metal-based catalysts for the generation of NADH in aqueous solution.

Steckhan and coworkers reported the first examples of metal catalysts capable of regenerating NADH via NAD<sup>+</sup> reduction in a buffered solution. Rh<sup>III</sup> bipyridine complexes (e.g. **10**, Figure 5) efficiently catalyzes the reduction of NAD<sup>+</sup> to NADH up to 8.2 regeneration cycles.<sup>56</sup> Süss-Fink and coworkers studied a series of complexes of phenanthroline-containing Ru<sup>II</sup>, Rh<sup>III</sup> and Ir<sup>III</sup> catalysts able to reduce NAD<sup>+</sup>, with Rh<sup>III</sup> and Ir<sup>III</sup> derivatives showing the highest catalytic activity. For example, [(Cp\*)Rh(phen)Cl]<sup>+</sup> (**11**, Figure 5) reached the best TOF value (2000 h<sup>-1</sup>) in aqueous media, twice the efficiency obtained by its bipyridine analogue [(Cp\*)Rh(bipy)Cl]<sup>+</sup>.<sup>57</sup>

A family of Ru<sup>II</sup> complexes containing ethylenediamine or acetylacetonate were investigated for the regioselective and catalytic regeneration of 1,4-NADH in the presence of formate. The hexamethylbenzene (hmb) Ru<sup>II</sup> derivative (**12**, Figure 5) provided the higher TOF value (1.46 h<sup>-1</sup>) in buffer and airtreated solution, although

higher rates were obtained under argon (TOF is  $1.14 \text{ h}^{-1}$  under argon compared with  $0.85 \text{ h}^{-1}$  under air condition). Remarkably, human lung cancer cells appear to tolerate high levels of formate, therefore the catalytic activity of these metal complexes may be proven in cells.<sup>58</sup>

Further development in the design of catalytic metallodrugs may consist in the use of artificial metalloenzymes in order to avoid metal poisoning. Ward and coworkers incorporated biotin into Noyori-type  $\text{Ir}^{\text{III}}$  complexes  $[\text{Cp}^*\text{Ir}(\text{biot-}p\text{-L})\text{Cl}]$  and demonstrated that, this derivative was able to oxidize GSH in combination with oxidizing agents obtaining an increased catalytic activity. In addition, the authors anchored the  $\text{Ir}^{\text{III}}$  complex within streptavidin, and used the resulting compound for asymmetric transfer hydrogenation with different redox enzymes which depend on NADH,  $\text{FADH}_2$  (reduced flavin adenine dinucleotide) and haem cofactors.<sup>59</sup> The therapeutic potential of the approach proposed by the Ward group still needs to be proven in cancer cell models.

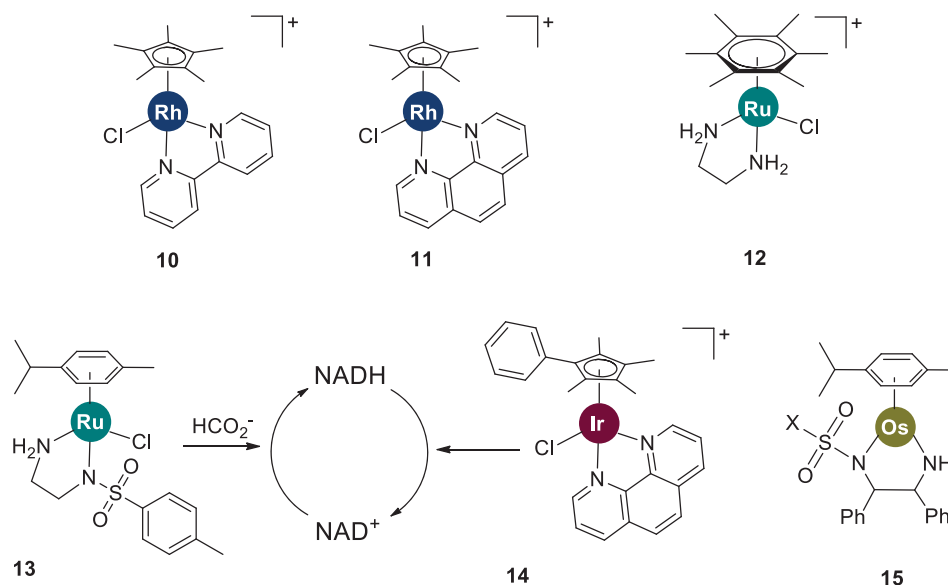


**Figure 5.** Chemical structures of metallodrug catalysts for transfer hydrogenation reactions.

Water-soluble Noyori-type  $\text{Ru}^{\text{II}}$  sulfonamide ethyleneamine complexes, such as **13** (Figure 5), have demonstrated to reduce  $\text{NAD}^+$  to NADH with higher TOFs (TOF =  $0.2\text{--}7 \text{ h}^{-1}$ ) than compound **12**. For this reason, they were evaluated in A2780 ovarian cancer, where they could reduce the levels of  $\text{NAD}^+$  by co-administration of sodium formate.



The antiproliferative potency of these complexes was comparable to that of cisplatin.<sup>60</sup> On the contrary, the Ir<sup>III</sup> complex [(Cp<sup>X</sup>)Ir(phen)H<sub>2</sub>O]<sup>2+</sup> (**14**, Figure 5) is able to accept hydrides from NADH prompting a higher NAD<sup>+</sup>/NADH ratio that alters the mitochondrial membrane potential (MMP), generates oxidative stress via ROS production and finally causes apoptosis in A2780 ovarian cancer cells after 24 h of exposure.<sup>60</sup> In the same manner, the Ir<sup>III</sup> complex [(Cp<sup>Xbiph</sup>)Ir(phpy)py]<sup>+</sup> (phpy = phenylpyridine) utilizes NADH as a biological hydride donor to produce an iridium-hydride complex which generates ROS in cancer cells.<sup>61</sup>

More recently, Sadler and coworkers demonstrated for the first time that the chiral half-sandwich Os<sup>II</sup> arene sulfonyl diamine complexes, as for example [Os(arene)(TsDPEN)] (TsDPEN = N-(p-toluenesulfonyl)-1,2-diphenylethylenediamine) (**15**, Figure 5), are capable to carry out the enantioselective reduction of pyruvate into D-lactate enantiomer in cells using non-toxic concentrations of sodium formate as hydride source.<sup>62</sup> D-lactate is naturally generated inside cells by the glyoxylase enzyme pathway, but it is only produced low concentrations compared with the L-lactate enantiomer. Importantly, the variation of this equilibrium can perturb cell pathways. Complex **15** displays high stability in both aqueous and DMSO solutions in the presence of cell culture media over 24 hours (310 K). TOF values of all the osmium complexes described were higher than the ruthenium analogues in the cetophenone reduction catalysis by a factor of 3.5, and values reached up to 78 h<sup>-1</sup>. They showed toxic effect in A2780 ovarian cancer cells and more remarkably, a novel mechanism of anticancer activity which is not related to DNA damage. Other unsaturated substrates of the cytosol may be targeted to yield a multitargeted mechanism of action for the drug.

### ***2.3 Bioorthogonal metal-based catalysis towards extracellular substrates***

Different catalysis concepts have been adopted to generate organic drugs directly in the cellular environment for therapy purposes.<sup>3,4,63</sup> These processes use abiotic substrates such as cage compounds or synthesis precursors, and typically rely on

cleavage and deprotection reactions, as well as on cycloadditions. *In situ* catalytic generation of bioactive molecules may give a handle to control the effects of drugs via chemical activation and potentially reduce systemic side effects. Ideally, catalysts are administered at low concentrations, eluding metal toxicity concerns.

The earliest breakthrough in bioorthogonal metal-based catalysis was reported by Streu and Meggers.<sup>64</sup> In 2006, they described the use of the Ru<sup>II</sup> half-sandwich complex [Cp\*<sub>2</sub>Ru(COD)Cl] (where Cp\* = pentamethylcyclopentadienyl and COD = 1,5-cyclooctadiene) (**16**, Figure 6) as catalyst for the conversion of an allylcarbamate-caged rhodamine in HeLa cells. This system was not ideal since exogenous aromatic thiols such as thiophenol (PhSH) were needed to attain a catalytic cycle. Furthermore, PhSH had non-negligible cellular toxicity which prompted the exploration of alternatives for improving application of this strategy *in vitro*.

Few years later, Meggers and coworkers reported that Ru<sup>IV</sup>-quinoline catalysts (**17a** and **b**) were capable of performing allylcarbamate cleavage employing weaker nucleophiles such as GSH, the abundant intracellular bioreductant.<sup>65,66</sup> This remarkable advance allowed performing catalysis in cell without the need of extracellular co-reactants, employing exclusively a prodrug (substrate) and its activator (catalyst). Compared to early bioorthogonal organoruthenium catalysts such as [Cp\*<sub>2</sub>Ru(COD)Cl] (**16**), complexes **17a** and **b** greatly increased the catalytic efficiency, providing TONs up to > 300. In particular, higher catalytic activity was afforded under biologically relevant conditions using donor and acceptor substituents in the 4- (-Cl) and 5-position (-Cl, -NO<sub>2</sub> and -COOMe) of the quinoline ligands. Substitution with a higher electron withdrawing methyl ester group to afford **18** (Figure 6) resulted in the most efficient catalyst of the series. This complex also demonstrated good catalytic activity in blood serum.

Besides protected fluorophores, **17a** and **b** catalyzed the activation of the anticancer prodrug N-(allyloxycarbonyl)doxorubicin inside HeLa cells, inducing cell death via apoptosis.<sup>65</sup> When cells exposed to alloc-doxorubicin (10 μM) were incubated with Ru catalyst **18** (1 μM), an IC<sub>50</sub> of 2.0 μM was determined. This corresponded to an almost

quantitative conversion of the prodrug, considering that direct administration of doxorubicin leads to an  $IC_{50}$  of 1.5  $\mu$ M.<sup>66</sup>

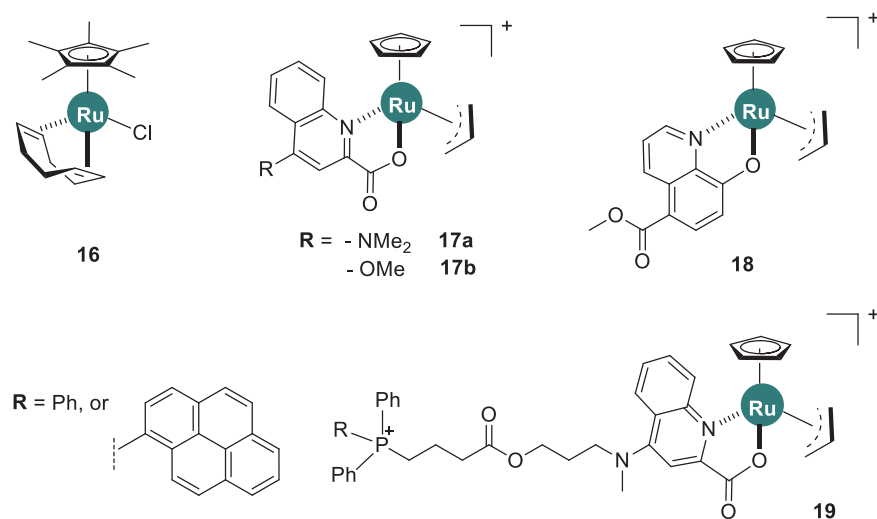


**Figure 6.** Chemical structures of selected Ru<sup>II</sup> and Ru<sup>IV</sup>-quinoline bioorthogonal catalysts for the allylcarbamate cleavage reaction.

The group of Mascareñas functionalized this family of Ru catalysts with the triphenylphosphonium (TPP) cationic ligand (**19**) for mitochondria targeting (Figure 6). The hydrophobic TPP cation drives the accumulation of functionalized molecules into the mitochondria in response to the mitochondrial membrane potential. Ru-catalyzed deprotection of profluorescent probes demonstrated that the approach could be applied to activate molecules in specific cellular organelles.<sup>67</sup>

The introduction of Pd in the bioorthogonal metal catalysis toolkit has been a fundamental discovery in the field. In their pioneering work, Bradley and Unciti-Broceta were the first to report on the catalytic uncaging of non-fluorescent allyl, propargyl, and benzyl carbamate-protected rhodamines by Pd<sup>0</sup> nanoparticles (5 nm) supported on amino-functionalised polystyrene microspheres.

In the context of new therapeutic approaches for controlled drug release, Pd<sup>0</sup>-microspheres were used for the extracellular activation of the drug 5-fluorouracil (5FU) from allyl, propargyl and benzyl caged precursors (Figure 7a). The Pd-mediated generation of 5FU induced apoptosis in colorectal and pancreatic cancer cells.<sup>68</sup>

## Chapter 2

Analogously, a propargyl-masked prodrug of the anticancer agent vorinostat (histone deacetylase inhibitor) was also activated via Pd<sup>0</sup> catalysis and subsequently by lowering the pH (Figure 7b).<sup>69</sup>

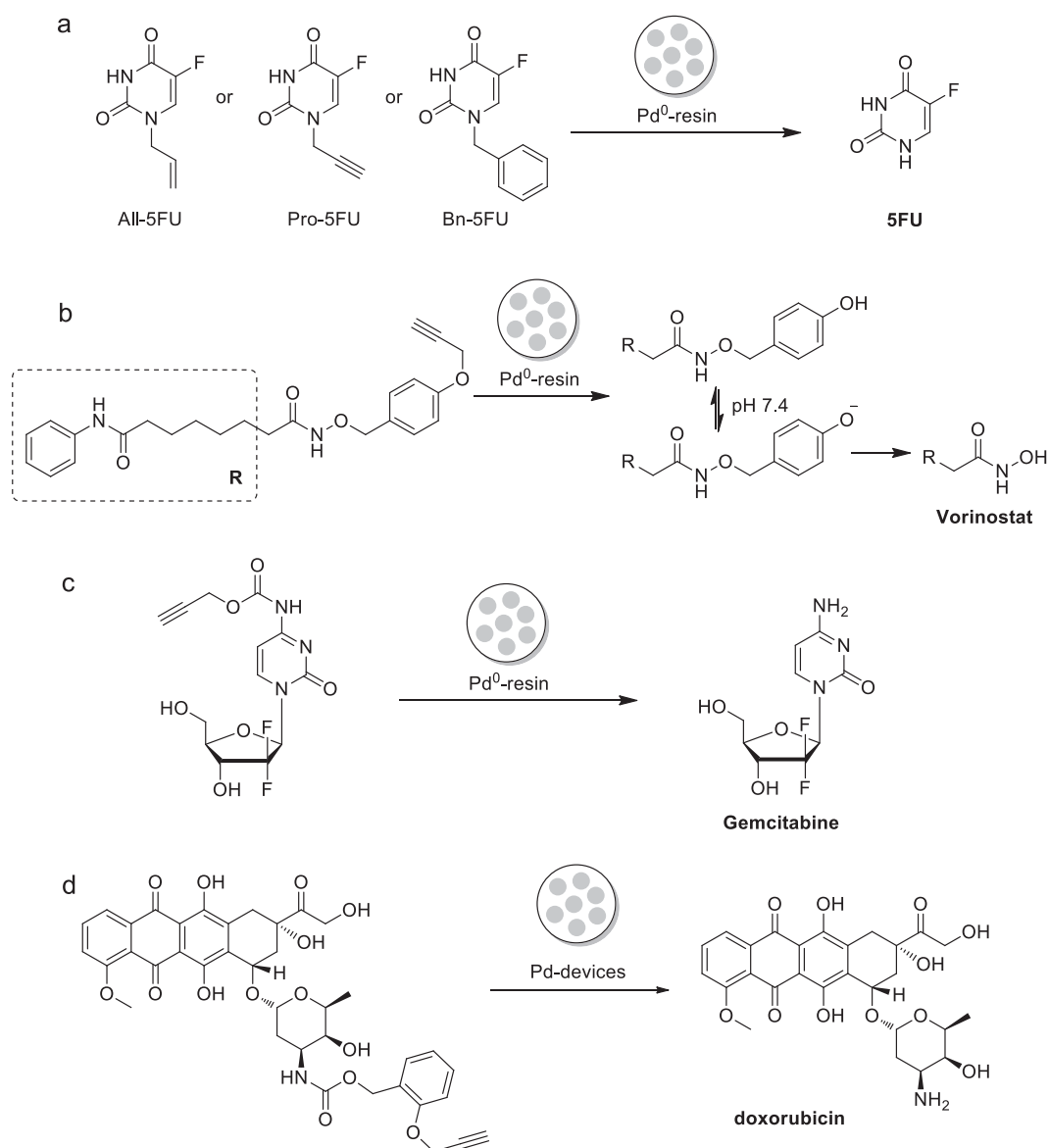


**Figure 7.** Different catalytic deprotection reactions of anticancer prodrugs by Pd nanoparticle catalysts.

Pd bioorthogonal catalysis was further extended for a controlled release of gemcitabine from carbamate-protected precursors (Figure 7c) in both buffered solution and cell culture medium.<sup>70</sup> Using the profluorescent dyes allyl, propargyl, and benzyl carbamate-protected rhodamines, this specific approach was translated to

zebrafishes to demonstrate applicability *in vivo*, however without using precursors for therapy.<sup>68,71</sup>

Recently, Unciti-Broceta and Leung demonstrated that Pd microspheres had promising biocompatibility when implanted in mice bearing a prostate tumor. Drug activation experiments demonstrated the capacity of these catalysts to carry out *ex vivo* carbamate cleavage of a masked doxorubicin (Figure 7d).<sup>72</sup> Zebrafish studies revealed that such caged doxorubicin derivative avoided the cardiotoxicity typically produced by doxorubicin alone.

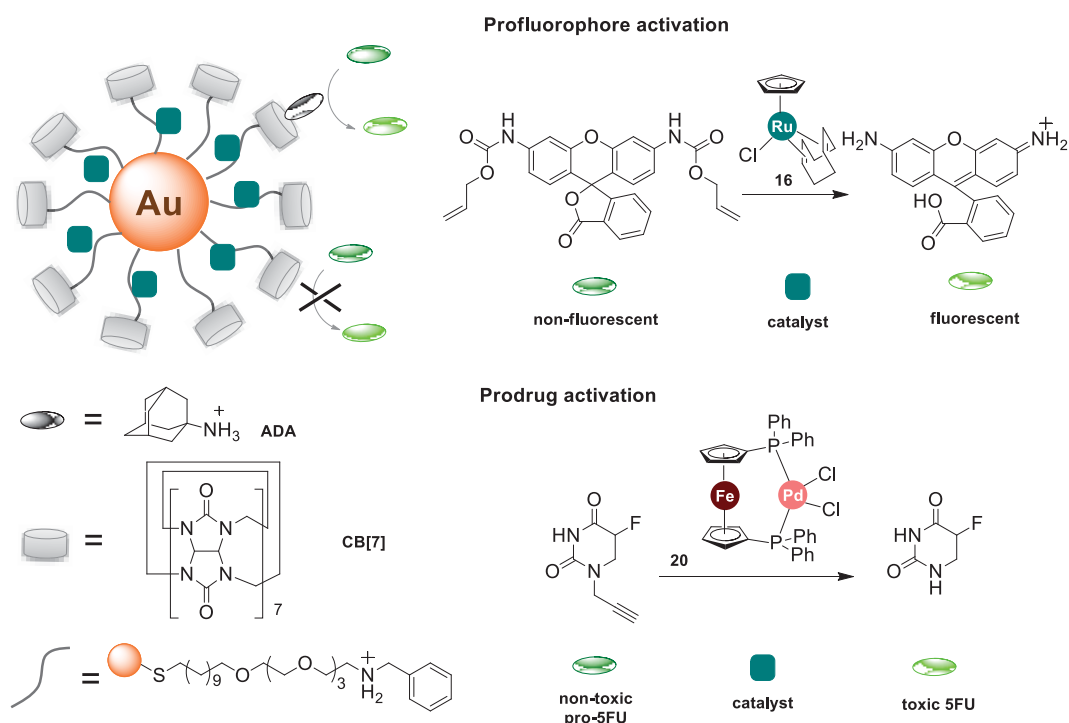


**Figure 8.** Schematic representation of Rotello's Au nanorobot for the catalytic activation of a profluorophore and prodrug.

Rotello and coworkers conceived nanozymes based on gold nanoparticles (AuNPs), integrating Ru- and Pd-mediated bioorthogonal catalysis. The protein-sized AuNPs (2 nm of nanoparticle diameter) presented a core covered with hydrophobic alkanes for encapsulation of the organometallic Ru and Pd catalysts, a tetra(ethylene glycol) unit for improving biocompatibility and a terminal dimethylbenzylammonium group for imparting water solubility. Host-guest interactions between the headgroup and the non-toxic curcubit[7]uril (CB[7]) transforms this supramolecular system in a 'gate keeper' nanozyme (Figure 8). Complexation with CB[7] inhibits the catalytic activity of

Ru and Pd catalysts blocking substrates from accessing the catalysts by steric hindrance. However, catalysis is restored as soon as the CB[7] competitive guest 1-adamantylamine (ADA) is added. Under these controlled conditions the Ru-catalyst [Cp\*Ru(COD)Cl] (**16**) is employed to turn on the fluorescence of allylcarbamate caged rhodamine 110 dye in HeLa cells. The gated activation approach is also applied for the cleavage of the propargyl protecting group of pro-5FU (1 mM) by AuNPs embedded with the Pd catalyst **20** (100 nM) (Figure 8). In HeLa cells, intracellular conversion of pro-5FU into 5FU using gated-catalysis results in a remarkable reduction of cell viability.<sup>73</sup>

A different bioorthogonal catalysis concept was proposed by the Bradley group. They applied copper-catalyzed azide-alkyne cycloaddition (CuAAC) for the extracellular generation of a cytotoxic combretastatin derivative. Combretastatin A4 is a tubulin polymerization inhibitor and a highly cytotoxic agent against a variety of cancer cell lines. The triazole analogue synthesized *in situ* via CuAAC from two non-toxic (up to 10  $\mu$ M) azide and alkyne precursors (Figure 9)<sup>74</sup> is known to inhibit K562 leukemia cancer cell growth with an IC<sub>50</sub> value of 1.3  $\mu$ M.<sup>75,76</sup> Polymeric microspheres supporting Cu nanoparticles (522 nm) were employed to generate catalytically the combretastatin analogue *in vitro* in SKOV-3 and HeLa cells. Moreover, application of the copper nanostructures in zebrafish embryos triggers the unmasking of a profluorophore and proved the usability of this approach in a living organism.

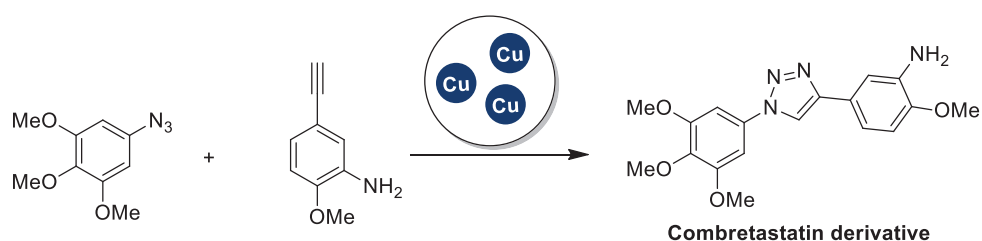


**Figure 9.** Formation of a combretastatin derivative mediated by Cu nanoparticle catalysis.

## ***2.4 A new approach - Outlook***

In catalysis, metal complexes are generally regarded as the catalysts. Specifically design mediators that facilitate the transformation of organic substrates in more valuable molecules. As shown, this also applies to the field of metal-based bioorthogonal catalysis. Changing this catalysis paradigm is a fine prospect for medicinal inorganic chemistry. There is in fact a wide range of metal-based agents that can be developed as substrates for catalytic activation processes. This approach is unorthodox, yet, may lead to devise new families of prodrugs and innovative strategies to exploit the rich medicinal chemistry of metal complexes, simultaneously reducing some of the unwanted biological effects characteristic of these systems. The experimental work of this thesis, described in the following chapters, is the first attempt to apply such new catalysis concept for therapy purposes.

## 2.5 References

- 1 H. C. Hang, C. Yu, D. L. Kato and C. R. Bertozzi, *P. Natl. Acad. Sci. USA*, 2003, **100**, 14846–14851.
- 2 E. M. Sletten and C. R. Bertozzi, *Acc. Chem. Res.*, 2011, **44**, 666–676.
- 3 M. Martínez-Calvo and J. L. Mascareñas, *Coordin. Chem. Rev.*, 2018, **359**, 57–79.
- 4 A. H. Ngo, S. Bose and L. H. Do, *Chem. Eur. J.*, 2018, **24**, 10584–10594.
- 5 A. Miyawaki, A. Sawano and T. Kogure, *Nat. Cell Biol.*, 2003, **Suppl**, S1-7.
- 6 Y. Takaoka, A. Ojida and I. Hamachi, *Angew. Chem. Int. Ed.*, 2013, **52**, 4088–4106.
- 7 J. Gallagher, O. Zelenko, A. D. Walts and D. S. Sigman, *Biochemistry*, 1998, **37**, 2096–2104.
- 8 D. Hoyer, H. Cho and P. G. Schultz, *J. Am. Chem. Soc.*, 1990, **112**, 3249–3250.
- 9 P. S. Chae, M. Kim, C.-S. Jeung, S. D. Lee, H. Park, S. Lee and J. Suh, *J. Am. Chem. Soc.*, 2005, **127**, 2396–2397.
- 10 J.-H. Lee, S.-H. Yoo, K.-H. Jeong, T.-Y. Lee, J.-Y. Ahn and J.-H. Suh, *B. Korean Chem. Soc.*, 2008, **29**, 882–884.
- 11 J. Suh, W. S. Chei, T. Y. Lee, M. G. Kim, S. H. Yoo, K. Jeong and J. Y. Ahn, *J. Biol. Inorg. Chem.*, 2008, **13**, 693–701.
- 12 S. Junghun, Y. S. Ho, K. M. Gyum, J. Keunhong, A. J. Young, K. Myoung-soon, C. P. Seok, L. T. Yeon, L. Jaehwa, L. Jeongkuk, J. Y. Ah and K. E. Hwa, *Angew. Chem. Int. Ed.*, 2007, **46**, 7064–7067.
- 13 W. S. Chei, H. Ju and J. Suh, *J. Biol. Inorg. Chem.*, 2011, **16**, 511–519.
- 14 J. C. Joyner, L. Hocharoen and J. A. Cowan, *J. Am. Chem. Soc.*, 2012, **134**, 3396–3410.
- 15 B. S. S, R. M. James, F. Insiya and C. J. A, *ChemMedChem*, 2014, **9**, 1275–1285.
- 16 S. Bradford and J. A. Cowan, *Chem. Commun.*, 2012, **48**, 3118–3120.
- 17 Y. Jin and J. A. Cowan, *J. Biol. Inorg. Chem.*, 2007, **12**, 637–644.
- 18 J. C. Joyner, K. D. Keuper and J. A. Cowan, *Chem. Sci.*, 2013, **4**, 1707–1718.



- 19 Z. Yu and J. A. Cowan, *Angew. Chem. Int. Ed.*, 2017, **56**, 2763–2766.
- 20 J. C. Joyner and J. A. Cowan, *Braz. J. Med. Biol. Res.*, 2013, **46**, 465–485.
- 21 T. Y. Lee and J. Suh, *Chem. Soc. Rev.*, 2009, **38**, 1949–1957.
- 22 L. Hocharoen and J. A. Cowan, *Chem. Eur. J.*, 2009, **15**, 8670–8676.
- 23 J. Suh and W. S. Chei, *Curr. Opin. Chem. Biol.*, 2008, **12**, 207–213.
- 24 Z. Yu and J. A. Cowan, *Chem. Eur. J.*, 2017, **23**, 14113–14127.
- 25 J. J. Soldevila-Barreda and P. J. Sadler, *Curr. Opin. Chem. Biol.*, 2015, **25**, 172–183.
- 26 J. Zhang, C. Jiang, J. P. Figueiró Longo, R. B. Azevedo, H. Zhang and L. A. Muehlmann, *Acta Pharm. Sinic. B*, 2018, **8**, 137–146.
- 27 L. K. McKenzie, H. E. Bryant and J. A. Weinstein, *Coordin. Chem. Rev.*, 2018, *in Press* DOI:10.1016/j.ccr.2018.03.020.
- 28 V. Brabec, J. Pracharova, J. Stepankova, P. J. Sadler and J. Kasparkova, *J. Inorg. Biochem.*, 2016, **160**, 149–155.
- 29 F. Schmitt, P. Govindaswamy, G. Süß-Fink, W. H. Ang, P. J. Dyson, L. Juillerat-Jeanneret and B. Therrien, *J. Med. Chem.*, 2008, **51**, 1811–1816.
- 30 F. Heinemann, J. Karges and G. Gasser, *Acc. Chem. Res.*, 2017, **50**, 2727–2736.
- 31 B. Peña, R. Barhoumi, R. C. Burghardt, C. Turro and K. R. Dunbar, *J. Am. Chem. Soc.*, 2014, **136**, 7861–7864.
- 32 A. Hussain, S. Gadadhar, T. K. Goswami, A. A. Karande and A. R. Chakravarty, *Eur. J. Med. Chem.*, 2012, **50**, 319–331.
- 33 S. P. Fricker, *Chem. Soc. Rev.*, 2006, **35**, 524–533.
- 34 A. Cavalett, T. Bortolotto, P. R. Silva, G. Conte, H. Gallardo and H. Terenzi, *Inorg. Chem. Commun.*, 2012, **20**, 77–80.
- 35 L. B. Josefsen and R. W. Boyle, *Met. Based Drugs*, 2008, DOI:10.1155/2008/276109.
- 36 S. G. Rockson, P. Kramer, M. Razavi, A. Szuba, S. Filardo, P. Fitzgerald, J. P. Cooke, S. Yousuf, A. R. DeVault, M. F. Renschler and D. C. Adelman, *Circulation*, 2000, **102**, 2322–2324.

## Chapter 2

- 37 T. S. Mang, R. Allison, G. Hewson, W. Snider and R. Moskowitz, *Cancer J. Sci. Am.*, 1998, **4**, 378–384.
- 38 Superoxide Dismutase (SOD) as Antioxidant Treatment of Age Related Macular Degeneration (ARMD) - ClinicalTrials.gov, <https://clinicaltrials.gov/ct2/show/NCT00800995>.
- 39 I. Batinić-Haberle, J. S. Rebouças and I. Spasojević, *Antioxid. Redox Sign.*, 2010, **13**, 877–918.
- 40 B. Glimelius, N. Manojlovic, P. Pfeiffer, B. Mosidze, G. Kurteva, M. Karlberg, D. Mahalingam, P. Buhl Jensen, J. Kowalski, M. Bengtson, M. Nittve and J. Näsström, *Acta Oncol.*, 2018, **57**, 393–402.
- 41 A Trial of PledOx + FOLFOX6 Compared to Placebo + FOLFOX6 in Patients With Metastatic Colorectal Cancer - ClinicalTrials.gov, <https://clinicaltrials.gov/ct2/show/NCT01619423>.
- 42 O. M. Ighodaro and O. A. Akinloye, *Alexandria J. Med.*, 2017, DOI:10.1016/j.ajme.2017.09.001.
- 43 Evaluation of M40403 for the Prevention of Dose Limiting Toxicities of High Dose IL-2 - ClinicalTrials.gov, <https://clinicaltrials.gov/ct2/show/NCT00033956>.
- 44 R. Coriat, W. Marut, M. Leconte, L. B. Ba, A. Vienne, C. Chéreau, J. Alexandre, B. Weill, M. Doering, C. Jacob, C. Nicco and F. Batteux, *Cell Death Dis.*, 2011, **2**, e191.
- 45 D. Trachootham, W. Lu, M. A. Ogasawara, N. R.-D. Valle and P. Huang, *Antioxid. Redox Sign.*, 2008, **10**, 1343–1374.
- 46 M. Vučetić, Y. Cormerais, S. K. Parks and J. Pouysségur, *Front. Oncol.*, 2017, doi: 10.3389/fonc.2017.00319.
- 47 S. J. Dougan, A. Habtemariam, S. E. McHale, S. Parsons and P. J. Sadler, *P. Natl. Acad. Sci. USA*, 2008, **105**, 11628–11633.
- 48 V. I. Lushchak, *J. Amino Acids*, 2011, dx.doi.org/10.1155/2012/736837.
- 49 R. Franco and J. A. Cidlowski, *Cell Death Differ.*, 2009, **16**, 1303–1314.
- 50 T. Bugarcic, A. Habtemariam, R. J. Deeth, F. P. A. Fabbiani, S. Parsons and P. J. Sadler, *Inorg. Chem.*, 2009, **48**, 9444–9453.
- 51 F. Giannini, J. Furrer, G. Süss-Fink, C. M. Clavel and P. J. Dyson, *J. Organomet. Chem.*, 2013, **744**, 41–48.

- 52 A.-F. Ibaio, M. Gras, B. Therrien, G. Süß-Fink, O. Zava and P. J. Dyson, *Eur. J. Inorg. Chem.*, **2012**, 1531–1535.
- 53 L. E. H. Paul, B. Therrien and J. Furrer, *J. Biol. Inorg. Chem.*, 2012, **17**, 1053–1062.
- 54 L. E. H. Paul, B. Therrien and J. Furrer, *Inorg. Chem.*, 2012, **51**, 1057–1067.
- 55 X. Wu, X. Li, W. Hems, F. King and J. Xiao, *Org. Biomol. Chem.*, 2004, **2**, 1818–1821.
- 56 S. Grammenudi, M. Franke, F. Vögtle and E. Steckhan, *J. Inclusion Phenom.*, 1987, **5**, 695–707.
- 57 J. Canivet, G. Süß-Fink and P. Štěpnička, *Eur. J. Inorg. Chem.*, **2007**, 4736–4742.
- 58 Y. K. Yan, M. Melchart, A. Habtemariam, A. F. A. Peacock and P. J. Sadler, *J. Biol. Inorg. Chem.*, 2006, **11**, 483–488.
- 59 T. R. Ward, *Acc. Chem. Res.*, 2011, **44**, 47–57.
- 60 J. J. Soldevila-Barreda, I. Romero-Canelón, A. Habtemariam and P. J. Sadler, *Nat. Commun.*, 2015, **6**, 6582.
- 61 Z. Liu, I. Romero-Canelón, B. Qamar, J. M. Hearn, A. Habtemariam, N. P. E. Barry, A. M. Pizarro, G. J. Clarkson and P. J. Sadler, *Angew. Chem. Int. Ed.*, **53**, 3941–3946.
- 62 J. P. C. Coverdale, I. Romero-Canelón, C. Sanchez-Cano, G. J. Clarkson, A. Habtemariam, M. Wills and P. J. Sadler, *Nat. Chem.*, 2018, **10**, 347–354.
- 63 P. K. Sasmal, C. N. Streu and E. Meggers, *Chem. Commun.*, 2013, **49**, 1581–1587.
- 64 C. Streu and E. Meggers, *Angew. Chem. Int. Ed.*, 2006, **45**, 5645–5648.
- 65 T. Völker, F. Dempwolff, P. L. Graumann and E. Meggers, *Angew. Chem. Int. Ed.*, 2014, **53**, 10536–10540.
- 66 T. Völker and E. Meggers, *ChemBioChem*, 2017, **18**, 1083–1086.
- 67 M. Tomás-Gamasa, M. Martínez-Calvo, J. R. Couceiro and J. L. Mascareñas, *Nat. Commun.*, 2016, **7**, 12538.
- 68 J. T. Weiss, J. C. Dawson, K. G. Macleod, W. Rybski, C. Fraser, C. Torres-Sánchez, E. E. Patton, M. Bradley, N. O. Carragher and A. Unciti-Broceta, *Nat. Commun.*, 2014, **5**, 3277.
- 69 B. Rubio-Ruiz, J. T. Weiss and A. Unciti-Broceta, *J. Med. Chem.*, 2016, **59**, 9974–9980.

## Chapter 2

- 70 J. T. Weiss, J. C. Dawson, C. Fraser, W. Rybski, C. Torres-Sánchez, M. Bradley, E. E. Patton, N. O. Carragher and A. Unciti-Broceta, *J. Med. Chem.*, 2014, **57**, 5395–5404.
- 71 T. Völker and E. Meggers, *Curr. Opin. Chem. Biol.*, 2015, **25**, 48–54.
- 72 T. L. Bray, M. Salji, A. Brombin, A. M. Pérez-López, B. Rubio-Ruiz, L. C. A. Galbraith, E. E. Patton, H. Y. Leung and A. Unciti-Broceta, *Chem. Sci.*, 2018, DOI:10.1039/C8SC02291G.
- 73 G. Y. Tonga, Y. Jeong, B. Duncan, T. Mizuhara, R. Mout, R. Das, S. T. Kim, Y.-C. Yeh, B. Yan, S. Hou and V. M. Rotello, *Nat. Chem.*, 2015, **7**, 597–603.
- 74 J. Clavadetscher, S. Hoffmann, A. Lilienkamp, L. Mackay, R. M. Yusop, S. A. Rider, J. J. Mullins and M. Bradley, *Angew. Chem. Int. Ed.*, 2016, **55**, 15662–15666.
- 75 K. Odlo, J. Fournier-Dit-Chabert, S. Ducki, O. A. B. S. M. Gani, I. Sylte and T. V. Hansen, *Bioorgan. Med. Chem.*, 2010, **18**, 6874–6885.
- 76 O. W. Akselsen, K. Odlo, J. J. Cheng, G. Maccari, M. Botta and T. V. Hansen, *Bioorg. Med. Chem.*, 2012, **20**, 234–242.

# 3

## **Riboflavin As Bioorthogonal Photocatalyst For The Activation Of A Pt<sup>IV</sup> Prodrug**

---

The work presented in this chapter has been published in Chem. Sci., 2017, 8, 4619-4625 (authors: S. Alonso-de Castro, E. Ruggiero, A. Ruiz-de Angulo, E. Rezabal, J.C. Mareque-Rivas, X. Lopez, F. López-Gallego and L. Salassa).



### 3.1 Introduction

The combination of catalysis and bioorthogonality<sup>1-3</sup> promises to impact drug discovery and bioimaging by facilitating the execution of non-natural chemical reactions in living systems. Catalytic turnover can boost the efficiency of bioorthogonal chemical reactions, unveiling new strategies for prodrug activation and uncaging of molecular probes.<sup>4-8</sup>

In this context, transition metal and organometallic catalysis have opened new avenues for the advance of bioorthogonal catalysis in cells.<sup>5,9-16</sup> The laboratories of Meggers, Mascareñas, Unciti-Broceta and Bradley used organoruthenium and palladium catalysis to deprotect pro-fluorescent substrates and activate prodrugs in cancer cells or in their compartments and surroundings.<sup>11-14,16</sup> Rotello devised biomimetic nanoenzymes for imaging and therapy, by encapsulating ruthenium and palladium catalysts into water-soluble gold nanoparticles and controlling their catalytic activity in HeLa cells through supramolecular chemistry.<sup>15</sup> These pioneering studies exploited metal-based catalytic uncaging of allylcarbamate- and propargyl-protected amines as viable strategies for bioorthogonal catalysis, however new biocompatible transformations are highly needed to further advance this extremely challenging field that is still in its infancy.



**Scheme 1** Transition metal complex acting as substrate and its bioorthogonal activation by riboflavin which functions as photocatalyst.

Herein, we describe an original photocatalysis approach to control the reactivity of transition metal complexes in a bioorthogonal fashion. In a new type of light-driven reaction, the exogenous biological molecule riboflavin (**Rf**) functions as a

### Chapter 3

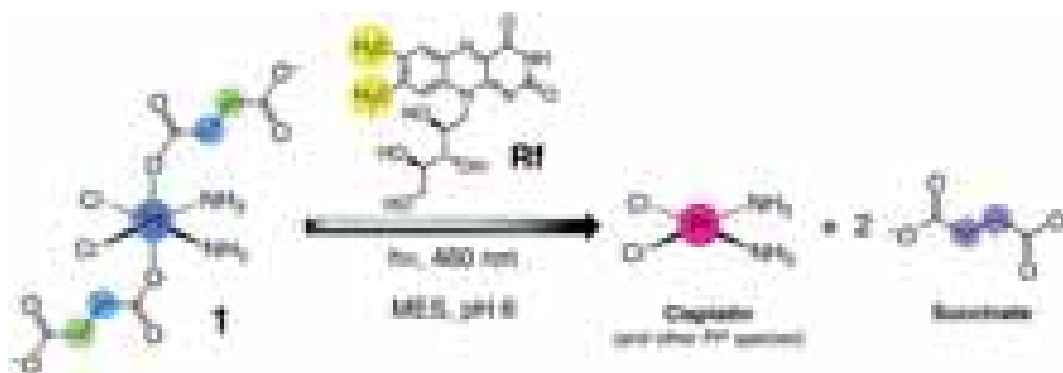
bioorthogonal photocatalyst and a metal complex as unconventional substrate (Scheme 1).

This unusual catalyst/substrate pair relies on the photoredox properties of **Rf** to enable the selective activation of a Pt<sup>IV</sup> prodrug of cisplatin with exceptionally low doses of blue light, and induce apoptotic death in PC-3 human prostate cancer cells.

Metal complexes are typically regarded as catalysts which convert organic substrates in more valuable compounds, whereas catalytic transformations of metal complexes are, to date, practically unknown and represent a paradigm shift in catalysis.<sup>17,18</sup> Their development can expand the scope of bioorthogonal chemical reactions to inorganic substances and metal-based prodrugs, fostering the creation of new inorganic chemistry toolkits for biology and medicine.

## 3.2 Results and Discussion

As part of our ongoing efforts to design innovative light-activation modes for anticancer platinum complexes,<sup>19</sup> we reasoned that **Rf** and its rich photochemistry would facilitate the photoreduction of *cis,cis,trans*-[Pt(NH<sub>3</sub>)<sub>2</sub>(Cl)<sub>2</sub>(O<sub>2</sub>CCH<sub>2</sub>CH<sub>2</sub>CO<sub>2</sub>)<sub>2</sub>]<sup>2-</sup> (**1**) to cisplatin by means of excitation wavelengths appropriate for use in biological systems (Scheme 2). Complex **1** is a cisplatin prodrug suitable for photochemotherapy because of its high dark stability in aqueous solutions and its negligible dark cytotoxicity in several cancer cell lines, e.g. prostate cancer PC-3 cells.<sup>20,21</sup>



**Scheme 2** Light-induced reduction of *cis,cis,trans*-[Pt(NH<sub>3</sub>)<sub>2</sub>(Cl)<sub>2</sub>(O<sub>2</sub>CCH<sub>2</sub>CH<sub>2</sub>CO<sub>2</sub>)<sub>2</sub>]<sup>2-</sup> (**1**) promoted by riboflavin (**Rf**) in MES buffer.



Upon UVA light excitation (385 nm) **1** undergoes photochemical activation. However, UVA light is of limited use in therapy and Pt<sup>IV</sup> complexes such as **1** rarely display satisfactory absorption features at wavelengths longer than 400 nm (Figure 1a).

**Rf** is vitamin B2 and the precursor of biologically important cofactors such as FMN and FAD, which are essential to humans and animals due to their redox activity.<sup>22</sup> The yellow-colored **Rf** absorbs in aqueous media with good extinction coefficients ( $\epsilon_{446} > 10^4 \text{ M}^{-1}\cdot\text{cm}^{-1}$ )<sup>23</sup> as far as ca. 500 nm (Figure 1a), and can promote a great variety of light-induced reactions which depend on its 7,8-dimethyl-10-alkylisoalloxazine fragment.<sup>22</sup> **Rf** has been adopted as photocatalyst in several organic reactions, including the photooxidation of benzyl alcohols and alkyl benzenes or the [2+2] cycloaddition of styrene dienes and bis(arylenones).<sup>24–26</sup>

### **3.2.1 Photocatalytic activation of a Pt<sup>IV</sup> prodrug by riboflavin in solution**

After confirming blue light has not direct effects on **1** (Figure S1–3), we investigated the capability of **Rf** to photoactivate the complex upon 460-nm excitation in MES buffer. Using low excitation power density ( $2.5 \text{ mW}\cdot\text{cm}^{-2}$ ), 120  $\mu\text{M}$  solutions of **1** were photolysed in the presence of **Rf** at various concentrations (12–120  $\mu\text{M}$ , Figure S4–7). The process was monitored via <sup>1</sup>H NMR by the evolution of diagnostic peaks corresponding to the Pt-bound (triplets) and free (singlet) succinate ligands (Figure 1b).

Sub-stoichiometric quantities of **Rf** are capable to produce full conversion of **1** into its photoproducts under light excitation, demonstrating that **Rf** does not act as a simple photosensitizer but is indeed a photocatalyst. The efficiency of this catalytic process is remarkable since 12  $\mu\text{M}$  **Rf** converts 100% of 120  $\mu\text{M}$  **1** in 5 minutes (light dose  $0.75 \text{ J}\cdot\text{cm}^{-2}$ ). A **Rf** concentration as low as 0.13  $\mu\text{M}$  still photocatalyses the transformation of **1** (120  $\mu\text{M}$ ), however more than 2 hours are required to achieve 27% of conversion (Figure S8). No reaction between **1** and **Rf** occurs in the dark within 1 week (Figure S9). Interestingly, photoconversion of **1** takes place in pure water (pH 5) or in phosphate buffer (PB, 100 mM, pH 5.5), but never reaches completion due to poor photostability of **Rf** in these media (vide infra). Thus, MES buffer plays a key role in the catalytic process preventing **Rf** from undergoing photodecomposition reactions.

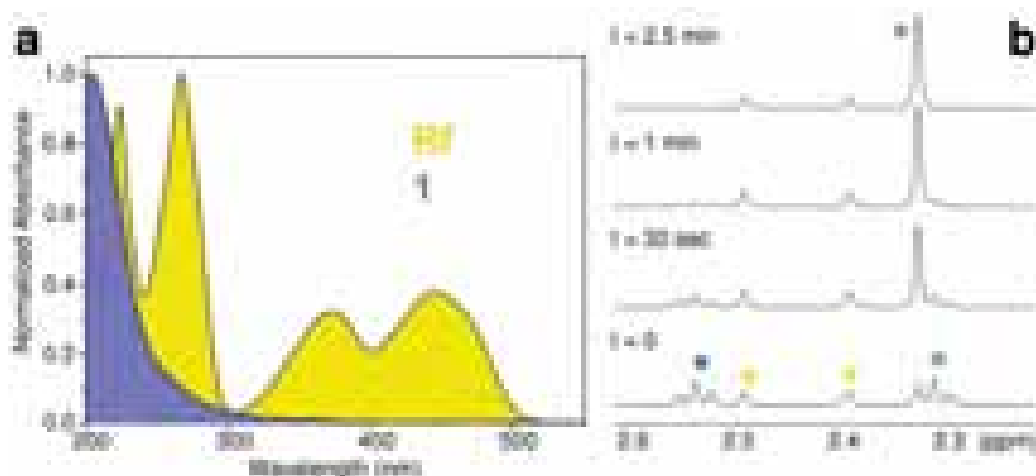


**Figure 1.** (a) Absorption spectrum of riboflavin (**Rf**) and *cis,cis,trans*-[Pt(NH<sub>3</sub>)<sub>2</sub>(Cl)<sub>2</sub>(O<sub>2</sub>CCH<sub>2</sub>CH<sub>2</sub>CO<sub>2</sub>)<sub>2</sub>]<sup>2-</sup> (**1**) in aqueous solution. (b) **Rf**-catalysed photoreduction of **1** in MES buffer (18 mM, pH 6) monitored by <sup>1</sup>H NMR. Spectra were recorded for a MES/D<sub>2</sub>O (9:1) solution of 120 μM **1** and 50 μM **Rf** upon t = 0 sec, 30 sec, 1 min and 2.5 min of 460-nm light irradiation (2.5 mW·cm<sup>-2</sup>). <sup>1</sup>H NMR signal labelling: ● Pt-OCOCH<sub>2</sub>CH<sub>2</sub>CO<sub>2</sub><sup>-</sup>, ● Pt-OCOCH<sub>2</sub>CH<sub>2</sub>CO<sub>2</sub><sup>-</sup>, ● methyl groups of **Rf** isoalloxazine ring, ● free <sup>-</sup>O<sub>2</sub>CCH<sub>2</sub>CH<sub>2</sub>CO<sub>2</sub><sup>-</sup>.

In order to assess the rate law for the **Rf**-catalysed photoreduction of **1** to Pt<sup>II</sup> species, we studied the reaction rate at different substrate concentrations (120 μM–1.92 mM, i.e. 2.4–38.4 mol equiv of **1** compared to **Rf**) in 18 mM MES buffer during 30 sec of irradiation at 298 K (Figure S10). The effect of MES on the reaction rate was evaluated in a separate set of experiments, in which MES concentration was varied in the 3–20 mM range (Figure S11). Results demonstrate that the rate of the reaction linearly increases with the concentration of **1** and MES, corresponding to a first-order reaction for both species. Importantly, the reaction shows a stronger dependency on the concentration of **1** than on MES, suggesting that Pt<sup>IV</sup> reduction is limiting step of the reaction.

Since our experiments employ a large excess of MES and all reaction steps are irreversible, the rate constant can be described using the pseudo-first order model (ESI<sup>+</sup>). Using 50 μM **Rf**, we obtained a pseudo-first order reaction constant ( $k_{\text{obs}} = 10.0 \pm 0.05 \cdot 10^{-3} \text{ s}^{-1}$ ) that increases with the catalyst concentration (Figure S12 and S13) and depends on MES concentration.

A turnover frequency (TOF) value of  $0.22 \pm 0.06 \text{ s}^{-1}$  was determined for the conversion of **1** (1.92 mM) by **Rf** (50 μM) under light irradiation at 298 K in 18 mM MES buffer.

Under such reaction conditions, the maximum total turnover number (TTN) value is 38 after 3 minutes of light irradiation, and no decomposition of catalyst is observed by  $^1\text{H}$  NMR. The **Rf/1** catalyst/substrate pair achieves approx. 700–70 times higher TOF compared to ruthenium(II) organometallic catalysts, which catalytically convert  $\text{NAD}^+$  in NADH or transform O-allyl carbamates into their respective amines under biologically relevant conditions and in cells.<sup>9,8</sup> High TOF is crucial for application in photochemotherapy since it guarantees rapid and sufficient conversion of **1** with short irradiation times and low light doses.

### 3.2.2 Mechanism of photocatalytic activation

**Rf** is extremely light sensitive and its photochemical reactivity strongly depends on the surrounding environment. Electron transfer and proton-coupled reactions or singlet-oxygen generation take place upon light excitation of **Rf**, depending on the availability of electron donors. In addition, light decomposes **Rf** into several fragments through intramolecular reactions in which the ribityl chain can be used as the electron source.<sup>27</sup>

Direct energy transfer from **Rf** to **1** can be ruled out since there is no overlap between the emission band of the flavin ( $\lambda_{\text{em}} = 535 \text{ nm}$ ) and the absorption spectrum of **1**.

Hence, the sensitizing and catalytic capacity of **Rf** in MES buffer reasonably relies on electron transfer processes triggered by light. In the triplet excited state ( $^3\text{Rf}^*$ ), **Rf** is a strong oxidant ( $E^{\circ} = 1.77 \text{ V}$ )<sup>22</sup> capable of efficiently extracting electrons from the abundant MES molecules, and generate the two-electron reduced **RfH<sub>2</sub>/RfH<sup>-</sup>** species ( $\text{pK}_a \sim 6$ ) together with morpholino radicals<sup>28</sup> which eventually evolve to the oxidized N-oxide form of MES (Figure S14).<sup>29</sup>

Employing ferrioxalate actinometry,<sup>30</sup> we determined the photochemical quantum yield for **Rf/1** (50  $\mu\text{M}$  / 1.0 mM, 18 mM MES) obtaining a value of  $1.4 \pm 0.1$  (Figure S15 and S16).

Yield values  $> 1$  are rather common in photoredox catalysis where radical chain propagation cycles form part of the catalytic mechanism.<sup>31</sup>

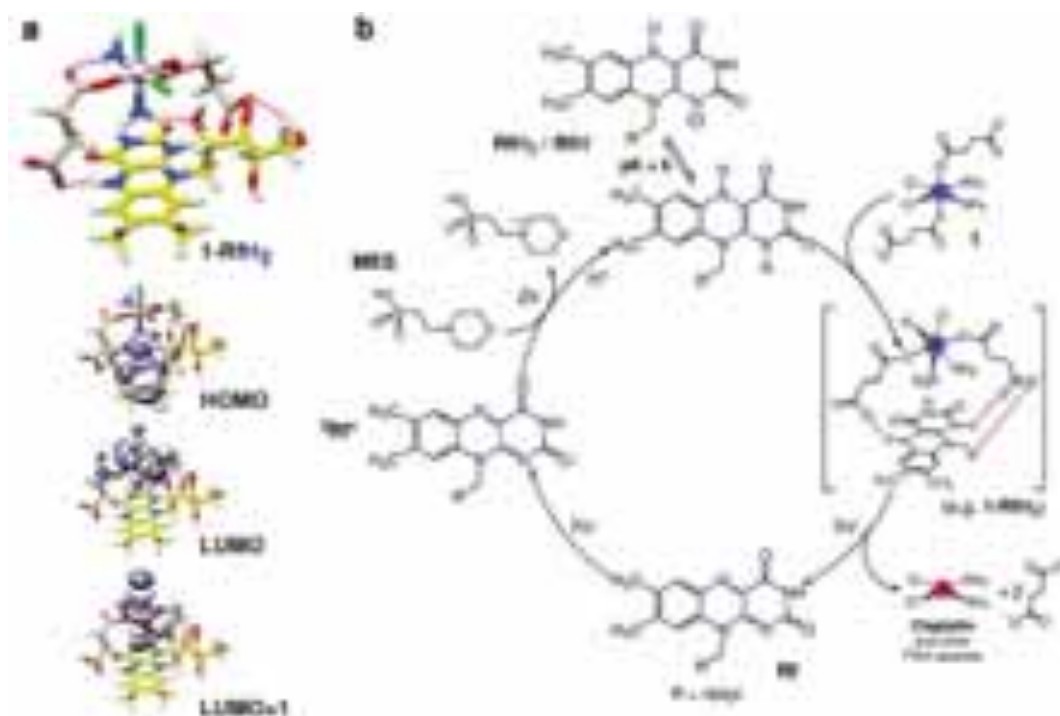


**Figure. 2** Proposed mechanism for the photocatalytic activation of **1** by **Rf**. (a) Computed structure and frontier molecular orbitals (DFT:PBE0/def2-SVP) of a selected **1-RfH<sub>2</sub>** adduct. Intermolecular H-bonds in **1-RfH<sub>2</sub>** are highlighted with magenta lines (top). Isodensity surfaces are plotted with the isovalue of  $0.02 \text{ e}^{-\text{bohr}^{-3}}$ . Atoms color code: Pt grey, Cl green, O red, N blue, C pale brown (**1**) or yellow (**Rf**), H white. (b) **Rf** absorbs 460-nm photons to generate the triplet excited state (<sup>3</sup>**Rf**<sup>\*</sup>) which oxidizes two MES molecules to give the reduced species **RfH<sub>2</sub>/RfH<sup>-</sup>**. Next, complex **1** forms stable adducts with either **RfH<sub>2</sub>** (shown in Figure 2a) or **RfH<sup>-</sup>** and undergoes photoreduction and elimination reactions upon absorption of more photons, liberating cytotoxic Pt<sup>II</sup> species and regenerating the **Rf** catalyst.

As a result, MES buffer dramatically improves **Rf** photostability by preventing that the isoalloxazine unit reacts with the ribityl moiety or with molecular oxygen. NMR and UV-Vis show that MES substantially preserves **Rf** from decomposition for over 30 min, whereas the catalyst is fully converted to the photoproduct lumichrome in water within 1 min of light irradiation, and then to 2,3-butanedione at longer irradiation times (Figure S17–19).<sup>32</sup>

The role of the buffer was confirmed using HEPES (18 mM, pH 6), an analogue zwitterionic buffering agent (Figure S20 and S21), in which **Rf** and **1** behave similarly to MES in terms of photocatalytic activity.

The presence of sodium azide (singlet oxygen scavenger) in water and PB also improves the efficiency of the photocatalytic reaction of **Rf** with **1** (Figure S22 and S23). When added to MES buffer, sodium azide does not improve **Rf/1** (Figure S24), excluding the participation of  $^1\text{O}_2$  and other oxygen radicals as major actors in the catalytic mechanism. On the other hand,  $\text{O}_2$  partially deactivates **Rf**, since under inert Ar atmosphere the photoconversion of **1** is faster (Figure S25).

Importantly, complex **1** (1.8 mM) does not affect the fluorescence lifetime of **Rf** in MES (Figure S26 and S27), indicating that the active catalyst is not likely to be a **Rf** excited-state species. Therefore, photooxidation of MES ultimately leads to the formation of reduced (ground-state)  $\text{RfH}_2/\text{RfH}^-$ , whose low redox potential (ca.  $-0.2\text{ V}$ )<sup>22</sup> cannot directly promote reduction of **1** ( $-0.9\text{ V}$ ).<sup>33</sup>

Yet, as suggested by density functional theory (DFT) modelling (PBE0/def2-SVP) and consistently with the results obtained under Ar atmosphere, **1** is capable to form adducts with either  $\text{RfH}_2$  (Figure 2a) or  $\text{RfH}^-$  (Figure S28–30) by means of H-bonding interactions between its succinate and amino ligands, and the isoalloxazine and ribityl groups of **Rf**. FMN and FAD also photocatalyze the  $\text{Pt}^{\text{IV}}$  conversion of **1**, displaying an efficiency comparable to **Rf** (Figure S31–34). FAD, however, is somewhat less active, possibly due to steric constraints introduced by its adenine moiety which would disfavour H-bonding between the complex and the flavin.

These computed adducts have HOMO localized on the **Rf** isoalloxazine rings, while LUMO and LUMO+1 are  $\sigma$ -antibonding orbitals of **1**. Absorption of a second photon and subsequent light-induced population of the dissociative LUMO orbitals can trigger photoreduction and ligand elimination reactions,<sup>34</sup> ultimately promoting the formation of cisplatin and other  $\text{Pt}^{\text{II}}$  species. Nevertheless, we cannot exclude that these strong and specific interactions could significantly lower the redox potential of **1** and cause direct reduction of the prodrug once the **Rf**-adducts are formed.<sup>35,36</sup> Calculated binding energy for  $\text{1-RfH}_2$  and  $\text{1-RfH}^-$  adducts are in range  $52\text{--}69\text{ kcal}\cdot\text{mol}^{-1}$ , indicating that these transient species are strongly stabilized and may bestow unique selectivity to the **Rf/1** catalyst/substrate pair (vide infra).

### Chapter 3

A pH-dependency profile for the photoreaction at fixed light-irradiation time (2.5 min) shows that complete photoconversion of **1** occurs above pH 6 in MES, whereas at lower pHs the photocatalysis is less efficient (Figure S35). The finding is in agreement with the prevalence of the  $\text{RfH}_2/\text{RfH}^-$  forms of reduced **Rf** at pHs higher than 6.<sup>22</sup>

On the basis of the described evidence, we have schematized a tentative photocatalytic mechanism for the **Rf/1** catalyst/substrate pair in Figure 2b, although further investigations will be needed for its complete elucidation.

#### 3.2.3 Photocatalysis in the biological environment

To test the potential of **Rf** photocatalysis as a bioorthogonal tool for photochemotherapy, we studied next the activation of **1** by **Rf** in cell culture medium and its effects in PC-3 cancer cells (in which **1** has no dark toxicity). At first, photocatalysis experiments and controls (Figure S36 and S37) were performed in Ham's F-12K medium supplemented with fetal bovine serum, in which biological components such as growth factors, antibodies, aminoacids, vitamins, and inorganic salts are present at concentrations ranging from  $\mu\text{M}$  to mM.

$^1\text{H}$  NMR data showed that 3 min of blue light irradiation (light dose  $1.08 \text{ J}\cdot\text{cm}^{-2}$ ) can fully convert 1.92 mM **1** to  $\text{Pt}^{\text{II}}$  species in the presence of 50  $\mu\text{M}$  **Rf** and 3 mM MES, without any significant side reaction affecting either medium components or the catalyst (Figure S38). Under such conditions the TOF and TTN for the **Rf** catalyst are as good as in pure MES buffer solutions, indicating that the catalytic process is bioorthogonal in cell culture medium.

The antiproliferative activity of **Rf/1** against PC-3 cancer cells was investigated in the dark and under 460-nm light irradiation by co-administering the catalyst/substrate pair at a molar ratio of 1:4 and using three different concentrations of complex (40, 80, 120  $\mu\text{M}$ ). In our cell experiments, **Rf** prevalently activates **1** in the extracellular space since we performed light irradiation after a short pre-incubation period and replaced culture medium after 6 h. MES is well tolerated by cells (Figure S39) and was hence employed during cell viability assays as an electron donor. Under these conditions, a short light irradiation period (1 min) and an extremely low light dose ( $0.36 \text{ J}\cdot\text{cm}^{-2}$ ) are sufficient for the full photoconversion of **1** by **Rf** (Figure S40 and S41). In the absence of MES the

photoactivation of **1** still takes place, although less efficiently (Figure S42), likely because other biological components of the medium act as electron donors. Against PC-3 cells, the **Rf/1** catalyst/substrate pair displays dose- dependent light-induced toxicity comparable to cisplatin in the dark. Remarkably, 120  $\mu\text{M}$  **1** and 30  $\mu\text{M}$  **Rf** induce a  $55 \pm 5\%$  reduction in cell biomass under light irradiation, against a  $65 \pm 5\%$  caused by cisplatin at the same concentration. Control experiments indicate that **Rf/1** does not reduce viability of PC-3 cells when kept in the dark, neither does any of the components when irradiated individually (Figure 3a).

The antiproliferative action of **Rf**-activated **1** is associated with the formation of cisplatin as one of the major cytotoxic photoproducts. Initial evidence was gathered from binding experiments with the RNA and DNA base model 5'-guanosin monophosphate (GMP).  $^1\text{H}$  NMR shows that irradiated **Rf/1** solutions incubated with GMP (0–24 h) present the diagnostic peak, corresponding to the cisplatin mono GMP- $\text{Pt}^{\text{II}}$  adduct (Figure S43 and S44).<sup>37</sup> When incubated with the pET28b as model of double stranded circular DNA (24 h, MES 1.5 mM, pH 6), light-activated **Rf/1** (2.5:10  $\mu\text{M}$ ) inhibits the polymerase chain reactions (PCR). Thirty sec of light irradiation are sufficient to stop DNA amplification and reach PCR inhibition level comparable with cisplatin (10  $\mu\text{M}$ ), hence confirming the capacity of this bioorthogonal system to target DNA (Figure S45).<sup>38,39</sup>

Fluorescence microscopy of PC-3 cells treated with either irradiated **Rf/1** (30:120  $\mu\text{M}$ ) or cisplatin (120  $\mu\text{M}$ ) is in agreement with this scenario (Figure 3b and Figure S46). In both cases, images obtained after 48 h of incubation show increased percentage of apoptotic versus viable cells, together with changes in cell morphology that are characteristic of apoptosis, i.e. cell shrinkage and rounding.

Non-treated cells and cells treated with **Rf/1** in the dark included as controls do not induce appreciable cell death. Consistently, flow cytometry results confirm that PC-3 cells exposed to the **Rf/1** mixture and light (30:120  $\mu\text{M}$ ) die through apoptosis 48 hours after irradiation. Cisplatin induces comparable levels of apoptosis under the same conditions.

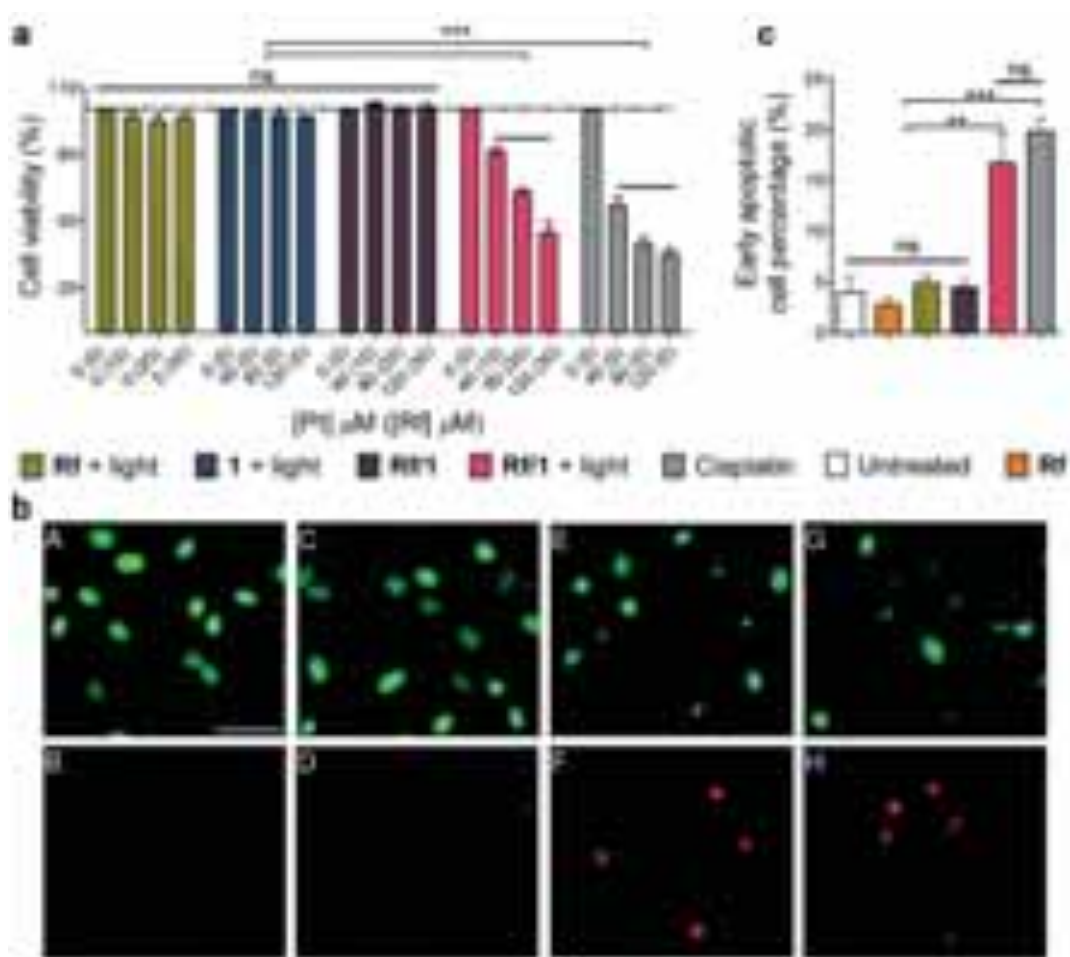


**Figure. 3** Antiproliferative activity in human prostate cancer PC-3 cells. (a) Percentage cell viability of PC-3 cells following treatment with **Rf**, **1**, **Rf/1** and cisplatin with and/or without light activation (460 nm,  $0.36 \text{ J}\cdot\text{cm}^{-2}$ ). (b) Fluorescence microscopy images showing the effects of **Rf/1** on PC-3 cells upon light irradiation. (A, B) untreated PC-3 cells, (C, D) **Rf/1** (30:120  $\mu\text{M}$ ) in the dark, (E, F) **Rf/1** (30:120  $\mu\text{M}$ ) activated by 460-nm light and (G, H) cisplatin (120  $\mu\text{M}$ ) in the dark. Top row: cell nuclei (green); bottom row: apoptotic cells (red). (c) Quantification of early apoptotic PC-3 cells (Annexin V+ / SYTOX-) treated by **Rf** (30  $\mu\text{M}$ ), **Rf/1** (30:120  $\mu\text{M}$ ) and cisplatin (120  $\mu\text{M}$ ) with and/or without light activation. Cell viability and flow cytometry data are presented as mean  $\pm$  SEM of at least three independent measurements. \*\*\*\* $P < 0.001$ , \*\* $P < 0.01$ , ns = non-significant by two-way ANOVA followed by Bonferroni's test (a) or by one-way ANOVA followed by Tukey's test (c).

Double staining with Pacific Blue™ Annexin V / SYTOX® allowed differentiating between early-stage and late-stage apoptosis. Upon treatment with irradiated **Rf/1**, the percentage of early apoptotic cells is  $16.7 \pm 2.8 \%$  against  $19.9 \pm 1.3 \%$  obtained for cisplatin. **Rf**, **1** and **Rf/1** in the dark exhibit no significant population of cells in either stage of apoptosis after 48 h of incubation (Figure 3c).



### 3.3 Conclusions

In summary, we have described the first photocatalytic activation of a metal-based prodrug in solution and in a biological environment. Co-administration of the **Rf/1** as catalyst/substrate couple enables photoconversion of **1** into biologically active species by light irradiation at 460 nm, a wavelength that is ineffective when directly applied to the prodrug. In addition, the **Rf/1** prodrug activation strategy induces an anticancer activity comparable to cisplatin with light doses as low as  $0.36 \text{ J}\cdot\text{cm}^{-2}$ , that is ca. 15–35 times lower than what is typically used for UVA and blue light activation of analogue platinum complexes.<sup>40,41</sup>

The photocatalytic turnover of  $\text{Pt}^{\text{IV}}$  into  $\text{Pt}^{\text{II}}$  species is an attractive prospect to amplify the antineoplastic action of metal-based prodrugs in a locoregional manner. This is particularly relevant for platinum anticancer agents, which have some of the poorest absorption properties amongst photoactivatable metal complexes, but are widely tested in preclinical work and nearly indispensable in clinical practice.

In principle, photocatalysis can help expanding the therapeutic potential of platinum prodrugs. Efficient light activation of  $\text{Pt}^{\text{IV}}$  complexes through catalysis may help localize the cytotoxic effects of Pt drugs, increase their dosing at the tumour target and reduce their systemic toxicity. **Rf** (vitamin B2) is a highly biocompatible molecule and its capacity to function in a bioorthogonal fashion may serve to enhance the selectivity of metal-based drugs by minimizing side reactions.

### 3.4 Experimental details

**Methods.** NMR, UV-Vis and fluorescence characterization of light-irradiated **Rf/1** and controls, PCR and microscopy data, photochemical quantum yield by actinometry, setup for cell work under light irradiation, computational methodology and instrumentation details are described in the ESI†.

**Light-irradiation experiments in solution.** Photocatalysis studies on **Rf/1** were performed under different solution conditions (buffers, cell culture medium and in presence of co-reactants). All reactions were carried out in air at 298 K and pH 6, employing an LED light source ( $\lambda_{\text{exc}} = 460 \text{ nm}$ ,  $2.5 \text{ mW}\cdot\text{cm}^{-2}$ ). Reaction kinetics, law rates of the reaction, turnover frequency (TOF) and total turnover number (TTN) were calculated by varying both reactants and catalyst concentration and quantifying via  $^1\text{H}$  NMR the amount of photoconverted **1**.

**Cell viability studies.** The antiproliferative activity of **Rf/1** was determined in human prostate cancer cells PC-3 (ATCC) in the dark and under light irradiation by co-administering **Rf** and **1** at a fixed molar ratio (1:4), and using three different concentrations (**Rf/1**: 10/40  $\mu\text{M}$ , 20/80  $\mu\text{M}$ , 30/120  $\mu\text{M}$ ). MES was employed in all cell experiments at a final concentration of 2 mM. PC-3 cells were seeded 24 h before the experiment in 96-well plates with a density of 4000 cells per well and grown under standard conditions (Ham's F-12K medium supplemented with 10% fetal bovine serum and 1% penicillin/streptomycin at 37°C, 5% CO<sub>2</sub> and 90% humidity). Stock solutions of **Rf/1** were added and incubated with cells for 1 h, light irradiated for 1 min at 460 nm (light dose 0.36 J·cm<sup>-2</sup>), and then incubated for other 6 h. Finally, cells were washed in fresh medium and grown for other 42 h. The Sulforhodamine B (SRB) colorimetric assay was used for cell density determination. As controls, **Rf** and **1** were tested under identical conditions, while parallel experiments were performed with **Rf/1** and cisplatin kept in the dark. A home-made LED plate was employed to irradiate cells in 96-well plates (Figure S47).

**Fluorescence microscopy assays.** PC-3 cells exposed to 30:120  $\mu\text{M}$  **Rf/1** were viewed using a Zeiss Axio Observer wide field fluorescence microscope (Carl Zeiss). Cells were plated in an ibidi  $\mu$ -Slide 0.4 (13500 PC-3 cells/channel) and allowed to adhere

overnight before they were treated with **Rf/1** as described for cell viability experiments (2 mM MES, 6 h of treatment plus 42 h incubation). Analysis of cellular morphological alteration was performed using a cell-permeable green fluorescent dye from the “Live and Dead Cell Staining Kit” (Abcam) for cell nuclei (green channel) and SYTOX<sup>®</sup> AADvanced<sup>™</sup> (Invitrogen<sup>™</sup>) for dead cells (red channel). Cells were stained following commercial protocols and using binding or 10 mM PBS buffer at the end of the incubation period (48 h). Images were acquired with a Plan Apochromat 20× objective and a multi-band pass Colibri filter to collect fluorescence emission signals. Control experiments in the dark (no light irradiation) were performed on untreated cells and on cells exposed to 30:120 μM **Rf/1** or 120 μM cisplatin.

**Flow cytometry analysis.** PC-3 cells were seeded in 96-well plates (2000 cells per well) and treated with **Rf/1** (30:120 μM) and MES (2 mM) as described above. After 48 hours of incubation, 7 wells for each sample were pooled into cytometer tubes, cells were washed with 10 mM PBS and stained using 100 μL per tube of the Pacific Blue<sup>™</sup> Annexin V/SYTOX<sup>®</sup> AADvanced<sup>™</sup> flow cytometry kit (Invitrogen<sup>™</sup>). Early and late apoptosis were measured using a FACS Canto II (BD Biosciences) and results analysed using the FlowJo, LCC software. The PC-3 population was electronically gated based on the forward and side scatter parameters and the non-single events leaved out based on forward area and height scatter parameters. Inside this final population, live cells were gated as negative for both dyes; early apoptotic cells were defined as Pacific Blue-Annexin V positive cells and SYTOX<sup>®</sup> negative; and late apoptotic cells were gated as double positive for both dyes. Non-labelled and singly labelled samples were included as control and as compensation samples, respectively. Experiments were repeated three times. Besides untreated cells, control experiments included cells treated with 30:120 μM **Rf/1** and 120 μM cisplatin in the dark (no light irradiation), and light-irradiated **Rf** and **1** alone.

### 3.5 References

- 1 C. R. Bertozzi, *Acc. Chem. Res.*, 2011, **44**, 651–653.
- 2 E. M. Sletten and C. R. Bertozzi, *Angew. Chem. Int. Ed.*, 2009, **48**, 6974–6998.
- 3 D. M. Patterson, L. A. Nazarova and J. A. Prescher, *ACS Chem. Biol.*, 2014, **9**, 592–605.
- 4 A. Unciti-Broceta, *Nat. Chem.*, 2015, **7**, 538–539.
- 5 P. K. Sasmal, C. N. Streu and E. Meggers, *Chem. Commun.*, 2013, **49**, 1581–1587.
- 6 J. Clavadetscher, S. Hoffmann, A. Lilienkamp, L. Mackay, R. M. Yusop, S. A. Rider, J. J. Mullins and M. Bradley, *Angew. Chem. Int. Ed.*, 2016, **55**, 15662–15666.
- 7 S. V. Chankeshwara, E. Indrigo and M. Bradley, *Curr. Opin. Chem. Biol.*, 2014, **21**, 128–135.
- 8 J. T. Weiss, J. C. Dawson, C. Fraser, W. Rybski, C. Torres-Sánchez, M. Bradley, E. E. Patton, N. O. Carragher and A. Unciti-Broceta, *J. Med. Chem.*, 2014, **57**, 5395–5404.
- 9 J. J. Soldevila-Barreda, I. Romero-Canelón, A. Habtemariam and P. J. Sadler, *Nat. Commun.*, 2015, **6**, 6582.
- 10 Z. Liu, I. Romero-Canelón, B. Qamar, J. M. Hearn, A. Habtemariam, N. P. E. Barry, A. M. Pizarro, G. J. Clarkson and P. J. Sadler, *Angew. Chem. Int. Ed.*, 2014, **53**, 3941–3946.
- 11 T. Völker, F. Dempwolff, P. L. Graumann and E. Meggers, *Angew. Chem. Int. Ed.*, 2014, **53**, 10536–10540.
- 12 P. K. Sasmal, S. Carregal-Romero, W. J. Parak and E. Meggers, *Organometallics*, 2012, **31**, 5968–5970.
- 13 J. T. Weiss, J. C. Dawson, K. G. Macleod, W. Rybski, C. Fraser, C. Torres-Sánchez, E. E. Patton, M. Bradley, N. O. Carragher and A. Unciti-Broceta, *Nat. Commun.*, 2014, **5**, 3277.
- 14 R. M. Yusop, A. Unciti-Broceta, E. M. V. Johansson, R. M. Sánchez-Martín and M. Bradley, *Nat. Chem.*, 2011, **3**, 239–243.
- 15 G. Y. Tonga, Y. Jeong, B. Duncan, T. Mizuhara, R. Mout, R. Das, S. T. Kim, Y.-C. Yeh, B. Yan, S. Hou and V. M. Rotello, *Nat. Chem.*, 2015, **7**, 597–603.

- 16 M. Tomás-Gamasa, M. Martínez-Calvo, J. R. Couceiro and J. L. Mascareñas, *Nat. Commun.*, 2016, **7**, 12538.
- 17 L. Gong, Z. Lin, K. Harms and E. Meggers, *Angew. Chem. Int. Ed.*, 2010, **49**, 7955–7957.
- 18 M. Fontecave, *ChemCatChem*, 2010, **2**, 1533–1534.
- 19 E. Ruggiero, J. Hernández-Gil, J. C. Mareque-Rivas and L. Salassa, *Chem. Commun.*, 2015, **51**, 2091–2094.
- 20 I. Infante, J. M. Azpiroz, N. G. Blanco, E. Ruggiero, J. M. Ugalde, J. C. Mareque-Rivas and L. Salassa, *J. Phys. Chem. C*, 2014, **118**, 8712–8721.
- 21 C. R. Maldonado, N. Gómez-Blanco, M. Jauregui-Osoro, V. G. Brunton, L. Yate and J. C. Mareque-Rivas, *Chem. Commun.*, 2013, **49**, 3985–3987.
- 22 S. Weber and E. Schleicher, Eds., *Flavins and Flavoproteins*, Springer New York, New York, NY, 2014, vol. 1146.
- 23 P. F. Heelis, *Chem. Soc. Rev.*, 1982, **11**, 15–39.
- 24 G. de Gonzalo and M. W. Fraaije, *ChemCatChem*, 2013, **5**, 403–415.
- 25 C. Feldmeier, H. Bartling, K. Magerl and R. M. Gschwind, *Angew. Chem. Int. Ed.*, 2015, **54**, 1347–1351.
- 26 B. Mühldorf and R. Wolf, *Angew. Chem. Int. Ed.*, 2016, **55**, 427–430.
- 27 M. Insińska-Rak and M. Sikorski, *Chem. Eur. J.*, 2014, **20**, 15280–15291.
- 28 C. J. Baker, N. M. Mock, D. P. Roberts, K. L. Deahl, C. J. Hapeman, W. F. Schmidt and J. Kochansky, *Free Radic. Biol. Med.*, 2007, **43**, 1322–1327.
- 29 G. Zhao and N. D. Chasteen, *Anal. Biochem.*, 2006, **349**, 262–267.
- 30 S. L. Hopkins, B. Siewert, S. H. C. Askes, P. Veldhuizen, R. Zwier, M. Heger and S. Bonnet, *Photochem. Photobiol. Sci.*, 2016, **15**, 644–653.
- 31 M. A. Cismesia and T. P. Yoon, *Chem. Sci.*, 2015, **6**, 6019–6019.
- 32 M. A. Sheraz, S. H. Kazi, S. Ahmed, Z. Anwar and I. Ahmad, *Beilstein J. Org. Chem.*, 2014, **10**, 1999–2012.
- 33 P. Gramatica, E. Papa, M. Luini, E. Monti, M. B. Gariboldi, M. Ravera, E. Gabano, L. Gaviglio and D. Osella, *J. Biol. Inorg. Chem.*, 2010, **15**, 1157–1169.

### Chapter 3

- 34 C. Garino and L. Salassa, *Philos. Trans. R. Soc. A*, 2013, **371**, 20120134.
- 35 G. Thiabaud, R. McCall, G. He, J. F. Arambula, Z. H. Siddik and J. L. Sessler, *Angew. Chem. Int. Ed.*, 2016, **55**, 12626–12631.
- 36 A. Garaikoetxea Arguinizoniz, N. Gómez Blanco, P. Ansorena Legarra and J. C. Mareque-Rivas, *Dalton Trans*, 2015, **44**, 7135–7138.
- 37 F. J. Dijt, G. W. Canters, J. H. J. Den Hartog, A. T. M. Marcelis and J. Reedijk, *J. Am. Chem. Soc.*, 1984, **106**, 3644–3647.
- 38 C. Ducani, A. Leczkowska, N. J. Hodges and M. J. Hannon, *Angew. Chem. Int. Ed.*, 2010, **49**, 8942–8945.
- 39 A. Terenzi, C. Ducani, L. Male, G. Barone and M. J. Hannon, *Dalton Trans*, 2013, **42**, 11220–11226.
- 40 J. Kasparova, H. Kostrhunova, O. Novakova, R. Křikavová, J. Vančo, Z. Trávníček and V. Brabec, *Angew. Chem. Int. Ed.*, 2015, **54**, 14478–14482.
- 41 Y. Zhao, J. A. Woods, N. J. Farrer, K. S. Robinson, J. Pracharova, J. Kasparova, O. Novakova, H. Li, L. Salassa, A. M. Pizarro, G. J. Clarkson, L. Song, V. Brabec and P. J. Sadler, *Chem. – Eur. J.*, 2013, **19**, 9578–9591.

# 4

## **Biological Activity of Pt<sup>IV</sup> Prodrugs Triggered by Riboflavin-Mediated Bioorthogonal Photocatalysis**

---

A manuscript based on the work presented in this chapter has been submitted to Scientific Reports (authors: S. Alonso-de Castro, A. Terenzi, S. Hager, B. Englinger, A. Faraone, M. Galanski, B. K. Keppler, W. Berger\* and L. Salassa\*)





## 4.1 Introduction

The Riboflavin (**Rf**), vitamin B2, is an essential exogenous biomolecule for our metabolism. **Rf** is rapidly converted intracellularly into flavin mononucleotide (FMN) and flavin adenine dinucleotide (**FAD**), which are then incorporated into a multitude of flavoproteins and flavoenzymes. These have motivated an enormous interest in research due to their key role in biological systems where they catalyze the oxidation of a broad range of substrates (sugars, alcohols or aminoacids), participate in oxidation/reduction processes involved in detoxification, and play a photocatalytic role in DNA repair.<sup>1,2</sup>

**Rf** has outstanding photophysical and photochemical features that make this natural photosensitizer a good candidate for light-triggered applications in medicine. A noteworthy use of **Rf** is the Mirasol PRT™ process employed to treat blood for transfusion, in which **Rf** inactivates significant levels of viruses and bacteria in platelets and plasma upon UV light irradiation.<sup>3</sup> Besides, **Rf** has been investigated for application in photodynamic therapy (PDT). This clinically approved treatment for cancer and other diseases employs light to activate a photosensitizer and generate singlet oxygen and other reactive oxygen species (ROS) capable to induce cell death locally in irradiated areas.<sup>4</sup> Under light irradiation, **Rf** generates singlet oxygen in aerated solutions with higher quantum yields ( $\Phi_{\Delta} = 0.54 \pm 0.07$ ) than other exogenous photosensitizers used in the clinics, such as Photofrin.<sup>5</sup>

A current limitation in PDT is the absolute O<sub>2</sub>-dependency, which reduces the effectiveness of this treatment in hypoxic tissues.<sup>4</sup> The search for newer O<sub>2</sub>-independent strategies with improved photosensitizers is an emerging focus in PDT and transition metal complexes have raised significant interest as photoactivatable prodrug candidates.<sup>6</sup> Despite their encouraging profiles as antineoplastic agents, light-switchable metal complexes often suffer from modest absorption properties and innovative approaches have been explored to turn on their activity at more convenient wavelengths.<sup>7-9</sup>

In our search for novel activation strategies, we recently showed that **Rf** and other flavins, including flavoproteins, can act as photosensitizers and unconventional

photocatalysts for the selective activation of anticancer metal-based prodrug candidates such as Pt<sup>IV</sup> complexes. These photocatalytic reactions efficiently take place by means of blue rather than UV-A light in the presence of zwitterionic buffers such as MES (2-(N-morpholino)ethanesulfonic acid), as well as with biological electron donors such as NAD(P)H.

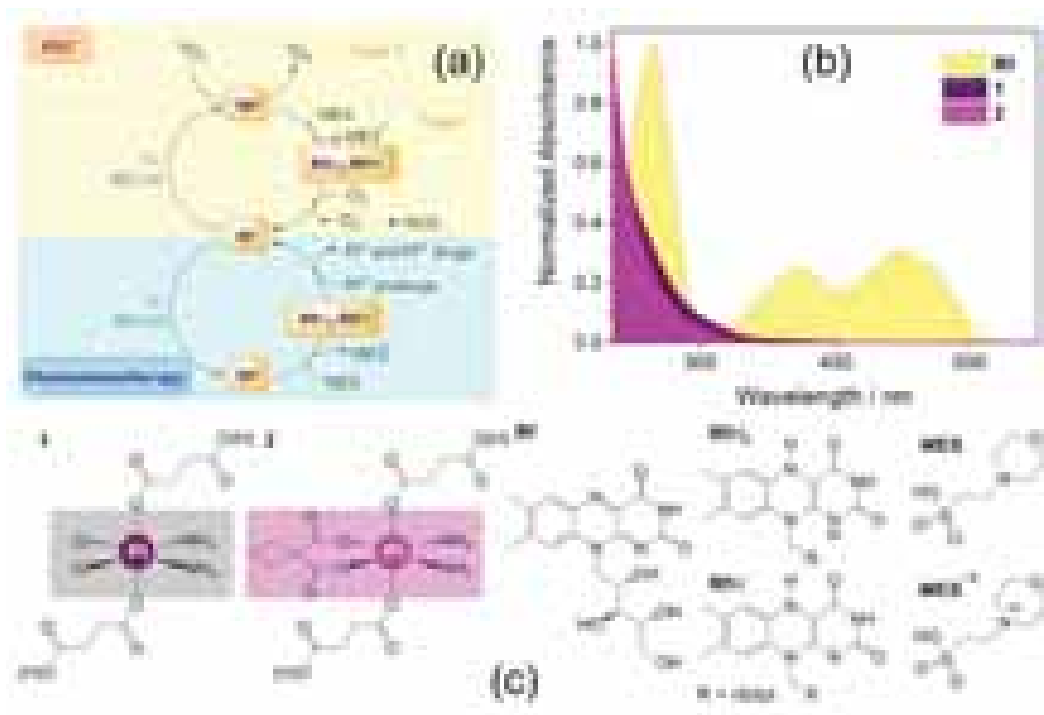


**Figure 1.** (a) Proposed photocatalytic mechanism for the bioorthogonal activation of Pt<sup>IV</sup> prodrugs by **Rf** (and other flavins); (b) UV-Vis absorption spectra of **Rf**, **1** and **2**; and (c) Schematic structures of the Pt<sup>IV</sup> prodrugs employed in this study (**1** and **2**), and chemical species involved in their photocatalytic activation.<sup>10,11</sup>

According to our current understanding of the process (**Figure 1**),<sup>10</sup> light excitation of **Rf** at 460 nm results in the formation of its triplet excited state, which is a highly oxidant species able to extract electrons from sacrificial electron donors (e.g. MES) to give the reduced riboflavin forms **RfH<sub>2</sub>** or **RfH<sup>-</sup>**. Afterwards, **RfH<sub>2</sub>** or **RfH<sup>-</sup>** catalytically affords the conversion of Pt<sup>IV</sup> complexes into biologically active Pt<sup>II</sup> species. Importantly, low doses of blue light are sufficient to fully convert high concentrations of Pt<sup>IV</sup> prodrugs in buffer solution and in cell culture medium. The **Rf** selectivity for Pt<sup>IV</sup> complexes demonstrated in the biological environment defines the bioorthogonal nature of these photocatalytic reactions.<sup>10,11</sup>

This report provides new insights on the cytotoxic effect and mechanism of action of two Pt<sup>IV</sup> prodrugs, namely *cis,cis,trans*-[Pt(NH<sub>3</sub>)<sub>2</sub>(Cl)<sub>2</sub>(O<sub>2</sub>CCH<sub>2</sub>CH<sub>2</sub>CO<sub>2</sub>H)<sub>2</sub>] (**1**) and *cis,cis,trans*-[Pt(NH<sub>3</sub>)<sub>2</sub>(CBDCA)(O<sub>2</sub>CCH<sub>2</sub>CH<sub>2</sub>CO<sub>2</sub>H)<sub>2</sub>] (**2**, where CBDCA = cyclobutane dicarboxylate), upon flavin-mediated photocatalytic activation. In particular, we describe here how the cisplatin prodrug **1** can be used in combination with **Rf** and extremely low doses of blue light to eradicate human pancreatic adenocarcinoma cells (Capan-1). This cell model was chosen because of its relatively high tolerance against PDT which allows establishing the interplay between this type of treatment and photoactivatable Pt<sup>IV</sup> prodrugs.

Pancreatic cancer is the 4<sup>th</sup> leading cause of cancer-related deaths, and its 5-years survival rate is lower than 5%. Recent studies reveal alternative treatments may change this dreadful prognosis.<sup>12–14</sup> For example, a prospective chemotherapeutic option consists on the combinatory treatment of gemcitabine with cisplatin, which revealed a significant improvement in the 6-months survival rate compared to the administration of gemcitabine alone.<sup>14</sup> In the treatment of pancreatic cancer, PDT also receives special attention since it is not accompanied by the heavy side effects of systemic chemotherapy.<sup>15</sup> Moreover, both platinum drugs<sup>16</sup> and PDT<sup>17</sup> have been shown to activate immune responses against pancreatic tumors and even immunogenic cell death.<sup>18,19</sup> The photochemistry of **Rf** may be a new tool to integrate singlet oxygen sensitization and bioorthogonal photocatalysis towards Pt<sup>IV</sup> prodrugs for exploiting some of these advantages introduced by PDT and combination therapies in the treatment of pancreatic cancer. A combined strategy for PDT and platinum drug activation may lead to synergistic antitumor drug and immune responses localized in the malignant tissue.<sup>14</sup>

## 4.2 Results and Discussion

### 4.2.1 Antiproliferative properties of Pt<sup>IV</sup> complexes photocatalytically activated by riboflavin

The potential of **Rf** in PDT is well documented.<sup>15–17</sup> We reasoned that our bioorthogonal photocatalytic strategy would be a worthy strategy to test in those cancers in which PDT is of limited efficiency or might become ineffective because of oxygen consumption.<sup>20</sup> Hence, we initially screened **Rf** photocytotoxicity in a number of human cell lines derived from different tumors including colon (SW480 and HTC116), ovarian (A2780 and A2780cis), cervix (HeLa –derivative KB-3-1), and pancreatic (Capan-1) carcinomas as well as a melanoma (VM47), and glioblastoma (H35 and H52).

In this preliminary screen, cells were treated with **Rf** concentrations up to 20  $\mu\text{M}$ . MES (1% vol., 2 mM) was added to the culture medium to prevent **Rf** photodecomposition<sup>1</sup> and mimic the conditions used for the catalytic activation of Pt<sup>IV</sup> prodrugs (*vide infra*). It is worth pointing out that no toxicity was observed due to the addition of MES alone (*data not shown*).

Cell viability experiments consisted in a drug-to-light interval of 1 h following administration, 1 min of blue light irradiation (460 nm, 0.36 J·cm<sup>-2</sup>) and 6 h of incubation. Afterwards, media was renewed and cells were incubated for a total of 72 h in the dark. Non-irradiated controls were directly incubated 7 h in the dark and then handled as described above for light-activated samples. After the 72 h, cell viability was determined by the MTT assay.

Among the panel of cell lines tested, Capan–1 showed the greatest survival and resistance against the **Rf** photosensitizing effects, retaining > 75% viability at 25  $\mu\text{M}$  **Rf** under light exposure. The low sensitivity of Capan-1 cells to PDT is enigmatic but can be ascribed to the high levels of antioxidant molecules (such as glutathione) and enzymes (such as superoxide dismutase, catalase and glutathione peroxidase) present in this cell line.<sup>4</sup> Moreover, Capan-1 cells harbor a mutated p53 tumor suppressor causing general cell death resistance<sup>20</sup> but also a BRCA2 mutation leading to enhanced

cisplatin sensitivity.<sup>22</sup> Conversely,<sup>23</sup> all the other cell lines displayed a cell viability below 10% at concentrations ranging between 5 and 15  $\mu\text{M}$  **Rf** (Figure S1).

In light of the capacity of Capan-1 cells to endure PDT at the light dose employed, we extended the concentration range of **Rf** and studied how the co-administration of MES (1% vol., 2 mM) affected **Rf** phototoxicity. In the absence of MES, no toxicity was observed for concentrations of **Rf** up to 75  $\mu\text{M}$ , both in dark and under light irradiation. However, addition of MES favors **Rf** phototoxic action, significantly decreasing cell survival (40 % cell death at 75  $\mu\text{M}$  **Rf**, Figure S2). On the basis of our previous work, this finding was anticipated. MES, as well as other zwitterionic buffers, preserves **Rf** from photodecomposition acting as electron donor, hence, extending the generation of singlet oxygen and other ROS.<sup>10</sup> In an analogous manner, acetylation of ribityl chain was demonstrated to improve **Rf** photostability and the PDT capacity of this photosensitizer.<sup>17</sup>

For sake of comparison, we also tested **FAD** under similar experimental conditions, observing a less pronounced but comparable behavior to **Rf**, and confirming the key role of MES as PDT enhancing agent for flavin photosensitizers (Figure S3).

Taking into consideration these results, we selected Capan-1 cells to evaluate the bioorthogonal **Rf**-mediated photocatalytic activation of two  $\text{Pt}^{\text{IV}}$  prodrug candidates (**Figure 1**). The compounds investigated were *cis,cis,trans*- $[\text{Pt}(\text{NH}_3)_2(\text{Cl})_2(\text{O}_2\text{CCH}_2\text{CH}_2\text{CO}_2\text{H})_2]$  (**1**) and *cis,cis,trans*- $[\text{Pt}(\text{NH}_3)_2(\text{CBDCA})(\text{O}_2\text{CCH}_2\text{CH}_2\text{CO}_2\text{H})_2]$  (**2**), which have deprotonated at carboxylic groups at physiological pH,<sup>10</sup> and are prodrugs of cisplatin and carboplatin respectively. Only a 10% load of the **Rf** catalyst was used in this set of experiments.

Both **Rf-1** and **Rf-2** catalyst-substrate pairs showed improved photocytotoxic profiles with respect to **Rf** alone under a light dose of only  $0.36 \text{ J}\cdot\text{cm}^{-2}$ . In fact, **Rf-1** and **Rf-2** induced reductions in cell viability analogous to the direct administration of the corresponding  $\text{Pt}^{\text{II}}$  drugs (Figure 2). At low  $\text{Pt}^{\text{IV}}$  concentrations, **Rf-1** is less effective in inducing cell death than cisplatin whereas light-irradiated **Rf-2** and carboplatin had similar cytotoxicity profiles. As shown previously by the Keppler group<sup>24</sup> and us<sup>25</sup>, this result may be ascribed to the fact that (photo)reductive elimination reactions of  $\text{Pt}^{\text{IV}}$

complexes are more likely to lead to single Pt<sup>II</sup> products in the case of carboplatin derivatives rather than for cisplatin ones. Control samples, which included **1** and **2** under light irradiation and in the dark, and **Rf-1/2** in the dark, showed minimal toxicity. The Pt-induced phototoxicity was lower for both **Rf-1** and **Rf-2** in the absence of MES (Figure S4 and S5). When employed as photocatalyst, **FAD** affected cell viability in a less efficient manner compared to **Rf** and even less without MES (Figure S6-9).

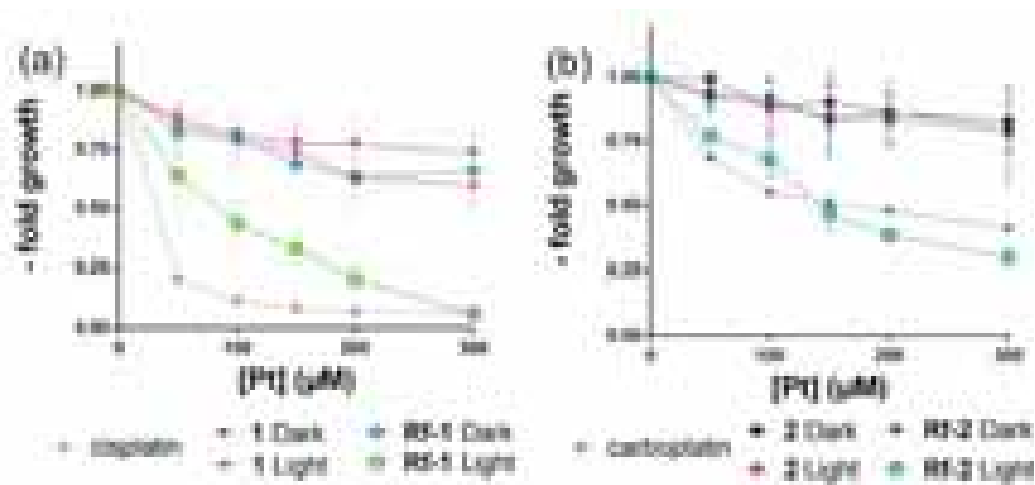


**Figure 2.** Photocatalytic effect of **Rf-1** and **Rf-2** against Capan-1 cells. Cell viability following exposure to (a) **1** and **Rf-1** and (b) **2** and **Rf-2** in the dark and under light irradiation (460 nm, 0.36 J·cm<sup>-2</sup>) compared to dark controls and cisplatin (dark).

Motivated by the activity of **Rf-1** upon light irradiation, we investigated in Capan-1 the role of catalyst loading and the O<sub>2</sub>-dependency on the prodrug activation. Fixing the concentration of **1** at 150 μM, we modified the catalyst-substrate ratio using 15 and 75 μM **Rf** (Figure S10). **Rf-1** showed high antiproliferative capacity and a small difference (10%) in cell viability between the two **Rf:1** ratios was found. Such disparity can be assigned to **Rf** phototoxicity at higher concentrations (>25 μM, Figure S2). Under hypoxic conditions (pO<sub>2</sub> < 1%), light-irradiated **Rf** alone does not produce any cytotoxicity, meanwhile **Rf-1** retains the biological activity exhibited in normoxia. For example, **Rf-1** at the catalyst-substrate ratio of 15:150 μM reduced Capan-1 cell viability to ca. 30% in both normoxic and hypoxic conditions (Figure S11). Therefore, flavin-based photocatalysis towards Pt<sup>IV</sup> complexes is an O<sub>2</sub>-independent strategy that could function in hypoxic environments where PDT generally does not work and in treatments where PDT has lost effectiveness because of O<sub>2</sub> depletion.

A remarkable aspect of this strategy is the low light dose needed for the Pt<sup>IV</sup> prodrug activation. Only 0.36 J·cm<sup>-2</sup> of 460-nm light was already sufficient to switch on cytotoxicity and provide antiproliferative effects resembling free cisplatin and carboplatin. In the case of analogue Pt<sup>IV</sup> complexes, the light dose needed for UV-A and blue light activation was more than 15 times higher than for **Rf**-mediated photocatalysis.<sup>26</sup>

#### 4.2.2 Insights in the mechanism of action

The remarkable light-induced activity of **Rf-1** in Capan-1 cells prompt us to select this prodrug system for further investigations of its mechanism of action. Additional experiments included <sup>195</sup>Pt NMR speciation studies, DNA interaction experiments by circular dichroism spectroscopy (CD), cell uptake by ICP-MS, Western blotting analysis and immunofluorescence microscopy.

<sup>1</sup>H,<sup>195</sup>Pt-HSQC NMR experiments were performed to determine the speciation of **1** upon **Rf**-mediated photocatalytic activation. The photoreduction of Pt<sup>IV</sup> metal complexes often results in multiple products, including Pt<sup>II</sup> and Pt<sup>IV</sup> species.<sup>24</sup> A sample solution of **1** (7.2 mM) and **Rf** (260 μM) in 2 mM MES (pH 6) was irradiated during 10 min (ratio **Rf:1** 1:27) and its <sup>195</sup>Pt NMR spectrum collected. The concentration of **1** in these experiments was increased compared to cell viability studies in view of the low sensitivity of <sup>195</sup>Pt NMR. **Rf** concentration was limited to 260 μM by its modest aqueous solubility.

<sup>1</sup>H,<sup>195</sup>Pt-HSQC NMR spectroscopy (Figure 3a) revealed that **1** was not completely converted under the adopted experimental conditions (signal of **1** at around 2720 ppm). Nevertheless, two new Pt species were generated by the photocatalytic process. The signal at 1310 ppm corresponded to an unknown Pt<sup>IV</sup> species, while the Pt<sup>II</sup> complex detected at around -520 ppm was identified as cisplatin, demonstrating that the photoreduction of the prodrug indeed took place. Control spectra of cisplatin and **1** with **Rf** (dark) were employed for assignment and are reported in Figures S12-15.

Considering that cisplatin anticancer activity mainly depends on its binding to DNA,<sup>27</sup> we investigated the interaction of the **Rf-1** catalyst-prodrug pair with a double stranded DNA model by circular dichroism, a technique used to monitor minor

variations on the DNA double helix.<sup>28</sup> We selected the oligodeoxyribonucleotide *ds26*, an auto-complementary sequence structured in a hairpin-duplex B-DNA fashion,<sup>29</sup> which is ideal for characterizing the formation of DNA-cisplatin adducts (Figure 3b) such as: i) intrastrand crosslinks between neighbouring guanine residues (accounting for 90% of the adducts);<sup>30–32</sup> ii) monofunctional adducts; iii) interstrand cross-links.<sup>33,34</sup> CD spectra were collected (Figure 3c and Figure S16) in the dark and after light irradiation (460 nm, 0.36 J·cm<sup>-2</sup>) using MES buffered solutions of cisplatin and **1**. These were incubated with *ds26* for 48 h at 37 °C, either in the presence or absence of **Rf**.

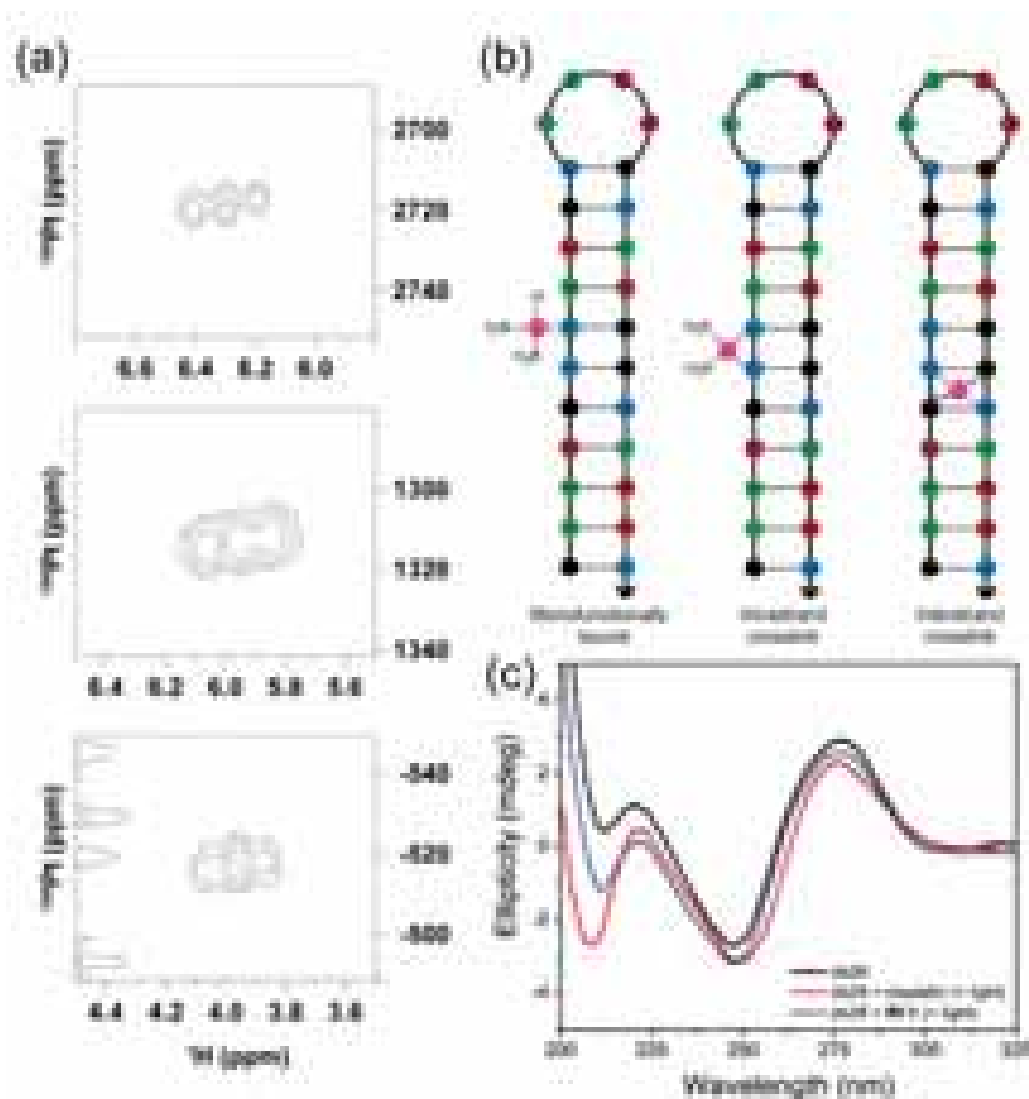


**Figure 3.** (a) <sup>1</sup>H,<sup>195</sup>Pt-HSQC NMR spectra of light irradiated **Rf-1**. Spectra were obtained using 7.2 mM **1** and 267 μM **Rf** (ratio Rf:Pt<sup>IV</sup> 1:27) in 2 mM MES buffer (pH 6) and irradiating at 460 nm for 10 min; (b) Schematic representation of the selected B-DNA model *ds26* and the possible Pt-DNA adducts formed upon treatment with cisplatin. (c) CD spectra of 1 μM *ds26* with 3 μM cisplatin and **Rf-1** (0.3/3 μM) after irradiation and incubation for 48 h at 37 °C.



Overall the global B-conformation of the DNA was retained upon complexation with Pt<sup>II</sup> species. However, spectroscopy data revealed a local perturbation of the DNA structure in the case of DNA treated with light-activated **Rf-1** and cisplatin. In particular, platinum species generated upon irradiation of **Rf-1** led to a decrease of the positive band of the B-DNA at around 275 nm, accompanied by a red shift in the 250–275 nm range. Such spectral change was previously interpreted for cisplatin as a B to C-like DNA conformational change involving the base pairs surrounding the platinated nucleosides. This feature is typical of intrastrand crosslinks which do not disrupt the Watson-Crick hydrogen bonding pattern.<sup>32,35,36</sup> On the other hand, the small increase of the negative band at 250 nm observed for cisplatin and **Rf-1** upon light activation ruled out the formation of interstrand crosslinks in *ds26*. This spectroscopic feature might be associated to a non-severe oxidative damage of DNA induced by light, as previously observed by Nowicka et al.<sup>37</sup> In fact, interstrand binding typically leads to a pronounced reduction of this negative CD band as a consequence of the disruption of the hydrogen bonds between the platinated guanines and the complementary cytosines.<sup>38</sup>

Importantly, when compared to controls (Figure S16), only irradiated **Rf-1** presented the same effects as cisplatin. These results further demonstrate the efficacy of our prodrug activation approach to deliver Pt<sup>II</sup> species capable of binding DNA bases. It is worth pointing out that the impact on the DNA CD bands induced by **Rf-1** photoproducts, although following the identical patterns, is less marked. This difference is most probably due the faster formation of the diaqua active species cis-[Pt(NH<sub>3</sub>)<sub>2</sub>(H<sub>2</sub>O)<sub>2</sub>]<sup>2+</sup> upon direct addition of cisplatin. On the contrary, **1** can undergo aquation only after photoreduction. Although obtained under different experimental conditions, <sup>1</sup>H-<sup>195</sup>Pt NMR indicated that photocatalytic activation of **1** can lead to the formation of more than one Pt species, one of which is a Pt<sup>IV</sup> derivative, supporting a significantly lower DNA binding capacity compared to an equimolar solution of cisplatin.

Cellular accumulation is a key aspect in the biological activity of a drug candidate. Therefore, Pt cell uptake experiments in Capan-1 cells were performed under different incubation regimes and irradiation protocols (Figure S17). The amount of Pt

#### Chapter 4

accumulated in cells was quantified using ICP-MS. Cisplatin and **1** alone or in combination with **Rf** (10  $\mu$ M) were used at a concentration of 100  $\mu$ M.

The quantity of Pt in Capan-1 cells found after the first hour of incubation in the dark is similar for cisplatin, **1** and **Rf-1**. After light was administered, the content of Pt found for **1** and **Rf-1** rapidly reached a plateau and did not change further between 3 h and 6 h of additional incubation. Crucially, no significant difference was observed for cells treated with **1** and **Rf-1** in the dark and upon light irradiation. On the contrary, cisplatin accumulated to a higher extent over time compared to **1** and **Rf-1**, both in the dark and when exposed to light.

The behaviour of light-irradiated **Rf-1** suggests that the antiproliferative action of the prodrug complex triggered by **Rf** under our general protocol (1h preincubation before irradiation) can be principally ascribed to a photocatalytic intracellular activation. In fact, extracellular production of Pt<sup>II</sup> species would lead to a progressive increase of the Pt content over time, as observed for cisplatin, which is not the case for **1** photocatalytically converted by **Rf**. To confirm this scenario, we performed additional cell viability experiments in which the Pt agents were removed by washing cells with fresh media immediately after 1h of preincubation and 1 min of light irradiation (Figure S18). This approach excluded that any toxicity effect could originate from species formed extracellularly. Differently from controls, light-activated **Rf-1** under such conditions reduced cell viability in a significant manner confirming the capacity of **Rf** to catalyse intracellularly the formation of cisplatin from **1**. In another control experiment, a higher Pt content was detected in Capan-1 cells in comparison to control samples when **Rf-1** was irradiated at 460 nm just after administration and then incubated for overall 7 h. Using such a modified irradiation treatment, the generation of cisplatin occurred completely outside the cell and the viability profile of **Rf-1** more closely resembles the one obtained for cisplatin (Figure S17 and S19).

Internalization of **Rf** in cancer cells is extremely rapid (in the order of minutes) due to active and passive transport mechanisms.<sup>39</sup> As demonstrated in previously reported studies, there is a predominance of passive transport over protein-mediated cellular uptake at **Rf** concentrations above normal human plasma levels (ca. 12 nM),<sup>40,41</sup> which

could support co-localization of **1** and **Rf** in the cytosol. Furthermore, the gene expression profile<sup>42</sup> of Capan-1 cells indicate that this cell line overexpresses riboflavin transporter proteins (solute carrier family 52), hence improving their ability to internalize the vitamin. So, the great majority of the **Rf** photocatalyst is only available within the cell after the first hour of preincubation and its extracellular concentration as well its capacity of generating cisplatin from extracellular **1** should be minimal. This is well in agreement with cell uptake and cytotoxicity results.

#### 4.2.3 Induction of a light-dependent DNA damage response

We next analyzed the expression and phosphorylation of characteristic proteins in the DNA damage response and cell death induction pathways by **Rf-1** under light irradiation (Figure 4a). Capan-1 cells were treated with **Rf-1** at a concentration of 10 and 100  $\mu\text{M}$  respectively and 2 mM MES under 1 min of 460-nm irradiation ( $0.36 \text{ J}\cdot\text{cm}^{-2}$ ). Control experiments included the mixture **Rf-1** in the dark and cisplatin (100  $\mu\text{M}$ ), **Rf** (10  $\mu\text{M}$ ), **1** (100  $\mu\text{M}$ ) as well as an untreated sample all in the dark and under light irradiation.

As a general remark, light is per se affecting the phosphorylation of the DNA-damage repair-initiating histone H<sub>2</sub>AX. Consequently, H<sub>2</sub>AX phosphorylation was slightly enhanced in all the irradiated samples compared with their corresponding dark analogues, probably suggesting low-level light-mediated DNA damage. Treatment with irradiated **Rf-1**, however, led to clear-cut hyperphosphorylation of H<sub>2</sub>AX compared to **Rf-1** in the dark, indicating the induction of double strand breaks (DSBs) in DNA. These DSBs in chromatin promptly initiated the phosphorylation of the histone H2A variant to generate p-H<sub>2</sub>AX. This result correlates with the extensive up-regulation observed for cisplatin samples. Nuclear foci in chromatin with accumulated p-H<sub>2</sub>AX can be conveniently detected by immunofluorescence microscopy and serve as beacons of DSB lesions. The respective photomicrographs clearly demonstrated an enhanced number of nuclear p-H<sub>2</sub>AX foci in irradiated cells in presence of **Rf-1** indicating efficient cisplatin release (Figure 4b, S21 and S22). Controls of untreated, **Rf**, **1**, **Rf-1** and also the photoreaction for **2** and **Rf-2** are shown in the supporting information (Figure S23 and S24). For complex **2**, a similar trend was observed.

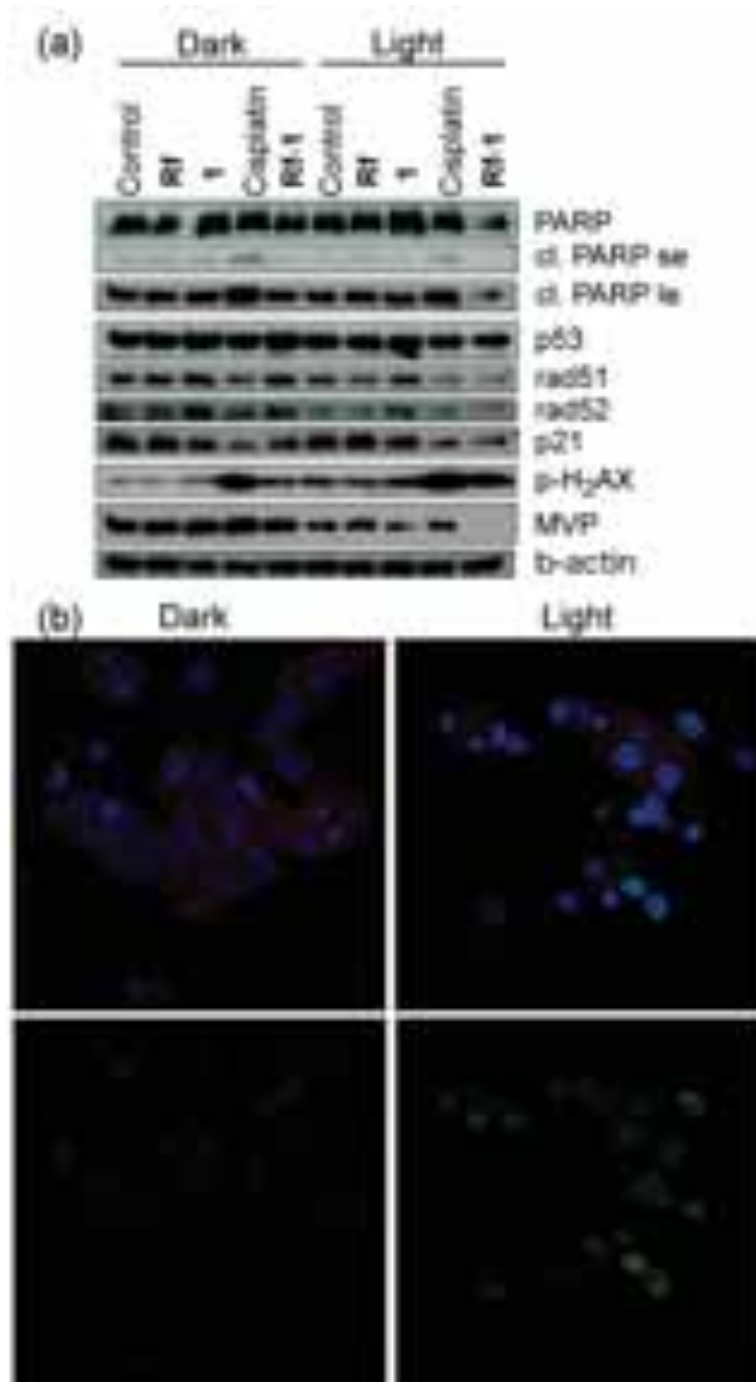


**Figure 4.** (a) Expression/phosphorylation of DNA damage and cell death proteins in Capan-1 cells analysed by Western blotting. Cells were: untreated (lane 1), or treated by 10  $\mu$ M **Rf** (lane 2), 100  $\mu$ M **1** (lane 3), 100  $\mu$ M cisplatin (lane 4) and **Rf-1** 10:100  $\mu$ M (lane 5) in the dark. Same treatments from lane 6 to 10 but under 460-nm light irradiation (460 nm, 0.36 J·cm<sup>-2</sup>). Membranes were probed for the indicated proteins or phosphorylation-specific epitopes. full-length blots/gels are presented in Supplementary Figure S20. (b) Immunofluorescence microscopy images of the DNA damage marker p-H<sub>2</sub>AX induced by **Rf-1** (10:100) in the dark and under 460-nm light irradiation. Treated and fixed Capan-1 cells were stained with DAPI (blue) to localize the nucleus, TRIC-phalloidin to visualize actin filaments (red), and p-H<sub>2</sub>AX (green) indicative for DNA DSBs.<sup>43</sup>

Rad51 and rad52 are essential proteins for repair of DNA breaks via homologous recombination<sup>44</sup> and normally upregulated by DNA damage e.g. by cisplatin.<sup>45</sup> However, in our experiment both rad51 and rad52 were rather downregulated in Capan-1 cells upon treatment with free cisplatin or **Rf-1** under light exposure. The cisplatin-induced downregulation of this repair proteins might be explained by the BRCA2-mutated background of Capan-1 cells, blocking accumulation of rad1/rad2 within DNA damage foci in the cell nucleus.<sup>46,47</sup> This is related to the distinct cisplatin sensitivity of BRCA2-mutant cancer cells.<sup>45</sup> Nevertheless, all these changes demonstrated efficient release of cisplatin upon photoactivation from **Rf-1**.

Expression of the DNA damage sensor p53 was already strongly detectable in untreated control cells reflecting the p53 mutated background of Capan-1 cells.<sup>21</sup> Accordingly, p53 levels remained widely stable after the diverse drug exposure regimes. This also explains why the p53 downstream cell cycle regulator p21<sup>48</sup> was not up- but rather downregulated by DNA-damaging cisplatin and by **Rf-1** after light exposure. On the contrary, the levels of cleaved PARP were down-regulated for irradiated **Rf-1** but up-regulated for cisplatin compared with controls. Caspase-mediated cleavage of PARP protein is a marker for apoptosis induction e.g. following DNA damage. Hence, upregulation in case of cisplatin confirmed induction of an apoptotic cell death pathway, while down-regulation for irradiated **Rf-1** would instead suggest that the prodrug system activated a caspase-independent cell death, a possible mechanism reported previously for PDT.<sup>40</sup> However, combined activation of apoptosis (by cisplatin) and non-apoptotic cell death (by PDT) might be postulated for **Rf-1** since cleaved PARP as well as total PARP were strongly diminished in the irradiated **Rf-1**-treated cells compared to the untreated and cisplatin-exposed samples.

Additionally, we investigated the impact of our therapeutic approach on the levels of major vault protein (MVP, also known as lung resistance protein LRP) upregulated by cisplatin and implicated in cisplatin resistance before.<sup>49</sup> MVP levels were generally sensitive to light with reduced expression levels in light-exposed samples. In addition, light exposure abrogated cisplatin-induced MVP upregulation. Interestingly, irradiated **Rf-1** samples were, in contrast to the corresponding cisplatin sample, completely

devoid of MVP. This suggests that photocatalytic activation strategy for Pt<sup>IV</sup> prodrugs might help overcoming MVP/LRP-mediated cisplatin resistance.<sup>50</sup>

### **4.3 Conclusions**

The photocatalytic activation of Pt<sup>IV</sup> complexes by **Rf** is an efficient strategy to control the delivery of active Pt<sup>II</sup> drugs with low light doses. Cell viability and uptake results obtained in this work evidence for the first time that **Rf** can act as bioorthogonal catalysts towards Pt<sup>IV</sup> substrates inside the cell. The details of this process within the cellular milieu still require further investigation due to the complexity of **Rf** homeostasis and Pt drugs uptake. Nevertheless, Capan-1 cells, with mutated p53 and a distinct antioxidant cell biology were effectively treated with our prodrug system **Rf-1** based on efficient cisplatin release after only 1 minute of light activation. The induced cell death was clearly mediated by the release and subsequent DNA-damage of cisplatin but also included some additional features. Hence, **Rf-1**-mediated cell death seems to include caspase-dependent and independent mechanisms and specifically suppressed the platinum drug resistance protein MVP/LRP. This treatment strategy has the potential to be further developed and tested in a photodynamic therapy setting *in vivo*.

## 4.4 Experimental details

**Cell culture.** Cell lines SW480 (Dukes' type B, colorectal adenocarcinoma; ATCC<sup>®</sup> CCL-228<sup>™</sup>), HCT-116 (colorectal carcinoma; ATCC<sup>®</sup> CCL-247<sup>™</sup>), A2780 and A2780cis (ovarian carcinoma, Sigma), KB-3-1 (Human papillomavirus-related endocervical adenocarcinoma; HELA derivative, obtained from Dr. D. W. Shen, Bethesda, Maryland) VM47 (primary melanoma as described previously<sup>51</sup>), H35 and H52 (primary glioblastoma as described previously<sup>52</sup>) and Capan-1 (liver metastatic pancreatic cancer; ATCC<sup>®</sup> HTB-79<sup>™</sup>) were grown as a monolayer at 37 °C in a humidified 5 % CO<sub>2</sub> atmosphere. RPMI growth medium was supplemented with 10% fetal bovine serum (PAA, Linz, Austria). Cell cultures were periodically checked for Mycoplasma contamination. All media were supplemented with 2 mM MES buffer (pH 6, 1% vol) or H<sub>2</sub>O (1% vol).

**MTT assay of the cell viability.** In a typical experiment,  $4 \times 10^4$  cells/ml ( $5 \times 10^4$  cells/ml in the case of Capan-1 only) were seeded in 96-well plates in 100  $\mu$ L of cell culture medium. After 48 h, cells were administered with the anticancer agents at the chosen concentrations, under dark conditions. After 1 h, cells were irradiated during 1 min at 460 nm ( $6 \text{ mW}\cdot\text{cm}^{-2}$ , corresponding to a light dose of  $0.36 \text{ J}\cdot\text{cm}^{-2}$ ) and left in the incubator for 6 h. Dark analogues were directly incubated 7 h. Cell culture media was replaced by fresh media and incubated for a total of 72 h. After this incubation period, cell viability was determined by means of the MTT assay following the instructions of the manufacturer (EZ4U Cell Proliferation and Cytotoxicity assay, from Biomedica Medizinprodukte GmbH & Co KG).

**Pt uptake in Capan-1 cells measured by ICP-MS.** Capan-1 cells in 6 well-plate with a concentration of  $3 \times 10^5$  cells/well were seeded and after 48 h exposed to cisplatin, **1** and **Rf-1** under different incubation conditions. In different set of experiments, cells were exposed to Pt agents as follows: a) 1 h in the dark, b) 1 h preincubation in the dark + 1 min of 460-nm light irradiation + 3 h in the dark, c) 1 h preincubation in the dark + 1 min of 460-nm light irradiation + 6 h in the dark, d) 1 min of 460-nm light irradiation + 7 h in the dark. All dark controls were not light irradiated and protected

## Chapter 4

from ambient light. The digestion protocol adopted was described by Keppler and coworkers previously.<sup>53</sup>

**Circular Dichroism.** Circular dichroism spectra were recorded on Chirascan™ CD (by Applied Photophysics) using 1 cm path-length quartz cuvettes, at 25 °C. The lyophilized *ds26* was firstly diluted in IDTE buffer (10 mM Tris, pH 7.5, 0.1 mM EDTA, Integrated DNA Technologies) to obtain 100 μM stock solution. The annealing process to ensure the 100% formation of the B-DNA conformation was performed by heating the *ds26* stock solution to 95 °C for 5 min, followed by slowly cooling to room temperature overnight. Stock solution of *ds26*, together with stock solutions of cisplatin, riboflavin, **1**, succinic acid, were used to prepare the final mixtures at the required concentrations diluting them with MES buffer. After irradiation for 5 minutes, the final solutions have been incubated at 37 °C for 24 or 48h and then measured.

The oligonucleotide *ds26* 5'-CAATCGGATCGAATTCGATCCGATTG-3' (GC content 46.2%) was purchased from IDT (Integrated DNA Technologies) in HPLC purity grade.

**Pt-NMR.** NMR measurements were recorded on a Bruker Avance III 500 MHz spectrometer at 500.32 (<sup>1</sup>H) and 107.38 (<sup>195</sup>Pt) MHz at 25 °C. <sup>195</sup>Pt resonances were referenced relative to external K<sub>2</sub>[PtCl<sub>4</sub>].

**Western blot analysis.** Preparation of samples: total cell protein extracts were separated by 10% sodium dodecyl sulfate- polyacrylamide gel electrophoresis (SDS-PAGE) and blotted onto polyvinylidene difluoride membranes (PVDF, Thermo Fisher Scientific). Anti-β-actin antibody (AC-15) was purchased from Sigma, anti-PARP (#9542), anti-cleaved PARP (Asp214, #5625), anti-rad51 (#8875), anti-rad52 (#3425), anti-p21 (#2947) and anti-p-H<sub>2</sub>AX (#9718) from Cell Signaling Technology, anti-p53 (DO-1) from Thermo Fisher Scientific and anti-MVP (#ALX-801-005) from Enzo Life Science. Secondary anti-mouse (#7076) and anti-rabbit (#7074) horseradish peroxidase-labeled antibodies were obtained from Cell Signaling Technologies.

**Immunofluorescence Microscopy.** 3 × 10<sup>4</sup> cells/well were seeded in 8-well spot slides (Thermo Fisher Scientific). After 48h, cells were co-incubated for 1 h with the different concentrations of cisplatin, **1**, **Rf**, **Rf-1** in darkness, in duplicates. Then, one slide was kept in the dark for 6 hours more and the other was irradiated during 1 minute at 460



nm with an LED light source ( $6 \text{ mW}\cdot\text{cm}^{-2}$ ), and also kept in the dark for 6 hours. Cells were rinsed with PBS and fixed with MeOH/Acetone 1:1 during 20 min at  $-20 \text{ }^{\circ}\text{C}$ , rinsed again with PBS and blocked with PBS + 10% BSA for 1 h. Blocking solution was aspirated and the diluted primary antibody p-H2AX Antibody 1:200 was applied and incubated at  $4 \text{ }^{\circ}\text{C}$  overnight. After rinsing with PBS, secondary antibody goat anti-rabbit antibody conjugated to AlexaFluor488 (1:500) (Thermo Fisher) was co-incubated with phalloidin (1:500) and DAPI ( $1.5 \mu\text{g}/\text{mL}$ ) for 1 h. Images were acquired on an inverted point scanning confocal microscope with PMTs (LSM700, Zeiss, Jena, Germany) using a 63 $\times$  Plan-Apochromat 63 $\times$ /1.4 oil immersion objective with Zen2010<sup>®</sup> software (Zeiss) using 405 nm (DAPI), 488 nm (AlexaFluor488) or 555 nm (phalloidin) solid state laser lines for excitation and 555 nm short pass (for DAPI and AlexaFluor488) and 560 nm long pass (phalloidin) emission filters, respectively.

## 4.5 References

- 1 A. M. Edwards, in *Flavins*, 2006, pp. 1–11.
- 2 M. Barile, T. A. Giancaspero, P. Leone, M. Galluccio and C. Indiveri, *J. Inherit. Metab. Dis.*, 2016, **39**, 545–557.
- 3 S. Marschner and R. Goodrich, *Transfus. Med. Hemoth.*, 2011, **38**, 8–18.
- 4 P. Agostinis, K. Berg, K. A. Cengel, T. H. Foster, A. W. Girotti, S. O. Gollnick, S. M. Hahn, M. R. Hamblin, A. Juzeniene, D. Kessel, M. Korbelik, J. Moan, P. Mroz, D. Nowis, J. Piette, B. C. Wilson and J. Golab, *CA-Cancer J. Clin.*, 2011, **61**, 250–281.
- 5 J. Baier, T. Maisch, M. Maier, E. Engel, M. Landthaler and W. Bäuml, *Biophys. J.*, 2006, **91**, 1452–1459.
- 6 N. A. Smith and P. J. Sadler, *Philos. T. Roy. Soc. A.*, 2013, DOI:10.1098/rsta.2012.0519.
- 7 E. Ruggiero, C. Garino, J. C. Mareque-Rivas, A. Habtemariam and L. Salassa, *Chem. Eur. J.*, 2016, **22**, 2801–2811.
- 8 E. Ruggiero, J. Hernández-Gil, J. C. Mareque-Rivas and L. Salassa, *Chem. Commun.*, 2015, **51**, 2091–2094.
- 9 S. H. C. Askes, A. Bahreman and S. Bonnet, *Angew. Chem. Int. Edit.*, 2014, **53**, 1029–1033.
- 10 S. Alonso-de Castro, E. Ruggiero, A. Ruiz-de-Angulo, E. Rezabal, J. C. Mareque-Rivas, X. Lopez, F. López-Gallego and L. Salassa, *Chem Sci*, 2017, **8**, 4619–4625.
- 11 S. Alonso-de Castro, A. L. Cortajarena, F. López-Gallego and L. Salassa, *Angew. Chem. Int. Edit.*, 2018, **57**, 3143–3147.
- 12 S. G. Bown, A. Z. Rogowska, D. E. Whitelaw, W. R. Lees, L. B. Lovat, P. Ripley, L. Jones, P. Wyld, A. Gillams and A. W. R. Hatfield, *Gut*, 2002, **50**, 549–557.
- 13 J. P. Celli, N. Solban, A. Liang, S. P. Pereira and T. Hasan, *Lasers Surg. Med.*, 2011, **43**, 565–574.
- 14 G. Ouyang, Z. Liu, S. Huang, Q. Li, L. Xiong, X. Miao and Y. Wen, *World J. Surg. Oncol.*, 2016, **14**, 59.
- 15 R. Oun, Y. E. Moussa and N. J. Wheate, *Dalton Trans.*, 2018, **47**, 6645–6653.

- 16 S. V. Hato, A. Khong, I. J. M. de Vries and W. J. Lesterhuis, *Clin. Cancer Res.*, 2014, **20**, 2831–2837.
- 17 A. D. Garg and P. Agostinis, *Photoch. Photobio. Sci.*, 2014, **13**, 474–487.
- 18 A. D. Garg and P. Agostinis, *Immunol. Rev.*, 2017, **280**, 126–148.
- 19 A. Terenzi, C. Pirker, B. K. Keppler and W. Berger, *J. Inorg. Biochem.*, 2016, **165**, 71–79.
- 20 D. E. J. G. J. Dolmans, D. Fukumura and R. K. Jain, *Nat. Rev. Cancer.*, 2003, **3**, 380–387.
- 21 S. Eisold, M. Linnebacher, E. Ryschich, D. Antolovic, U. Hinz, E. Klar and J. Schmidt, *World J. Gastroentero.*, 2004, **10**, 3583–3589.
- 22 W. Sakai, E. M. Swisher, B. Y. Karlan, M. K. Agarwal, J. Higgins, C. Friedman, E. Villegas, C. Jacquemont, D. J. Farrugia, F. J. Couch, N. Urban and T. Taniguchi, *Nature*, 2008, **451**, 1116–1120.
- 23 A. Lewis, J. Du, J. Liu, J. M. Ritchie, L. W. Oberley and J. J. Cullen, *Clin. Exp. Metastas.*, 2005, **22**, 523–532.
- 24 H. P. Varbanov, M. A. Jakupec, A. Roller, F. Jensen, M. Galanski and B. K. Keppler, *J. Med. Chem.*, 2013, **56**, 330–344.
- 25 I. Infante, J. M. Azpiroz, N. G. Blanco, E. Ruggiero, J. M. Ugalde, J. C. Mareque-Rivas and L. Salassa, *J. Phys. Chem. C*, 2014, **118**, 8712–8721.
- 26 Y. Zhao, J. A. Woods, N. J. Farrer, K. S. Robinson, J. Pracharova, J. Kasparkova, O. Novakova, H. Li, L. Salassa, A. M. Pizarro, G. J. Clarkson, L. Song, V. Brabec and P. J. Sadler, *Chem. Eur. J.*, 2013, **19**, 9578–9591.
- 27 S. Dasari and P. B. Tchounwou, *Eur. J. Pharmacol.*, 2014, **740**, 364–378.
- 28 J. Kypr, I. Kejnovská, D. Renčiuk and M. Vorlíčková, *Nucleic Acids Res.*, 2009, **37**, 1713–1725.
- 29 E. Largy and J.-L. Mergny, *Nucleic Acids Res.*, 2014, **42**, e149.
- 30 P. M. Takahara, A. Rosenzweig, C., C. Frederick, A., S. Lippard and J., *Nature*, 1995, **377**, 649–652.
- 31 A. M. J. Fichtinger-Schepman, P. H. M. Lohman, J. L. van der Veer, J. H. J. den Hartog and J. Reedijk, *Biochemistry*, 1985, **24**, 707–713.

#### Chapter 4

- 32 D. Yang, S. S. G. E. van Boom, J. Reedijk, J. H. van Boom and A. H. J. Wang, *Biochemistry*, 1995, **34**, 12912–12920.
- 33 H. Huang, L. Zhu, B. R. Reid, G. P. Drobny and P. B. Hopkinst, *Science*, 1995, **270**, 1–4.
- 34 O. Vrána, V. Boudný and V. Brabec, *Nucleic Acids Res.*, 1996, **24**, 3918–3925.
- 35 M. Uemura, Y. Yoshikawa, M. Chikuma and S. Komeda, *Metallomics*, 2012, **4**, 641–644.
- 36 V. Brabec, V. Kleinwächter, J.-L. Butour and N. P. Johnson, *Biophys. Chem.*, 1990, **35**, 129–141.
- 37 A. M. Nowicka, A. Kowalczyk, S. Sek and Z. Stojek, *Anal. Chem.*, 2013, **85**, 355–361.
- 38 C. Hofr and V. Brabec, *J. Biol. Chem.*, 2001, **276**, 9655–9661.
- 39 A. B. Foraker, C. M. Khantwal and P. W. Swaan, *Adv. Drug. Deliver. Rev.*, 2003, **55**, 1467–1483.
- 40 L. M. Bareford, M. A. Phelps, A. B. Foraker and P. W. Swaan, *Mol. Pharm.*, 2008, **5**, 839–848.
- 41 H. M. Said, A. Ortiz, M. P. Moyer and N. Yanagawa, *Am. J. Physiol-Cell Ph.*, 2000, **278**, C270–C276.
- 42 Gene Set - CAPAN1:  
[http://amp.pharm.mssm.edu/Harmonizome/gene\\_set/CAPAN1/CCLC+Cell+Line+Gene+Expression+Profiles](http://amp.pharm.mssm.edu/Harmonizome/gene_set/CAPAN1/CCLC+Cell+Line+Gene+Expression+Profiles).
- 43 A. Kinner, W. Wu, C. Staudt and G. Iliakis, *Nucleic Acids Res.*, 2008, **36**, 5678–5694.
- 44 S. C. West, *Nat. Rev. Mol. Cell Bio.*, 2003, **4**, 435–445.
- 45 S. N. Powell and L. A. Kachnic, *Anti-cancer Agent Me.*, 2008, **8**, 448–460.
- 46 B. Wan, L. Dai, L. Wang, Y. Zhang, H. Huang, G. Qian and T. Yu, *Endocr-Relat. Cancer*, 2018, **25**, 69–82.
- 47 S.-S. F. Yuan, S.-Y. Lee, G. Chen, M. Song, G. E. Tomlinson and E. Y.-H. P. Lee, *Cancer Res.*, 1999, **59**, 3547–3551.
- 48 T. Abbas and A. Dutta, *Nat. Rev. Cancer*, 2009, **9**, 400–414.

- 49 E. Steiner, K. Holzmann, L. Elbling, M. Micksche and W. Berger, *Curr. Drug Targets*, 2006, **7**, 923–934.
- 50 L. Xu, Y. Fu, Y. Li and X. Han, *Cancer Chemoth. Pharm.*, 2017, **80**, 235–242.
- 51 V. Mathieu, C. Pirker, W. M. Schmidt, S. Spiegl-Kreinecker, D. Lötsch, P. Heffeter, B. Hegedus, M. Grusch, R. Kiss, W. Berger, V. Mathieu, C. Pirker, W. M. Schmidt, S. Spiegl-Kreinecker, D. Lötsch, P. Heffeter, B. Hegedus, M. Grusch, R. Kiss and W. Berger, *Oncotarget*, 2012, **3**, 399–413.
- 52 S. Spiegl-Kreinecker, D. Lötsch, B. Ghanim, C. Pirker, T. Mohr, M. Laaber, S. Weis, A. Olschowski, G. Webersinke, J. Pichler and W. Berger, *Neuro-Oncology*, 2015, **17**, 1231–1240.
- 53 A. E. Egger, C. Rappel, M. A. Jakupec, C. G. Hartinger, P. Heffeter and B. K. Keppler, *J. Anal. At. Spectrom.*, 2009, **24**, 51–61.



# 5

## **Bioorthogonal Catalytic Activation Of Pt And Ru Anticancer Complexes By FAD And Flavoproteins**

---

The work presented in this chapter has been published in *Angew. Chem. Int. Ed.* 2018, 57, 3143–3147  
(authors: S. Alonso-de Castro, A. L. Cortajarena, F. López-Gallego and L. Salassa)





## 5.1 Introduction

The latest advancements in bioorthogonal chemistry<sup>1</sup> demonstrate how organometallic compounds and inorganic materials are capable of catalyzing the activation of profluorescent substrates and prodrugs with remarkable efficiency in biological environments.<sup>2-10</sup> These selective catalysts carry out non-natural reactions dodging the interference of biological molecules, using in some cases endogenous cellular components as co-reactants.<sup>3, 9</sup>

In this context, we recently reported a new bioorthogonal reaction in which riboflavin photoactivates a Pt<sup>IV</sup> prodrug with extremely low doses of blue light through a catalytic mechanism in the presence of zwitterionic electron donors. Light activation of the riboflavin-prodrug pair triggers cisplatin-related antiproliferative activity in PC3 cancer cells.<sup>[11]</sup> Unlike classic organometallic catalysis, where metals act as catalysts, in this reaction the metal complex is an unconventional substrate<sup>12</sup> and the biocompatible riboflavin is the catalyst.

Herein, we report fundamental discoveries in this new type of bioorthogonal chemistry by (i) investigating the catalytic behavior of various flavin catalysts, including four flavoproteins with diverse biological functions and flavin binding pockets, (ii) increasing the pool of inorganic reactions to different Pt<sup>IV</sup> and Ru<sup>II</sup> prodrug complexes and (iii) evaluating the efficiency of (bio)organic electron donors (Figure 1). Furthermore, our work shows for the first time that certain flavoproteins may be directly implicated in the activation of metallodrugs under biologically relevant conditions in the absence of light.

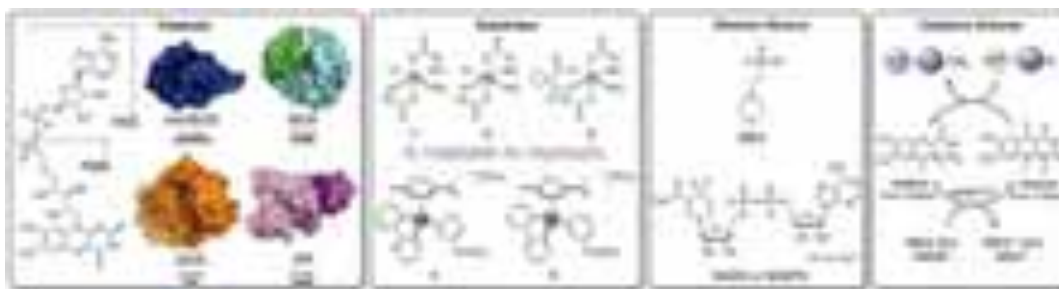


**Figure 1.** Structures of catalysts, substrates and electron donors employed in this study.

## 5.2 Results and Discussion

Initially we investigated the capacity of FAD (flavin adenine dinucleotide) as catalyst for the photoactivation of two classes of anticancer metal complexes, namely Pt<sup>IV</sup> octahedral and Ru<sup>II</sup>-arene piano-stool complexes. Complexes **1–3** are prodrugs of cisplatin and carboplatin,<sup>13</sup> and complexes **4** and **5** are photoactivatable scaffolds capable of generating reactive Ru–OH<sub>2</sub> species, which can bind to biomacromolecules (Figure 2a).<sup>14–17</sup> Importantly, these Pt<sup>IV</sup> and Ru<sup>II</sup> complexes have poor absorption properties in the visible (Figure 2b) compared to other photoactivatable complexes, e.g. Ru polypyridyls. Therefore, novel strategies to prompt their photochemistry at longer wavelengths are pivotal for use in photochemotherapy. Complexes **1–5** are stable towards hydrolysis in the dark, and have either no or poor photoreactivity under blue light excitation.<sup>11, 17–18</sup>

FAD photocatalysis towards **1–5** was performed employing 10 μM of catalyst and 200 μM of metal substrate (5% catalyst load). In all irradiation experiments, we used an LED light source (6 mW·cm<sup>-2</sup>) with an emission maximum at 460 nm and <sup>1</sup>H NMR to monitor and quantify the evolution of the photoreactions. Description of experimental methods and a complete set of dark and light-irradiation experiments are provided in the Supporting Information (Figure S1–S76).



**Figure 2.** (a) Flavin-mediated photoactivation reactions of complexes **1–5**; (b) absorption spectra of FAD and **1–5**.

In first instance, we evaluated the effect of electron donors on the catalytic process using complex **1**, with the aim of optimizing reaction conditions. Three concentrations (0.2, 2 and 20 mM) of MES (as buffer, pH 6) or NADH (pH 7, 100 mM PB, i.e. phosphate buffer) were employed for this purpose. MES was selected as electron donor to follow up our previous work on riboflavin,<sup>11</sup> while NADH for its relevance as biological

cofactor in numerous reactions catalyzed by flavoenzymes.<sup>19</sup> Moreover, metal-based catalytic drugs have been recently shown to kill cancer cells by interfering with the cellular NAD<sup>+</sup>/NADH homeostasis.<sup>20-22</sup>

Upon 460-nm light excitation, FAD photoconverted the Pt<sup>IV</sup> substrate and showed a catalytic efficiency which increased linearly alongside the MES concentration. FAD was fully inactive in the dark at any tested MES concentration. In the absence of light, 0.2 and 2 mM NADH did not induce any reaction for **1**, whereas light irradiation switched on the generation of photoproducts at 2 mM when FAD was present. At 2 mM NADH, FAD photocatalyzed the full conversion of **1** in only 2.5 min against the 5–10 min required by 20 mM MES. At the lowest concentration (0.2 mM), NADH was instantaneously photooxidized to NAD<sup>+</sup> by molecular oxygen (O<sub>2</sub>), precluding any catalytic reaction between FAD and the complex. Conversely, reduction of **1** at 20 mM NADH took place readily in the dark when FAD was present, or under light irradiation when the flavin was absent (Figure S1–8).

On this basis, we used 20 mM MES and 2 mM NADH to determine FAD photocatalytic activity towards **1–5** (Figure 2).<sup>23</sup> All complexes underwent photochemical activation in the presence of catalytic quantities of FAD (Figure S1–38). Consistently with their redox chemistry in the biological context,<sup>24</sup> FAD photoactivation of **1–4** with NADH was approximately twice as fast as MES. The only exception was **5**, towards which FAD displayed 3.4 times lower turnover frequency (TOF) using NADH than using MES (Table 1).

The kinetics of these catalytic reactions showed clear dependency on the substrate nature. Complexes **1**, **2** and **4** were the best substrates, having the highest TOFs and total turnover numbers (TTNs). Remarkably, FAD was able to complete the conversion of **1** and **2** into its corresponding photoproducts regardless of the electron donor used.

FAD allowed employing a convenient excitation wavelength (460 nm) and an extremely low light dose for the photoactivation of **1–5**. In the case of **1**, **2** and **4**, a light dose of ca. 1 J·cm<sup>-2</sup> was sufficient to fully convert the complexes in their activated photoproducts. Ru<sup>II</sup>-arene derivatives such as **4** and **5** typically require irradiation times exceeding 1 hour to reach ca. 50% conversion (Figure S24 and S32).<sup>14-17</sup>

## Chapter 5

Herein, we show that less than 15 min are sufficient to achieve comparable effects in **4** and **5** when FAD was used as photocatalyst.

**Table 1.** Turnover frequency (TOF, min<sup>-1</sup>) and total turnover number (TTN) for the FAD- and flavoprotein-catalyzed photoactivation of complexes **1–5** in the presence of MES and NADH.

Complex	MES (20 mM)			NADH (2 mM) <sup>[a]</sup>		
	TOF	TTN	% Conv.	TOF	TTN	% Conv.
	<b>FAD</b>					
<b>1</b>	2.3 ± 0.2	20	100	5.0 ± 1.7	20	100
<b>2</b>	4.0 ± 0.5	20	100	7.1 ± 1.8	20	100
<b>3</b>	0.6 ± 0.1	11	55	2.3 ± 0.6	14	70
<b>4</b>	4.5 ± 0.6	16	80	9.0 ± 2.3	20	100
<b>5</b>	2.2 ± 0.5	16	80	0.6 ± 0.1	14	70
	<b>miniSOG</b>					
<b>1</b>	1.0 ± 0.2	20	100	7.1 ± 0.4	20	100
<b>2</b>	1.2 ± 0.1	20	100	8.6 ± 2.2	20	100
	<b>NOX</b>					
<b>1</b>	0.62 ± 0.01	20	100	4.3 ± 1.6 <sup>[b]</sup>	20	100
<b>2</b>	4.7 ± 1.2	20	100	8.3 ± 1.6 <sup>[b]</sup>	20	100
	<b>GOX</b>					
<b>1</b>	Not active					
<b>2</b>	<0.1	5	20	<0.2	7.4	37
	<b>GR<sup>[a]</sup></b>					
<b>1</b>	<0.1	10	50	0.42 ± 0.07	20	100
<b>2</b>	Not active			1.2 ± 0.3	20	100

[a] = experiments for GR were run using NADPH; [b] = in the dark

In the cell milieu, flavins are bound to proteins through covalent and non-covalent interactions,<sup>19</sup> which control their (photo)redox properties.<sup>24</sup> Exploiting flavoproteins as selective catalysts is therefore an exciting prospect for the design of bioorthogonal activation strategies for metal-based prodrugs. Accordingly, we selected four flavoproteins for their diverse flavin-binding pockets and explored their capacity to

catalyze the photoreduction of **1** and **2** as substrates. This part of the study was limited to these derivatives for their relevance as anticancer compounds<sup>13, 25</sup> with respect to the Ru<sup>II</sup> complexes **4** and **5**. Furthermore, FAD had superior activity towards these Pt<sup>IV</sup> substrates with respect to **3**. The use of **2** was also aimed at gauging the role played by the charge of the substrates on the catalysis, having this complex a neutral alkyl chain at the axial position compared to the negatively charged succinate of **1**.

The flavoprotein catalysts tested were miniSOG (mini Singlet Oxygen Generator),<sup>26</sup> NOX (NADH oxidase from *Thermus thermophilus*),<sup>27</sup> GOX (glucose oxidase from *Aspergillus niger*)<sup>28</sup> and GR (glutathione reductase from *S. cerevisiae*).<sup>29</sup> MiniSOG is an FMN-containing (flavin mononucleotide) small protein investigated as a genetically encodable photosensitizer for the selective generation of singlet O<sub>2</sub>.<sup>30-32</sup> The bacterial NOX enzyme generates hydrogen peroxide (H<sub>2</sub>O<sub>2</sub>) from O<sub>2</sub> oxidizing NADH, while the eukaryotic GOX naturally oxidizes glucose to H<sub>2</sub>O<sub>2</sub> and D-glucono- $\delta$ -lactone. NOX and GOX have been both widely exploited in biocatalysis.<sup>27, 33</sup> GR is a NADPH-dependent oxidoreductase exerting a central role in glutathione metabolism for most aerobic organisms.<sup>34</sup> Conversely from the other flavoproteins, GR was selected because does not generate reactive oxygen metabolites.

Different chemical environments surround the flavin binding-pocket in these four flavoproteins, controlling solvent and substrate accessibility to the active site. As shown in Figure 3, miniSOG<sup>35</sup> and NOX, have more exposed flavins than GOX and GR, in which FAD is deeply buried into the protein scaffold. Solvent accessible surface areas of the flavins are 45.50 Å<sup>2</sup> for miniSOG, 67.92 Å<sup>2</sup> for NOX, while only 2.39 Å<sup>2</sup> for GOX and 4.01 Å<sup>2</sup> for GR. Moreover, they display different electrostatic surfaces in the proximity of the flavin binding-pocket (Figure S39–43). At pH 6–7, the NOX and GR active sites are neutral, whereas miniSOG and GOX display positive and negative electrostatic charges respectively.

Unless otherwise stated, photocatalysis experiments (Figure S44–76) were performed employing 10  $\mu$ M flavoprotein catalysts, 200  $\mu$ M **1** or **2** and either 20 mM MES or 2 mM NADH, in order to directly compare activities with the corresponding free flavin. Concentrations of flavins bound to proteins were calibrated by optical methods using

## Chapter 5

FAD and FMN (for miniSOG) absorbance at 460 nm. Catalysis results for flavoproteins are summarized in Table 1.

As anticipated from inspecting their flavin active site, GOX and GR showed the lowest catalytic activity towards the Pt<sup>IV</sup> substrates. GOX presented no catalytic activity towards **1** under none of the experimental conditions tested. Lack of activity was also found when glucose (20 mM), a natural substrate for the enzyme, was employed as source of electrons instead of MES or NADH. Conversion of **2** by GOX occurred in the presence of both electron donors, however reactions were slow and did not reach completion after 1 h of light irradiation (conversion < 40%). In MES, GR was poorly or no active towards **1** and **2**. On the contrary, NADPH prompted significantly higher TOF values and complete substrate conversion within few minutes of light exposure.

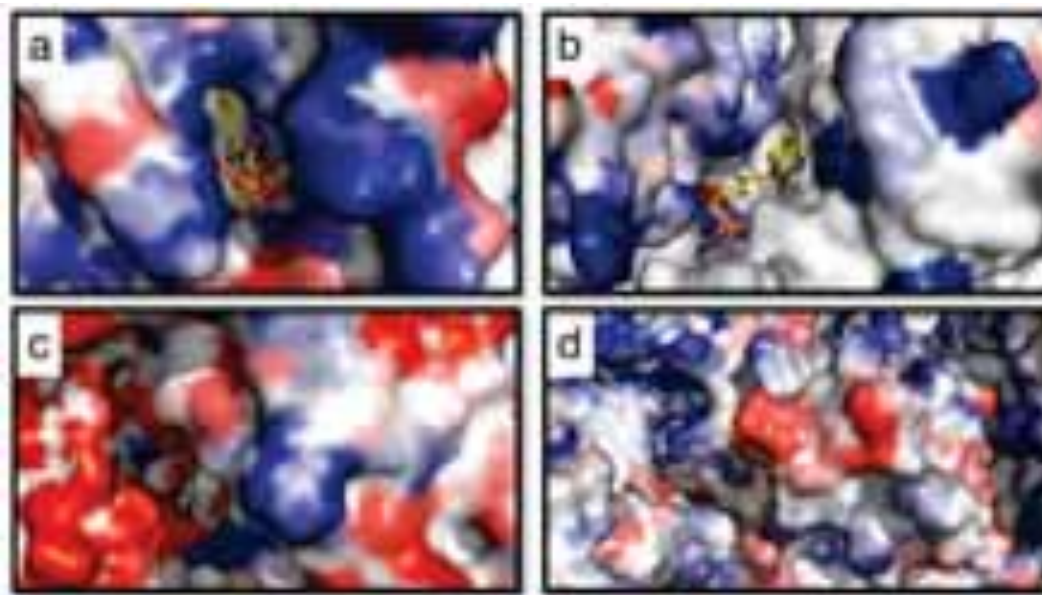


**Figure 3.** Electrostatic surface potential of the binding sites of (a) miniSOG, (b) NOX, (c) GOX and (d) GR (calculated using Bluees server). Red and blue colors represent anionic and cationic residues, respectively.<sup>36</sup>

In MES, miniSOG and NOX converted **1** and **2** into their photoproducts exclusively upon blue light excitation. Whereas miniSOG showed no preference between the two substrates, NOX was ca. 7 times more efficient towards **2** than **1**. Light irradiation also switched on the catalytic activity of miniSOG in PB/NADH. The flavoprotein achieved full conversion of 200  $\mu$ M **1** and **2** in ca. 4 min. In the case of **1**, this is approximately 5 times less efficient than free FMN (TOF  $35.6 \pm 4.3 \text{ min}^{-1}$ , Figure S50).

To our surprise, NOX behaved differently, activating **1** and **2** in the dark when co-incubated with 2 mM NADH. Under such conditions, 10  $\mu\text{M}$  NOX completely converted **1** in less than 7.5 min, while free FAD did not give any reaction with **1** over 3 h (*vide supra*). The TOF values of **1** and **2** for NOX were estimated to be  $4.3 \pm 1.6 \text{ min}^{-1}$  and  $8.3 \pm 1.6 \text{ min}^{-1}$  respectively, using less than 2  $\mu\text{M}$  of flavoprotein to allow monitoring of the reaction by NMR.

The discovery of NOX catalytic activity in the dark has broad relevance for understanding the mechanism of action of  $\text{Pt}^{\text{IV}}$  anticancer agents. It is common assumption that  $\text{Pt}^{\text{IV}}$  complexes are converted into active species by biological molecular reductants, such as glutathione or ascorbic acid, under physiological conditions.<sup>37</sup> Nevertheless, NOX-catalyzed activation of **1** and **2** in the presence of 2 mM NADH is significantly rapid and suggests that flavoproteins can provide alternative and highly efficient activation pathways for metallodrugs.<sup>38</sup>

Considering that the cellular concentration of NADH is in the 0.1–0.2 mM range,<sup>39</sup> we evaluated the capacity of NOX to convert 200  $\mu\text{M}$  **1** with an equimolar quantity of NADH in PB (Figure S64). NOX naturally uses  $\text{O}_2$  as electron acceptor to generate  $\text{H}_2\text{O}_2$  in the presence of NADH.<sup>27</sup> At such low concentration, the enzyme consumed NADH too rapidly, precluding any catalytic conversion of **1**. For this reason, the reaction was studied under  $\text{N}_2$  atmosphere. Accordingly, we determined that NOX could activate approximately a third of **1** in the absence of  $\text{O}_2$ , revealing that indeed flavoenzymes may turn on Pt drug activity under certain cellular conditions, i.e. hypoxia. Although the  $\text{Pt}^{\text{IV}}$  conversion did not reach completion, the concentration of activated **1** should reasonably be sufficient to induce cell death in cancer tissues.

At higher concentrations of electron donor in aerated solution, the enzyme reaction pathway is altered by **1**, which effectively competes with  $\text{O}_2$  and intercepts electrons from the reduced flavoenzyme. In fact, the activity of NOX was increased by 2.3 fold while the production of  $\text{H}_2\text{O}_2$  simultaneously lowered (Figure 4a) when 1 mM **1** was incubated with equimolar NADH. Under these conditions, the enzyme worked faster because it had access to higher concentrations of electron acceptors (**1** and  $\text{O}_2$ ), and produced lower amounts of  $\text{H}_2\text{O}_2$  because the hydride of NADH ought to be shared

## Chapter 5

between  $O_2$  and the metal complex reduction reactions. Conversely, miniSOG production of  $H_2O_2$  is independent of the presence of **1** (Table S1), as it is likely occurring via photosensitization.<sup>40</sup>

The capacity of miniSOG and NOX to act as bioorthogonal catalysts towards  $Pt^{IV}$  prodrugs was investigated using **1** in cell culture medium, where components such as proteins, vitamins and salts can interfere with the activation process. Reactions in the presence of NADH (2 mM) showed that miniSOG converted **1** in the biological environment only under light irradiation, while the same reaction occurred already in the dark with NOX (Figure 4b and Figure S75). The flavoproteins retained practically the same selectivity and efficiency of free FAD under the same conditions (Figure S76).

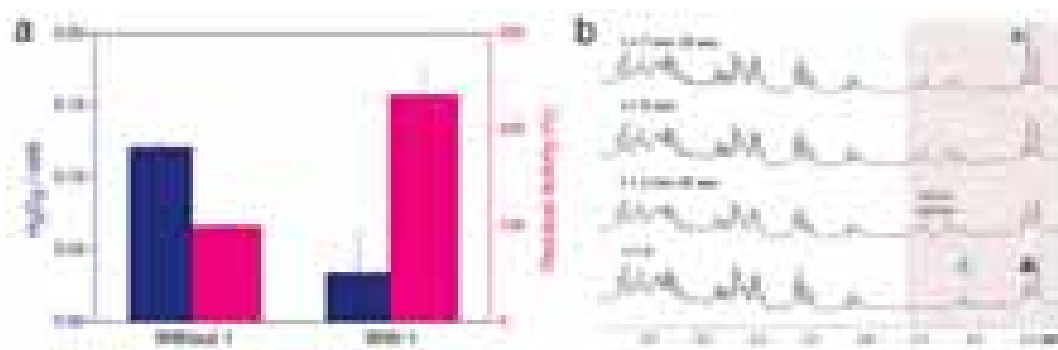


**Figure 4.** (a) NOX catalytic consumption rate of NADH (magenta) and generation of  $H_2O_2$  (blue) measured employing a 1:1 ration of **1** and NADH at a concentration of 1 mM; (b) Dark catalytic activity of NOX in cell culture medium (pH 7) in the presence of NADH.  $^1H$  NMR spectra were recorded for solutions of 200  $\mu M$  **1** and 10  $\mu M$  NOX and 2 mM NADH.  $^1H$  NMR signal labelling:  $\blacktriangle$   $Pt-OCOCH_2CH_2CO_2^-$ ,  $\blacktriangle$   $Pt-OCOCH_2CH_2CO_2^-$ ,  $\bullet$  free  $^-O_2CCH_2CH_2CO_2^-$ .

A molecular description of the catalytic mechanism through which free flavins and flavoproteins activate  $Pt^{IV}$  and  $Ru^{II}$  complexes requires further investigations and is out of the scope of this manuscript. Our previous study suggests the catalysis is linked to the generation of the reduced forms of FAD and FMN (e.g.  $FADH_2$  and  $FMNH_2$ ), either through photoinduced electron transfer (MES) or by hydride transfer (NADH/NADPH). High levels of electron donors and light help increasing the catalytic efficiency of the flavins by stabilizing their active species and consequently enhancing reaction rates. Metal complexes may form transient adducts with the reduced flavins and undergo chemical and photochemical transformations.<sup>11</sup>



Nevertheless, it is clear from the results of this study that protein scaffolds play a crucial role in governing the accessibility of the metal substrate to the flavin catalytic site. So, the negative electrostatic surface of GOX and the shielded channel in which its FAD is bound prevent any interaction with the negatively charged **1**. Consistently, we observed that the consumption of glucose by GOX was not affected by the presence of equimolar **1** (Table S2). Although with poor efficiency, GOX activated **2** in agreement with the absence of charged chemical groups in the complex and its lower reduction potential compared to **1**.<sup>41</sup>

In the case of miniSOG and NOX, however, the protein scaffold enables the artificial catalysis by facilitating the formation of reduced FMN/FAD and favoring its stabilization for the subsequent electron transfer interaction with the Pt<sup>IV</sup> substrates. Actually, miniSOG and NOX have more solvent exposed flavins and suitable electrostatic surfaces to allow metal substrates to access the active site. The role played by the protein scaffold is dramatic for NOX, which is an enzyme optimized by nature to transfer hydrides from NADH to electron acceptors. Consistently, NOX activity towards **1** and **2** is observed almost instantaneously in the dark with NADH. On the contrary, miniSOG, a protein derived from phototropin 2, which naturally does not use NADH as cofactor, requires light activation. Similarly to NOX and in contrast to GOX, GR has a mostly neutral FAD binding pocket and slightly positive surface charge, which allow catalytic activation of the **1** and **2**. Nonetheless, GR requires light triggering for the catalysis likely due to the limited accessibility of its FAD with respect to NOX.

### **5.3 Conclusions**

In conclusion, we show that free flavins and flavoproteins can catalyze artificial reactions of Pt<sup>IV</sup> and Ru<sup>II</sup> complexes, operating either in the dark or upon light excitation. Some of these unconventional reactions have promising catalytic efficiency and bioorthogonal selectivity. These findings open new opportunities for the design of chemically- and light-activated metal-based prodrugs, whose biological effects could be triggered endogenously by bioorthogonal flavoprotein catalysts.

## 5.4 Experimental details

**Materials.** Flavin adenine dinucleotide disodium salt hydrate (FAD), riboflavin 5'-monophosphate sodium salt hydrate (FMN), 2-(N-morpholino)ethanesulfonic acid (MES),  $\beta$ -nicotinamide adenine dinucleotide reduced disodium salt hydrate, sodium phosphate monobasic monohydrate, glucose oxidase from *Aspergillus niger*, glutathione reductase from *S. cerevisiae* and ABTS (2,2'-Azino-bis(3-ethylbenzothiazoline-6-sulfonic acid) diammonium salt) were purchased from Sigma Aldrich. Sodium phosphate dibasic was obtained from PANREAC and  $K_2PtCl_4$  and  $RuCl_3 \cdot 3H_2O$  from Precious Metals Online. All chemicals were used as received without additional purification. Ham's F-12K (Kaighn's) medium nutrient mixture and fetal bovine serum (FBS) were purchased from Invitrogen. Penicillin-Streptomycin mixture was purchased from Teknovas.

**Synthesis of complexes 1–5.** Complexes *cis,cis,trans*-[Pt(NH<sub>3</sub>)<sub>2</sub>(Cl)<sub>2</sub>(O<sub>2</sub>CCH<sub>2</sub>CH<sub>2</sub>CO<sub>2</sub>H)<sub>2</sub>] (**1**), *cis,cis,trans*-[Pt(NH<sub>3</sub>)<sub>2</sub>(Cl)<sub>2</sub>(O<sub>2</sub>C(CH<sub>2</sub>)<sub>3</sub>CH<sub>3</sub>)<sub>2</sub>] (**2**) and *cis,cis,trans*-[Pt(NH<sub>3</sub>)<sub>2</sub>(O<sub>4</sub>C<sub>6</sub>H<sub>6</sub>)(O<sub>2</sub>CCH<sub>2</sub>CH<sub>2</sub>CO<sub>2</sub>H)<sub>2</sub>] (**3**) were synthesized as described previously.<sup>42-44</sup> Complexes [( $\eta^6$ -p-cym)Ru(bpm)(m-COOMe-Py)](PF<sub>6</sub>)<sub>2</sub> (**4**) and [( $\eta^6$ -p-cym)Ru(bpy)(m-COOMe-Py)](PF<sub>6</sub>)<sub>2</sub> (**5**) (where p-cym = para-cymene, bpy = 2,2'-bipyridine and bpm = 2,2'-bipyrimidine) were prepared as described by us elsewhere.<sup>45</sup>

**Nuclear Magnetic Resonance and catalysis experiments.** <sup>1</sup>H NMR spectra of the various samples were recorded on an AVANCE III Bruker 500 NMR spectrometer using standard pulse programs. Chemical shifts were reported in parts-per-million ( $\delta$ , ppm) and referenced to the residual solvent peak. Catalysis studies were performed under different solution conditions (MES and PB buffers and cell culture medium). All reactions were carried out in air at 298 K and pH 6 (MES) or 7 (PB and NADH<sup>1</sup>). Light irradiation experiments were performed employing an LED light source ( $\lambda_{max} = 460$  nm, 6 mW·cm<sup>-2</sup>).<sup>11</sup> Turnover frequency (TOF), total turnover number (TTN) and % conversion for the catalytic reactions were determined by quantifying the amount of

---

<sup>1</sup> NADH was chosen in all experiments since the NOX enzyme used in this work is approx. 10 times more efficient with this cofactor/electron donor than with NADPH (Park, H.-J.; et al., Eur. J. Biochem. 1992, 205, 881-885).

converted **1–5** via  $^1\text{H}$  NMR. Integration of the free succinate and hexanoate ligand signals (singlet at 2.25–2.35 ppm and triplet at 2.04 ppm) were used for monitoring the reaction progress of **1–3**. In the case of **4** and **5**, either the signals of the p-cymene methyl groups (doublet at 0.6–1.20 ppm) or of the p-cymene ring (doublets at 5.9–6.5 ppm) were employed for the same purpose with equivalent results. TOF values were determined employing 10  $\mu\text{M}$  of flavin (either in its free or protein-bound forms) and 200  $\mu\text{M}$  of metal substrate (5% catalyst load) in the presence of 20 mM MES or 2 mM NADH. Values were calculated for substrate conversion not exceeding 40%. In the case of NOX, a concentration of protein as low as 1 or 2  $\mu\text{M}$  was used in order to allow monitoring the reaction progression by NMR.

**NOX expression, purification and FAD loading.** Plasmid harboring the gen of NADH from *Thermus thermophilus* HB27 (NOX) was transformed into the expression strain *E. coli* BL21(DE3), which carries the RNA polymerase gene from the T7 phage under the control of an inducible promoter.<sup>27</sup> The transformed cells were grown at 37°C in LB broth supplemented with ampicillin until the culture reached an optical density of 0.6 at 600 nm. Then, the expression of NOX was induced by addition of iso-propyl-1-thio- $\beta$ -D-galactopyranoside (IPTG) to a concentration of 1 mM. The bacterial culture was incubated at 37°C for further 2 h, and then the cells were harvested and washed in sodium phosphate buffer by centrifugation (10000  $\times$  g, 10 min). Afterwards, cells were lysed by sonication, and the cell debris was eliminated by centrifugation (10,000  $\times$  g for 10 min). Crude protein extracts were diluted 10 fold in 10 mM sodium phosphate at pH 7 and incubated at 80°C and pH 7 for 45 min. Protein aggregates were discarded after centrifugation (10,000  $\times$  g for 10 min), and the clarified supernatant. Finally, the pure protein was reconstituted with free FAD to assure that all NOX molecules contain at least 1 molecule of FAD. The pure protein was incubated with 0.15 mM of soluble FAD<sup>+</sup> in 100 mM sodium phosphate at pH 7 for 30 min. Afterwards, this solution was passed through a gel-filtration column (NAP<sup>TM</sup>-10 column, GE life sciences) to remove the excess of unbound free FAD<sup>+</sup> and change the buffer of the protein solution. Depending on the experiments where NOX was used, the enzyme was exchanged with 0.1 M MES at pH 6 or 25 mM sodium phosphate at pH 7.

## Chapter 5

**MiniSOG expression and purification.** miniSOG gene was amplified from the pBAD-Myc-HisA plasmid encoding miniSOG (from Tsien Lab) by polymerase chain reaction (PCR). The gene encoding miniSOG was cloned into a pPRO-EX-HTa bacteria expression vector (Invitrogen), using the restriction sites BamHI and HindIII in order to generate a His-tagged miniSOG version. The pPRO-EX-HTa vector contains a TEV recognition site before the his-tag sequence. The plasmids encoding miniSOG protein was transformed into *Escherichia coli* C41 cells. Bacteria cultures were grown in LB medium with ampicillin, at 37°C to an OD600 of 0.6-0.8, then induced with 0.6 mM IPTG and grown 5 h at 30°C. The cells were harvested by centrifugation and the pellets re-suspended with lysis buffer (300 mM NaCl, 50 mM phosphate pH 7.4) supplemented with protease inhibitor cocktail (Roche, Basel, Switzerland). Cells were lysed by sonication and the lysate was cleared by centrifugation during 30 min at 4°C and 15.000xg. His-tagged miniSOG was purified from the supernatant using a Nickel-agarose affinity column (Jena bioscience, Jena, Germany). The eluted fractions with protein were dialyzed into 150 mM NaCl, 50 mM phosphate pH 7.4 (PBS buffer). The His-tag was cleaved by overnight TEV protease digestion in 5mM EDTA, 1 mM DTT, 10 % glycerol, 50 mM Tris pH = 8.0 at 4°C. MiniSOG was purified from the His-tag and the tagged TEV protease by a second nickel affinity chromatography. Protein purity was determined by SDS-PAGE gel and MALDI-TOF mass spectrometry. Purified protein was concentrated by centrifugation using Millipore concentration devices and aliquots at the appropriate concentrations are frozen and stored at -20°C. The total protein concentration was determined by measuring the absorbance at 280 nm, using extinction coefficients calculated from amino acid composition and the total concentration of the flavin mononucleotide (FMN) chromophore was determined by absorbance at 448 nm using an extinction coefficient of 16760 M<sup>-1</sup>·cm<sup>-1</sup>.

**MiniSOG molecular model.** The miniSOG molecular model was generated as described previously.<sup>31</sup> Briefly, the model is based on the structure of the homologous protein iLOV (PBD ID: 4eet),<sup>46</sup> and generated by manual modelling by automated homology modelling using Swiss-Model (<http://swissmodel.expasy.org/SWISS-MODEL.html>).<sup>47</sup> The model was minimized using GROMOS 43B1 force field included in Swiss-PdbViewer program and YASARA minimization server

(<http://www.yasara.org/minimizationserver.htm>).<sup>48</sup> The geometry and stereochemical properties of the final model were checked and validated with Molprobity (<http://molprobity.biochem.duke.edu/>).<sup>49</sup>

**Protein electrostatic surface.** The electrostatic surfaces were calculated using Blues server based on the Poisson Boltzmann equation.<sup>36</sup> Firstly the .pdb file of each protein was converted into .pqr file to assign the electrostatic charges at pH 7 using PDB2PQR server.<sup>50</sup> The .pqr file is then upload in the Blues server obtaining a .pdb file where the b-factor columns have been replace by the corresponding electrostatic charge for each atom. The images were created using pymol 0.99 (DeLano, USA).

**Protein quantification.** Protein was quantified by Bradford's method<sup>51</sup> adapted to 96-well plates. Briefly, 5  $\mu\text{L}$  of enzyme solution were mixed with 200  $\mu\text{L}$  of Bradford reagent, incubated at room temperature for 5 min. Then the absorbance was measured at 595 nm and the protein content was estimated employing a calibration curve using BSA as a standard.

**Enzyme activity assays.** The activity of NOX was analyzed spectrophotometrically recording the absorbance at 340 nm ( $\epsilon_{\text{NADH}} = 6.22 \text{ mM}^{-1} \text{ cm}^{-1}$ ) promoted by the oxidation of in presence of different electron acceptors. Enzyme solution at different concentration was incubated with 1mM NADH and different concentrations of **1** (0–1 mM) in 25 mM sodium phosphate at pH 7 and 25 °C. The assay was adapted to 96-well plate using 200  $\mu\text{L}$  as total reaction volume. One NOX international unit (IU) was defined as the amount of enzyme needed to oxidize 1  $\mu\text{mol}$  of NADH per minute at pH 7 and 25 °C.

The activity of GOX was analyzed spectrophotometrically recording the absorbance at 414 nm ( $\epsilon_{\text{ABTS}} = 36.8 \text{ mM}^{-1} \text{ cm}^{-1}$ ) which results from the oxidation of 2,2'-Azino-bis(3-ethylbenzothiazoline-6-sulfonic acid) diammonium salt (ABTS), by coupling the peroxidase to the assay according to Bateman. Briefly, the assay was adapted to 96-well microplate with a final reaction volume of 200  $\mu\text{L}$  containing 30  $\mu\text{M}$  ABTS, 30 mM of glucose, 29  $\mu\text{g}/\text{mL}$  of horseradish peroxidase (HRP) and 0.05 mg/mL of GOX in 25 mM sodium phosphate at pH 7 in presence and absence of 0.2 mM **1**. One GOX

## Chapter 5

international unit (IU) was defined as the amount of enzyme needed to oxidize 1  $\mu\text{mol}$  of ABTS per minute at pH 7 and 25 °C.

***H<sub>2</sub>O<sub>2</sub> spectrophotometric determination.*** Once NOX quantitatively oxidized the NADH, the resulting H<sub>2</sub>O<sub>2</sub> concentration was measured by a horseradish peroxidase (HRP) assay coupled to 3,3',5,5'-Tetramethylbenzidine (TMB). 150  $\mu\text{L}$  of NOX reaction were incubated with 50  $\mu\text{L}$  of TMB solution containing 0.035 mg/mL of HRP, 2.1 mM TMB and 8.8 % (v:v) of DMSO. The reaction was incubated for 5 minutes and measure at 650 nm. The assay was calibrated with H<sub>2</sub>O<sub>2</sub> (0–0.1 mM) to quantify the H<sub>2</sub>O<sub>2</sub> produced by the action of NOX in presence of different electron acceptors.

A similar approach was employed for miniSOG. After light irradiation (460 nm, 5 min), 50  $\mu\text{L}$  of a solution containing 200  $\mu\text{M}$  **1** and 10  $\mu\text{M}$  miniSOG were mixed with 50  $\mu\text{L}$  of a solution containing horseradish peroxidase (HRP, 60  $\mu\text{g}/\text{mL}$ ) and 2 mM ABTS in 20 mM MES at pH 6. The generation of H<sub>2</sub>O<sub>2</sub> was determined by spectrophotometrical analysis measuring the absorbance at 414 nm ( $\epsilon_{\text{ABTS}} = 36.8 \text{ mM}^{-1} \text{ cm}^{-1}$ ), which results from the oxidation of ABTS.

## 5.5 References

- 1 J. A. Prescher, C. R. Bertozzi, *Nat. Chem. Biol.* 2005, **1**, 13–21.
- 2 P. K. Sasmal, C. N. Streu, E. Meggers, *Chem. Commun.* 2013, **49**, 1581–1587.
- 3 T. Völker, F. Dempwolff, P. L. Graumann, E. Meggers, *Angew. Chem. Int. Ed.* 2014, **53**, 10536–10540.
- 4 A. M. Pérez-López, B. Rubio-Ruiz, V. Sebastián, L. Hamilton, C. Adam, T. L. Bray, S. Irusta, P. M. Brennan, G. C. Lloyd-Jones, D. Sieger, J. Santamaría, A. Unciti-Broceta, *Angew. Chem. Int. Ed.* 2017, **56**, 12548–12552.
- 5 J. T. Weiss, J. C. Dawson, K. G. Macleod, W. Rybski, C. Fraser, C. Torres-Sánchez, E. E. Patton, M. Bradley, N. O. Carragher, A. Unciti-Broceta, *Nat. Commun.* 2014, **5**, 3277.
- 6 R. M. Yusop, A. Unciti-Broceta, E. M. V. Johansson, R. M. Sánchez-Martín, M. Bradley, *Nat. Chem.* 2011, **3**, 239–243.
- 7 J. Clavadetscher, S. Hoffmann, A. Lilienkamp, L. Mackay, R. M. Yusop, S. A. Rider, J. J. Mullins, M. Bradley, *Angew. Chem. Int. Ed.* 2016, **55**, 15662–15666.
- 8 M. I. Sanchez, C. Penas, M. E. Vazquez, J. L. Mascareñas, *Chem. Sci.* 2014, **5**, 1901–1907.
- 9 M. Tomás-Gamasa, M. Martínez-Calvo, J. R. Couceiro, J. L. Mascareñas, *Nat. Commun.* 2016, **7**, 12538.
- 10 G. Y. Tonga, Y. Jeong, B. Duncan, T. Mizuhara, R. Mout, R. Das, S. T. Kim, Y.-C. Yeh, B. Yan, S. Hou, V. M. Rotello, *Nat. Chem.* 2015, **7**, 597–603.
- 11 S. Alonso-de Castro, E. Ruggiero, A. Ruiz-de-Angulo, E. Rezabal, J. C. Mareque-Rivas, X. Lopez, F. Lopez-Gallego, L. Salassa, *Chem. Sci.* 2017, **8**, 4619–4625.
- 12 L. Gong, Z. Lin, K. Harms, E. Meggers, *Angew. Chem. Int. Ed.* 2010, **49**, 7955–7957.
- 13 T. C. Johnstone, K. Suntharalingam, S. J. Lippard, *Chem. Rev.* 2016, **116**, 3436–3486.
- 14 F. Barragán, P. López-Senín, L. Salassa, S. Betanzos-Lara, A. Habtemariam, V. Moreno, P. J. Sadler, V. Marchán, *J. Am. Chem. Soc.* 2011, **133**, 14098–14108.
- 15 S. Betanzos-Lara, L. Salassa, A. Habtemariam, O. Novakova, A. M. Pizarro, G. J. Clarkson, B. Liskova, V. Brabec, P. J. Sadler, *Organometallics* 2012, **31**, 3466–3479.

## Chapter 5

- 16 S. Betanzos-Lara, L. Salassa, A. Habtemariam, P. J. Sadler, *Chem. Commun.* 2009, 6622–6624.
- 17 A. Habtemariam, C. Garino, E. Ruggiero, S. Alonso-de Castro, C. J. Mareque-Rivas, L. Salassa, *Molecules* 2015, **20**, 7276–7291.
- 18 I. Infante, J. M. Azpiroz, N. G. Blanco, E. Ruggiero, J. M. Ugalde, J. C. Mareque-Rivas, L. Salassa, *J. Phys. Chem. C* 2014, **118**, 8712–8721.
- 19 D. P. H. M. Heuts, N. S. Scrutton, W. S. McIntire, M. W. Fraaije, *FEBS J.* 2009, **276**, 3405–3427.
- 20 R. J. Needham, C. Sanchez-Cano, X. Zhang, I. Romero-Canelón, A. Habtemariam, M. S. Cooper, L. Meszaros, G. J. Clarkson, P. J. Blower, P. J. Sadler, *Angew. Chem. Int. Ed.* 2017, **56**, 1017–1020.
- 21 J. J. Soldevila-Barreda, I. Romero-Canelón, A. Habtemariam, P. J. Sadler, *Nat. Commun.* 2015, **6**, 6582.
- 22 S. Bose, A. H. Ngo, L. H. Do, *J. Am. Chem. Soc.* 2017, **139**, 8792–8795.
- 23 After conversion to their aqua complexes, **3** and **4** underwent formation of DMSO and NADH adducts in MES and PB buffer (Figure S30 and 38).
- 24 *Flavins and Flavoproteins*, Vol. S. Weber, E. Schleicher, Springer, New York, 2014.
- 25 S. Dhar, F. X. Gu, R. Langer, O. C. Farokhzad, S. J. Lippard, *Proc. Nat. Acad. Sci. USA* 2008, **105**, 17356–17361.
- 26 X. Shu, V. Lev-Ram, T. J. Deerinck, Y. Qi, E. B. Ramko, M. W. Davidson, Y. Jin, M. H. Ellisman, R. Y. Tsien, *PLOS Biol.* 2011, **9**, e1001041.
- 27 J. Rocha-Martín, D. Vega, J. M. Bolivar, C. A. Godoy, A. Hidalgo, J. Berenguer, J. M. Guisán, F. López-Gallego, *BMC Biotechnol.* 2011, **11**, 101.
- 28 V. Leskovac, S. Trivić, G. Wohlfahrt, J. Kandrač, D. Peričin, *Int. J. Biochem. Cell Biol.* 2005, **37**, 731–750.
- 29 J. Yu, C.-Z. Zhou, *Proteins* 2007, **68**, 972–979.
- 30 A. Rodriguez-Pulido, A. L. Cortajarena, J. Torra, R. Ruiz-Gonzalez, S. Nonell, C. Flors, *Chem. Commun.* 2016, **52**, 8405–8408.
- 31 R. Ruiz-González, A. L. Cortajarena, S. H. Mejias, M. Agut, S. Nonell, C. Flors, *J. Am. Chem. Soc.* 2013, **135**, 9564–9567.



- 32 M. Westberg, L. Holmegaard, F. M. Pimenta, M. Etzerodt, P. R. Ogilby, *J. Am. Chem.Soc.* 2015, **137**, 1632–1642.
- 33 M. D. Gouda, M. S. Thakur, N. G. Karanth, *Biotechnol. Tech.* 1997, **11**, 653–655.
- 34 M. Deponte, *Biochim. Biophys. Acta* 2013, **1830**, 3217–3266.
- 35 Information on the miniSOG structural model is provided in the Experimental Section.
- 36 I. Walsh, G. Minervini, A. Corazza, G. Esposito, S. C. E. Tosatto, F. Fogolari, *Bioinformatics* 2012, **28**, 2189–2190.
- 37 E. Wexselblatt, D. Gibson, *J. Inorg. Biochem.* 2012, **117**, 220–229.
- 38 A. Nemirovski, Y. Kasherman, Y. Tzaraf, D. Gibson, *J. Med. Chem.* 2007, **50**, 5554–5556.
- 39 N. Ma, M. A. Digman, L. Malacrida, E. Gratton, *Biomed. Opt. Express* 2016, **7**, 2441–2452.
- 40 F. M. Pimenta, R. L. Jensen, T. Breitenbach, M. Etzerodt, P. R. Ogilby, *Photochem. Photobiol.* 2013, **89**, 1116–1126.
- 41 P. Gramatica, E. Papa, M. Luini, E. Monti, M. B. Gariboldi, M. Ravera, E. Gabano, L. Gaviglio, D. Osella, *J. Biol. Inorg. Chem.* 2010, **15**, 1157–1169.
- 42 M. Reithofer, M. Galanski, A. Roller, B. K. Keppler, *Eur. J. Inorg. Chem.* 2006, **2006**, 2612–2617.
- 43 H. P. Varbanov, S. M. Valiahdi, C. R. Kowol, M. A. Jakupec, M. Galanski, B. K. Keppler, *Dalton Trans.* 2012, **41**, 14404–14415.
- 44 S. Dhar, F. X. Gu, R. Langer, O. C. Farokhzad, S. J. Lippard, *Proc. Nat. Acad. Sci. USA* 2008, **105**, 17356–17361.
- 45 A. Habtemariam, C. Garino, E. Ruggiero, S. Alonso-de Castro, C. J. Mareque-Rivas, L. Salassa, *Molecules* 2015, **20**, 7276–7291.
- 46 J. M. Christie, K. Hitomi, A. S. Arvai, K. A. Hartfield, M. Mettlen, A. J. Pratt, J. A. Tainer, E. D. Getzoff, *J. Biol.Chem.* 2012, **287**, 22295–22304.
- 47 T. Schwede, J. Kopp, N. Guex, M. C. Peitsch, *Nucleic Acids Res.* 2003, **31**, 3381–3385.

## Chapter 5

- 48 E. Krieger, K. Joo, J. Lee, J. Lee, S. Raman, J. Thompson, M. Tyka, D. Baker, K. Karplus, *Proteins* 2009, **77 Suppl 9**, 114–122.
- 49 S. C. Lovell, I. W. Davis, W. B. Arendall, P. I. W. de Bakker, J. M. Word, M. G. Prisant, J. S. Richardson, D. C. Richardson, *Proteins: Structure, Function, and Bioinformatics* 2003, **50**, 437–450.
- 50 T. J. Dolinsky, J. E. Nielsen, J. A. McCammon, N. A. Baker, *Nucleic Acids Res.* 2004, **32**, W665–W667.
- 51 M. M. Bradford, *Anal. Biochem.* 1976, **72**, 248–254.

## Conclusions

The use of photoactivatable metal complexes as anticancer prodrugs is a promising approach that merges the benefits of light as spatio-temporal trigger, with the well-known antineoplastic effects of metal-based drugs. In particular, photoactivatable Pt<sup>IV</sup> complexes attract much attention since they can be transformed into clinically approved Pt<sup>II</sup> drugs (e.g. cisplatin, carboplatin). Nevertheless, photoactivatable Pt<sup>IV</sup> complexes generally suffer from poor absorption profiles. For this reason, a complementary strategy to efficiently deliver cytotoxic Pt<sup>II</sup> species at more convenient excitation wavelengths (i.e. 460 nm) has been explored by introducing flavin cofactors and flavoproteins as photosensitizers. This allows excluding the use of UVA light, a range of wavelengths that is unsuitable for biomedical applications since it directly damages cellular components. Additionally, flavins are good candidates for use in biology and medicine since they take part in a great variety of processes occurring in living organisms. Nonetheless, flavins are more than simple photosensitizers in the activation chemistry of these metal-based prodrugs. They simultaneously act as unconventional catalysts and metal complexes, typically considered as catalysts, behave as substrates.

This Ph.D. project has exploited such an atypical reactivity to devise a new prodrug activation approach, in which bioorganic flavin catalysts are able of photocatalyzing the transformation of anticancer metal agents with high efficiency and without being disrupted in biological media. Few other catalysis-based strategies have been reported to successfully deliver biologically active species in a bioorthogonal fashion. However, none of them is applied to metal-based prodrugs. They typically use metal complexes as catalysts for the activation of organic drugs and often suffer from metal poisoning or interferences by other biomolecules.

Fundamental for the development of my Ph.D project has been the initial discovery that the co-administration of the riboflavin (Rf) and the photoactivatable Pt<sup>IV</sup> complex *cis,cis,trans*-[Pt(NH<sub>3</sub>)<sub>2</sub>(Cl)<sub>2</sub>(O<sub>2</sub>CCH<sub>2</sub>CH<sub>2</sub>CO<sub>2</sub>)<sub>2</sub>]<sup>2-</sup> as catalyst/substrate couple enables photoconversion of Pt<sup>IV</sup> into biologically active species by light irradiation at 460 nm.

This Rf-Pt<sup>IV</sup> pair induces an anticancer activity comparable to cisplatin in prostate cancer PC3 cells with light doses as low as 0.36 J·cm<sup>-2</sup>. The need of only such a small light dose is valuable since long expositions to blue light have non-negligible tissue damage. The remarkable photocatalytic turnover obtained for the conversion of Pt<sup>IV</sup> into Pt<sup>II</sup> species is an attractive prospect to amplify the antineoplastic action of metal-based prodrugs specifically in the tumor tissue.

During the Ph.D stay in the group of Dr. Walter Berger at the Medical University of Vienna, more insights into the photocytotoxic activity and mechanism of action of this prodrug system have been obtained. Cell viability and uptake results in pancreatic carcinoma Capan-1 cells evidence for the first time that Rf can act as bioorthogonal catalyst towards Pt<sup>IV</sup> substrates intracellularly. Capan-1 cells, which are characterized by a mutated p53 and a distinct antioxidant cell biology, are effectively induced into cell death after treatment with Rf-Pt<sup>IV</sup> and only 1 minute of blue light activation. This photocytotoxic effect is clearly mediated by the release of cisplatin and subsequent DNA-damage, but other pathways are targeted as well, such as the specifically suppressed platinum drug resistance protein MVP/LRP.

The last part of this Ph.D thesis has aimed at further expanding this chemistry by exploring the capability of flavoproteins to catalyze artificial reactions on two different classes of anticancer metal complexes, specifically Pt<sup>IV</sup> octahedral and Ru<sup>II</sup>-arene piano-stool complexes. The latter are photoactivatable scaffolds that generate reactive Ru-OH<sub>2</sub> species, which can bind to biomacromolecules and exert anticancer activity. Free FAD displays good catalysis features for all the metal-based substrates in the presence of two different electron donors (MES and NADH). Flavoproteins showed as well the capacity to function as photocatalysts, however a disparity in their catalytic efficiency and bioorthogonal selectivity is observed, depending on the accessibility of the flavin binding pocket and the protein electrostatic surface potential. As a result, GOX and GR have lower reactivity while miniSOG and NOX are more efficient catalysts. Interestingly, NOX in the presence of its natural cofactor NADH was able to activate the Pt<sup>IV</sup> prodrugs also in the dark.

These findings are relevant since they support that enzymes of this type may also be involved in the activation of Pt<sup>IV</sup> prodrugs. Besides, the discovery may open new designs of metal-based prodrugs which can be bioorthogonally activated by endogenous flavoprotein catalysts.

Overall, my Ph.D work represents the starting point of a long-term project that aims at developing unconventional photocatalysis approaches for drug activation. Many details of the flavin-based catalysis process still require elucidation and their understanding would help to improve the design of photoactivatable prodrug systems. At this stage, I envision that the following points are crucial to further advancing the bioorthogonal catalytic activation of anticancer metal complexes towards preclinical studies:

- a) Obtaining insights in the catalysis mechanism such as thorough determination of reaction kinetics and detection/isolation of key intermediates. In this context, I believe modeling methods (i.e. Density Functional Theory DFT) can provide useful information on the nature of catalyst-substrate adducts which appear to play a key role in the catalysis.
- b) Performing biological studies to elucidate which cell death pathways follow the flavin-activated Pt drugs (e.g. caspase dependent or independent). Such work serves to assess the potential of our strategy to combine the benefits of PDT and chemotherapy (i.e. generation of <sup>1</sup>O<sub>2</sub> and liberation of toxic metal-containing species). In addition, the use of intracellularly or/and artificially expressed flavoproteins as bioorthogonal catalysts would be an intriguing approach to employ cellular components to selectively activate anticancer metal complexes in specific compartments.
- c) Introducing as photocatalyst the flavin derivative roseoflavin ( $\lambda_{\text{max}} = 505 \text{ nm}$ ) for its improved absorption properties, with the aim further red-shifting the excitation wavelength employed to trigger the photoactivation.
- d) Formulating viable delivery systems for *in vivo* applications, as for example, by the incorporation of catalysts and/or substrates into nanoparticles (e.g. upconverting nanoparticles) or other bioorganic platforms (e.g. polymeric micro-beads).



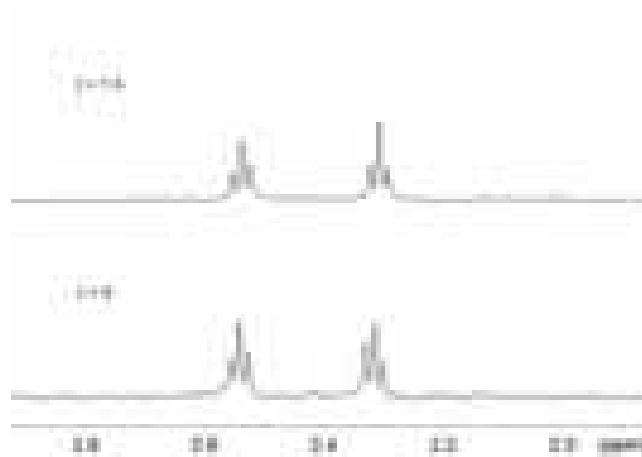
# 3

## Supporting Information

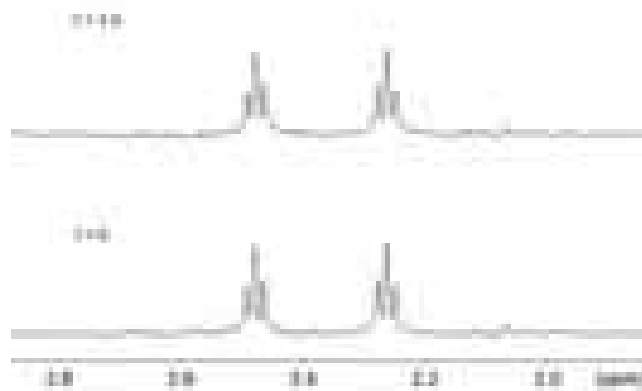
**Riboflavin As Bioorthogonal  
Photocatalyst For The Activation Of A  
Pt<sup>IV</sup> Prodrug**



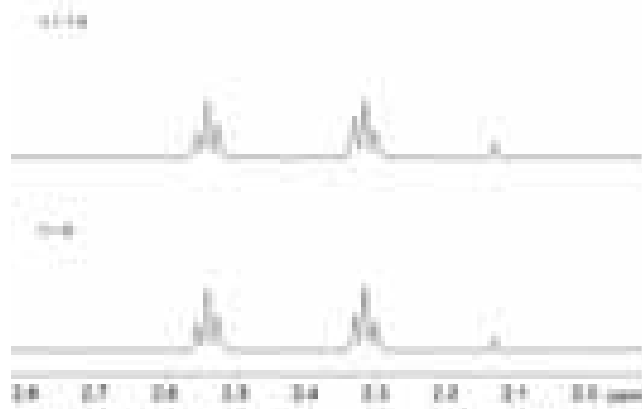




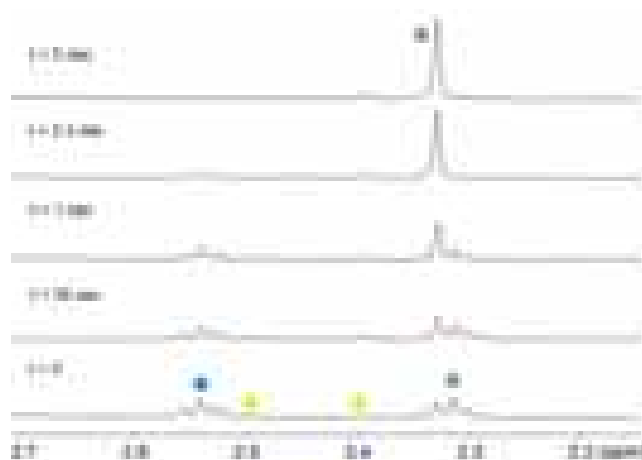
**Figure S1.** Photostability of **1** in H<sub>2</sub>O (pH 6). <sup>1</sup>H NMR control spectra of a H<sub>2</sub>O/D<sub>2</sub>O solution (9:1) of **1** under 460-nm light irradiation (2.5 mW·cm<sup>-2</sup>) for 1 h.



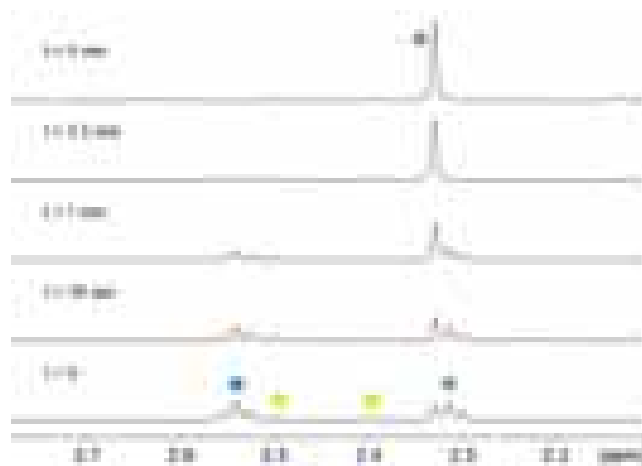
**Figure S2.** Photostability of **1** in phosphate buffer (PB). <sup>1</sup>H NMR control spectra of a PB/D<sub>2</sub>O solution (9:1, PB 100 mM, pH 5.5) of **1** under 460-nm light irradiation (2.5 mW·cm<sup>-2</sup>) for 1 h.



**Figure S3.** Photostability of **1** in MES buffer. <sup>1</sup>H NMR control spectra of a MES/D<sub>2</sub>O solution (9:1, MES 18 mM, pH 6.0) of **1** under 460-nm light irradiation (2.5 mW·cm<sup>-2</sup>) for 1 h.

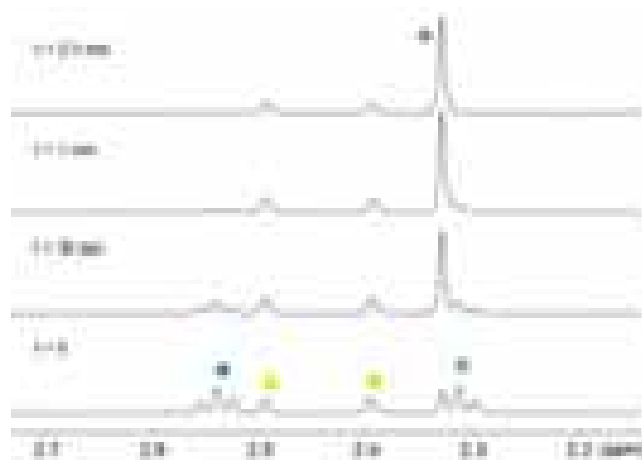
[Rf] = 12  $\mu$ M

**Figure S4.** Photolysis of **1** in MES buffer in the presence of 12  $\mu$ M **Rf**.  $^1\text{H}$  NMR spectra of a MES/ $\text{D}_2\text{O}$  solution (9:1, MES 18 mM, pH 6.0) of 120  $\mu$ M **1** and 12  $\mu$ M **Rf** under 460-nm light irradiation ( $2.5 \text{ mW}\cdot\text{cm}^{-2}$ ) for  $t_{\text{irr}} = 0 \text{ sec}$ , 30 sec, 1 min, 2.5 min and 5 min.  $^1\text{H}$  NMR signal labelling: ● Pt-OCOCH<sub>2</sub>CH<sub>2</sub>CO<sub>2</sub><sup>-</sup>, ● Pt-OCOCH<sub>2</sub>CH<sub>2</sub>CO<sub>2</sub><sup>-</sup>, ● methyl groups of **Rf** isoalloxazine ring, ● free <sup>-</sup>O<sub>2</sub>CCH<sub>2</sub>CH<sub>2</sub>CO<sub>2</sub><sup>-</sup>.

[Rf] = 24  $\mu$ M

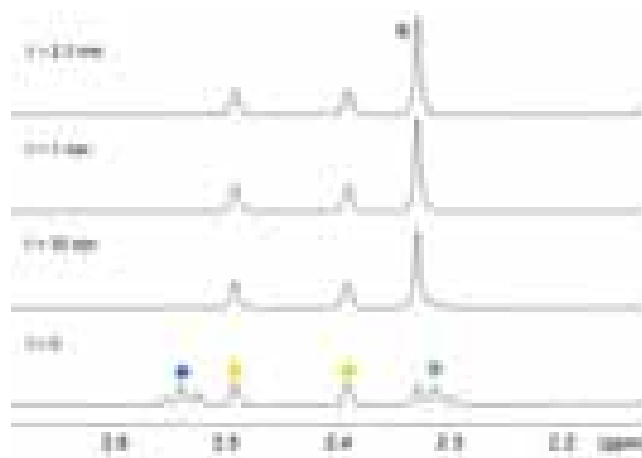
**Figure S5.** Photolysis of **1** in MES buffer in the presence of 24  $\mu$ M **Rf**.  $^1\text{H}$  NMR spectra of a MES/ $\text{D}_2\text{O}$  solution (9:1, MES 18 mM, pH 6.0) of 120  $\mu$ M **1** and 24  $\mu$ M **Rf** under 460-nm light irradiation ( $2.5 \text{ mW}\cdot\text{cm}^{-2}$ ) for  $t_{\text{irr}} = 0 \text{ sec}$ , 30 sec, 1 min, 2.5 min and 5 min.  $^1\text{H}$  NMR signal labelling: ● Pt-OCOCH<sub>2</sub>CH<sub>2</sub>CO<sub>2</sub><sup>-</sup>, ● Pt-OCOCH<sub>2</sub>CH<sub>2</sub>CO<sub>2</sub><sup>-</sup>, ● methyl groups of **Rf** isoalloxazine ring, ● free <sup>-</sup>O<sub>2</sub>CCH<sub>2</sub>CH<sub>2</sub>CO<sub>2</sub><sup>-</sup>.

[Rf] = 50  $\mu\text{M}$

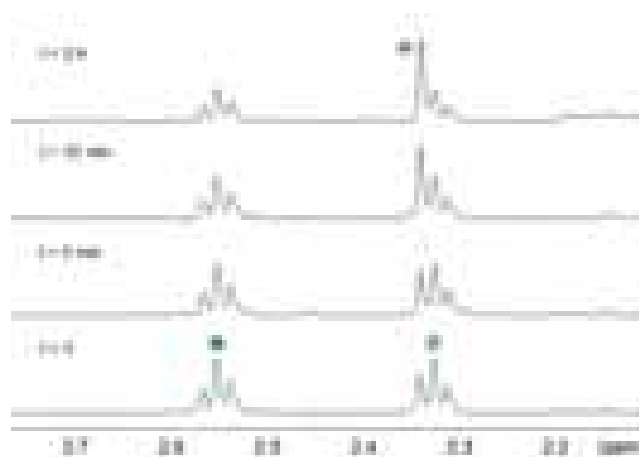


**Figure S6.** Photolysis of **1** in MES buffer in the presence of 50  $\mu\text{M}$  **Rf**.  $^1\text{H}$  NMR spectra of a MES/D<sub>2</sub>O solution (9:1, MES 18 mM, pH 6.0) of 120  $\mu\text{M}$  **1** and 50  $\mu\text{M}$  **Rf** under 460-nm light irradiation ( $2.5 \text{ mW}\cdot\text{cm}^{-2}$ ) for  $t_{\text{irr}} = 0 \text{ sec}$ , 30 sec, 1 min and 2.5 min.  $^1\text{H}$  NMR signal labelling: ● Pt-OCOCH<sub>2</sub>CH<sub>2</sub>CO<sub>2</sub><sup>-</sup>, ● Pt-OCOCH<sub>2</sub>CH<sub>2</sub>CO<sub>2</sub><sup>-</sup>, ● methyl groups of **Rf** isoalloxazine ring, ● free <sup>-</sup>O<sub>2</sub>CCH<sub>2</sub>CH<sub>2</sub>CO<sub>2</sub><sup>-</sup>.

[Rf] = 120  $\mu\text{M}$



**Figure S7.** Photolysis of **1** in MES buffer in the presence of 120  $\mu\text{M}$  **Rf**.  $^1\text{H}$  NMR spectra of a MES/D<sub>2</sub>O solution (9:1, MES 18 mM, pH = 6.0) of 120  $\mu\text{M}$  **1** and 120  $\mu\text{M}$  **Rf** under 460-nm light irradiation ( $2.5 \text{ mW}\cdot\text{cm}^{-2}$ ) for  $t_{\text{irr}} = 0 \text{ sec}$ , 30 sec, 1 min and 2.5 min.  $^1\text{H}$  NMR signal labelling: ● Pt-OCOCH<sub>2</sub>CH<sub>2</sub>CO<sub>2</sub><sup>-</sup>, ● Pt-OCOCH<sub>2</sub>CH<sub>2</sub>CO<sub>2</sub><sup>-</sup>, ● methyl groups of **Rf** isoalloxazine ring, ● free <sup>-</sup>O<sub>2</sub>CCH<sub>2</sub>CH<sub>2</sub>CO<sub>2</sub><sup>-</sup>.

[Rf] = 0.13  $\mu\text{M}$ 

**Figure S8.** Photolysis of **1** in MES buffer in the presence of 0.13  $\mu\text{M}$  **Rf**.  $^1\text{H}$  NMR spectra of a MES/ $\text{D}_2\text{O}$  solution (9:1, MES 18 mM, pH 6.0) of 120  $\mu\text{M}$  **1** and 0.13  $\mu\text{M}$  **Rf** under 460-nm light irradiation ( $2.5 \text{ mW}\cdot\text{cm}^{-2}$ ) for  $t_{\text{irr}} = 0, 5, 35$  and 120 min.  $^1\text{H}$  NMR signal labelling: ●  $\text{Pt}-\text{OCOCH}_2\text{CH}_2\text{CO}_2^-$ , ●  $\text{Pt}-\text{OCOCH}_2\text{CH}_2\text{CO}_2^-$  ● free  $^- \text{O}_2\text{CCH}_2\text{CH}_2\text{CO}_2^-$ . Methyl groups of **Rf** isoalloxazine ring are not detectable by NMR at this concentration.

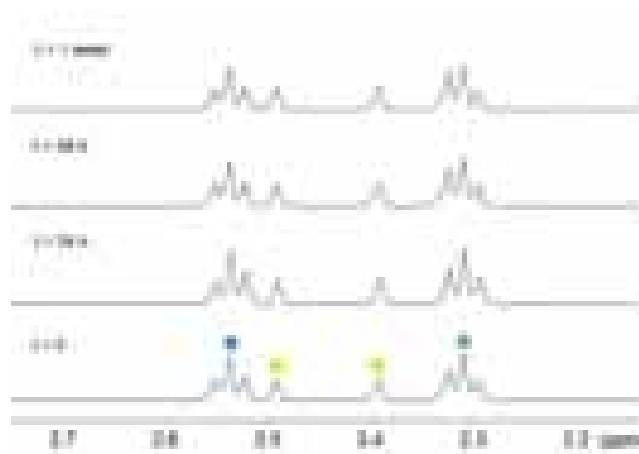


**Figure S9.** Stability control in the dark for **Rf/1** in MES buffer.  $^1\text{H}$  NMR spectra of MES/ $\text{D}_2\text{O}$  solution (9:1, MES 18 mM, pH 6.0) containing 120  $\mu\text{M}$  **1** and 50  $\mu\text{M}$  **Rf** in the dark for  $t = 0, 24 \text{ h}, 48 \text{ h}$  and 1 week.  $^1\text{H}$  NMR signal labelling: ●  $\text{Pt}-\text{OCOCH}_2\text{CH}_2\text{CO}_2^-$ , ●  $\text{Pt}-\text{OCOCH}_2\text{CH}_2\text{CO}_2^-$ , and ● methyl groups of **Rf** isoalloxazine ring.

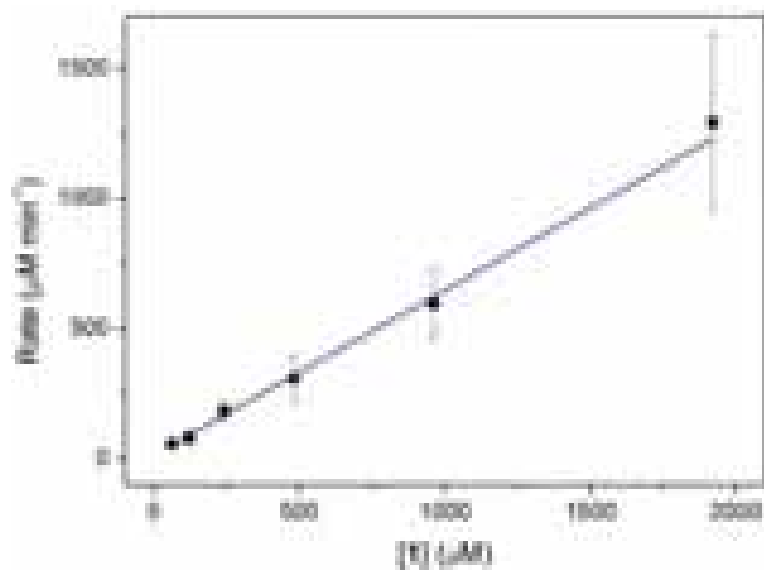


**Figure S10.** Dependency of photocatalytic rate on substrate (**1**). Study of the photocatalytic activation of **1** at increasing substrate concentrations ( $[1] = 60, 120, 240, 480, 960$  and  $1920 \mu\text{M}$ ) and fixed concentrations of **Rf** ( $50 \mu\text{M}$ ) and MES ( $18 \text{ mM}$ ). An irradiation time of 30 sec was used for all the samples ( $\lambda_{\text{exc}} = 460 \text{ nm}$ ,  $2.5 \text{ mW}\cdot\text{cm}^{-2}$ ).

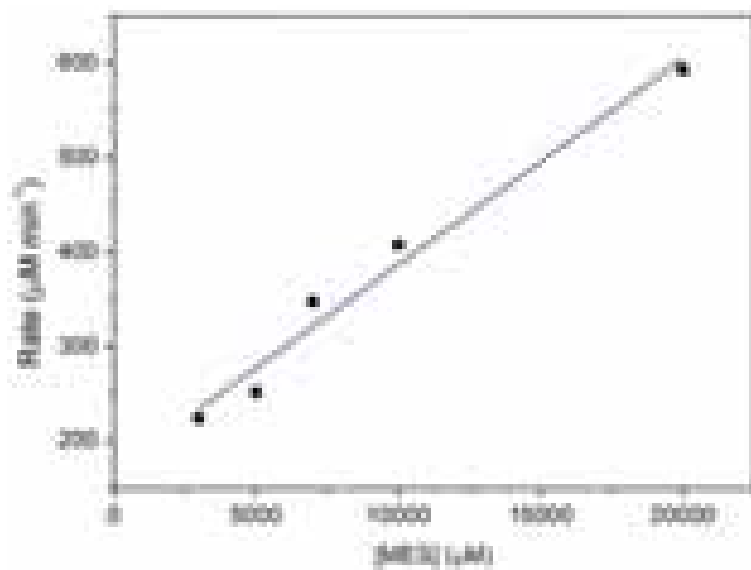


**Figure S11.** Dependency of photocatalytic rate on MES concentration. Photocatalytic activation of **1** at increasing concentrations of MES ( $[\text{MES}] = 3, 5, 7, 10,$  and  $20 \text{ mM}$ ) and at a fixed concentration of **Rf** ( $50 \mu\text{M}$ ) and **1** ( $500 \mu\text{M}$ ). An irradiation time of 30 sec was set for all the samples ( $\lambda_{\text{exc}} = 460 \text{ nm}$ ,  $2.5 \text{ mW}\cdot\text{cm}^{-2}$ ).

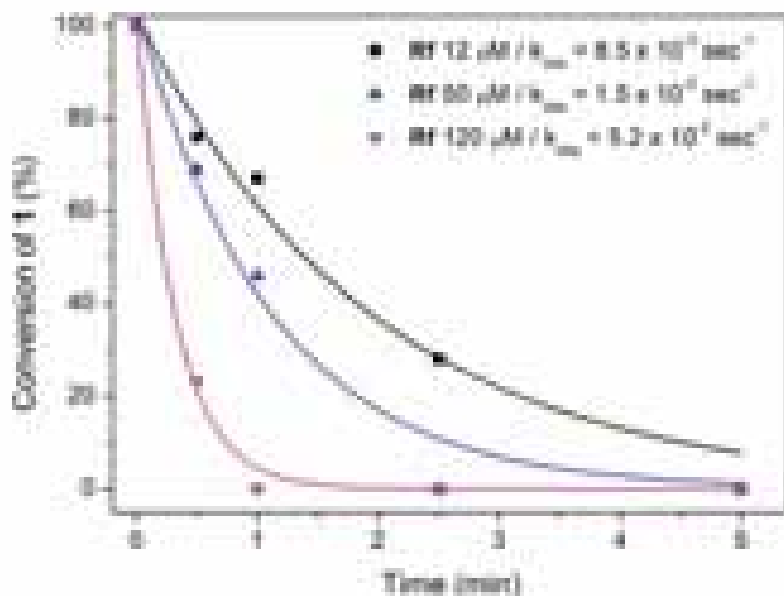


**Figure S12.** Dependency of photocatalytic rate on **Rf** concentration. Study of the photocatalytic activation of **1** at three different concentrations of **Rf** (12, 50 and 120  $\mu\text{M}$ ) and at fixed concentrations of **1** (120  $\mu\text{M}$ ) and MES (18 mM). The different colours lines corresponds to the fitting of the corresponding experimental data to the pseudo-first order equation  $[1] = [1]_0 e^{-k_{\text{obs}}t}$ , where  $t$  = time and  $k_{\text{obs}}$  = observed kinetic constant defined as  $k_{\text{obs}} = k[\text{MES}]$  where  $k$  = constant of the second order reaction.

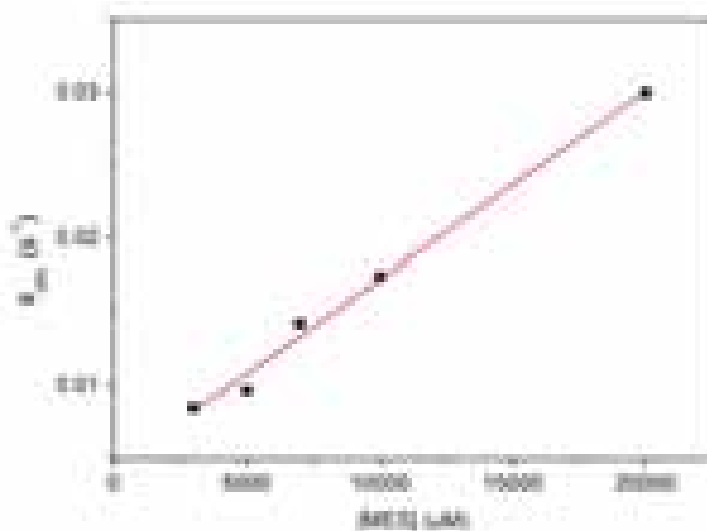


**Figure S13.** Dependency of photocatalytic rate constant  $k_{\text{obs}}$  on MES concentration. Study of the photocatalytic activation of **1** at increasing concentrations of MES ( $[\text{MES}] = 3, 5, 7, 10,$  and  $20$  mM) and at a fixed concentration of **Rf** (50  $\mu\text{M}$ ) and **1** (500  $\mu\text{M}$ ). An irradiation time of 30 sec was set for all samples ( $\lambda_{\text{exc}} = 460$  nm,  $2.5$  mW $\cdot\text{cm}^{-2}$ ).

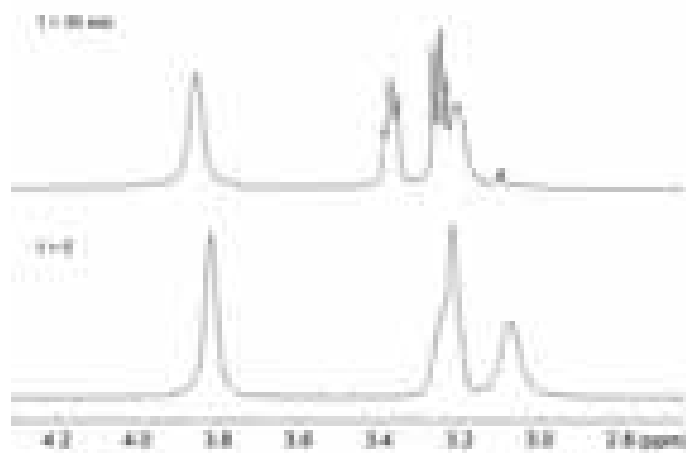


**Figure S14.** Light-induced MES oxidation by **Rf**.  $^1\text{H}$  NMR spectra of a MES solution (3 mM) containing 500  $\mu\text{M}$  **1** and 50  $\mu\text{M}$  **Rf** under 460-nm light irradiation ( $2.5 \text{ mW}\cdot\text{cm}^{-2}$ ) for  $t_{\text{irr}} = 0$  and 30 sec. The newly formed peaks are assigned to oxidized MES species.

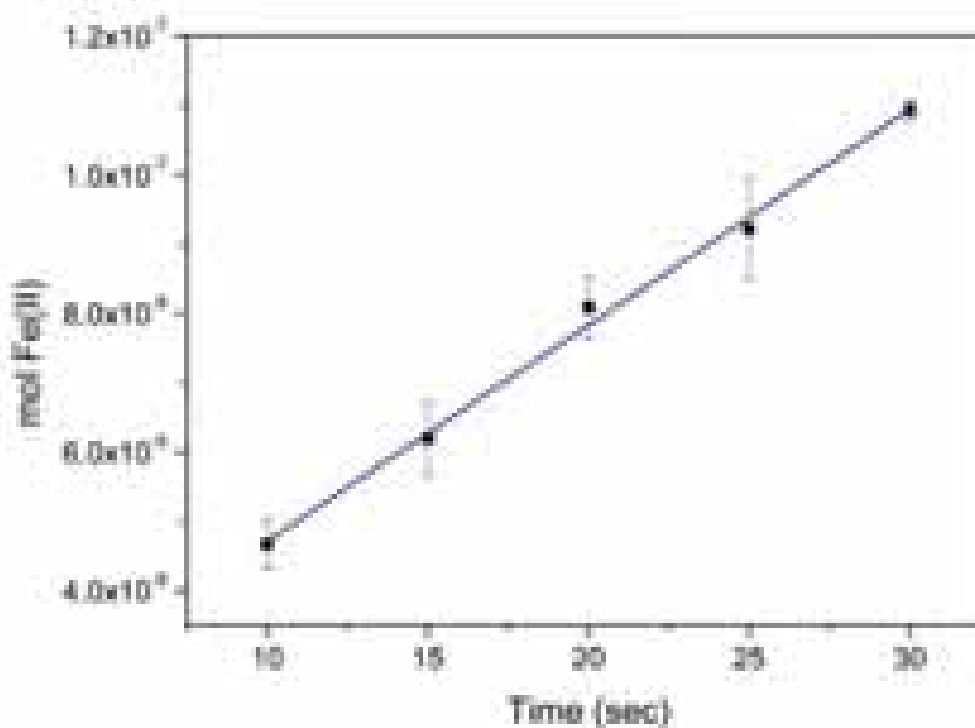


**Figure S15.** Plot of Fe(II) mol vs. irradiation time at 460 nm. The ferrioxalate actinometer ( $K_3[Fe(C_2O_4)_3]$ ) (0.15 M) was irradiated with a 460-nm light source in a plate reader and a phenatroline-based developing solution was then added to determine spectrophotometrically the amount of Fe(II) ions generated by irradiation, as described by S. L. Hopkins et al.<sup>3</sup> Data were fitted with the equation  $y = (3.12 \cdot 10^{-9} \pm 0.17 \cdot 10^{-9})x + (1.60 \cdot 10^{-8} \pm 4.52 \cdot 10^{-9})$ . R-Square = 0.998. Being the absolute quantum yield  $\phi_{Fe(II)}$  for ( $K_3[Fe(C_2O_4)_3]$ ) (0.15 M) at 460 nm equal to 0.65,<sup>3</sup> a photon flux of  $8.09 \cdot 10^{-9} \pm 0.94 \cdot 10^{-9}$  mol photon $\cdot$ sec $^{-1}$  was obtained for the light source using the equation:

$$\phi_{Fe(II)} = \frac{\eta_{Fe(II)}}{I_{abs}}$$

where  $\eta_{Fe(II)}$  the moles of Fe(II) produced photochemically and  $I_{abs}$  the absorbed photon dose by the Fe-oxalate complex.<sup>4</sup>



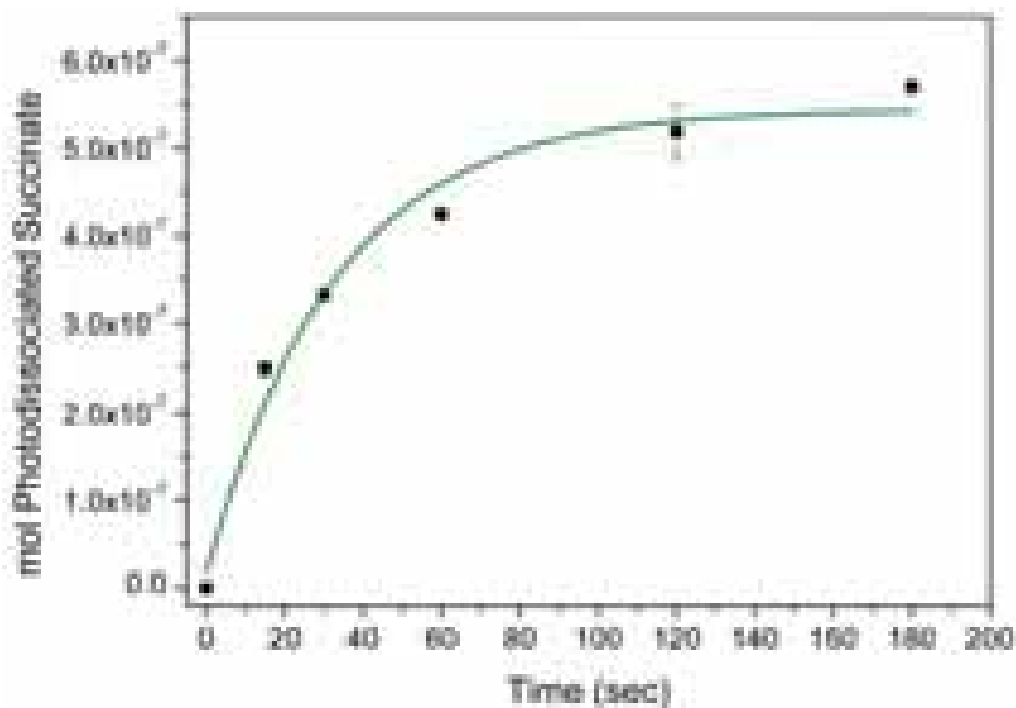


**Figure S16.** Moles of photodissociated succinate ligand vs. irradiation time at 460 nm. MES (18 mM) solutions of **1** (1.00 mM) and **Rf** (50  $\mu$ M) placed in a plate reader were irradiated at 460 nm for different time intervals and using the same setup employed for the ferrioxalate actinometry. The amount of photodissociated succinate was quantified by  $^1\text{H}$  NMR spectroscopy and data were fitted with the equation  $y = (-5.26 \cdot 10^{-7} \pm 4.2 \cdot 10^{-8})e^{\frac{-x}{32.89 \pm 6.45}} + (-5.44 \cdot 10^{-7} \pm 2.9 \cdot 10^{-8})$ . R-Square = 0.969.

By employing the equation

$$\phi = \frac{\text{number of molecules (or moles) consumed or produced per unit time}}{\text{number of photons adsorbed per unit time}}$$

$$= \frac{\frac{d[\text{Succinate}]}{dt} \cdot 2}{\text{Lamp Intensity}}$$

a quantum yield  $\phi$  of  $1.4 \pm 0.1$  was determined.

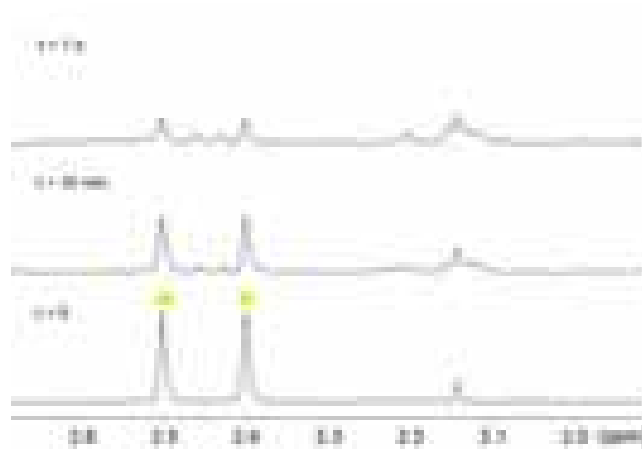


**Figure S17.** Photostability of **Rf** in MES buffer.  $^1\text{H}$  NMR spectra of a MES/ $\text{D}_2\text{O}$  (9:1, MES 18 mM, pH 6.0) solution of 240  $\mu\text{M}$  **Rf** under 460-nm light irradiation ( $2.5 \text{ mW}\cdot\text{cm}^{-2}$ ) for  $t_{\text{irr}} = 0, 30$  and 60 min.  $^1\text{H}$  NMR signal labelling: ● methyl groups of **Rf** isoalloxazine ring.

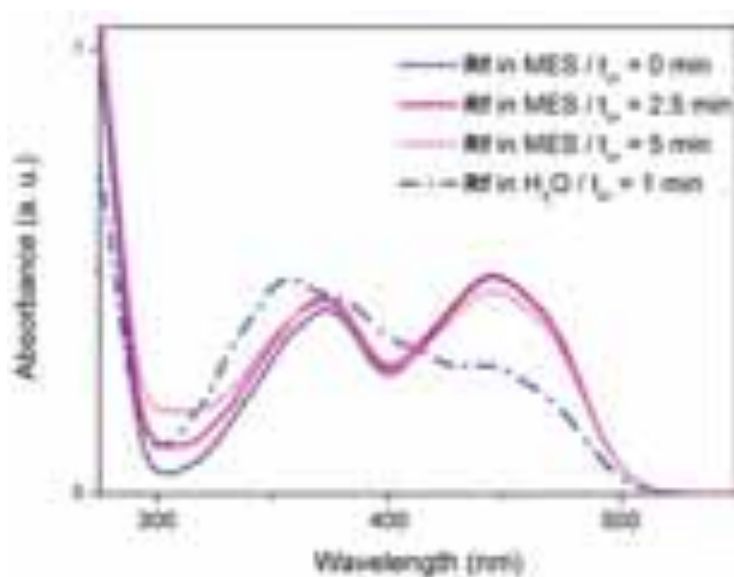


**Figure S18.** Photostability of **Rf** in MES buffer and water. UV-Vis spectrum of **Rf** (50  $\mu\text{M}$ ) in MES buffer (20 mM, pH 6) and in water (pH 7) at different irradiation times ( $\lambda_{\text{irr}} = 460 \text{ nm}$ ,  $2.5 \text{ mW}\cdot\text{cm}^{-2}$ ; MES: violet  $t_{\text{irr}} = 0$ , magenta  $t_{\text{irr}} = 2.5$  min, and pink  $t_{\text{irr}} = 5$  min; Water: dashed-blue  $t_{\text{irr}} = 1$  min). The absorption profile obtained after light irradiation in water (dashed blue line) corresponds to lumichrome, a common photoproduct of **Rf** photolysis.

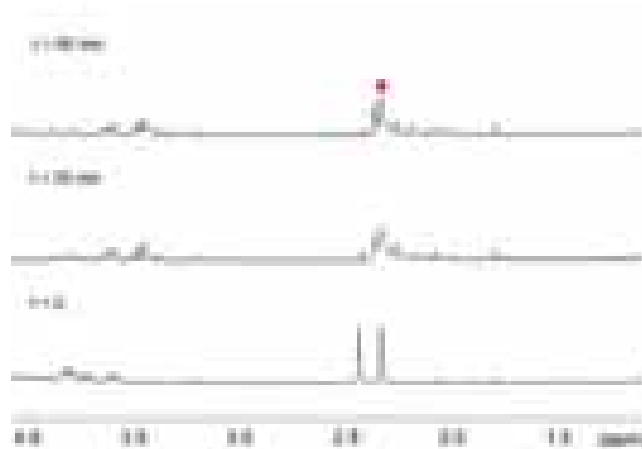


**Figure S19.** Photostability of **Rf** in Phosphate Buffer (PB).  $^1\text{H}$  NMR spectra of a PB/ $\text{D}_2\text{O}$  (9:1, 100 mM, pH 5.5) solution of  $240\ \mu\text{M}$  **Rf** under 460-nm light irradiation ( $2.5\ \text{mW}\cdot\text{cm}^{-2}$ ) for  $t_{\text{irr}} = 0, 30$  and  $60$  min. Changes in the  $^1\text{H}$  NMR signal at 3.5–3.8 ppm indicate the ribityl side chain is undergoing intramolecular photodegradation. Appearance of the peak at at 2.33 ppm (●) is consistent with the formation of 2,3-butanedione, a photoproduct obtained by  $\text{O}_2$ -oxidation of the isoalloxazine ring.

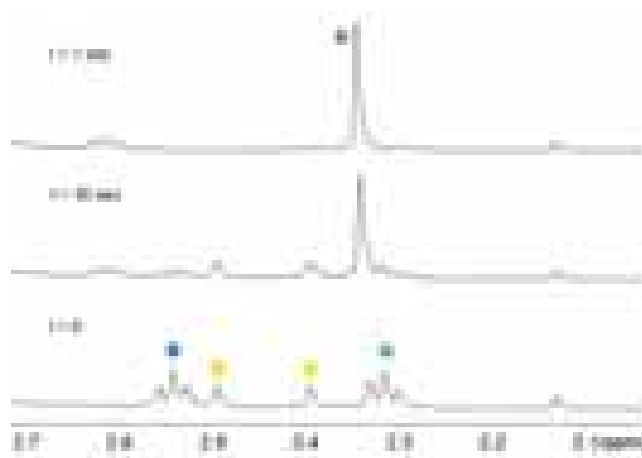


**Figure S20.** Photolysis of **1** in HEPES buffer in the presence of  $50\ \mu\text{M}$  **Rf**.  $^1\text{H}$  NMR spectra of a HEPES/ $\text{D}_2\text{O}$  solution (9:1, HEPES 18 mM, pH 6.0) of  $120\ \mu\text{M}$  **1** and  $50\ \mu\text{M}$  **Rf** under 460-nm light irradiation ( $2.5\ \text{mW}\cdot\text{cm}^{-2}$ ) for  $t_{\text{irr}} = 0$  sec, 30 sec, 1 min.  $^1\text{H}$  NMR signal labelling: ●  $\text{Pt}-\text{OCOCH}_2\text{CH}_2\text{CO}_2^-$ , ●  $\text{Pt}-\text{OCOCH}_2\text{CH}_2\text{CO}_2^-$ , ● methyl groups of **Rf** isoalloxazine ring, ● free  $^- \text{O}_2\text{CCH}_2\text{CH}_2\text{CO}_2^-$ .

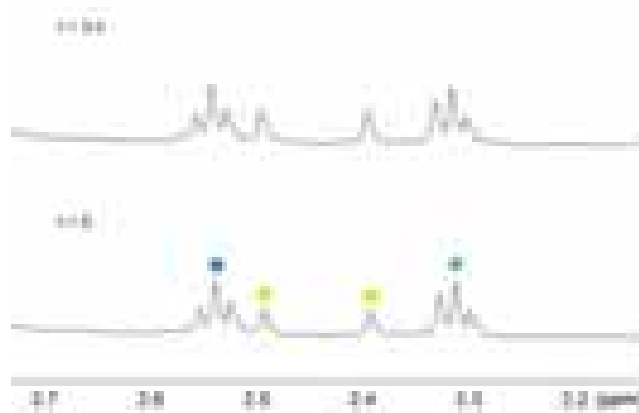


**Figure S21.** Stability control in the dark for **Rf/1** in HEPES buffer.  $^1\text{H}$  NMR spectra of HEPES/ $\text{D}_2\text{O}$  solution (9:1, HEPES 18 mM, pH 6.0) containing 120  $\mu\text{M}$  **1** and 50  $\mu\text{M}$  **Rf** in the dark for  $t = 0$  and 3 h.  $^1\text{H}$  NMR signal labelling: ● Pt-OCOCH<sub>2</sub>CH<sub>2</sub>CO<sub>2</sub><sup>-</sup>, ● Pt-OCOCH<sub>2</sub>CH<sub>2</sub>CO<sub>2</sub><sup>-</sup> and ● methyl groups of **Rf** isoalloxazine ring.

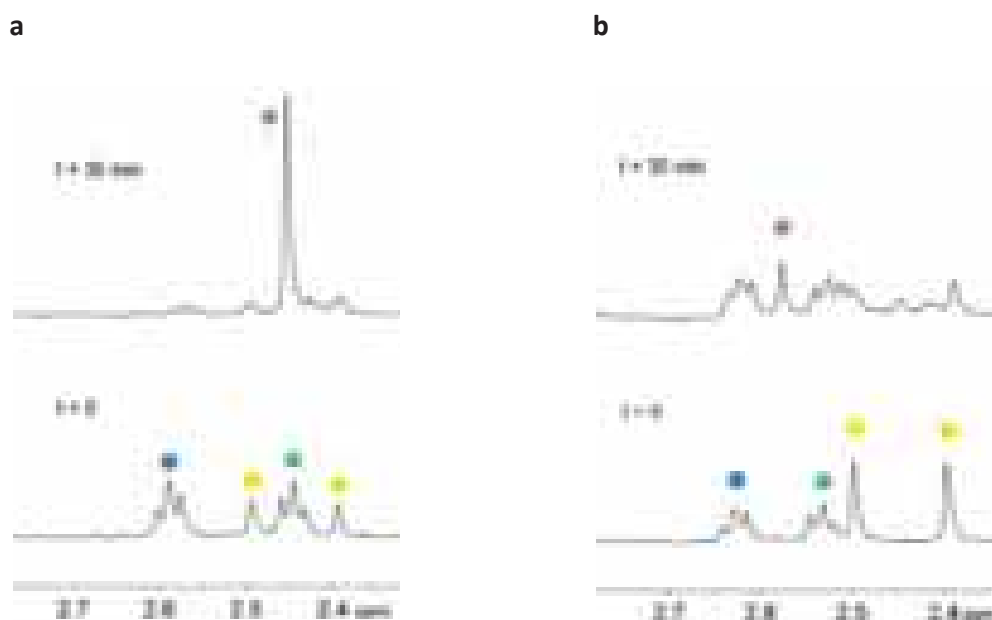


**Figure S22.** Photolysis of **1** in the presence of **Rf** and  $\text{NaN}_3$  in water. (a)  $^1\text{H}$  NMR spectra of a  $\text{H}_2\text{O}/\text{D}_2\text{O}$  (9:1, pH 3) solution of **Rf/1** (50/120  $\mu\text{M}$ ) with 3 mM  $\text{NaN}_3$  under 460-nm light irradiation ( $2.5 \text{ mW}\cdot\text{cm}^{-2}$ ) for  $t_{\text{irr}} = 0$  and 30 min; (b)  $^1\text{H}$  NMR spectra of a  $\text{H}_2\text{O}/\text{D}_2\text{O}$  (9:1, pH 2.7) solution of **Rf/1** (240/120  $\mu\text{M}$ ) without  $\text{NaN}_3$  irradiated under the same conditions. In all experiments, HCOOH was added (3 mM and 24 mM for **a** and **b** respectively) to improve the photoconversion of **1** and slightly reduce the photodecomposition of **Rf**.  $^1\text{H}$  NMR signal labelling: ● Pt-OCOCH<sub>2</sub>CH<sub>2</sub>CO<sub>2</sub><sup>-</sup>, ● Pt-OCOCH<sub>2</sub>CH<sub>2</sub>CO<sub>2</sub><sup>-</sup>, ● methyl groups of **Rf** isoalloxazine ring, ● free  $^-\text{O}_2\text{CCH}_2\text{CH}_2\text{CO}_2^-$ .

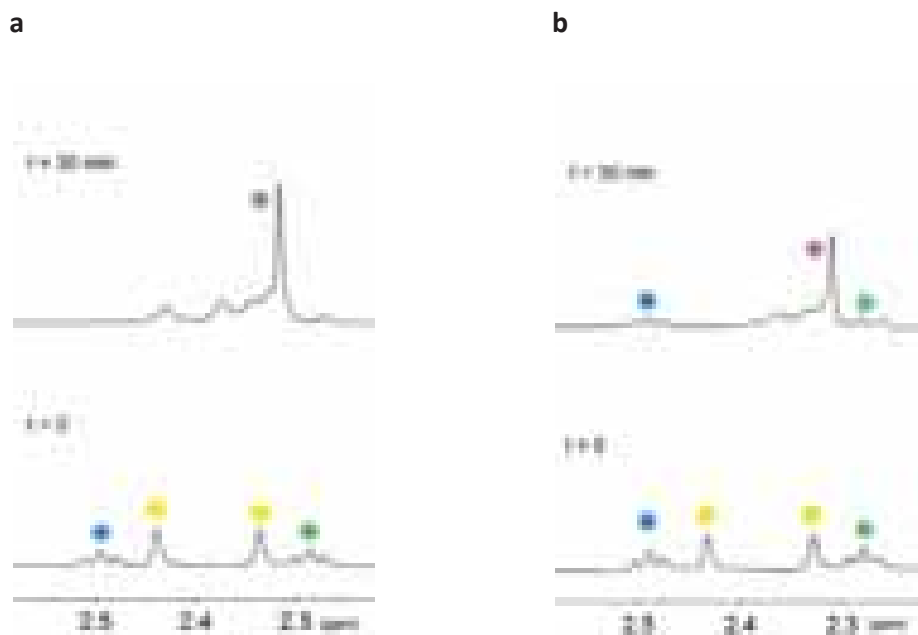


**Figure S23.** Photolysis of **1** in the presence of **Rf** and  $\text{NaN}_3$  in Phosphate Buffer (PB).  $^1\text{H}$  NMR spectra of a PB/ $\text{D}_2\text{O}$  (9:1, 100 mM, pH 5.5) solution of **Rf/1** (240/120  $\mu\text{M}$ ), with (a) or without (b) 1 mM  $\text{NaN}_3$  under 460-nm light irradiation ( $2.5 \text{ mW}\cdot\text{cm}^{-2}$ ) for  $t_{\text{irr}} = 0$  and 30 min. In all experiments, 24 mM  $\text{HCOOH}$  was added to improve the photoconversion of **1** and slightly reduce the photodecomposition of **Rf**.  $^1\text{H}$  NMR signal labelling: ●  $\text{Pt-OCOCH}_2\text{CH}_2\text{CO}_2^-$ , ●  $\text{Pt-OCOCH}_2\text{CH}_2\text{CO}_2^-$ , ● methyl groups of **Rf** isoalloxazine ring, ● free  $^- \text{O}_2\text{CCH}_2\text{CH}_2\text{CO}_2^-$ .

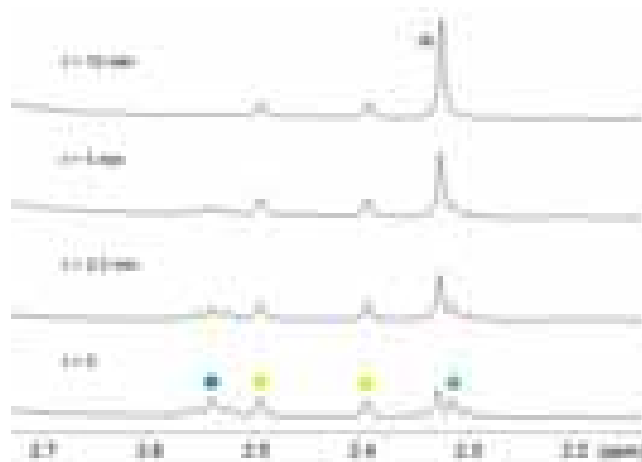


**Figure S24.** Photolysis of **1** in MES buffer in the presence of **Rf** and  $\text{NaN}_3$ .  $^1\text{H}$  NMR spectra of a MES/ $\text{D}_2\text{O}$  (9:1, 18 mM, pH 6.0) solution of **Rf/1** (50/120  $\mu\text{M}$ ) with 18 mM  $\text{NaN}_3$  under 460-nm light irradiation ( $2.5 \text{ mW}\cdot\text{cm}^{-2}$ ) for  $t_{\text{irr}} = 0, 2.5, 5$  and 10 min.  $^1\text{H}$  NMR signal labelling: ●  $\text{Pt-OCOCH}_2\text{CH}_2\text{CO}_2^-$ , ●  $\text{Pt-OCOCH}_2\text{CH}_2\text{CO}_2^-$ , ● methyl groups of **Rf** isoalloxazine ring, ● free  $^- \text{O}_2\text{CCH}_2\text{CH}_2\text{CO}_2^-$ .

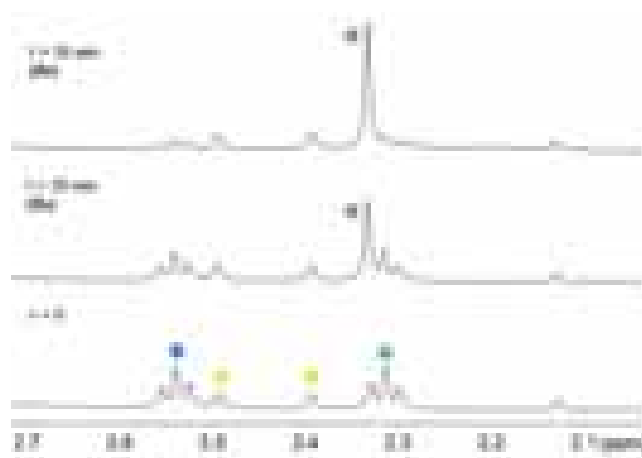


**Figure S25.** Photolysis of **1** in MES buffer in the presence of **Rf** under Ar atmosphere or in air. <sup>1</sup>H NMR spectra of a MES/D<sub>2</sub>O (9:1, 18 mM, pH 6.0) solution of **Rf/1** (50/200 μM) under 460-nm light irradiation (6 mW·cm<sup>-2</sup>) for t<sub>irr</sub> = 0 and 30 sec. <sup>1</sup>H NMR signal labelling: ● Pt-OCOCH<sub>2</sub>CH<sub>2</sub>CO<sub>2</sub><sup>-</sup>, ● Pt-OCOCH<sub>2</sub>CH<sub>2</sub>CO<sub>2</sub><sup>-</sup>, ● methyl groups of **Rf** isoalloxazine ring, ● free <sup>-</sup>O<sub>2</sub>CCH<sub>2</sub>CH<sub>2</sub>CO<sub>2</sub><sup>-</sup>.

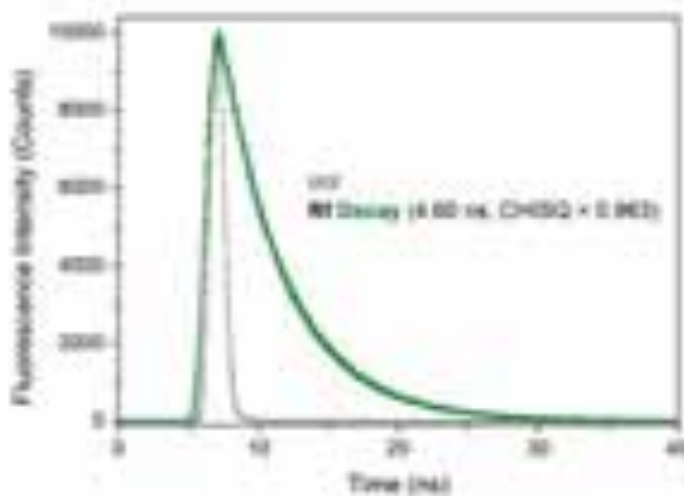


**Figure S26.** Lifetime decay profile for **Rf**. Fluorescence lifetime measurement for a 5  $\mu\text{M}$  **Rf** solution in MES buffer (10 mM) measured in a time-correlated single photon counting (TCSPC) setup. **Rf** exhibits a mono-exponential decay with a lifetime of 4.60 ns (green dots). IRF (grey dots) = instrument response function (prompt).

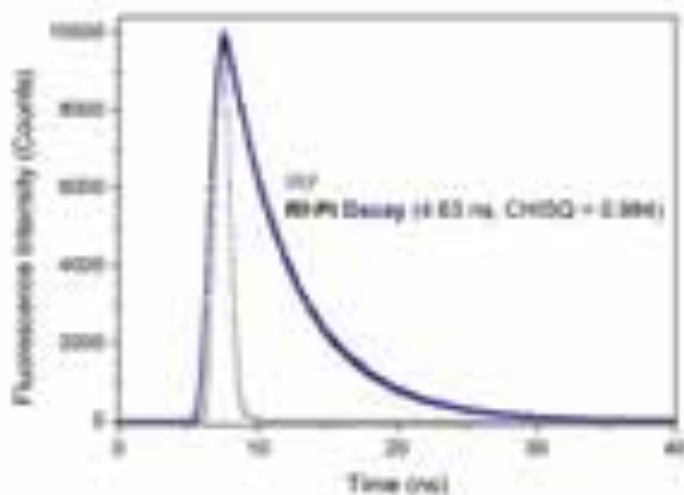


**Figure S27.** Lifetime decay profile for **Rf** in the presence of **1**. Fluorescence lifetime measurement for a 5  $\mu\text{M}$  **Rf** solution in MES buffer (10 mM) measured in the presence of 1.8 mM of **1** in a time-correlated single photon counting (TCSPC) setup. **Rf** exhibits a mono-exponential decay with a lifetime of 4.63 ns (blue dots). IRF (grey dots) = instrument response function (prompt).

a



b



HOMO

c



LUMO

d



LUMO+1

**Figure S28.** DFT-optimized structure and frontier orbitals of a selected **1-RfH<sub>2</sub>** adduct. (a) Conformation of a selected **1-RfH<sub>2</sub>** adduct optimized by DFT at the PBE0/def2-SVP<sup>1,2</sup> level (H-bond contacts highlighted with violet lines). (b–d) Frontier orbitals for the optimized conformation of the **1-RfH<sub>2</sub>** adduct (isodensity surfaces plotted with the isovalue of 0.02 e<sup>-</sup>bohr<sup>-3</sup>). The stabilization energy for **1-RfH<sub>2</sub>** is -52.0 kcal·mol<sup>-1</sup> and is calculated using the formula  $\Delta E = E_{1-RfH_2} - (E_1 + E_{RfH_2})$ .



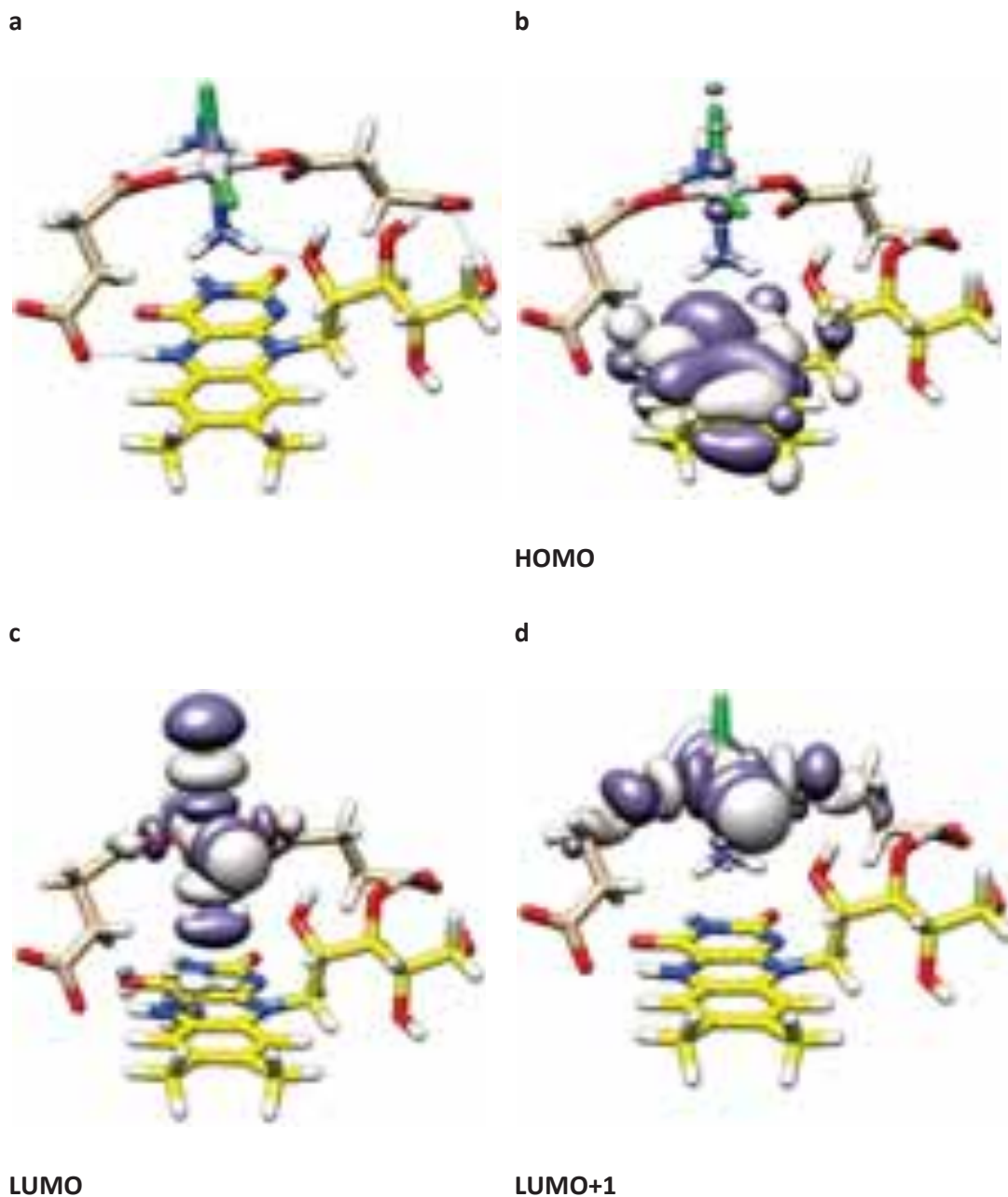


**Figure S29.** DFT-optimized structure and frontier orbitals of a selected  $\text{RfH}^-$  adduct (N5). **(a)** Conformation of a selected  $\mathbf{1-RfH}^-$  adduct (N5-protonated) optimized by DFT at the PBE0/def2-SVP<sup>1,2</sup> level (H-bond contacts highlighted with violet lines). **(b–d)** Frontier orbitals for the optimized conformation of the  $\mathbf{1-RfH}^-$  adduct (isodensity surfaces plotted with the isovalue of  $0.02 \text{ e}^- \text{ bohr}^{-3}$ ). The stabilization energy for  $\mathbf{1-RfH}^-$  is  $-68.8 \text{ kcal}\cdot\text{mol}^{-1}$  and is calculated using the formula  $\Delta E = E_{\mathbf{1-RfH}^-} - (E_1 + E_{\text{RfH}})$ .

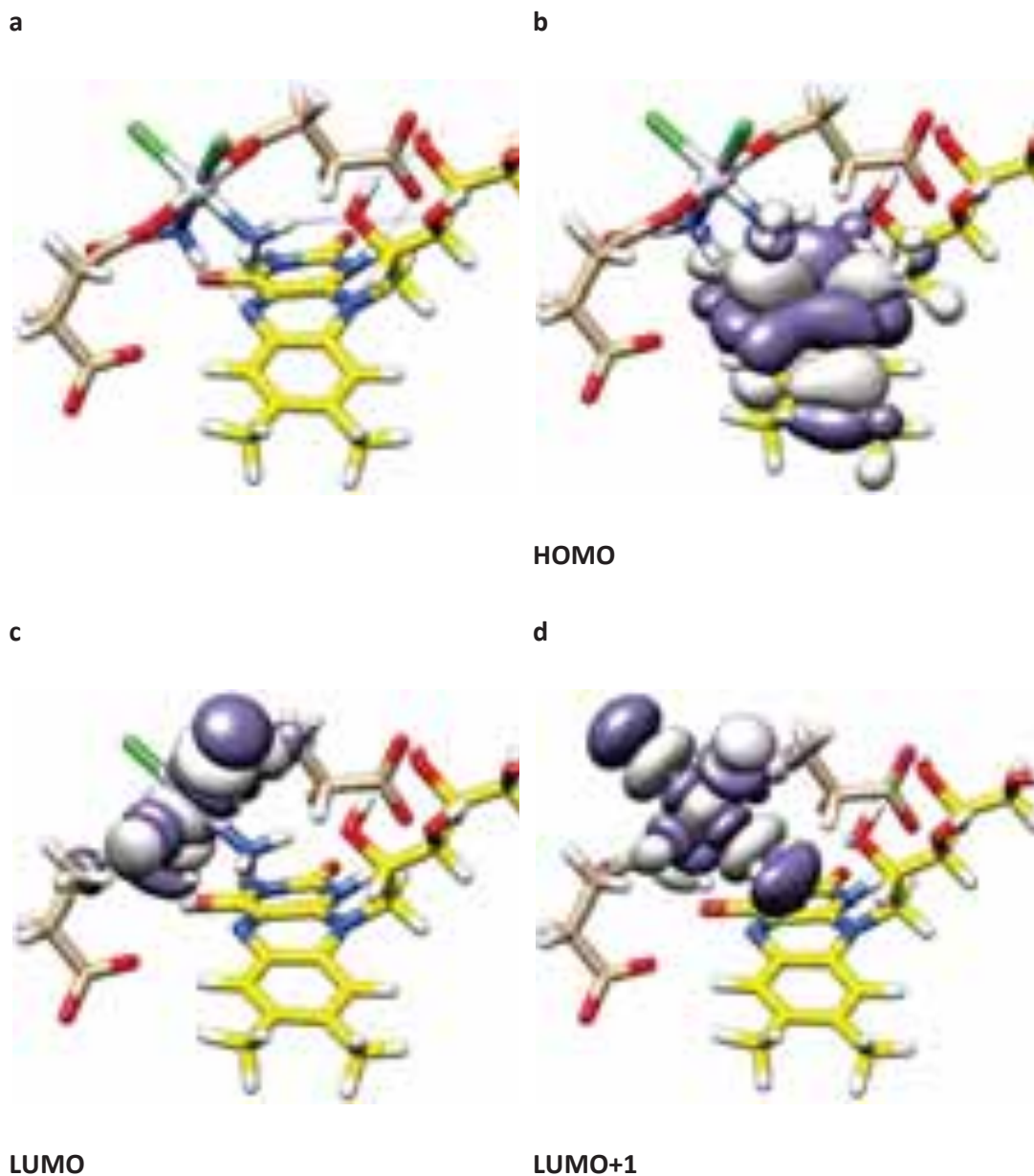


**Figure S30.** DFT-optimized structure and frontier orbitals of a selected  $\text{RfH}^-$  adduct (N1). (a) Conformation of a selected  $\mathbf{1-RfH}^-$  adduct (N1-protonated) optimized by DFT at the PBE0/def2-SVP<sup>1,2</sup> level (H-bond contacts highlighted with violet lines). (b–d) Frontier orbitals for the optimized conformation of the  $\mathbf{1-RfH}^-$  adduct (isodensity surfaces plotted with the isovalue of  $0.02 \text{ e}^- \text{ bohr}^{-3}$ ). The stabilization energy for  $\mathbf{1-RfH}^-$  is  $-61.2 \text{ kcal}\cdot\text{mol}^{-1}$  and is calculated using the formula  $\Delta E = E_{1-\text{RfH}} - (E_1 + E_{\text{RfH}})$ .

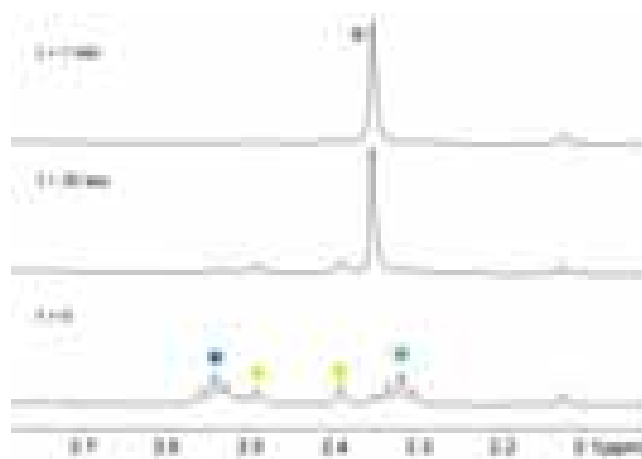


**Figure S31.** Photolysis of **1** in MES buffer in the presence of 50  $\mu\text{M}$  FMN.  $^1\text{H}$  NMR spectra of a MES/ $\text{D}_2\text{O}$  solution (9:1, MES 18 mM, pH 6.0) of 120  $\mu\text{M}$  **1** and 50  $\mu\text{M}$  FMN under 460-nm light irradiation ( $2.5 \text{ mW}\cdot\text{cm}^{-2}$ ) for  $t_{\text{irr}} = 0 \text{ sec}$ , 30 sec and 1 min.  $^1\text{H}$  NMR signal labelling: ● Pt-OCOCH<sub>2</sub>CH<sub>2</sub>CO<sub>2</sub><sup>-</sup>, ● Pt-OCOCH<sub>2</sub>CH<sub>2</sub>CO<sub>2</sub><sup>-</sup>, ● methyl groups of FMN isoalloxazine ring and ● free <sup>-</sup>O<sub>2</sub>CCH<sub>2</sub>CH<sub>2</sub>CO<sub>2</sub><sup>-</sup>.

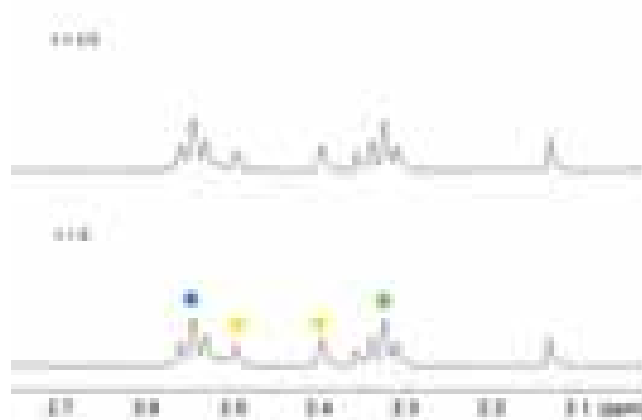


**Figure S32.** Stability of **1** in MES buffer in the presence of 50  $\mu\text{M}$  FMN.  $^1\text{H}$  NMR control spectra of a MES/ $\text{D}_2\text{O}$  solution (9:1, MES 18 mM, pH 6.0) of 120  $\mu\text{M}$  **1** and 50  $\mu\text{M}$  FMN in the dark for 3 h.  $^1\text{H}$  NMR signal labelling: ● Pt-OCOCH<sub>2</sub>CH<sub>2</sub>CO<sub>2</sub><sup>-</sup>, ● Pt-OCOCH<sub>2</sub>CH<sub>2</sub>CO<sub>2</sub><sup>-</sup>, ● methyl groups of FMN isoalloxazine ring.

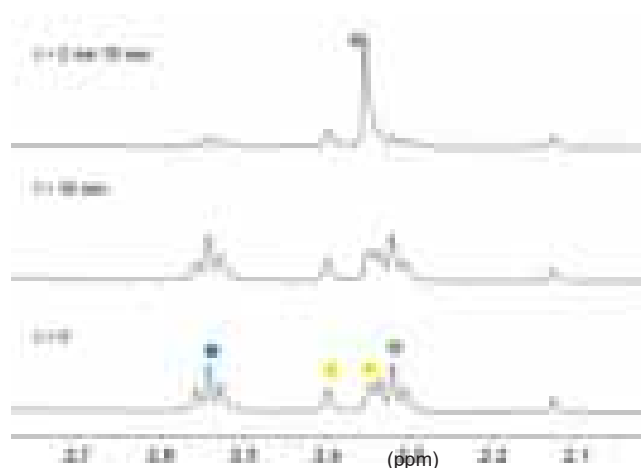


**Figure S33.** Photolysis of **1** in MES buffer in the presence of 50  $\mu\text{M}$  FAD.  $^1\text{H}$  NMR spectra of a MES/ $\text{D}_2\text{O}$  solution (9:1, MES 18 mM, pH 6.0) of 120  $\mu\text{M}$  **1** and 50  $\mu\text{M}$  FAD under 460-nm light irradiation ( $2.5 \text{ mW}\cdot\text{cm}^{-2}$ ) for  $t_{\text{irr}} = 0 \text{ sec}$ , 30 sec and 2.5 min.  $^1\text{H}$  NMR signal labelling: ● Pt-OCOCH<sub>2</sub>CH<sub>2</sub>CO<sub>2</sub><sup>-</sup>, ● Pt-OCOCH<sub>2</sub>CH<sub>2</sub>CO<sub>2</sub><sup>-</sup>, ● methyl groups of FAD isoalloxazine ring and ● free <sup>-</sup>O<sub>2</sub>CCH<sub>2</sub>CH<sub>2</sub>CO<sub>2</sub><sup>-</sup>.

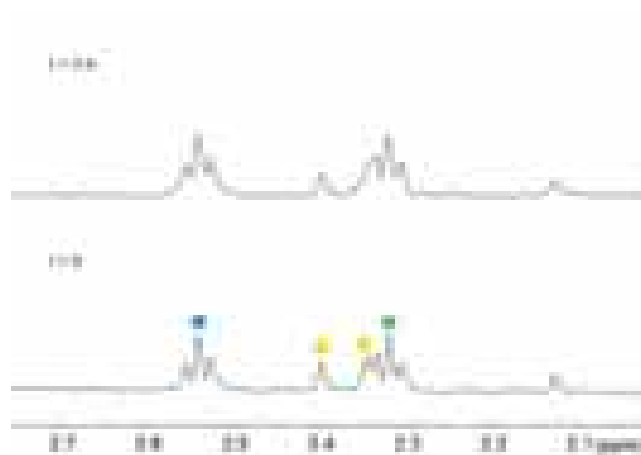


**Figure S34.** Stability of **1** in MES buffer in the presence of 50  $\mu\text{M}$  FAD.  $^1\text{H}$  NMR control spectra of a MES/ $\text{D}_2\text{O}$  solution (9:1, MES 18 mM, pH 6.0) of 120  $\mu\text{M}$  **1** and 50  $\mu\text{M}$  FAD in the dark for 3 h.  $^1\text{H}$  NMR signal labelling: ● Pt-OCOCH<sub>2</sub>CH<sub>2</sub>CO<sub>2</sub><sup>-</sup>, ● Pt-OCOCH<sub>2</sub>CH<sub>2</sub>CO<sub>2</sub><sup>-</sup>, ● methyl groups of FAD isoalloxazine ring.

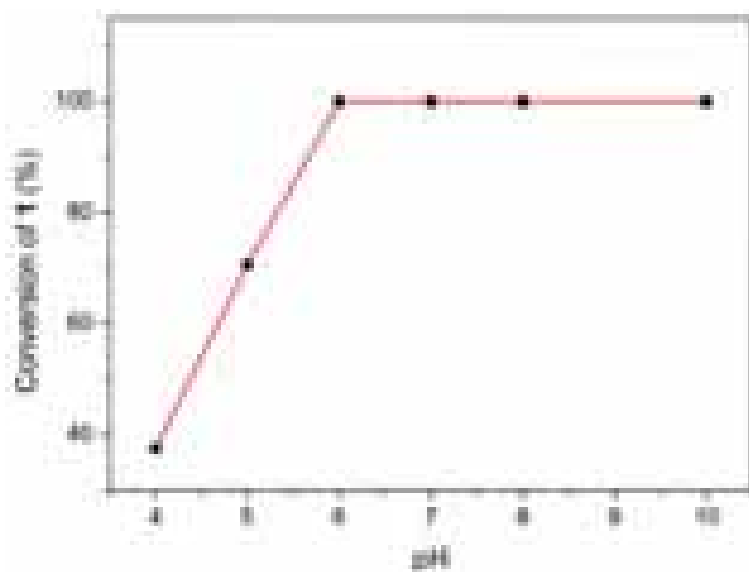


**Figure S35.** Dependency of photocatalytic prodrug activation on pH. Photocatalytic activation of **1** at different pHs (4-10) and at a fixed concentration of **Rf** (50  $\mu\text{M}$ ), **1** (120  $\mu\text{M}$ ) and MES (18 mM). An irradiation time of 2 min and 30 sec was set for all the samples ( $\lambda_{\text{exc}} = 460 \text{ nm}$ ,  $2.5 \text{ mW}\cdot\text{cm}^{-2}$ ).

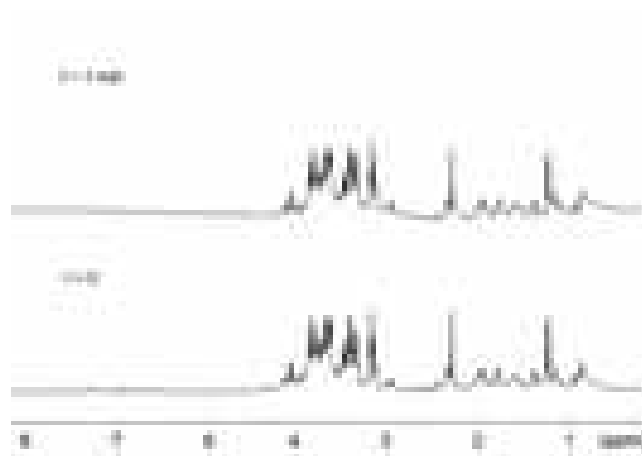


**Figure S36.** Photostability of cell culture medium.  $^1\text{H}$  NMR spectra of cell culture medium (Ham's F-12K supplemented with 10% fetal bovine serum and 1% penicillin/streptomycin) before and after 1 min of irradiation with 460-nm light ( $6 \text{ mW}\cdot\text{cm}^{-2}$ ).

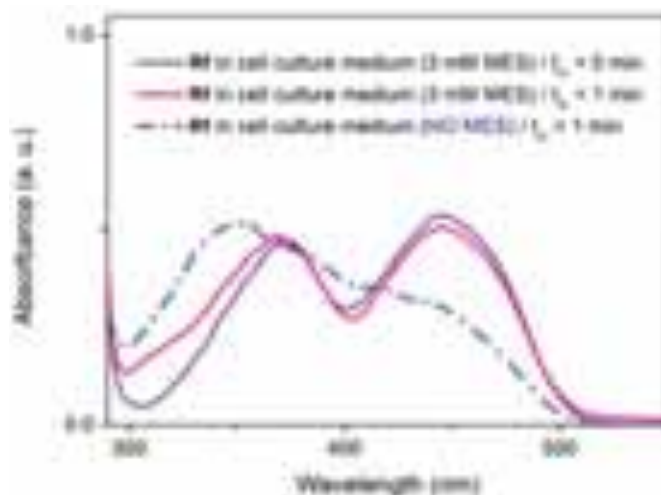


**Figure S37.** Photostability of **Rf** in cell culture medium. UV-Vis spectra of **Rf** (50  $\mu$ M) in cell culture medium (Ham's F-12K supplemented with 10% fetal bovine serum and 1% penicillin/streptomycin) with 3 mM MES in the dark (violet line), after 1 min of irradiation (pink line) at 460 nm ( $6 \text{ mW}\cdot\text{cm}^{-2}$ ) and after 1 min of irradiation in the absence of MES (blue line) at 460 nm ( $6 \text{ mW}\cdot\text{cm}^{-2}$ ).

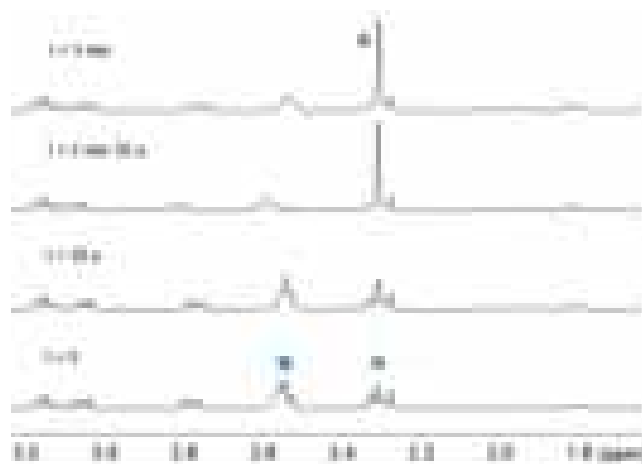


**Figure S38.** Photolysis of **1** in cell culture medium in the presence of **Rf** and MES.  $^1\text{H}$  NMR spectra of cell culture medium/MES/ $\text{D}_2\text{O}$  (7.5:1.5:1, 3 mM MES) solution containing 1.92 mM **1** and 50  $\mu$ M **Rf** under 460-nm light irradiation ( $6 \text{ mW}\cdot\text{cm}^{-2}$ ) for  $t_{\text{irr}} = 0, 30 \text{ sec}, 2.5 \text{ min}$  and 3 min. Cell culture medium corresponds to Ham's F-12K medium supplemented with 10% fetal bovine serum and 1% penicillin/streptomycin.  $^1\text{H}$  NMR signal labelling: ● Pt-OCOCH<sub>2</sub>CH<sub>2</sub>CO<sub>2</sub><sup>-</sup>, ● Pt-OCOCH<sub>2</sub>CH<sub>2</sub>CO<sub>2</sub><sup>-</sup> ● free <sup>-</sup>O<sub>2</sub>CCH<sub>2</sub>CH<sub>2</sub>CO<sub>2</sub><sup>-</sup>.

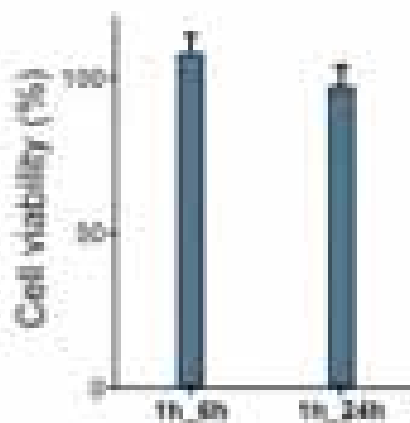


**Figure S39.** MES toxicity in PC-3 cells. Control experiments performed treating PC-3 cells with MES (2 mM) under light irradiation, using two different incubation conditions. Cells were plated in 96-well plates with a density of 4000 cells per well supplemented with serum and antibiotics and left to grow for 24 h at 37 °C with 5% CO<sub>2</sub> and 90% humidity. MES was then dissolved in the cell culture medium to reach a 2 mM concentration and cells were incubated for 1 h and then irradiated for 1 min with 460-nm light (light dose 0.36 J·cm<sup>-2</sup>). Afterwards, cells were either incubated for other i) 6 hours or ii) 24 h before medium was replaced and cells grown of a total of 48 h. The SRB assay was employed for both incubation conditions to evaluate cell density.

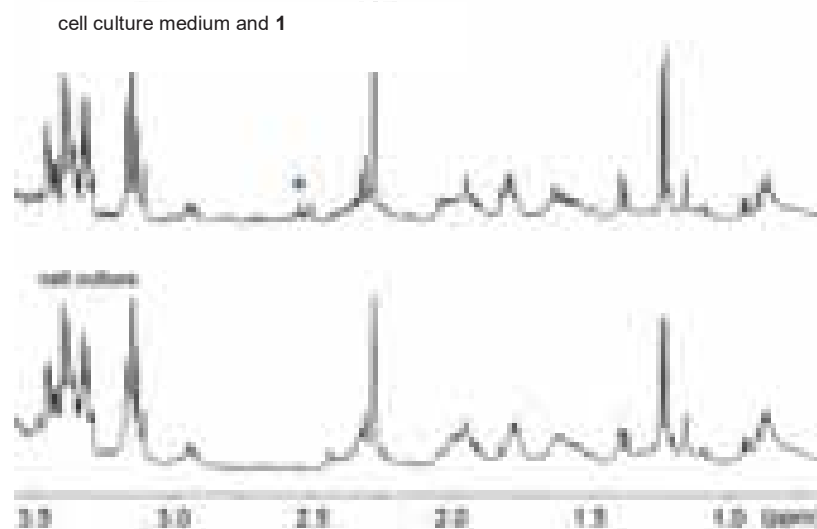


**Figure S40.** Assessment of the presence of **1** in cell culture medium without MES buffer. <sup>1</sup>H NMR spectra of cell culture medium/D<sub>2</sub>O (9:1) solution containing 120 μM **1**. Cell culture medium corresponds to Ham's F-12K medium supplemented with 10% fetal bovine serum and 1% penicillin/streptomycin. <sup>1</sup>H NMR signal labelling: ● Pt-OCOCH<sub>2</sub>CH<sub>2</sub>CO<sub>2</sub><sup>-</sup>.

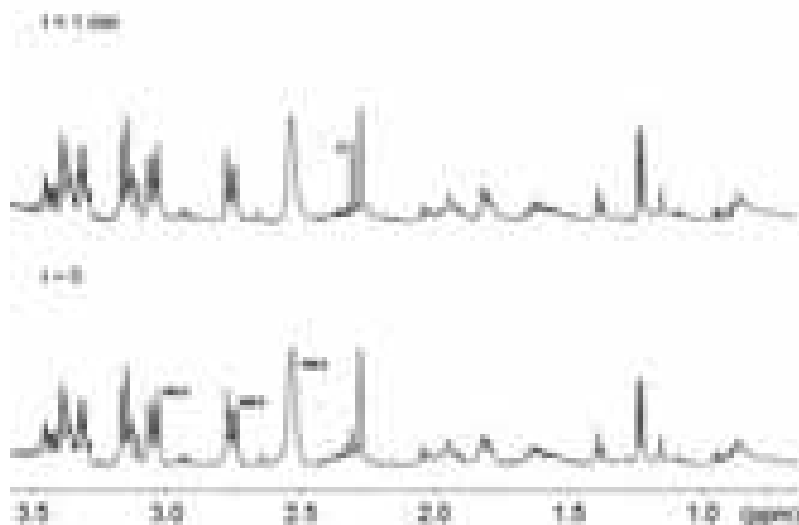


**Figure S41.** Photolysis of **1** in cell culture medium in the presence of **Rf** and MES.  $^1\text{H}$  NMR spectra of cell culture medium/MES/ $\text{D}_2\text{O}$  (7.5:1.5:1) solution containing  $120\ \mu\text{M}$  **1** and  $40\ \mu\text{M}$  **Rf** under 460-nm light irradiation ( $6\ \text{mW}\cdot\text{cm}^{-2}$ ) for  $t_{\text{irr}} = 0$  and 1 min. Cell culture medium corresponds to Ham's F-12K medium supplemented with 10% fetal bovine serum and 1% penicillin/streptomycin.  $^1\text{H}$  NMR signal labelling: ● free  $^-\text{O}_2\text{CCH}_2\text{CH}_2\text{CO}_2^-$  (compared to Figure S30, the triplet signal of **1** at 2.55 ppm is here buried under one of the MES signals).

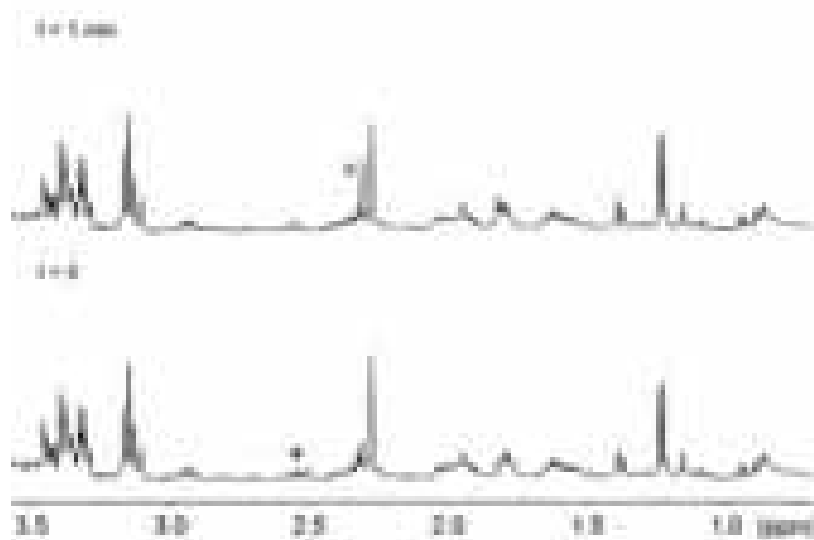


**Figure S42.** Photolysis of **1** in cell culture medium in the presence of **Rf**.  $^1\text{H}$  NMR spectra of cell culture medium/ $\text{H}_2\text{O}/\text{D}_2\text{O}$  (7.5:1.5:1) solution containing  $120\ \mu\text{M}$  **1** and  $40\ \mu\text{M}$  **Rf** under 460-nm light irradiation ( $6\ \text{mW}\cdot\text{cm}^{-2}$ ) for  $t_{\text{irr}} = 0$  and 1 min. Cell culture medium corresponds to Ham's F-12K medium supplemented with 10% fetal bovine serum and 1% penicillin/streptomycin.  $^1\text{H}$  NMR signal labelling: ● Pt- $\text{OCOCH}_2\text{CH}_2\text{CO}_2^-$ , ● free  $^-\text{O}_2\text{CCH}_2\text{CH}_2\text{CO}_2^-$ .



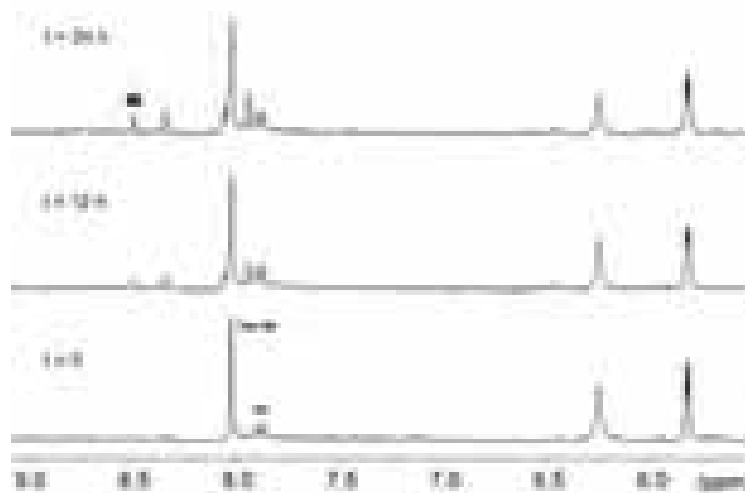


**Figure S43.** Light-activated platinumation of 5'-guanosin monophosphate (GMP) by **Rf/1**.  $^1\text{H}$  NMR spectra of a MES/ $\text{D}_2\text{O}$  (9:1) solution (1.5 mM, pH 6.0) of 120  $\mu\text{M}$  **1**, 50  $\mu\text{M}$  **Rf** after 460-nm light irradiation (1 min,  $2.5 \text{ mW}\cdot\text{cm}^{-2}$ ) and incubation with GMP (0.5 mM) for  $t = 0, 12$  and 24 h.  $^1\text{H}$  NMR signal labelling: ■ mono-adduct  $\text{cis-}[\text{Pt}(\text{NH}_3)_2(\text{N7-GMP})_2]^{2-}$ .

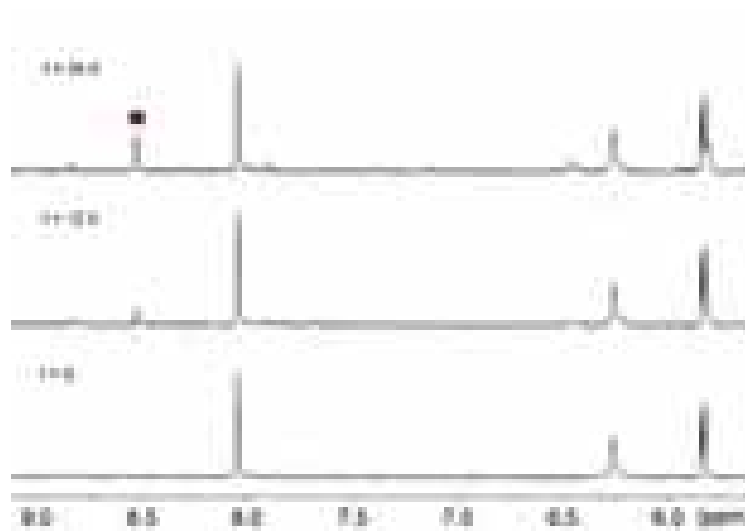


**Figure S44.** Platinumation of 5'-guanosin monophosphate (GMP) by cisplatin.  $^1\text{H}$  NMR spectra of a MES/ $\text{D}_2\text{O}$  (9:1) solution (2 mM, pH 6.0) of 120  $\mu\text{M}$  cisplatin and incubation with GMP (0.5 mM) for  $t = 0, 12$  and 24 h.  $^1\text{H}$  NMR signal labelling: ■ mono-adduct  $\text{cis-}[\text{Pt}(\text{NH}_3)_2(\text{N7-GMP})_2]^{2-}$ .

**Chapter 3 Supporting Information**

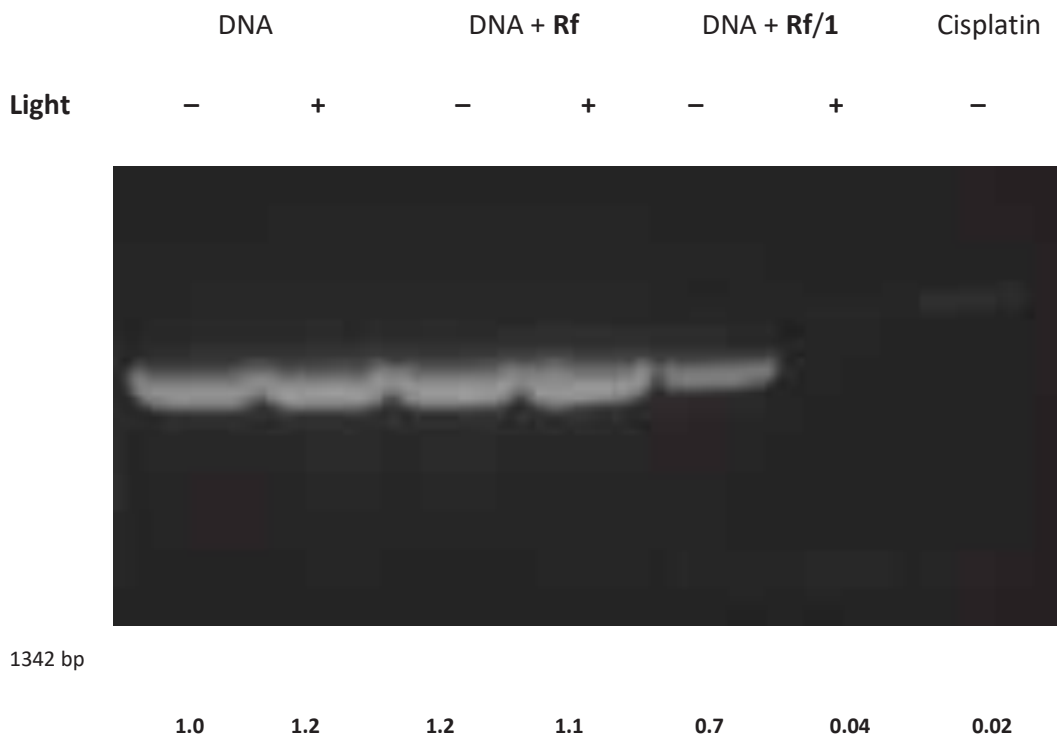


**Figure S45.** Inhibition of the polymerase chain reaction (PCR) using as template pET28b incubated with **Rf** (2.5  $\mu\text{M}$ ), **Rf/1** (2.5:10  $\mu\text{M}$ ) and cisplatin (10  $\mu\text{M}$ ) in the dark and under 30 s of light irradiation at 460 nm (2.5  $\text{mW}\cdot\text{cm}^{-2}$ , 1.5 mM MES and pH 6). Values below the gel indicate intensities of amplified DNA fragment normalized by that of the DNA control in the dark.

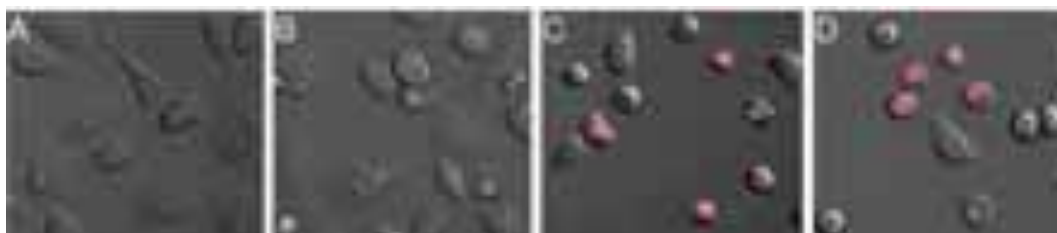


**Figure S46.** Morphological analysis of PC-3 cells. Merged DIC (Differential Interference Contrast) and fluorescence microscopy images showing the effects of **Rf/1** on PC-3 cells upon light irradiation. (A) untreated PC-3 cells, (B) **Rf/1** (30:120  $\mu\text{M}$ ) in the dark, (C) **Rf/1** (30:120  $\mu\text{M}$ ) activated by 460-nm light (light dose 0.36  $\text{J}\cdot\text{cm}^{-2}$ ) and (D) cisplatin (120  $\mu\text{M}$ ) in the dark. All samples were treated in the presence of 2 mM of MES. Cells were stained at the end of the incubation period (48 h) using the dye SYTOX<sup>®</sup> AADvanced<sup>™</sup> (Invitrogen<sup>™</sup>) for dead cells (red channel).

**a**



**b**

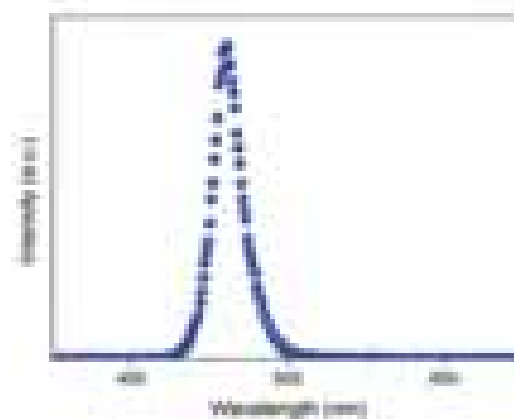


**Figure S47.** LED setup for cell work and emission profile. **(a)** Custom-made array of blue emitting LEDs used for irradiation of 96-well plates. **(b)** Emission profile of the LED array (460 nm,  $6 \text{ mW}\cdot\text{cm}^{-2}$ ) employed in the cell work experiment.

## **Experimental details**

**Materials.** (-)-Riboflavin (**Rf**), formic acid, 2-(N-morpholino)ethanesulfonic acid (MES), sodium phosphate monobasic monohydrate, guanosine 5'-monophosphate disodium salt hydrate (GMP), cisplatin were purchased from Sigma Aldrich, sodium phosphate dibasic from PANREAC and  $K_2PtCl_4$  from Precious Metals Online. All chemicals were used as received without additional purification. Ham's F-12K (Kaighn's) medium nutrient mixture and fetal bovine serum (FBS) were purchased from Invitrogen. Penicillin – Streptomycin was purchased from Teknovas. The pET28b plasmid was purchased from Novagen, DNA primers from Sigma and the Dream Taq polymerase and SYBR Safe dye from Thermo-Fisher.

**Synthesis of *cis,cis,trans*-[Pt(NH<sub>3</sub>)<sub>2</sub>(Cl)<sub>2</sub>(O<sub>2</sub>CCH<sub>2</sub>CH<sub>2</sub>CO<sub>2</sub>H)<sub>2</sub>] (**1**).** The platinum complex was synthesized by following the procedure described by M. Reithofer et al.<sup>5</sup>

### **Instrumentation.**

*Nuclear Magnetic Resonance (NMR).* <sup>1</sup>H NMR spectra of the various samples were recorded on an AVANCE III Bruker 500 NMR spectrometer using standard pulse programs. Chemical shifts were reported in parts-per-million ( $\delta$ , ppm) and referenced to the residual solvent peak.

*UV-Vis absorption spectroscopy (UV-vis).* All spectra of **1** and **Rf** were acquired in aqueous solution or buffers using a Varian Cary 5000 spectrophotometer.

**Photoirradiation experiments.** Photoirradiation experiments were performed on aqueous and buffer solutions obtained dissolving **1** and **Rf** at different concentrations in a 1 mL glass vial and irradiating the whole volume with a LED light source ( $\lambda_{irr} = 460$  nm, 2.5 mW·cm<sup>-2</sup>, Prizmatix LED Multi-Wavelength MWLLS-11).

In the case of cell experiments, black 96-well plates were photoirradiated using the blue LED array shown in Figure S37 ( $\lambda_{irr} = 460$  nm, 6 mW·cm<sup>-2</sup>). Power densities were measured with a Ophir photonics power meter.

**Quantum yield determination by actinometry.** Ferrioxalate actinometry was employed to determine the photon flux of the blue LED array ( $\lambda_{irr} = 460$  nm, 6 mW·cm<sup>-2</sup>).

<sup>2</sup>) and the yield of the photochemical activation for the **Rf/1** system. Samples were irradiated in 96-well plates as described in the modified method of Bonnet and co-worker.<sup>3</sup> <sup>1</sup>H NMR was employed to quantify the concentration of succinate ligand photoreleased and determine the yield of the photochemical reaction. Actinometry experiments were repeated three times.

**Computational details.** All calculations were performed with the Gaussian 09 program.<sup>6</sup> The systems were analyzed with Density Functional Theory, using the PBE0/def2-SVP combination, which was previously used in similar studies.<sup>7</sup> Solvent was considered by means of the polarized continuum model (PCM) with water as implicit solvent, and dispersion interactions were taken into account using Grimme's dispersion correction with Becke and Johnson's damping.<sup>8</sup> The geometries were optimized and frequency calculations were run to ensure the lack of imaginary modes. Several isomers were found for each of the complexes presented; only the global minima are presented in this work. The binding energy was calculated as the electronic energy balance of the reaction **Rf + 1** → **Rf/1**.

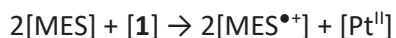
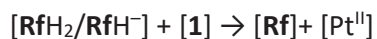
**Polymerase chain reaction (PCR)-inhibition assay using Rf/1-treated DNA.** 2 ng/μL pET28b was light irradiated at 460 nm for 30 s (2.5 mW·cm<sup>-2</sup>) in presence of 2.5 μM of **Rf** and 10 μM of **1** in 1.5 mM MES at pH 6. As negative controls, DNA and DNA incubated with 2.5 μM **Rf** were also irradiated. Moreover, non-irradiated controls were run for each sample. As positive control, DNA was also incubated with 10 μM cisplatin. After incubating irradiated and non-irradiated mixtures for 24 h in the dark, 2 ng of plasmid DNA were used as template for the amplification of 1342 bps fragment by using the following primers: AACTTAATGGGCCCGCTAACAG (primer forward) and CGTCCCATTCGCCATCC (primer reverse). PCR was performed using the Dream Taq polymerase according to the manufacturer's protocol. PCR was run for 30 cycles and its products were analysed by DNA electrophoresis using 1% agarose gels and SYBR Safe as dye to visualize DNA. The DNA bands were quantified using Image J.

**Photocatalysis kinetic model.** Assuming the reaction scheme reported below in which **Rf** acts as a photocatalyst, we have adopted a simplified kinetic model in which the reaction rate depends on both **1** and **MES** Eq. (1) (Figure S10 and S11). Nevertheless,

### Chapter 3 Supporting Information

such rate can be approximated with as a pseudo-first order reaction considering that the initial concentration of MES is much larger than the initial concentration of **1**. Thus, the concentration of MES remains constant during the chemical reaction. Within this approach, a pseudo-first order reaction constant ( $k_{obs} = 10.0 \pm 0.1 \cdot 10^{-3} \text{ s}^{-1}$ ) can be calculated fitting experimental data to Eq (2) (Figure S12) or to Eq (3) (Figure S10). Moreover, a second order reaction constant ( $k = 1.3 \pm 0.1 \text{ M}^{-1}\text{s}^{-1}$ ) can be calculated using Eq (4) by fitting the experimental data for  $k_{obs}$  at different  $[\text{MES}]_0$  (Figure S13).

#### Reaction scheme



#### Kinetic Model

$$\text{rate}(v) = k[\text{MES}][\mathbf{1}] \quad (1)$$

$$[\mathbf{1}] = [\mathbf{1}]_0 e^{-k_{obs}t} \quad (2)$$

$$v = k_{obs} [\mathbf{1}] \quad [\text{MES}]_0 \gg [\mathbf{1}]_0 \quad (3)$$

$$k_{obs} = k[\text{MES}]_0 \quad (4)$$

## References

1. C. Adamo and V. Barone, *J. Chem. Phys.*, 1999 **110**, 6158–6170.
2. F. Weigend and R. Ahlrichs, *Phys. Chem. Chem. Phys.*, 2005, **7**, 3297–3305.
3. S. L. Hopkins, *et al. Photochem. Photobiol. Sci.*, 2016, **15**, 644–653.
4. J. N. Demas, W. D. Bowman, E. F. Zalewski and R. A. Velapoldi, *J. Phys. Chem.*, 1981, **85**, 2766–2771.
5. M. Reithofer, M. Galanski, A. Roller and B. K. Keppler, *Eur. J. Inorg. Chem.*, 2006, 2612–2617.
6. Frisch, M. J. *et al. Gaussian 09*. (Gaussian, Inc., 2009).
7. I. Infante, *et al., J. Phys. Chem. C*, 2004, **118**, 8712–8721.
8. S. Grimme, S. Ehrlich and L. Goerigk, *J. Comput. Chem.*, 2011, **32**, 1456–1465.





# 4

## Supporting Information

**Biological Activity of Pt<sup>IV</sup> Prodrugs  
Triggered by Riboflavin-Mediated  
Bioorthogonal Photocatalysis**



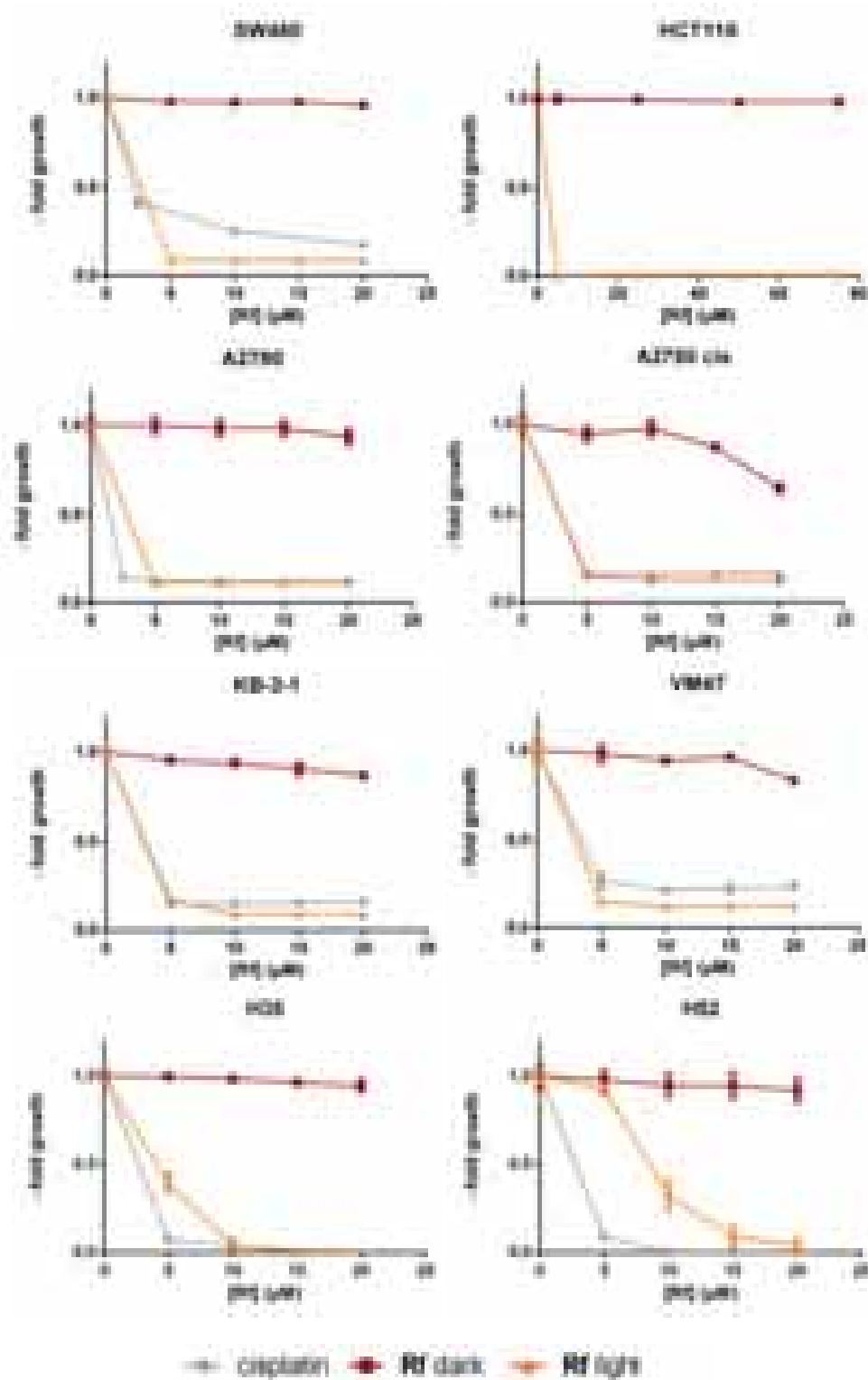


**Figure S1.** Phototoxic effect of Rf (2 mM MES) on the cell viability of different cell lines after 72 h with and without light irradiation (460 nm, 0.36 J·cm<sup>-2</sup>). Cisplatin was employed as positive control (10x [Rf]).

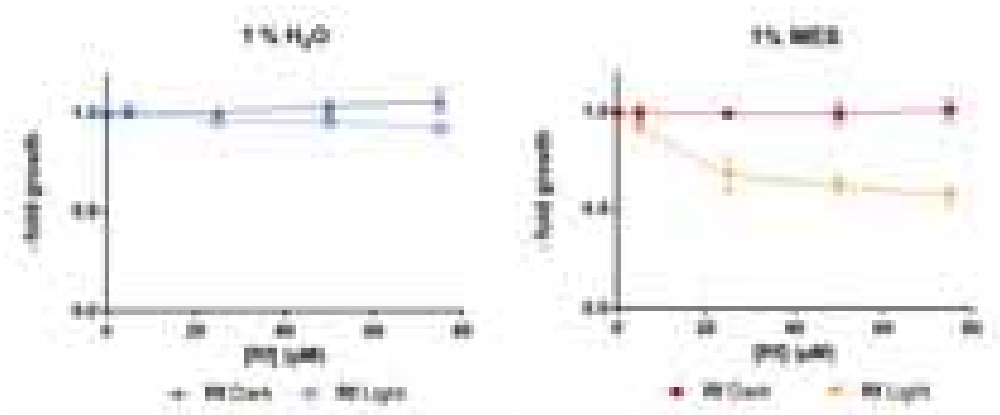


**Figure S2.** Rf phototoxic effect on the cell viability of Capan-1 after 72 h in the absence (1% H<sub>2</sub>O) and in the presence of 2 mM MES (1%). Experiments were performed in the dark and under light irradiation (460 nm, 0.36 J·cm<sup>-2</sup>).

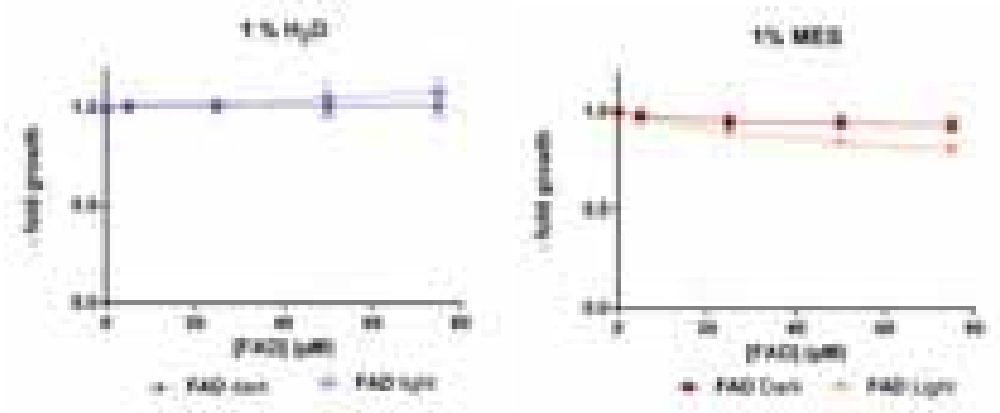


**Figure S3.** FAD phototoxic effect on the cell viability of Capan-1 after 72 h in the absence (1% H<sub>2</sub>O) and in the presence of 2 mM MES (1%). Experiments were performed in the dark and under light irradiation (460 nm, 0.36 J·cm<sup>-2</sup>).

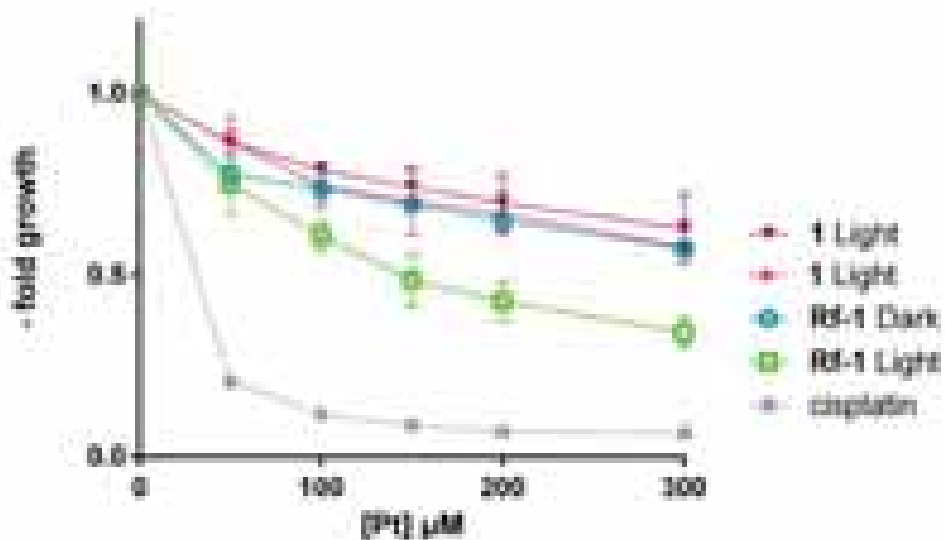


**Figure S4.** Photocatalytic Rf-1 effect against Capan-1 cells. Cell viability of Capan-1 upon incubation with Rf-1 (1:10) and **1** in the absence of MES under light irradiation (460 nm, 0.36 J·cm<sup>-2</sup>) and in the dark. Cisplatin is shown as positive control.

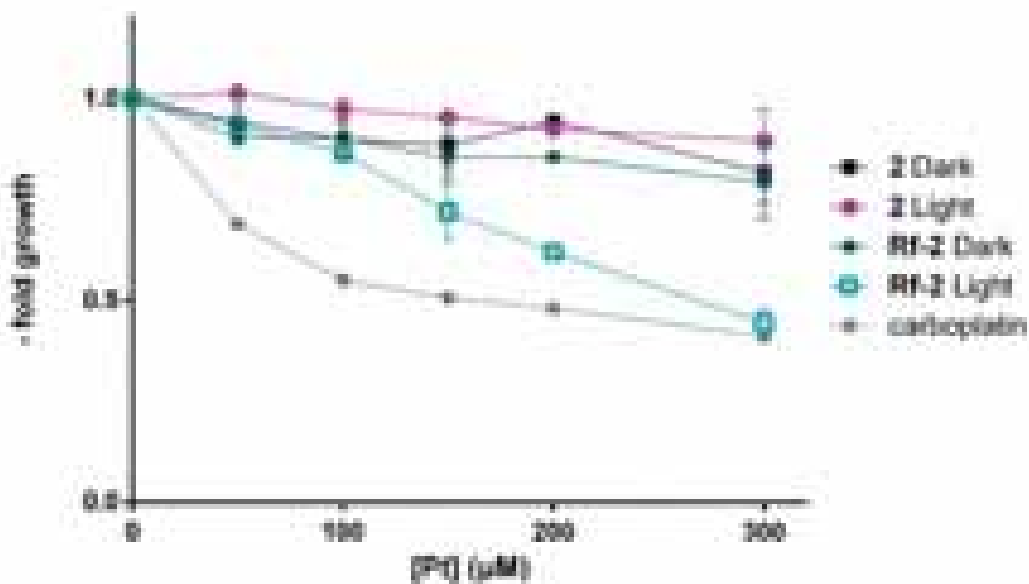


**Figure S5.** Photocatalytic Rf-2 effect against Capan-1 cells. Cell viability of Capan-1 upon incubation with Rf-2 (1:10) and **2** in the absence of MES under light irradiation (460 nm, 0.36 J·cm<sup>-2</sup>) and in the dark (n = 2). Carboplatin is shown as positive control.

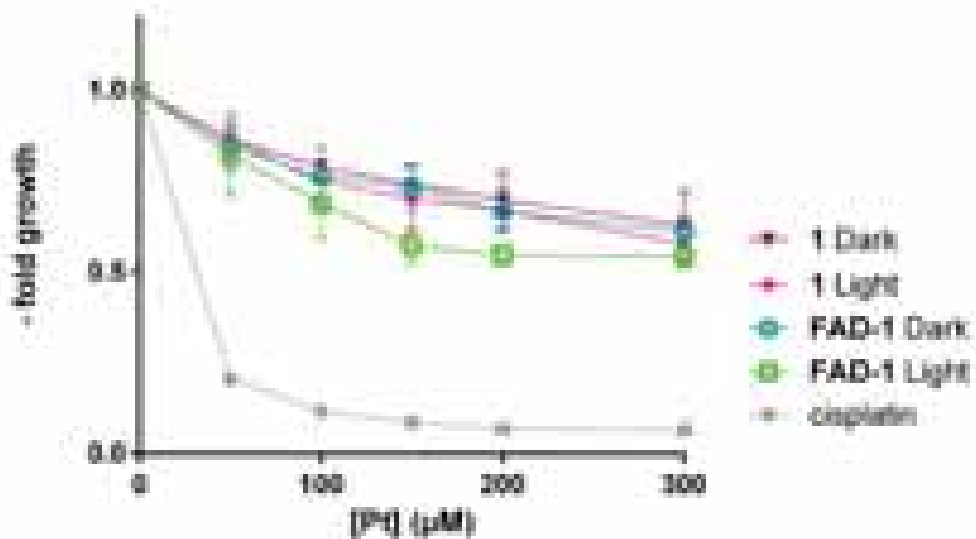


**Figure S6.** Photocatalytic **FAD-1** effect against Capan-1 cells. Cell viability of Capan-1 upon incubation with **FAD-1** (1:10) and **1** in the absence of MES under light irradiation (460 nm, 0.36 J·cm<sup>-2</sup>) and in the dark. Cisplatin is shown as positive control.

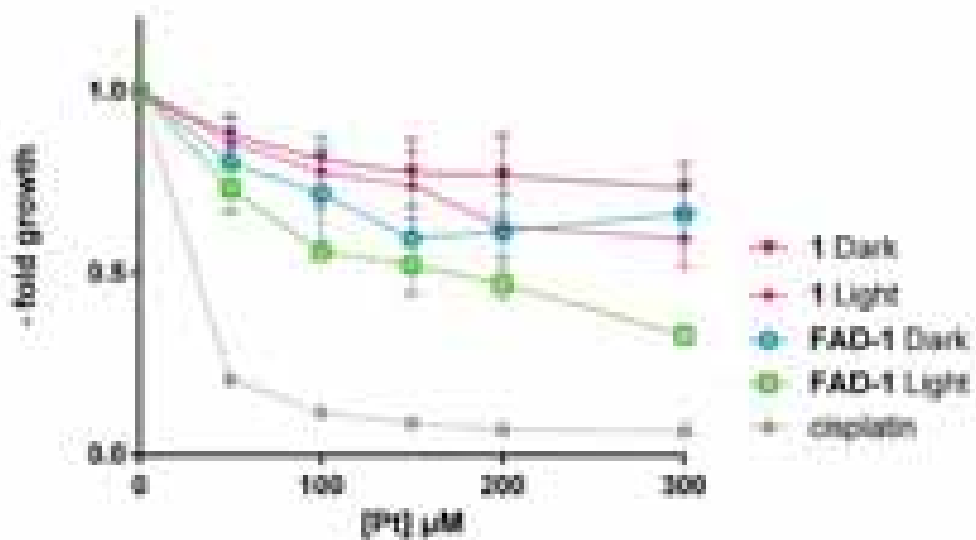


**Figure S7.** Photocatalytic **FAD-1** effect against Capan-1 cells. Cell viability of Capan-1 upon incubation with **FAD-1** (1:10) and **1** in the presence of 2 mM MES under light irradiation (460 nm, 0.36 J·cm<sup>-2</sup>) and in the dark. Cisplatin is shown as positive control.

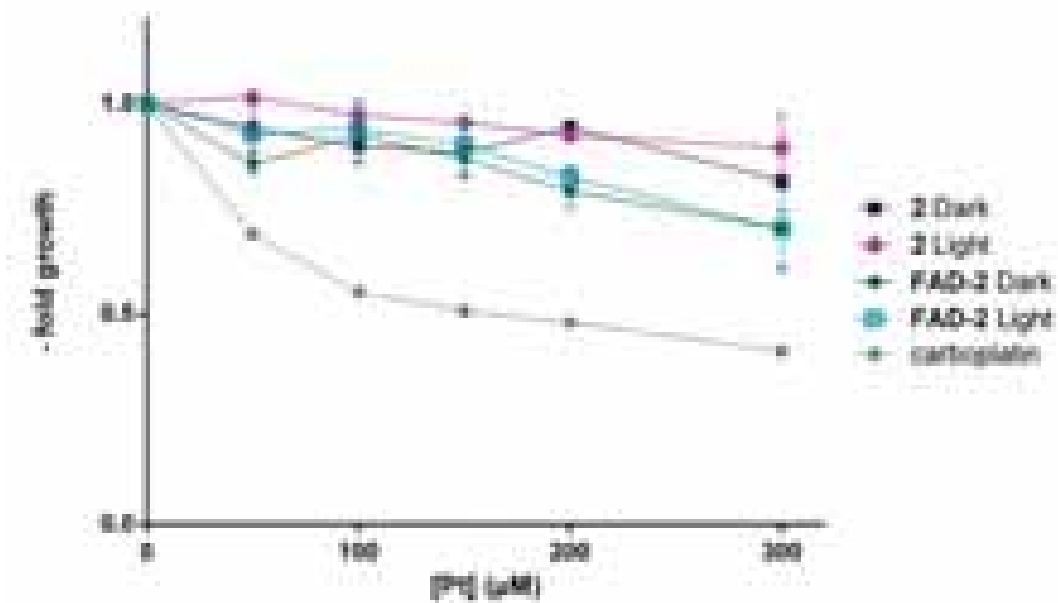


**Figure S8.** Photocatalytic **FAD-2** effect against Capan-1 cells. Cell viability of Capan-1 upon incubation with **FAD-2** (1:10) and **2** in the absence of MES under light irradiation (460 nm, 0.36 J·cm<sup>-2</sup>) and in the dark. Carboplatin is shown as positive control.

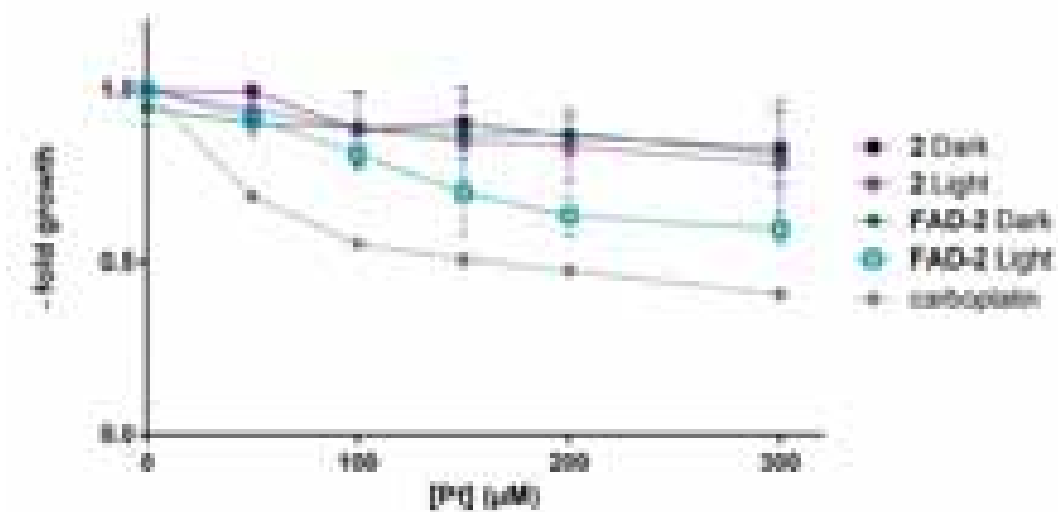


**Figure S9.** Photocatalytic **FAD-2** effect against Capan-1 cells. Cell viability of Capan-1 upon incubation with **FAD-2** (1:10) and **2** in the presence of 2 mM MES under light irradiation (460 nm, 0.36 J·cm<sup>-2</sup>) and in the dark. Carboplatin is shown as positive control.

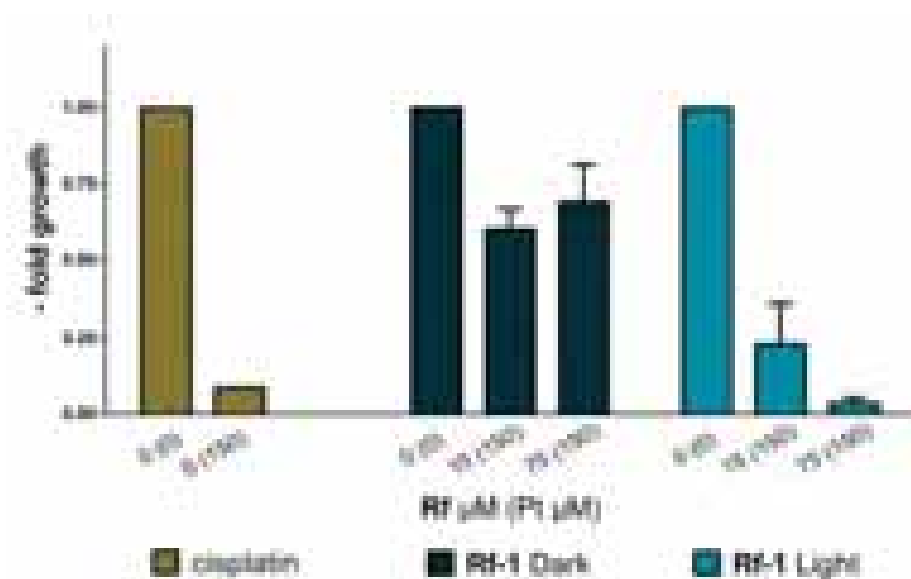


**Figure S10.** Cell viability of Capan-1 cells treated with two different **Rf-1** ratios (1:10 and 1:2) with 2 mM MES, under light irradiation (460 nm, 0.36 J·cm<sup>-2</sup>) and in the dark. Cisplatin is shown as positive control.

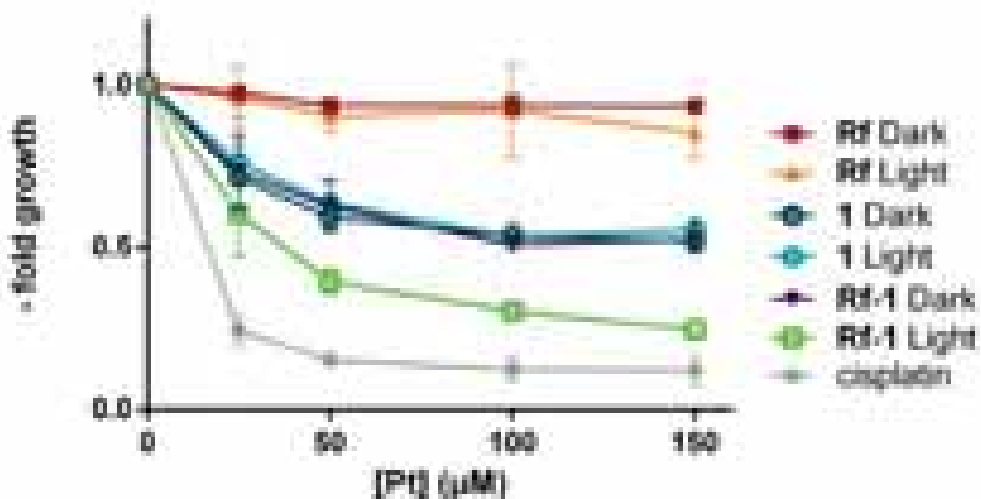


**Figure S11.** Photocatalytic **Rf-1** effect against Capan-1 cells in hypoxia conditions. Cell viability of Capan-1 cells upon incubation with **Rf-1** (1:10), **Rf** and **1** in the presence of 2 mM MES, under light irradiation (460 nm, 0.36 J·cm<sup>-2</sup> 1 min at 6 mW cm<sup>-2</sup>) and in the dark. Cisplatin is shown as positive control.



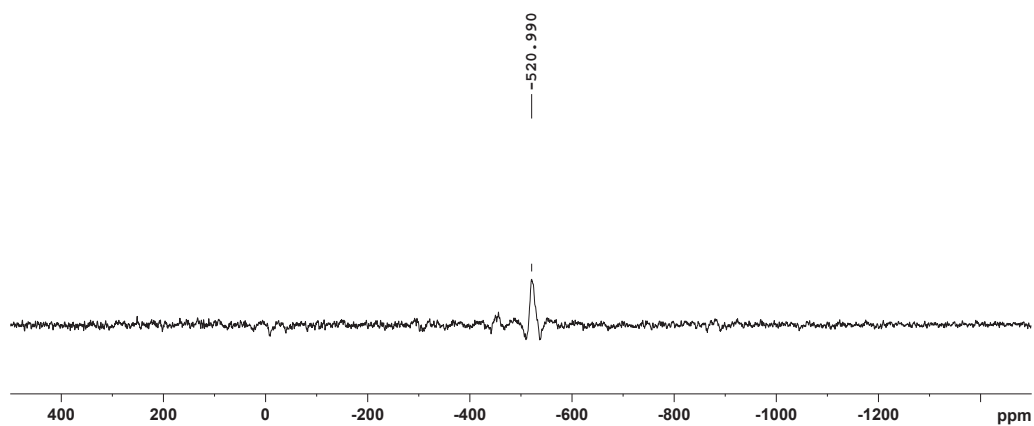


**Figure S12.**  $^{195}\text{Pt}$ -NMR spectrum of cisplatin. A solution of 2.7 mM cisplatin dissolved in 2 mM MES buffer pH 6 was measured.

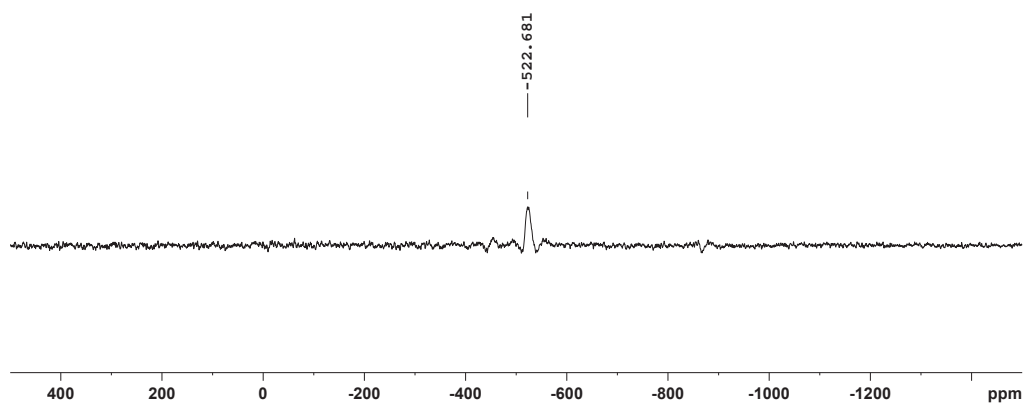


**Figure S13.**  $^{195}\text{Pt}$ -NMR spectrum of cisplatin. A solution of 2.7 mM cisplatin and 267  $\mu\text{M}$  Rf (ratio Rf:cisplatin 1:10) dissolved in 2 mM MES buffer pH 6 was measured.

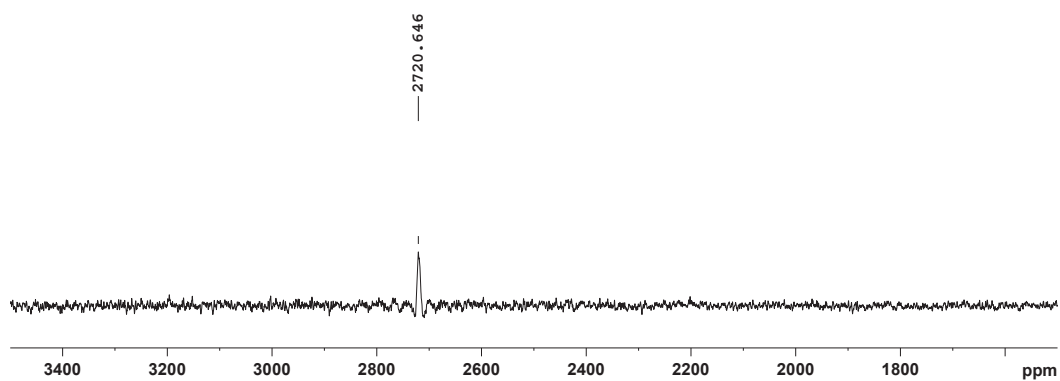


**Figure S14.**  $^{195}\text{Pt}$ -NMR spectrum. A solution of 7.2 mM **1** and 267  $\mu\text{M}$  Rf (ratio Rf:cisplatin 1:26.7) were dissolved in 2 mM MES buffer pH 6 was measured in the dark.

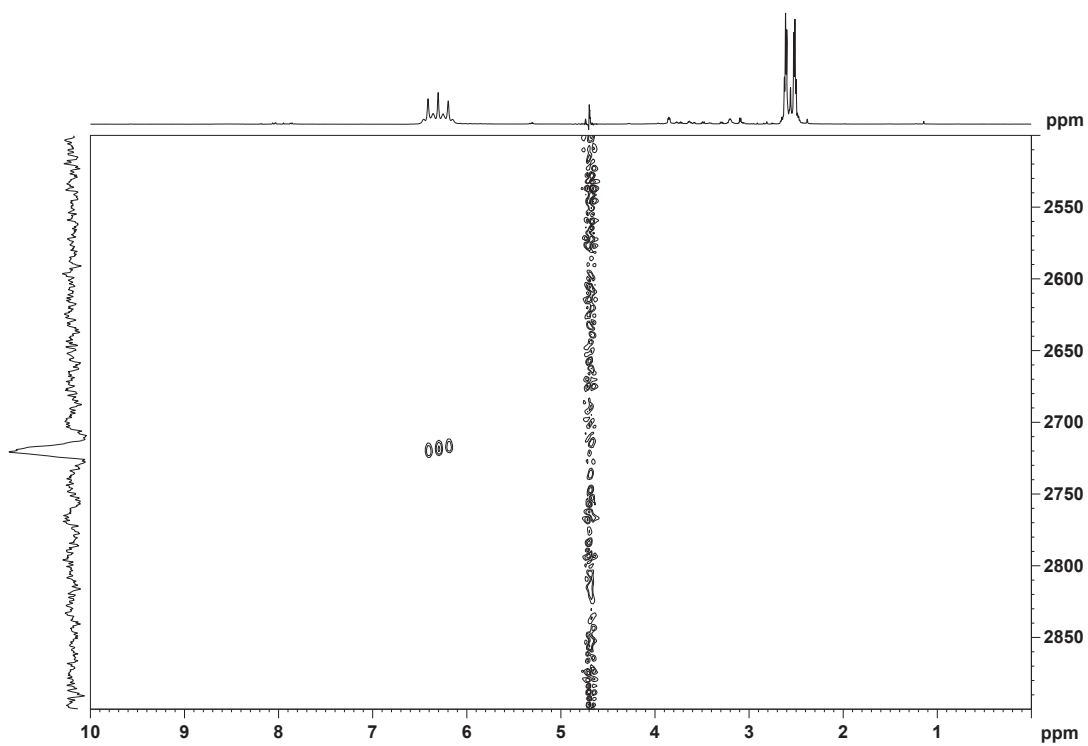


**Figure S15.**  $^1\text{H},^{195}\text{Pt}$ -HSQC NMR spectrum. A solution of 7.2 mM **1** and 267  $\mu\text{M}$  **Rf** (ratio **Rf**:cisplatin 1:27) dissolved in 2 mM MES buffer pH 6 was measured in the dark.

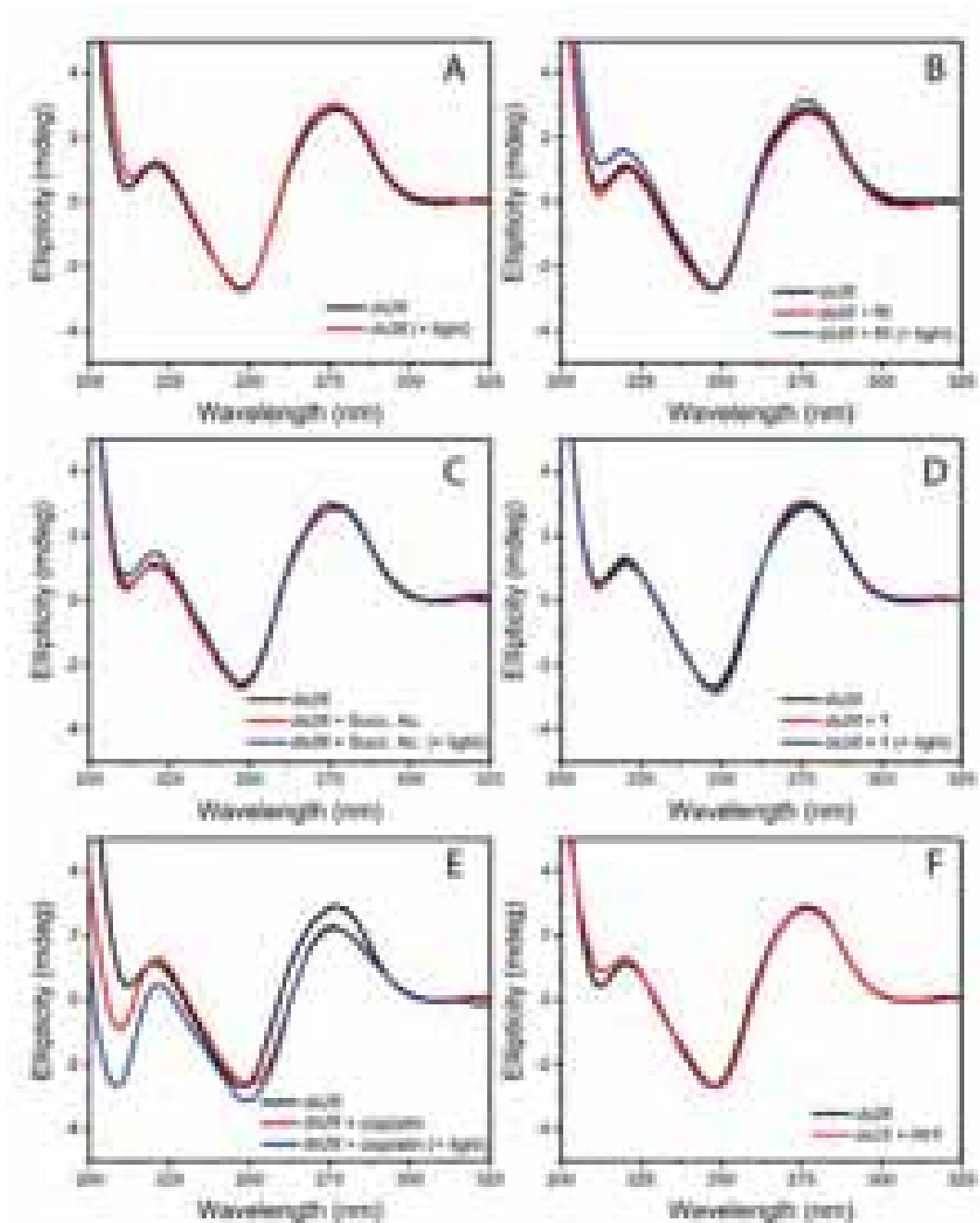


**Figure S16.** CD spectra of a) 1  $\mu\text{M}$  *ds26* in the dark and after irradiation; b) 1  $\mu\text{M}$  *ds26* in combination with 0.3  $\mu\text{M}$  **Rf** in the dark and after irradiation; c) 1  $\mu\text{M}$  *ds26* in combination with 6  $\mu\text{M}$  succinic acid in the dark and after irradiation; d) 1  $\mu\text{M}$  *ds26* in combination with 3  $\mu\text{M}$  **1** in the dark and after irradiation; e) 1  $\mu\text{M}$  *ds26* in combination with 3  $\mu\text{M}$  cisplatin in the dark and after irradiation; f) 1  $\mu\text{M}$  *ds26* in combination with 3  $\mu\text{M}$  **1** and 0.3  $\mu\text{M}$  **Rf** in the dark. Incubation: 48h at 37  $^{\circ}\text{C}$ . Buffer: MES 20 mM (pH=6.0). Light irradiations were performed at 460 nm ( $0.36 \text{ J}\cdot\text{cm}^{-2}$ ).

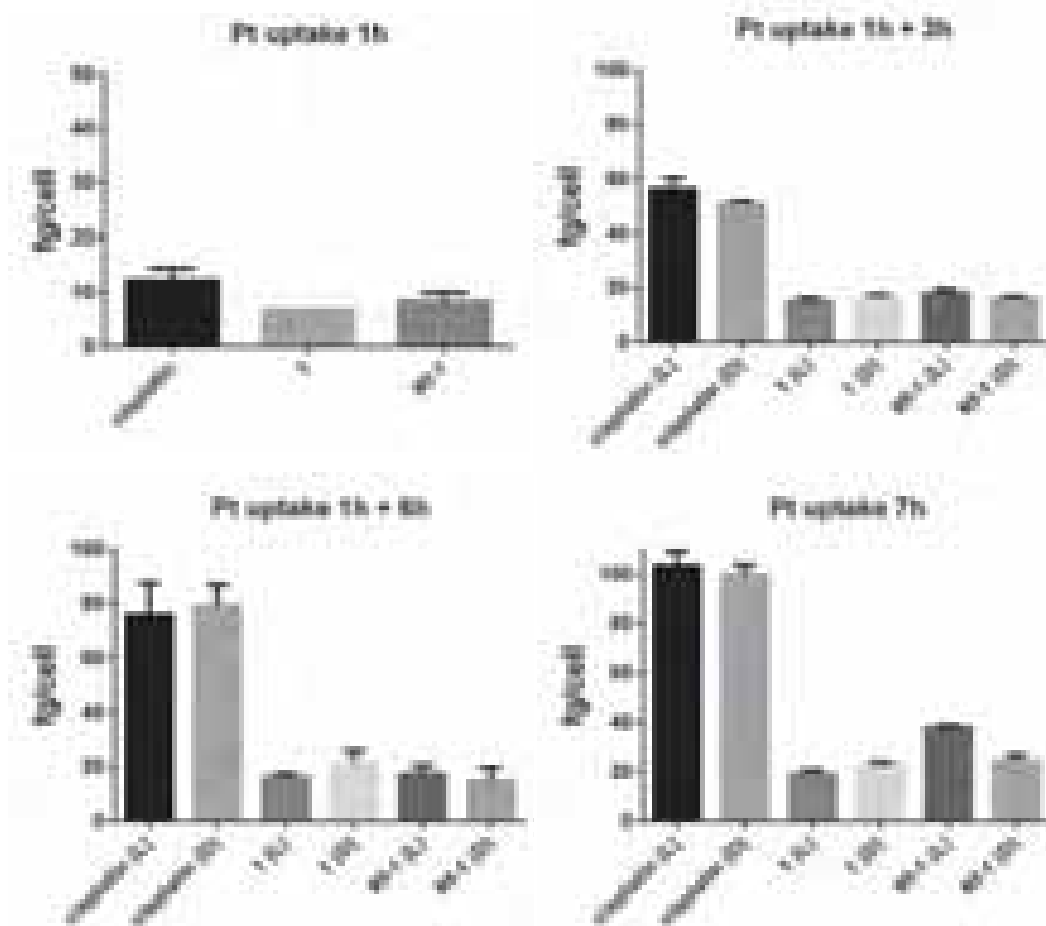


**Figure S17.** Pt accumulation in Capan-1 cells measured by ICP-MS at different time points. Cells treated with 100  $\mu\text{M}$  cisplatin, 100  $\mu\text{M}$  **1** and 10:100  $\mu\text{M}$  **Rf-1** were incubated a) 1 h in the dark, b) 1 h preincubation in the dark + 1 min of 460-nm light irradiation + 3 h in the dark, c) 1 h preincubation in the dark + 1 min of 460-nm light irradiation + 6 h in the dark, d) 1 min of 460-nm light irradiation + 7 h in the dark. All dark controls were not light irradiated and protected by ambient light.

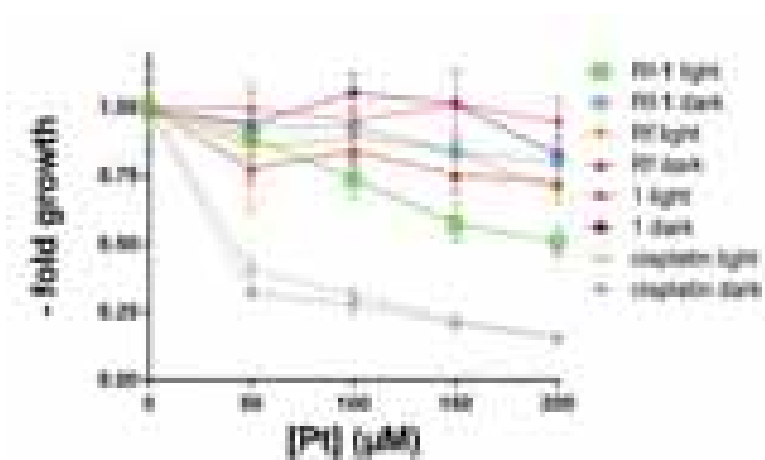


**Figure S18.** Photocatalytic **Rf-1** effect against Capan-1 cells. Cell viability of Capan-1 cells upon incubation with **Rf-1** (1:10), **Rf** and **1** in the presence of 2 mM MES during 1 h and followed by light irradiation (460 nm, 0.36 J·cm<sup>-2</sup>). Media was renewed immediately after irradiation. Dark controls were performed accordingly. Cisplatin is shown as positive control.

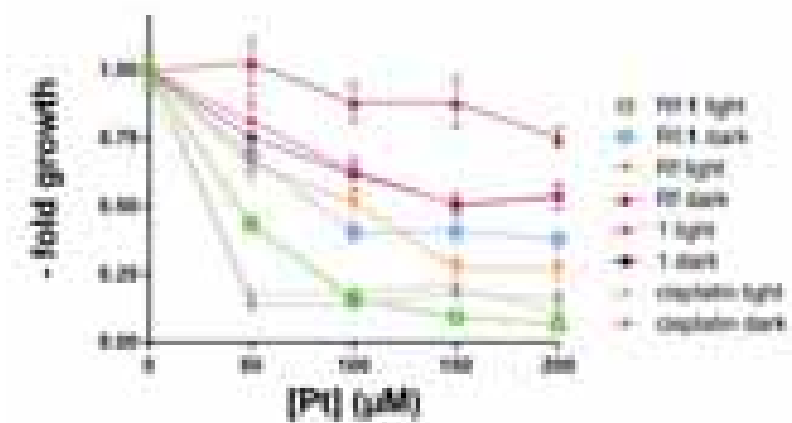


**Figure S19.** Photocatalytic **Rf-1** effect against Capan-1 cells. Cell viability of Capan-1 cells upon incubation with **Rf-1** (1:10), **Rf** and **1** in the presence of 2 mM MES were irradiated (460 nm, 0.36 J·cm<sup>-2</sup>) and incubated for 7 h. Media was renewed after these 7 h. Dark controls were performed accordingly. Cisplatin is shown as positive control.

Chapter 4 Supporting Information

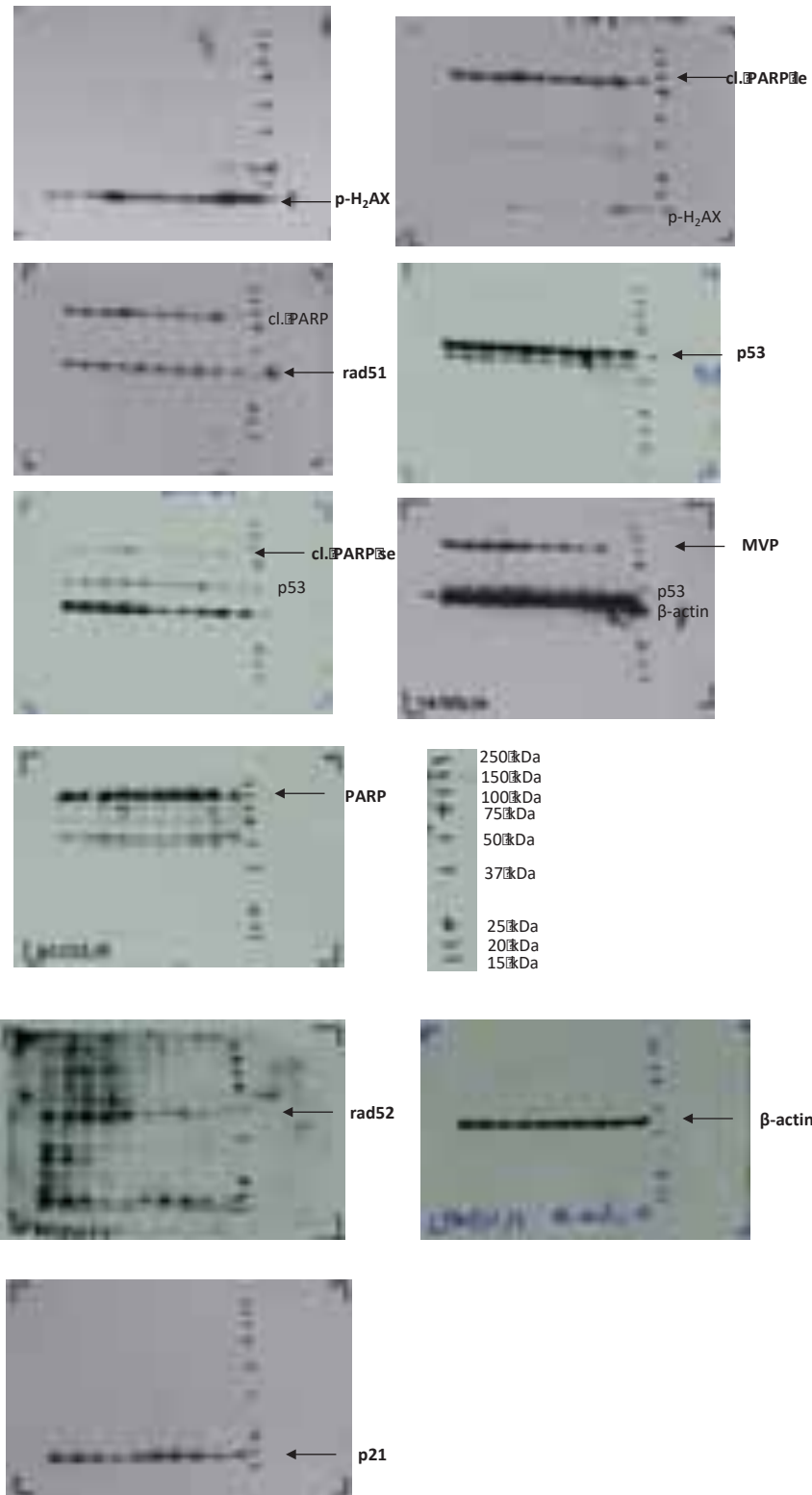


**Figure S20.** Original films for protein detection by Western blot analyses. Bands shown in Figure 4a of the main manuscript are indicated in bold face and by arrows.

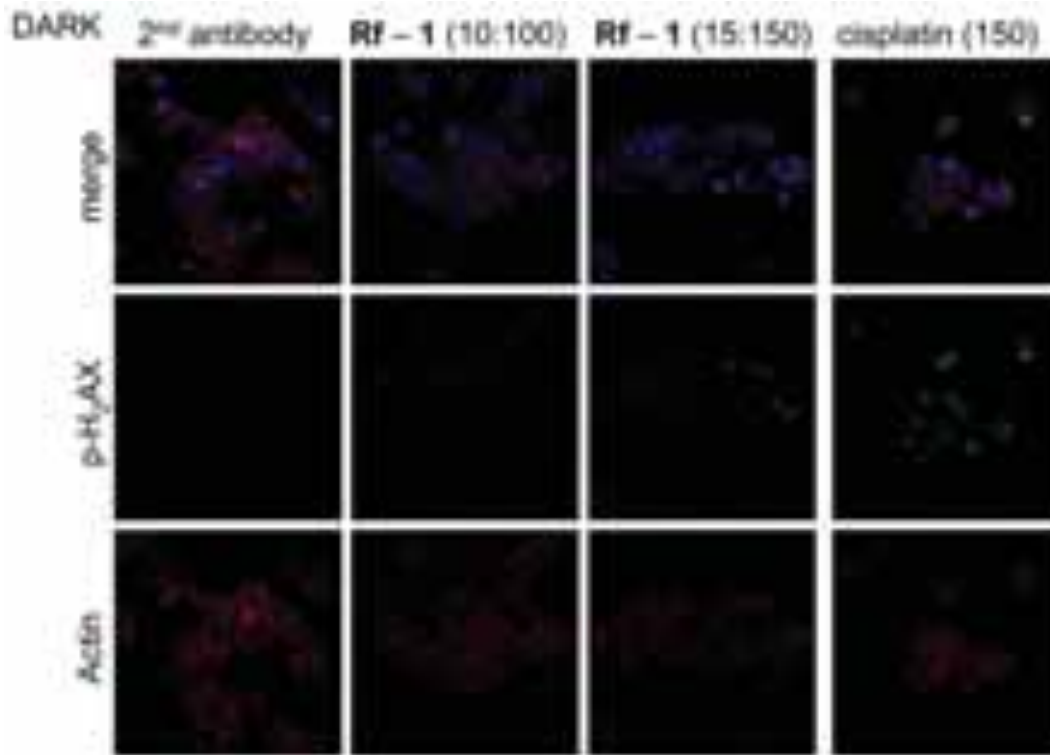


**Figure S21.** Immunofluorescence microscopy images of Capan-1 cells. Images correspond to control samples: **Rf** (15  $\mu$ M), **Rf-1** (10–100  $\mu$ M and 15–150  $\mu$ M) and cisplatin (150  $\mu$ M) under dark conditions. Cells were stained using DAPI for nuclei localization (blue channel), TRIC-phalloidin to visualize actin filaments (red channel) and primary antibody histone H<sub>2</sub>AX antibody (green channel).

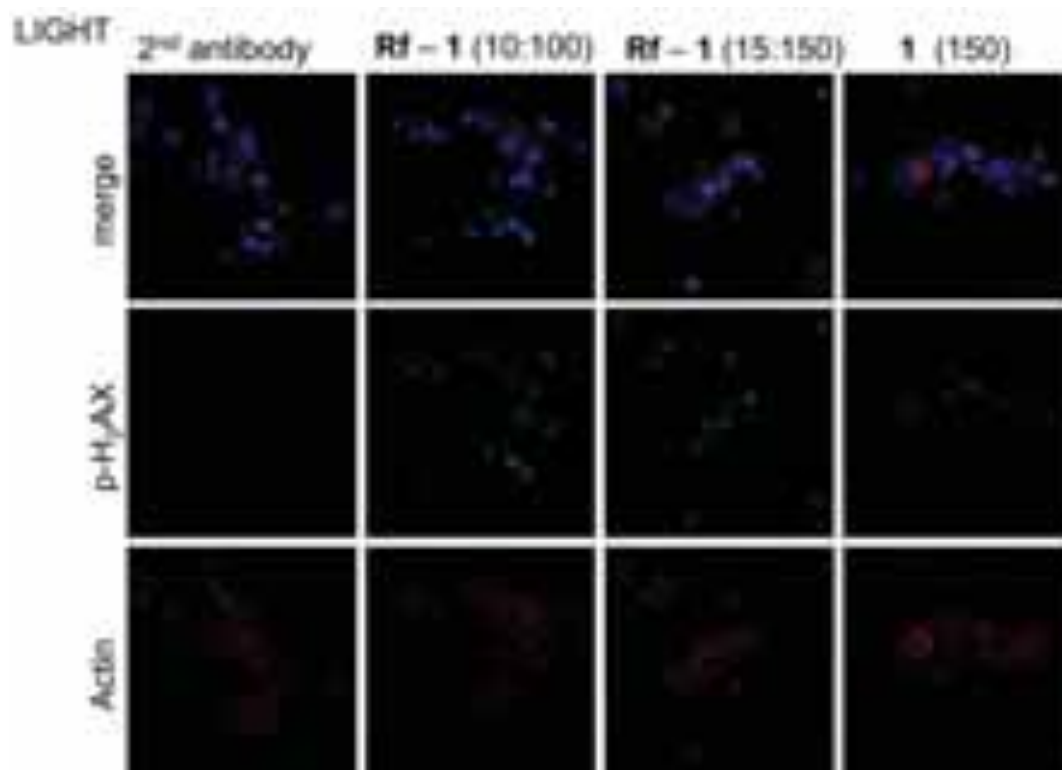


**Figure S22.** Immunofluorescence microscopy images of Capan-1 cells. Images correspond to control sample: **Rf-1** (10–100  $\mu$ M and 15–150  $\mu$ M) and **1** (150  $\mu$ M) irradiated 1 min at 460 nm ( $0.36 \text{ J}\cdot\text{cm}^{-2}$ ). Cells were stained using DAPI for nuclei localization (blue channel), TRIC-phalloidin to visualize actin filaments (red channel) and primary antibody histone H<sub>2</sub>AX antibody (green channel).



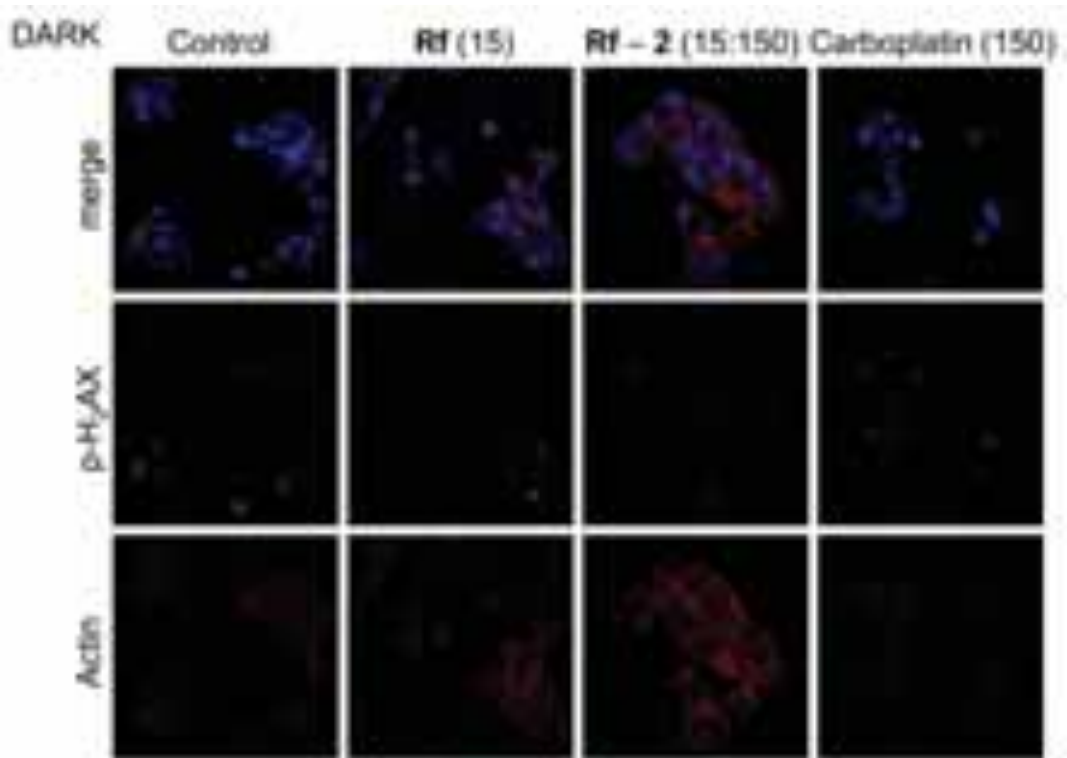


**Figure S23.** Immunofluorescence microscopy images of Capan-1 cells. Images correspond to control samples: Rf (15  $\mu$ M), Rf-2 (15–150  $\mu$ M) and carboplatin (150  $\mu$ M) in the dark. Cells were stained using DAPI for nuclei localization (blue channel), TRIC-phalloidin to visualize actin filaments (red channel) and primary antibody histone H<sub>2</sub>AX antibody (green channel).

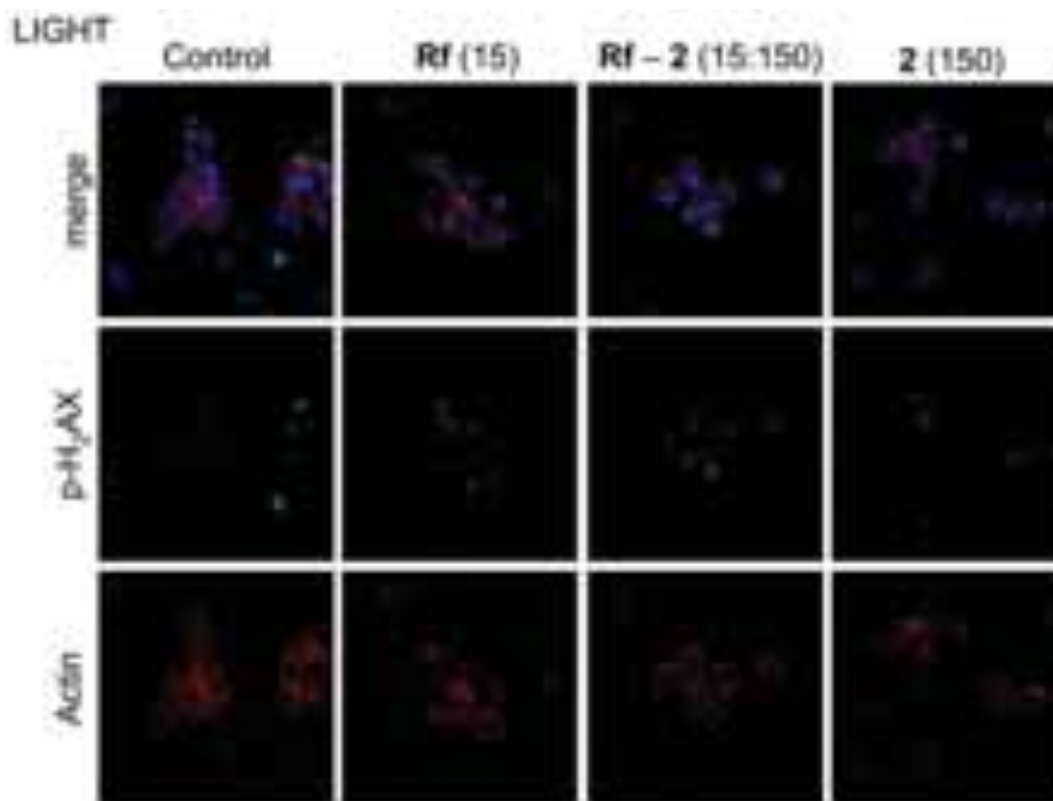


**Figure S24.** Immunofluorescence microscopy images of Capan-1 cells. Images correspond to control samples: **Rf** (15  $\mu\text{M}$ ), **Rf-2** (15–150  $\mu\text{M}$ ) and **2** (150  $\mu\text{M}$ ) irradiated 1 min at 460 nm ( $0.36 \text{ J}\cdot\text{cm}^{-2}$ ). Cells were stained using DAPI for nuclei localization (blue channel), TRIC-phalloidin to visualize actin filaments (red channel) and primary antibody histone H<sub>2</sub>AX antibody (green channel).

# 5

## Supporting Information

**Bioorthogonal Catalytic Activation Of  
Pt And Ru Anticancer Complexes By  
FAD and Flavoproteins**



### Complex 1

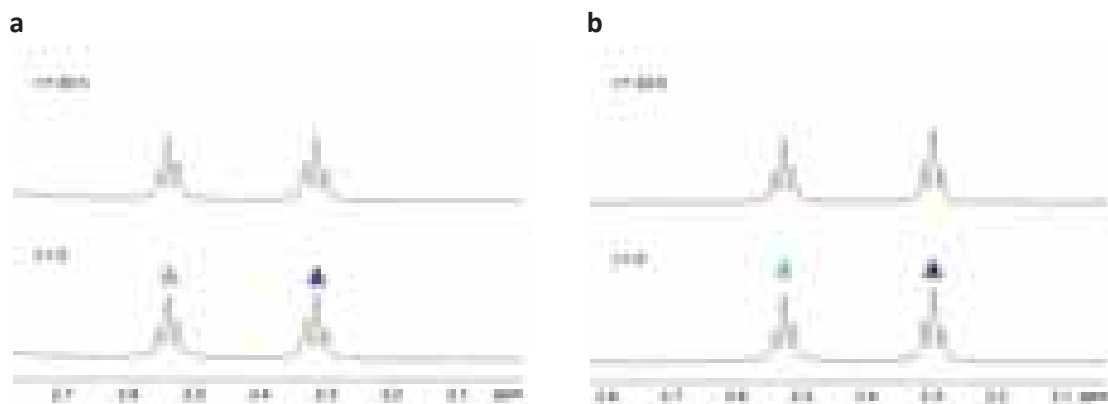


**Figure S1.** Dark stability of 0.2 mM **1** in (a) MES (pH 6, 20 mM, 10% D<sub>2</sub>O) and (b) PB buffer (pH 7, 100 mM, 10% D<sub>2</sub>O) over 24 h. <sup>1</sup>H NMR signal labelling: ▲ Pt-OCOCH<sub>2</sub>CH<sub>2</sub>CO<sub>2</sub><sup>-</sup>, ▲ Pt-OCOCH<sub>2</sub>CH<sub>2</sub>CO<sub>2</sub><sup>-</sup>.

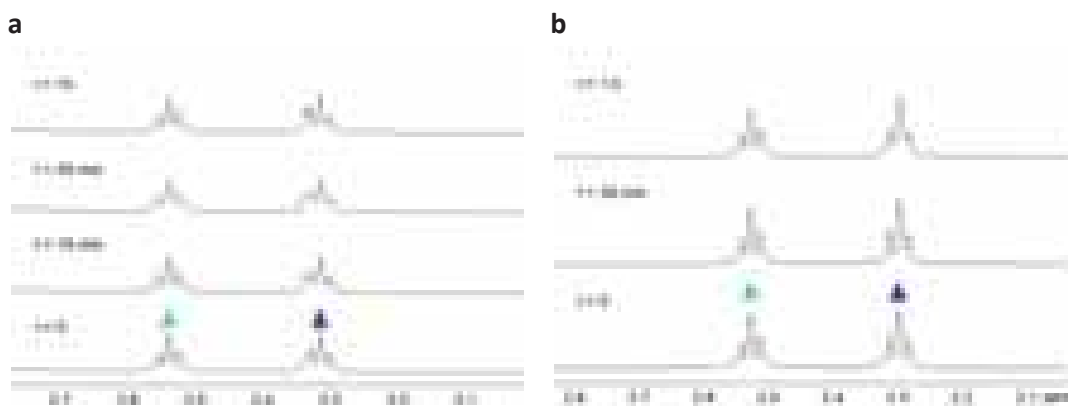


**Figure S2.** Photostability of 0.2 mM **1** in (a) MES (pH 6, 20 mM, 10% D<sub>2</sub>O) and (b) PB buffer (pH 7, 100 mM, 10% D<sub>2</sub>O). <sup>1</sup>H NMR spectra were recorded upon 460-nm light irradiation (6 mW·cm<sup>-2</sup>) for 1 h. <sup>1</sup>H NMR signal labelling: ▲ Pt-OCOCH<sub>2</sub>CH<sub>2</sub>CO<sub>2</sub><sup>-</sup>, ▲ Pt-OCOCH<sub>2</sub>CH<sub>2</sub>CO<sub>2</sub><sup>-</sup>.

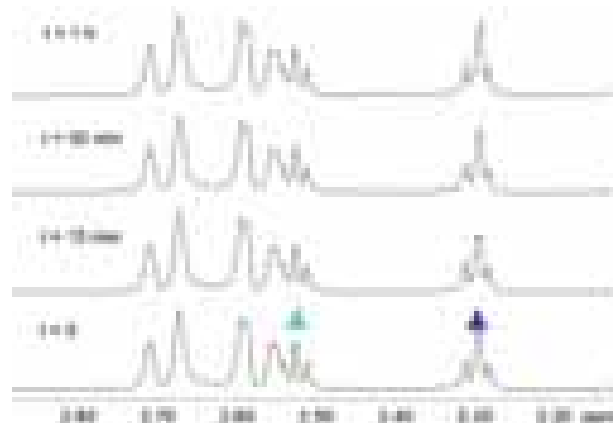


**Figure S3.** <sup>1</sup>H NMR spectra showing the PB buffer (pH 7, 100 mM, 10% D<sub>2</sub>O) stability of **1** under light irradiation (460 nm, 6 mW·cm<sup>-2</sup>) in the presence of 2 mM NADH. <sup>1</sup>H NMR signal labelling: ▲ Pt-OCOCH<sub>2</sub>CH<sub>2</sub>CO<sub>2</sub><sup>-</sup>, ▲ Pt-OCOCH<sub>2</sub>CH<sub>2</sub>CO<sub>2</sub><sup>-</sup>.

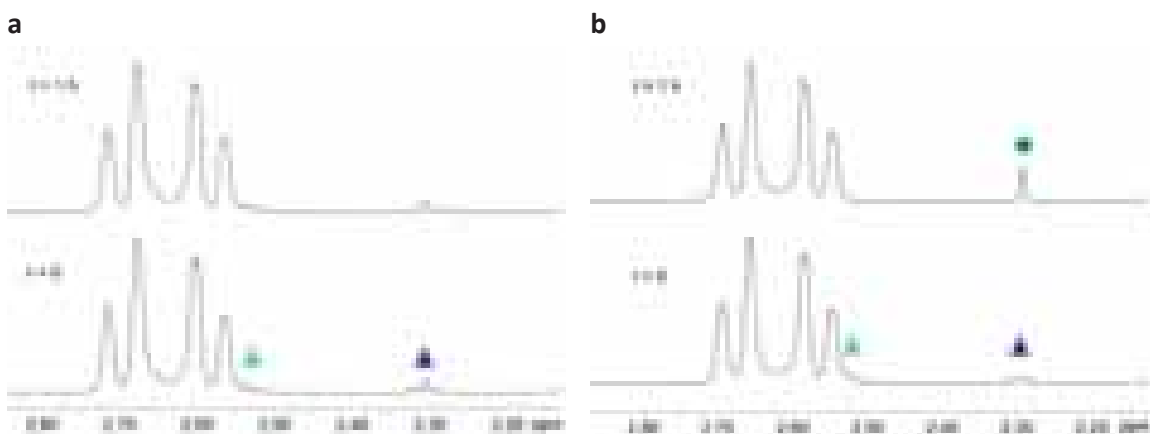


**Figure S4.**  $^1\text{H}$  NMR spectra showing the PB buffer (pH 7, 100 mM, 10%  $\text{D}_2\text{O}$ ) stability of **1** in the dark (a) and under light irradiation (b, 460 nm,  $6\text{ mW}\cdot\text{cm}^{-2}$ ) in the presence of 20 mM NADH.  $^1\text{H}$  NMR signal labelling: ▲ Pt-OCOCH<sub>2</sub>CH<sub>2</sub>CO<sub>2</sub><sup>-</sup>, ▲ Pt-OCOCH<sub>2</sub>CH<sub>2</sub>CO<sub>2</sub><sup>-</sup>, ● free <sup>-</sup>O<sub>2</sub>CCH<sub>2</sub>CH<sub>2</sub>CO<sub>2</sub><sup>-</sup>.

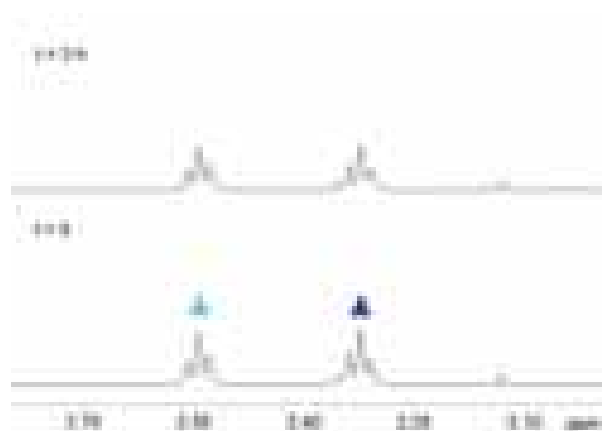


**Figure S5.** Dark stability of 0.2 mM **1** in MES (pH 6, 20 mM, 10%  $\text{D}_2\text{O}$ ) in the presence of 10  $\mu\text{M}$  FAD over 3 h.  $^1\text{H}$  NMR signal labelling: ▲ Pt-OCOCH<sub>2</sub>CH<sub>2</sub>CO<sub>2</sub><sup>-</sup>, ▲ Pt-OCOCH<sub>2</sub>CH<sub>2</sub>CO<sub>2</sub><sup>-</sup>.



**Figure S6.** FAD-catalyzed photoreduction of **1** in MES buffer (a 200  $\mu\text{M}$ ; b 2 mM; c 20 mM) monitored by  $^1\text{H}$  NMR. Spectra were recorded for MES (10%  $\text{D}_2\text{O}$ ) solutions of 200  $\mu\text{M}$  **1** and 10  $\mu\text{M}$  FAD upon  $t = 0$  sec, 2.5 min, 5 min and 10 min of 460-nm light irradiation ( $6\text{ mW}\cdot\text{cm}^{-2}$ ).  $^1\text{H}$  NMR signal labelling: ▲ Pt-OCOCH<sub>2</sub>CH<sub>2</sub>CO<sub>2</sub><sup>-</sup>, ▲ Pt-OCOCH<sub>2</sub>CH<sub>2</sub>CO<sub>2</sub><sup>-</sup>, ● free <sup>-</sup>O<sub>2</sub>CCH<sub>2</sub>CH<sub>2</sub>CO<sub>2</sub><sup>-</sup>.

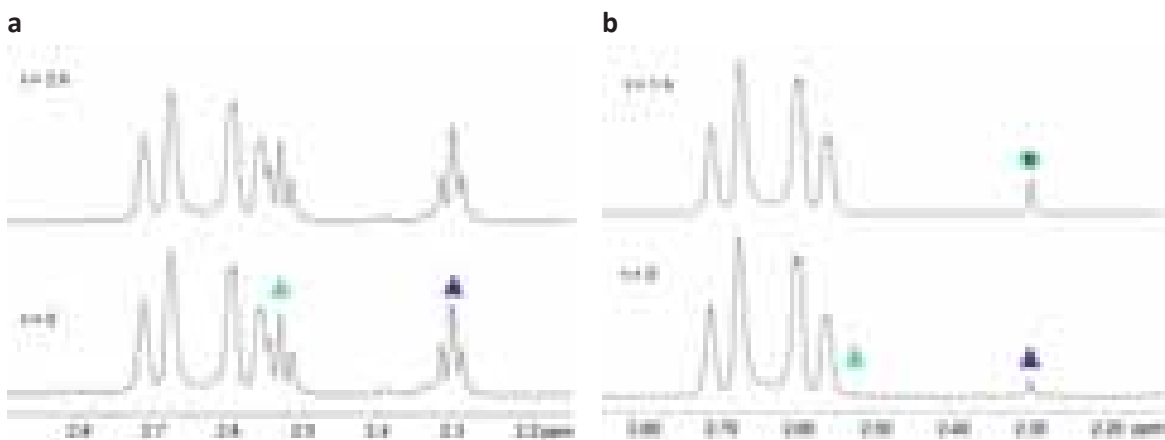


**Figure S7.** Dark stability of **1** in the dark and in PB buffer (pH 7, 100 mM) in the presence of NADH (**a**, 2 mM; **b**, 20 mM) and FAD monitored by  $^1\text{H}$  NMR. Spectra were recorded for PB (10%  $\text{D}_2\text{O}$ ) solutions of 200  $\mu\text{M}$  **1** and 10  $\mu\text{M}$  FAD.  $^1\text{H}$  NMR signal labelling: ▲ Pt-OCOCH<sub>2</sub>CH<sub>2</sub>CO<sub>2</sub><sup>-</sup>, ▲ Pt-OCOCH<sub>2</sub>CH<sub>2</sub>CO<sub>2</sub><sup>-</sup>, ● free <sup>-</sup>O<sub>2</sub>CCH<sub>2</sub>CH<sub>2</sub>CO<sub>2</sub><sup>-</sup>.

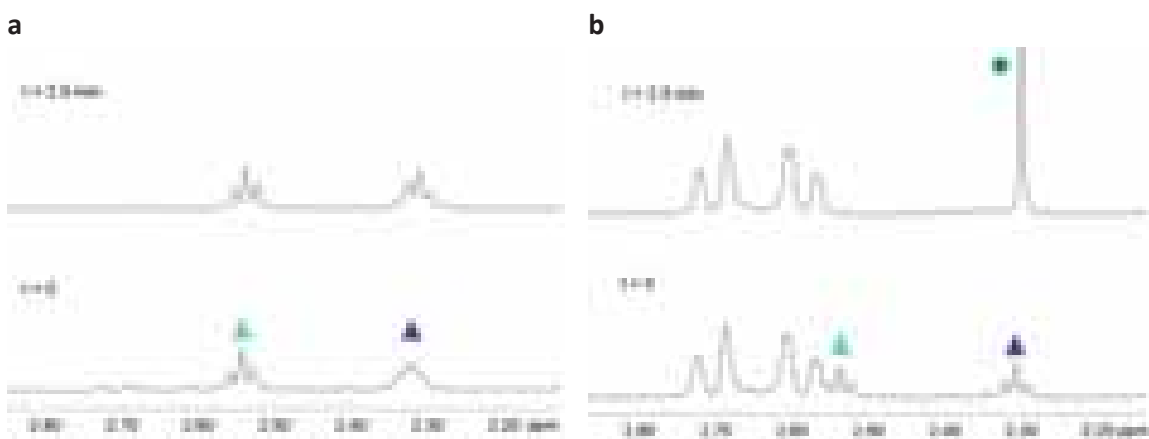


**Figure S8.** FAD-catalyzed photoreduction of **1** in PB buffer (pH 7, 100 mM) in the presence of NADH (**a**, 200  $\mu\text{M}$ ; **b**, 2 mM) monitored by  $^1\text{H}$  NMR. Spectra were recorded for PB (10%  $\text{D}_2\text{O}$ ) solutions of 200  $\mu\text{M}$  **1** and 10  $\mu\text{M}$  FAD upon  $t = 0$  sec and 2.5 min of 460-nm light irradiation ( $6 \text{ mW}\cdot\text{cm}^{-2}$ ).  $^1\text{H}$  NMR signal labelling: ▲ Pt-OCOCH<sub>2</sub>CH<sub>2</sub>CO<sub>2</sub><sup>-</sup>, ▲ Pt-OCOCH<sub>2</sub>CH<sub>2</sub>CO<sub>2</sub><sup>-</sup>, ● free <sup>-</sup>O<sub>2</sub>CCH<sub>2</sub>CH<sub>2</sub>CO<sub>2</sub><sup>-</sup>.

## Complex 2

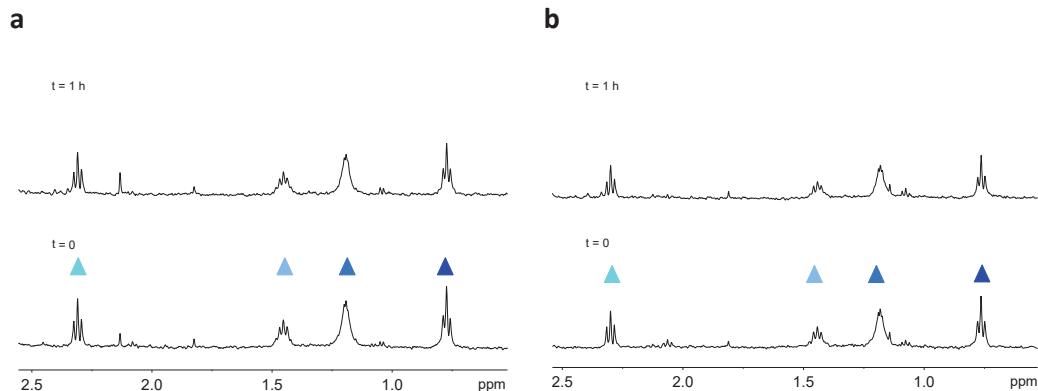


**Figure S9.** Photostability of 0.2 mM **2** in (a) MES (pH 6, 20 mM, 10% D<sub>2</sub>O, 1% dmsO-d<sub>6</sub>) and (b) PB buffer (pH 7, 100 mM, 10% D<sub>2</sub>O, 1% dmsO-d<sub>6</sub>) with 2 mM NADH. <sup>1</sup>H NMR spectra were recorded upon 460-nm light irradiation (6 mW·cm<sup>-2</sup>) for 1 h. <sup>1</sup>H NMR signal labelling: ▲ Pt-OCOCH<sub>2</sub>CH<sub>2</sub>CH<sub>2</sub>CH<sub>2</sub>CH<sub>3</sub>, ▲ Pt-OCOCH<sub>2</sub>CH<sub>2</sub>CH<sub>2</sub>CH<sub>2</sub>CH<sub>3</sub>, ▲ Pt-OCOCH<sub>2</sub>CH<sub>2</sub>CH<sub>2</sub>CH<sub>2</sub>CH<sub>3</sub>, ▲ Pt-OCOCH<sub>2</sub>CH<sub>2</sub>CH<sub>2</sub>CH<sub>2</sub>CH<sub>3</sub>.

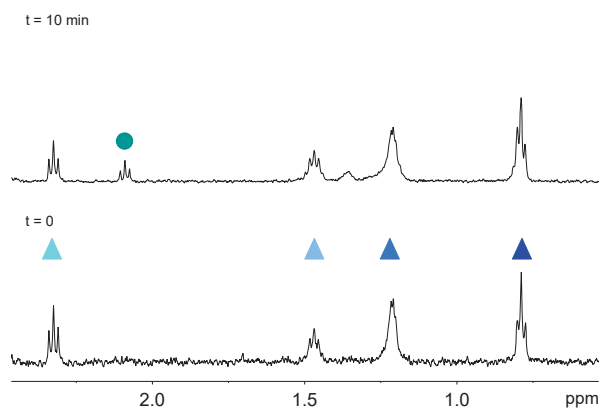


**Figure S10.** Photoactivation of 0.2 mM **2** in water (10% D<sub>2</sub>O, 1% dmsO-d<sub>6</sub>) upon 365-nm light irradiation for 10 min. <sup>1</sup>H NMR signal labelling: ▲ Pt-OCOCH<sub>2</sub>CH<sub>2</sub>CH<sub>2</sub>CH<sub>2</sub>CH<sub>3</sub>, ▲ Pt-OCOCH<sub>2</sub>CH<sub>2</sub>CH<sub>2</sub>CH<sub>2</sub>CH<sub>3</sub>, ▲ Pt-OCOCH<sub>2</sub>CH<sub>2</sub>CH<sub>2</sub>CH<sub>2</sub>CH<sub>3</sub>, ▲ Pt-OCOCH<sub>2</sub>CH<sub>2</sub>CH<sub>2</sub>CH<sub>2</sub>CH<sub>3</sub>, ● free <sup>-</sup>OCOCH<sub>2</sub>CH<sub>2</sub>CH<sub>2</sub>CH<sub>2</sub>CH<sub>3</sub>.

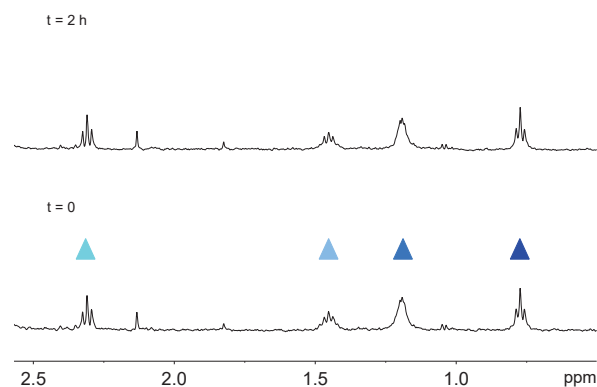


**Figure S11.** Dark stability of 0.2 mM **2** in MES (pH 6, 20 mM, 10% D<sub>2</sub>O, 1% dmsO-d<sub>6</sub>) in the presence of 10 μM FAD over 2 h. <sup>1</sup>H NMR signal labelling: ▲ Pt-OCOCH<sub>2</sub>CH<sub>2</sub>CH<sub>2</sub>CH<sub>2</sub>CH<sub>3</sub>, ▲ Pt-OCOCH<sub>2</sub>CH<sub>2</sub>CH<sub>2</sub>CH<sub>2</sub>CH<sub>3</sub>, ▲ Pt-OCOCH<sub>2</sub>CH<sub>2</sub>CH<sub>2</sub>CH<sub>2</sub>CH<sub>3</sub>, ▲ Pt-OCOCH<sub>2</sub>CH<sub>2</sub>CH<sub>2</sub>CH<sub>2</sub>CH<sub>3</sub>.



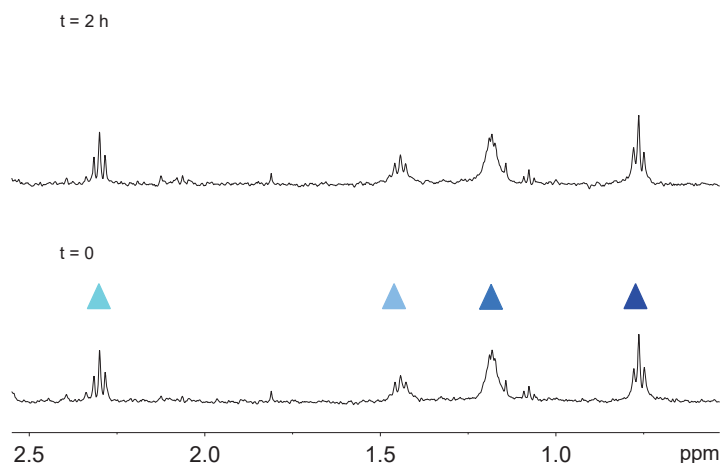


**Figure S13.** Dark stability of **2** in the dark and in PB buffer (pH 7, 100 mM) in the presence of NADH (2 mM) and FAD monitored by  $^1\text{H}$  NMR. Spectra were recorded for PB (10%  $\text{D}_2\text{O}$ , 1% dms $-\text{d}_6$ ) solutions of 200  $\mu\text{M}$  **2** and 10  $\mu\text{M}$  FAD.  $^1\text{H}$  NMR signal labelling:  $\blacktriangle$  Pt-OCOCH $_2$ CH $_2$ CH $_2$ CH $_2$ CH $_2$ CH $_3$ ,  $\blacktriangle$  Pt-OCOCH $_2$ CH $_2$ CH $_2$ CH $_2$ CH $_2$ CH $_3$ ,  $\blacktriangle$  Pt-OCOCH $_2$ CH $_2$ CH $_2$ CH $_2$ CH $_2$ CH $_3$ ,  $\blacktriangle$  Pt-OCOCH $_2$ CH $_2$ CH $_2$ CH $_2$ CH $_2$ CH $_3$ .

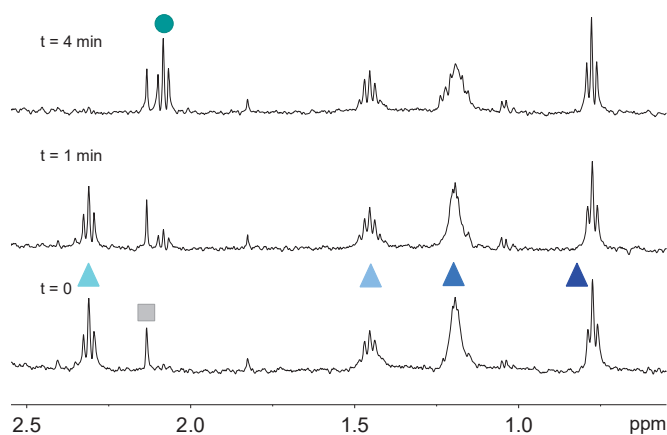


**Figure S14.** FAD-catalyzed photoreduction of **2** in MES buffer (pH 6, 20 mM) monitored by  $^1\text{H}$  NMR. Spectra were recorded for MES (10%  $\text{D}_2\text{O}$ , 1% dms $-\text{d}_6$ ) solutions of 200  $\mu\text{M}$  **2** and 10  $\mu\text{M}$  FAD upon  $t = 0, 1$  min and 4 min of 460-nm light irradiation ( $6 \text{ mW}\cdot\text{cm}^{-2}$ ).  $^1\text{H}$  NMR signal labelling:  $\blacktriangle$  Pt-OCOCH $_2$ CH $_2$ CH $_2$ CH $_2$ CH $_2$ CH $_3$ ,  $\blacktriangle$  Pt-OCOCH $_2$ CH $_2$ CH $_2$ CH $_2$ CH $_2$ CH $_3$ ,  $\blacktriangle$  Pt-OCOCH $_2$ CH $_2$ CH $_2$ CH $_2$ CH $_2$ CH $_3$ ,  $\blacktriangle$  Pt-OCOCH $_2$ CH $_2$ CH $_2$ CH $_2$ CH $_2$ CH $_3$ ,  $\bullet$  free  $^-\text{OCOCH}_2\text{CH}_2\text{CH}_2\text{CH}_2\text{CH}_2\text{CH}_3$ ,  $\blacksquare$  acetone impurity.

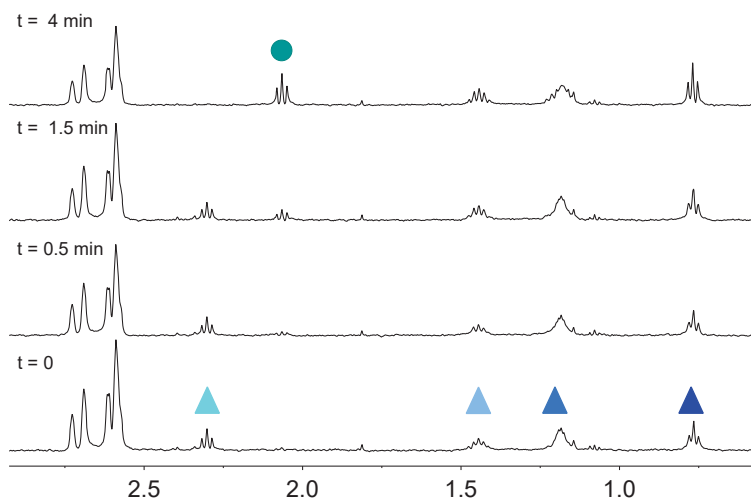


**Figure S15.** FAD-catalyzed photoreduction of **2** in PB buffer (pH 7, 100 mM) in the presence of NADH (2 mM) monitored by  $^1\text{H}$  NMR. Spectra were recorded for PB (10%  $\text{D}_2\text{O}$ , 1%  $\text{dms}\text{-}d_6$ ) solutions of 200  $\mu\text{M}$  **2** and 10  $\mu\text{M}$  FAD upon  $t = 0, 0.5 \text{ min}, 1.5 \text{ min}$  and 4 min of 460-nm light irradiation ( $6 \text{ mW}\cdot\text{cm}^{-2}$ ).  $^1\text{H}$  NMR signal labelling:  $\blacktriangle$   $\text{Pt-OCOCH}_2\text{CH}_2\text{CH}_2\text{CH}_2\text{CH}_3$ ,  $\blacktriangle$   $\text{Pt-OCOCH}_2\text{CH}_2\text{CH}_2\text{CH}_2\text{CH}_3$ ,  $\blacktriangle$   $\text{Pt-OCOCH}_2\text{CH}_2\text{CH}_2\text{CH}_2\text{CH}_3$ ,  $\blacktriangle$   $\text{Pt-OCOCH}_2\text{CH}_2\text{CH}_2\text{CH}_2\text{CH}_3$ ,  $\bullet$  free  $^- \text{OCOCH}_2\text{CH}_2\text{CH}_2\text{CH}_2\text{CH}_3$ .

## Complex 3

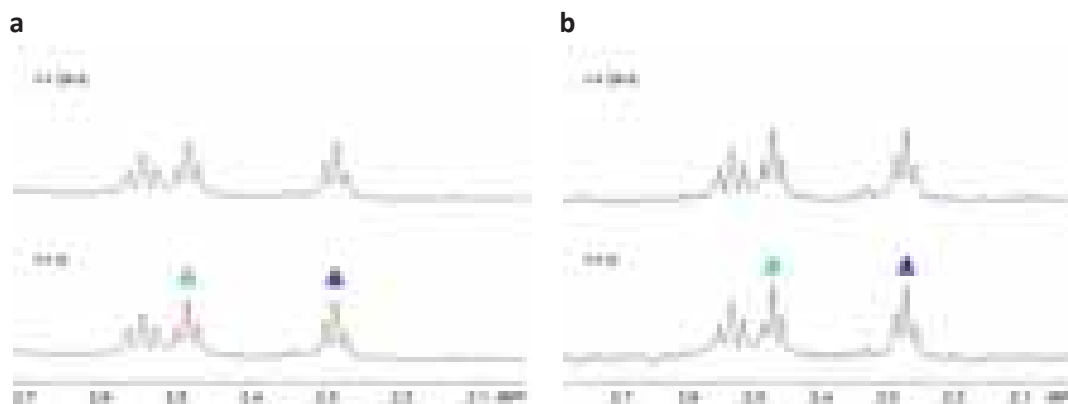


**Figure S16.** Dark stability of 0.2 mM **3** in (a) MES (pH 6, 20 mM, 10%  $\text{D}_2\text{O}$ ) and (b) PB buffer (pH 7, 100 mM, 10%  $\text{D}_2\text{O}$ ) over 24 h.  $^1\text{H}$  NMR signal labelling:  $\blacktriangle$   $\text{Pt-OCOCH}_2\text{CH}_2\text{CO}_2^-$ ,  $\blacktriangle$   $\text{Pt-OCOCH}_2\text{CH}_2\text{CO}_2^-$ .

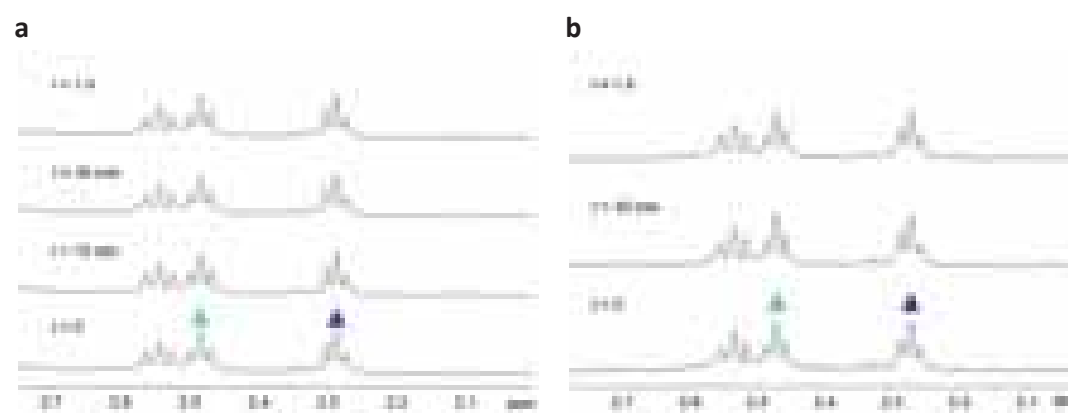


**Figure S17.** Photostability of 0.2 mM **3** in (a) MES (pH 6, 20 mM, 10%  $\text{D}_2\text{O}$ ) and (b) PB buffer (pH 7, 100 mM, 10%  $\text{D}_2\text{O}$ ).  $^1\text{H}$  NMR spectra were recorded upon 460-nm light irradiation ( $6 \text{ mW}\cdot\text{cm}^{-2}$ ) for 1 h.  $^1\text{H}$  NMR signal labelling:  $\blacktriangle$   $\text{Pt-OCOCH}_2\text{CH}_2\text{CO}_2^-$ ,  $\blacktriangle$   $\text{Pt-OCOCH}_2\text{CH}_2\text{CO}_2^-$ .

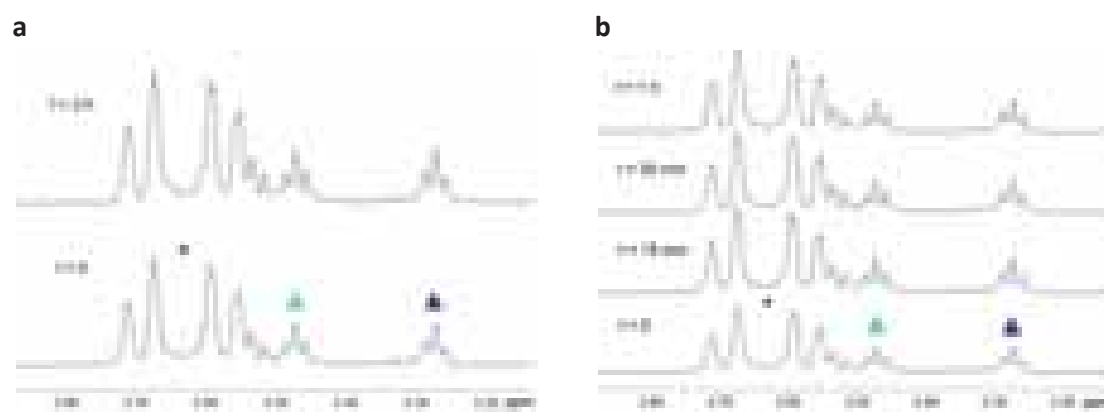


**Figure S18.** Stability in the dark (a) and under light irradiation (b) of 0.2 mM **3** in the presence of 2 mM NADH (PB buffer pH 7, 100 mM) monitored by  $^1\text{H}$  NMR. Light source: 460 nm,  $6 \text{ mW}\cdot\text{cm}^{-2}$ .  $^1\text{H}$  NMR signal labelling:  $\blacktriangle$   $\text{Pt-OCOCH}_2\text{CH}_2\text{CO}_2^-$ ,  $\blacktriangle$   $\text{Pt-OCOCH}_2\text{CH}_2\text{CO}_2^-$ .

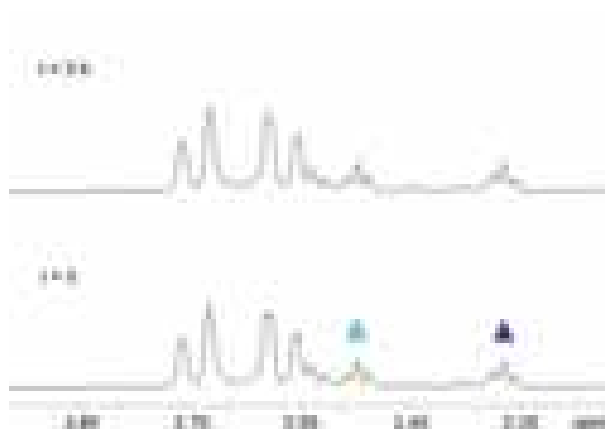


**Figure S19.** Dark stability of **3** in PB buffer (pH 7, 100 mM, 10% D<sub>2</sub>O) in the presence of NADH and FAD over 3 h. <sup>1</sup>H NMR spectra were recorded for solutions of 200 μM **3** and 10 μM FAD and 2 mM NADH. <sup>1</sup>H NMR signal labelling: ▲ Pt-OCOCH<sub>2</sub>CH<sub>2</sub>CO<sub>2</sub><sup>-</sup>, ▲ Pt-OCOCH<sub>2</sub>CH<sub>2</sub>CO<sub>2</sub><sup>-</sup>.

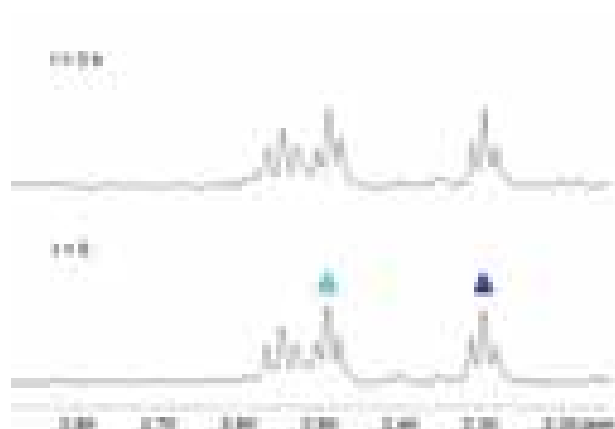


**Figure S20.** Dark stability of 0.2 mM **3** in MES (pH 6, 20 mM, 10% D<sub>2</sub>O) in the presence of 10 μM FAD over 3 h. <sup>1</sup>H NMR signal labelling: ▲ Pt-OCOCH<sub>2</sub>CH<sub>2</sub>CO<sub>2</sub><sup>-</sup>, ▲ Pt-OCOCH<sub>2</sub>CH<sub>2</sub>CO<sub>2</sub><sup>-</sup>.

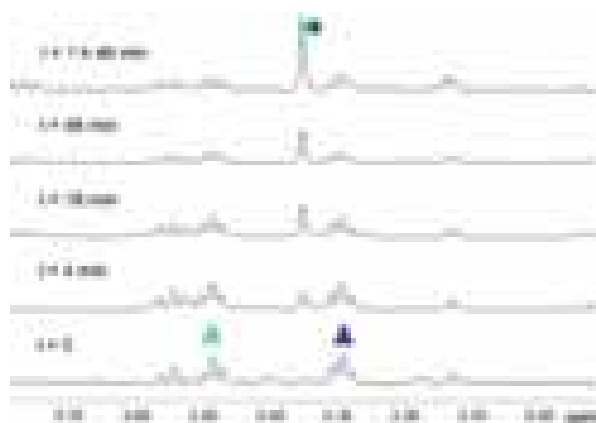


**Figure S21.** FAD-catalyzed photoreduction of **3** in MES buffer (pH 6, 20 mM) monitored by <sup>1</sup>H NMR. Spectra were recorded for MES (10% D<sub>2</sub>O) solutions of 200 μM **3** and 10 μM FAD upon t = 0 min, 4 min, 16 min, 46 min and 1 h and 46 min of 460-nm light irradiation (6 mW·cm<sup>-2</sup>). <sup>1</sup>H NMR signal labelling: ▲ Pt-OCOCH<sub>2</sub>CH<sub>2</sub>CO<sub>2</sub><sup>-</sup>, ▲ Pt-OCOCH<sub>2</sub>CH<sub>2</sub>CO<sub>2</sub><sup>-</sup>, ● free <sup>-</sup>O<sub>2</sub>CCH<sub>2</sub>CH<sub>2</sub>CO<sub>2</sub><sup>-</sup>.

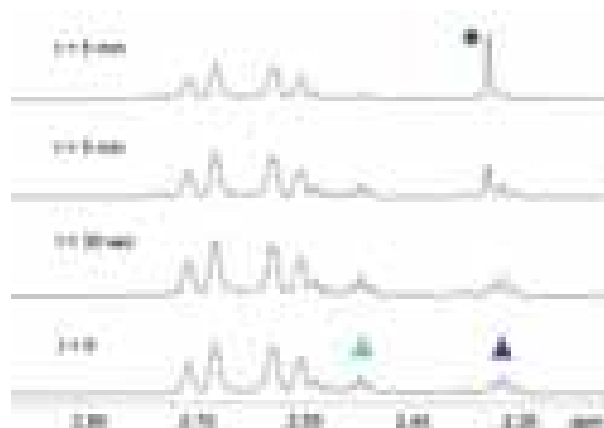


**Figure S22.** FAD-catalyzed photoreduction of **3** in PB buffer (pH 7, 100 mM) in the presence of NADH (2 mM) monitored by  $^1\text{H}$  NMR. Spectra were recorded for PB (10%  $\text{D}_2\text{O}$ ) solutions of 200  $\mu\text{M}$  **3** and 10  $\mu\text{M}$  FAD upon  $t = 0$  sec, 30 sec, 3 min and 5 min of 460-nm light irradiation ( $6 \text{ mW}\cdot\text{cm}^{-2}$ ).  $^1\text{H}$  NMR signal labelling:  $\blacktriangle$   $\text{Pt-OCOCH}_2\text{CH}_2\text{CO}_2^-$ ,  $\blacktriangle$   $\text{Pt-OCOCH}_2\text{CH}_2\text{CO}_2^-$ ,  $\bullet$  free  $^- \text{O}_2\text{CCH}_2\text{CH}_2\text{CO}_2^-$ .

## Complex 4

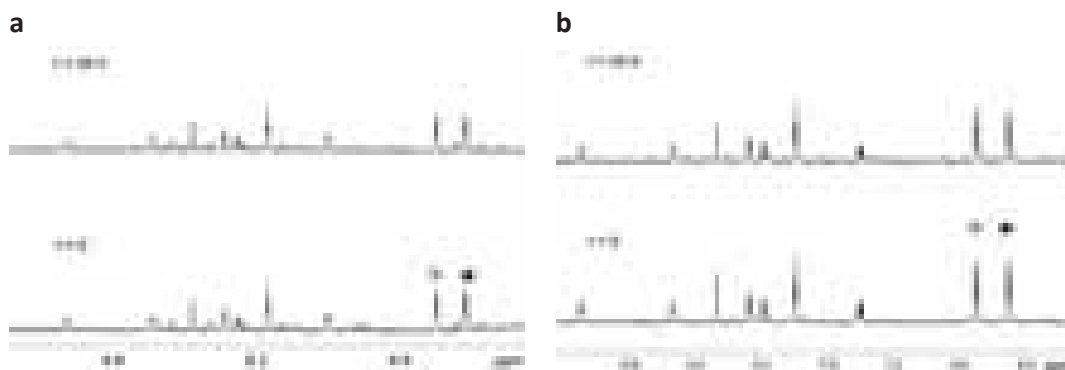


**Figure S23.** Dark stability of 0.2 mM **4** in (a) MES (pH 6, 20 mM, 10% D<sub>2</sub>O, 3.3% dms<sub>o</sub>-d<sup>6</sup>) and (b) PB bufer (pH 7, 100 mM, 10% D<sub>2</sub>O, 3.3% dms<sub>o</sub>-d<sup>6</sup>) over 24 h. <sup>1</sup>H NMR signal labelling: ◆ and ◆ Ru-(p-cymene).

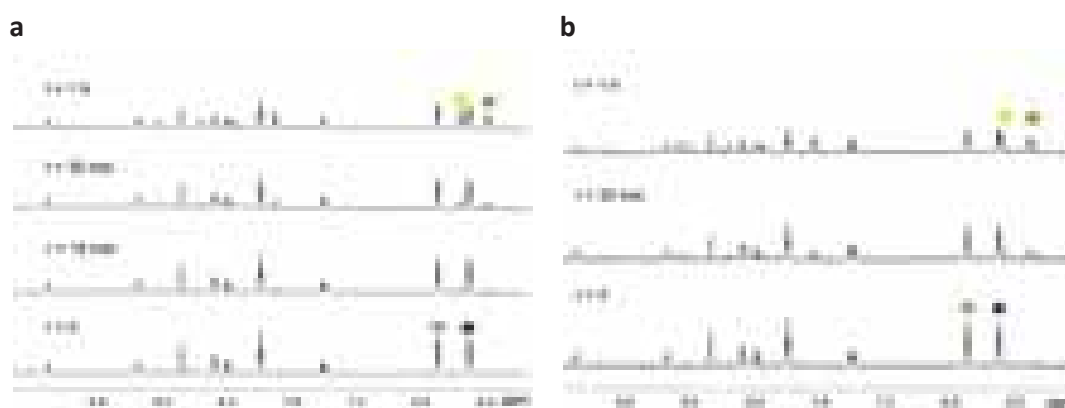


**Figure S24.** Photostability of 0.2 mM **4** in (a) MES (pH 6, 20 mM, 10% D<sub>2</sub>O, 3.3% dms<sub>o</sub>-d<sup>6</sup>) and (b) PB buffer (pH 7, 100 mM, 10% D<sub>2</sub>O, 3.3% dms<sub>o</sub>-d<sup>6</sup>). <sup>1</sup>H NMR control spectra were recorded upon 460-nm light irradiation (6 mW·cm<sup>-2</sup>) for 1 h. <sup>1</sup>H NMR signal labelling: ◆ and ◆ Ru-(p-cymene) of **4**, ◆ and ◆ Ru-(p-cymene) of the corresponding aqua complex.

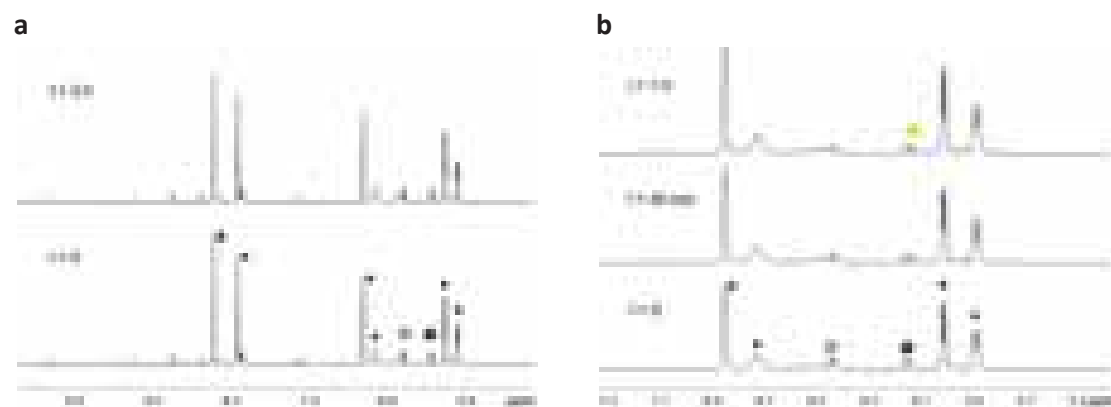


**Figure S25.** Stability in the dark (a) and under light irradiation (b) of **4** in the presence of 2 mM NADH (PB buffer pH 7, 100 mM, 10% D<sub>2</sub>O, 3.3% dms<sub>o</sub>-d<sup>6</sup>) monitored by <sup>1</sup>H NMR over time. Light source: 460 nm, 6 mW·cm<sup>-2</sup>. <sup>1</sup>H NMR signal labelling: ◆ and ◆ Ru-(p-cymene) of **4**, ◆ Ru-(p-cymene) of the corresponding aqua complex, ● NADH.

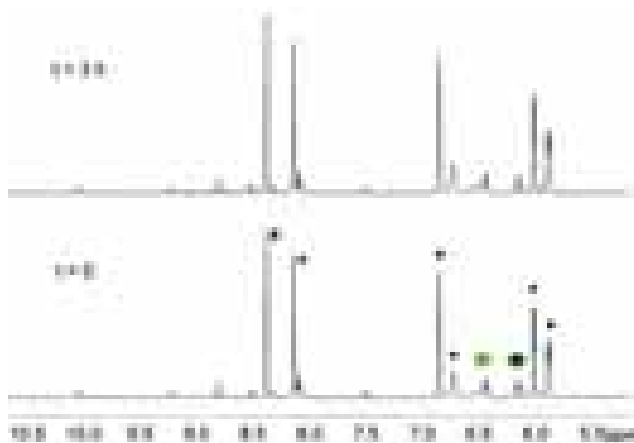


**Figure S26.**  $^1\text{H}$  NMR spectra showing the PB buffer (pH 7, 100 mM, 10%  $\text{D}_2\text{O}$ , 3.3%  $\text{dmsO-d}_6$ ) stability of **4** in the dark in the presence of NADH and FAD over 3 h. Spectra were recorded for solutions of 200  $\mu\text{M}$  **4** and 10  $\mu\text{M}$  FAD and 2 mM NADH.  $^1\text{H}$  NMR signal labelling:  $\blacklozenge$  and  $\blacklozenge$  Ru-(p-cymene) of **4**,  $\bullet$  NADH.

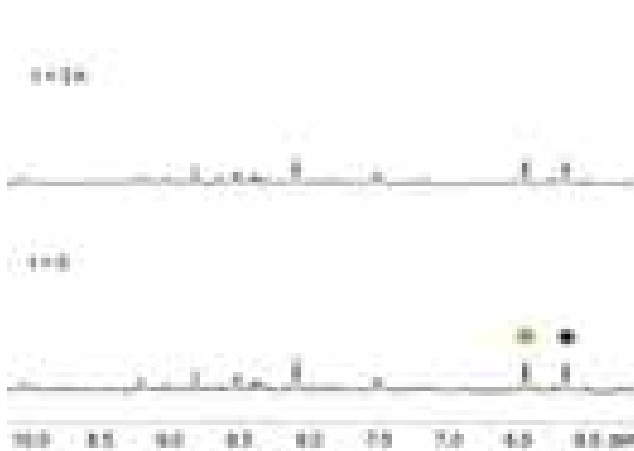


**Figure S27.** Dark stability of 0.2 mM **4** in MES (pH 6, 20 mM, 10%  $\text{D}_2\text{O}$ , 3.3%  $\text{dmsO-d}_6$ ) in the presence of 10  $\mu\text{M}$  FAD over 3 h.  $^1\text{H}$  NMR signal labelling:  $\blacklozenge$  and  $\blacklozenge$  Ru-(p-cymene) of **4**.

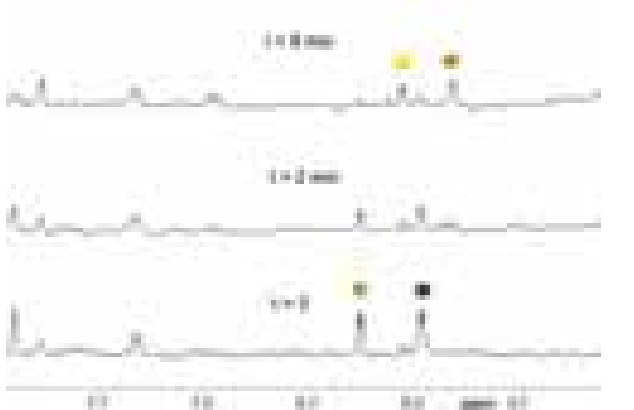


**Figure S28.** FAD-catalyzed photoreduction of **4** in MES buffer (20 mM, 10%  $\text{D}_2\text{O}$ , 3.3%  $\text{dmsO-d}_6$ ) monitored by  $^1\text{H}$  NMR. Spectra were recorded for MES (10%  $\text{D}_2\text{O}$ ) solutions of 200  $\mu\text{M}$  **4** and 10  $\mu\text{M}$  FAD upon  $t = 0$  min, 2 min, 6 min of 460-nm light irradiation ( $6 \text{ mW}\cdot\text{cm}^{-2}$ ).  $^1\text{H}$  NMR signal labelling:  $\blacklozenge$  and  $\blacklozenge$  Ru-(p-cymene) of **4**,  $\yellowlozenge$  and  $\brownlozenge$  Ru-(p-cymene) of the corresponding aqua complex.

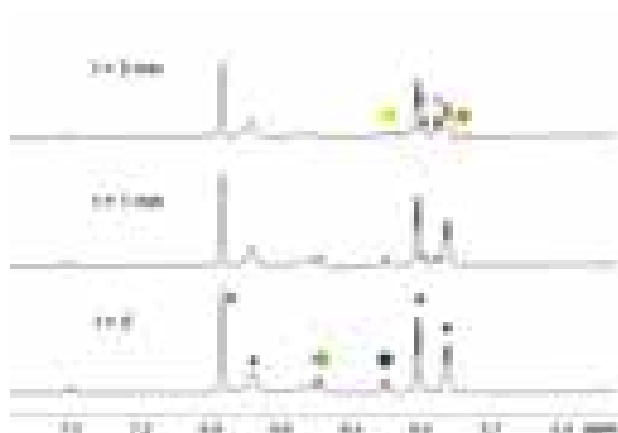


**Figure S29.** FAD-catalyzed photoreduction of **4** in PB buffer (pH 7, 100 mM, 10% D<sub>2</sub>O, 3.3% dms<sup>o</sup>-d<sup>6</sup>) in the presence of NADH (2 mM) monitored by <sup>1</sup>H NMR. Spectra were recorded for PB (10% D<sub>2</sub>O) solutions of 200 μM **4** and 10 μM FAD upon t = 0 sec, 1min and 3 min of 460-nm light irradiation (6 mW·cm<sup>-2</sup>). <sup>1</sup>H NMR signal labelling: ◆ and ◆ Ru-(p-cymene) of **4**, ◆ and ◆ Ru-(p-cymene) of the corresponding aqua complex, ● NADH, ● NAD<sup>+</sup>.

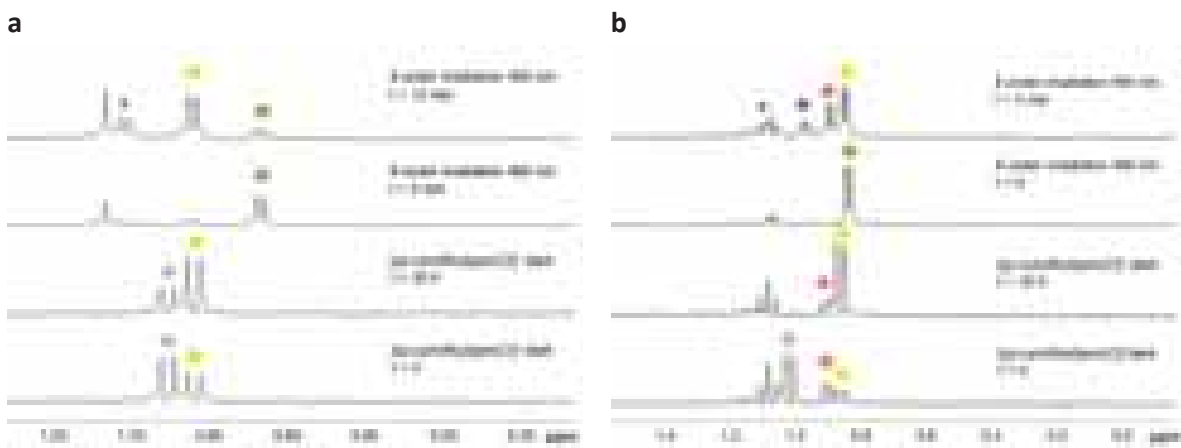


**Figure 30.** Speciation of **4** and  $[(\eta^6\text{-p-cym})\text{Ru}(\text{bpm})\text{Cl}][\text{PF}_6]$  in (a) MES (20 mM, 10% D<sub>2</sub>O, 3.3% dms<sup>o</sup>-d<sup>6</sup>) and (b) PB (pH 7, 100 mM, 10% D<sub>2</sub>O, 3.3% dms<sup>o</sup>-d<sup>6</sup>) with 2 mM NADH under different conditions. <sup>1</sup>H NMR spectra show the chemical shift range corresponding to the isopropyl group of the p-cymene ligand (methyl resonances). <sup>1</sup>H NMR signal labelling: ◆ **4**, ◆  $[(\eta^6\text{-p-cym})\text{Ru}(\text{bpm})\text{Cl}]^+$ , ◆  $[(\eta^6\text{-p-cym})\text{Ru}(\text{bpm})(\text{dmsO})]^{2+}$ , ◆  $[(\eta^6\text{-p-cym})\text{Ru}(\text{bpm})(\text{H}_2\text{O})]^{2+}$ , ◆  $[(\eta^6\text{-p-cym})\text{Ru}(\text{bpm})(\text{H}_2\text{O})]^{2+}$ -NADH adduct, \* not assigned.<sup>[1-2]</sup>



## Complex 5

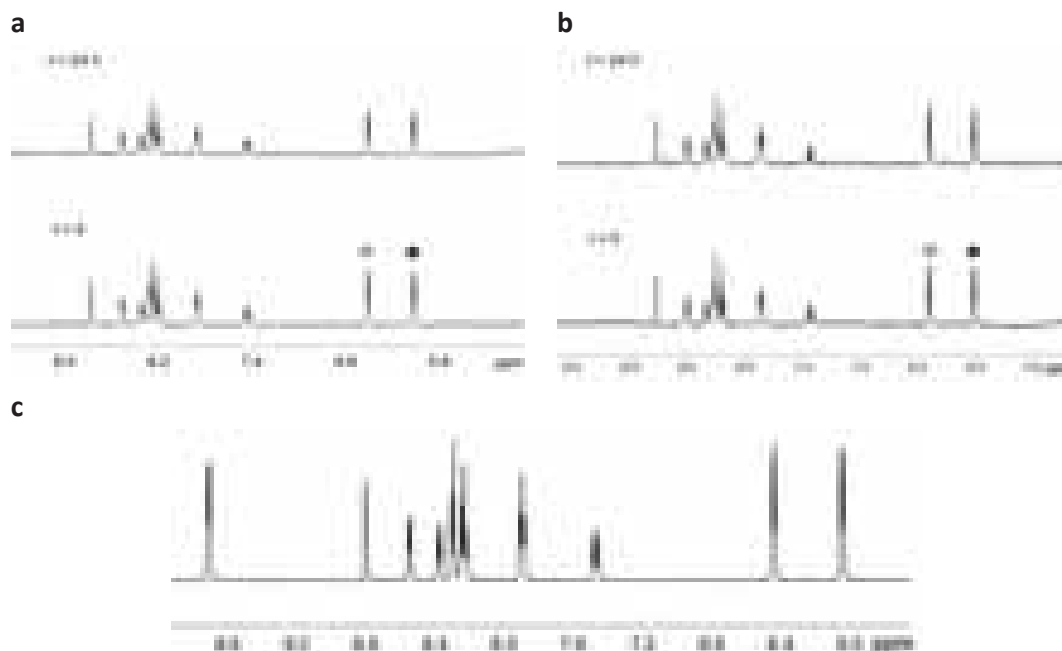


**Figure S31.** Dark stability of 0.2 mM **5** in (a) MES (pH 6, 20 mM, 10% D<sub>2</sub>O, 3.3% dmsO-d<sup>6</sup>) and (b) PB buffer (pH 7, 100 mM, 10% D<sub>2</sub>O, 3.3% dmsO-d<sup>6</sup>) over 24 h. <sup>1</sup>H NMR signal labelling: ◆ and ◆ Ru-(p-cymene). The <sup>1</sup>H NMR spectrum in (c) was recorded in pure D<sub>2</sub>O without using the 1D excitation sculpting sequence (zgpgw5, Bruker Avance III) for the suppression of the water signal and shows an extra doublet at 9.71 ppm due to the bpy H6/H6' protons. This signal does not appear in all the spectra recorded for **5** in buffers (90/10 H<sub>2</sub>O/D<sub>2</sub>O).

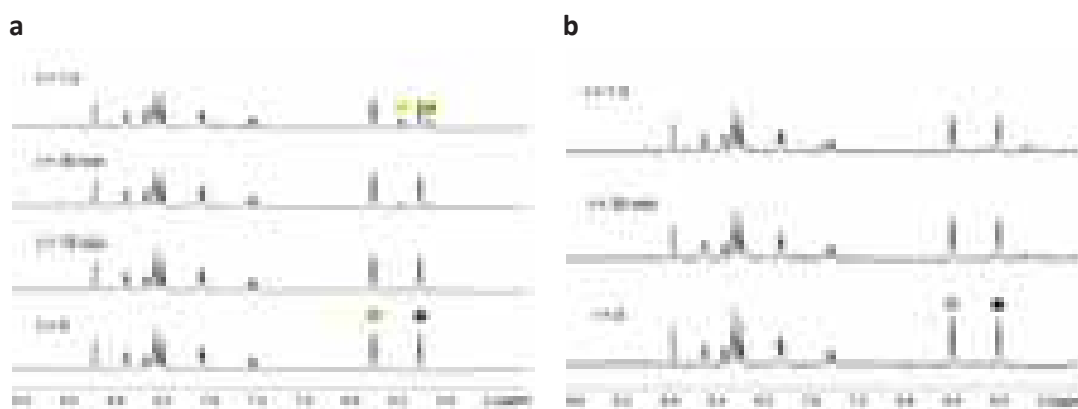


**Figure S32.** Photostability of 0.2 mM **5** in (a) MES (pH 6, 20 mM, 10% D<sub>2</sub>O, 3.3% dmsO-d<sup>6</sup>) and (b) PB buffer (pH 7, 100 mM, 10% D<sub>2</sub>O, 3.3% dmsO-d<sup>6</sup>). <sup>1</sup>H NMR control spectra were recorded upon 460-nm light irradiation (6 mW·cm<sup>-2</sup>) for 1 h. <sup>1</sup>H NMR signal labelling: ◆ and ◆ Ru-(p-cymene) of **5**, ◆ and ◆ Ru-(p-cymene) of the corresponding aqua complex.

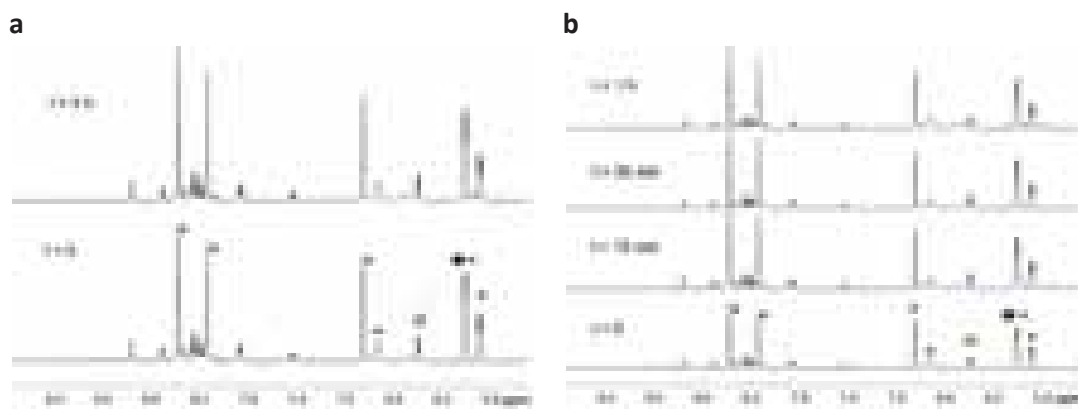


**Figure S33.** Stability in the dark (a) and under light irradiation (b) of **5** in the presence of 2 mM NADH (PB buffer pH 7, 100 mM, 10% D<sub>2</sub>O, 3.3% dms<sup>o</sup>-d<sup>6</sup>) monitored by <sup>1</sup>H NMR. Light source: 460 nm, 6 mW·cm<sup>-2</sup>. <sup>1</sup>H NMR signal labelling: ◆ and ◆ Ru-(p-cymene) of **5**, ● NADH.

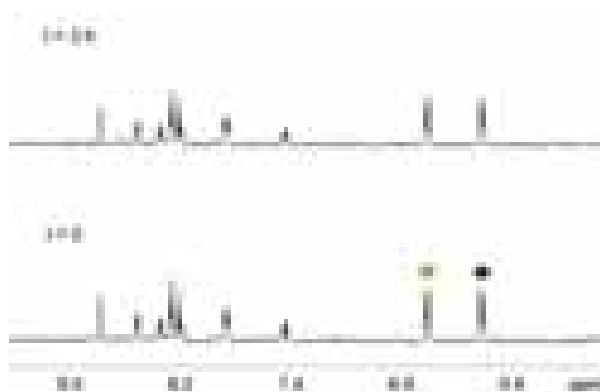


**Figure S34.** Dark stability of 0.2 mM **5** in MES (pH 6, 20 mM, 10% D<sub>2</sub>O, 3.3% dms<sup>o</sup>-d<sup>6</sup>) in the presence of 10 μM FAD over 3 h. <sup>1</sup>H NMR signal labelling: ◆ and ◆ Ru-(p-cymene) of **5**.

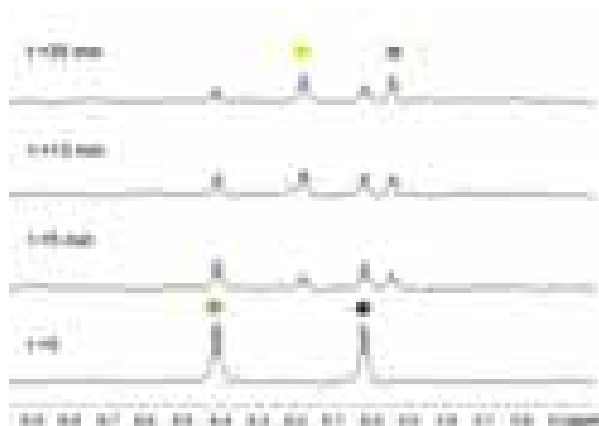


**Figure S35.** FAD-catalyzed photoreduction of **5** in MES buffer (20 mM) monitored by <sup>1</sup>H NMR. Spectra were recorded for MES (10% D<sub>2</sub>O, 3.3% dms<sup>o</sup>-d<sup>6</sup>) solutions of 200 μM **5** and 10 μM FAD upon t = 0 sec, 5 min, 13 min and 35 min of 460-nm light irradiation (6 mW·cm<sup>-2</sup>). <sup>1</sup>H NMR signal labelling: ◆ and ◆ Ru-(p-cymene) of **5**, ◆ and ◆ Ru-(p-cymene) of the corresponding aqua complex.

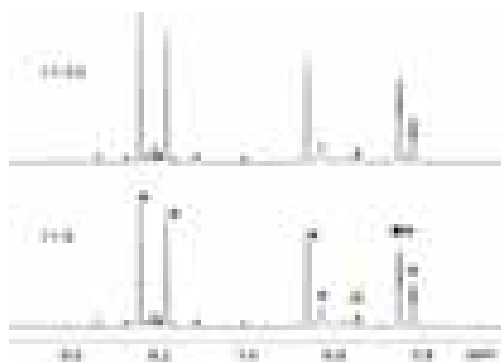


**Figure S36.**  $^1\text{H}$  NMR spectra showing the PB buffer (pH 7, 100 mM, 10%  $\text{D}_2\text{O}$ , 3.3%  $\text{dmsO-d}^6$ ) stability of **5** in the dark in the presence of NADH and FAD over 3 h. Spectra were recorded for solutions of 200  $\mu\text{M}$  **5** and 10  $\mu\text{M}$  FAD and 2 mM NADH.  $^1\text{H}$  NMR signal labelling:  $\blacklozenge$  and  $\blacklozenge$  Ru-(p-cymene) of **5**,  $\bullet$  NADH.



**Figure S37.** FAD-catalyzed photoreduction of **5** in PB buffer (pH 7, 100 mM) in the presence of NADH (2 mM) monitored by  $^1\text{H}$  NMR. Spectra were recorded for PB (10%  $\text{D}_2\text{O}$ , 3.3%  $\text{dmsO-d}^6$ ) solutions of 200  $\mu\text{M}$  **5** and 10  $\mu\text{M}$  FAD upon  $t = 0, 15, 25$  and 85 min of 460-nm light irradiation ( $6 \text{ mW}\cdot\text{cm}^{-2}$ ).  $^1\text{H}$  NMR signal labelling:  $\blacklozenge$  and  $\blacklozenge$  Ru-(p-cymene) of **5**,  $\yellowlozenge$  and  $\brownlozenge$  Ru-(p-cymene) of the corresponding aqua complex,  $\bullet$  NADH,  $\bullet$   $\text{NAD}^+$ .

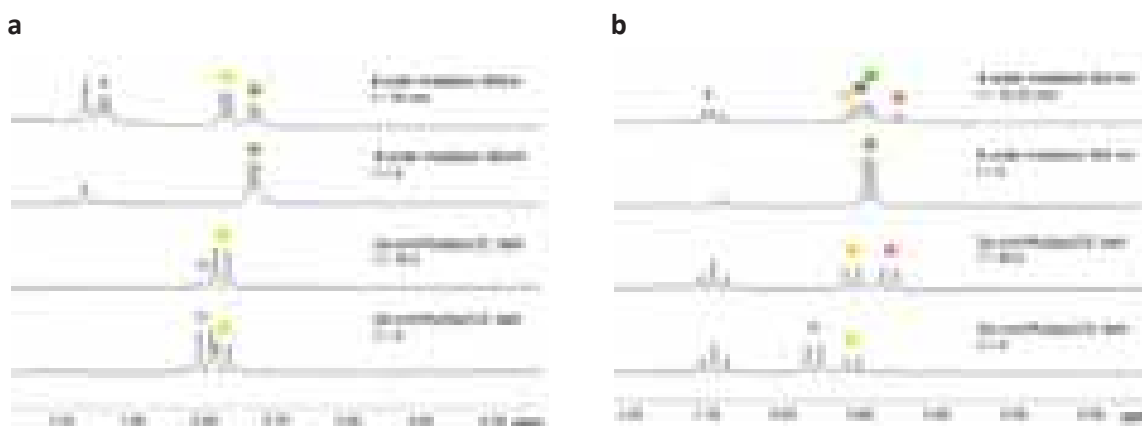


**Figure 38.** Speciation of **5** and  $[(\eta^6\text{-p-cym})\text{Ru}(\text{bpy})\text{Cl}][\text{PF}_6]$  in (a) MES (20 mM, 10%  $\text{D}_2\text{O}$ , 3.3%  $\text{dmsO-d}^6$ ) and (b) PB (pH 7, 100 mM, 10%  $\text{D}_2\text{O}$ , 3.3%  $\text{dmsO-d}^6$ ) with 2 mM NADH under different conditions.  $^1\text{H}$  NMR spectra show the chemical shift range corresponding to the isopropyl group of the p-cymene ligand (methyl resonances).  $^1\text{H}$  NMR signal labelling:  $\blacklozenge$  **5**,  $\brownlozenge$   $[(\eta^6\text{-p-cym})\text{Ru}(\text{bpy})\text{Cl}]^+$ ,  $\redlozenge$   $[(\eta^6\text{-p-cym})\text{Ru}(\text{bpy})(\text{dmsO})]^{2+}$ ,  $\yellowlozenge$   $[(\eta^6\text{-p-cym})\text{Ru}(\text{bpy})(\text{H}_2\text{O})]^{2+}$ ,  $\blue.lozenge$   $[(\eta^6\text{-p-cym})\text{Ru}(\text{bpy})(\text{H}_2\text{O})]^{2+}$ -NADH adduct, \* not assigned.<sup>[1-2]</sup>

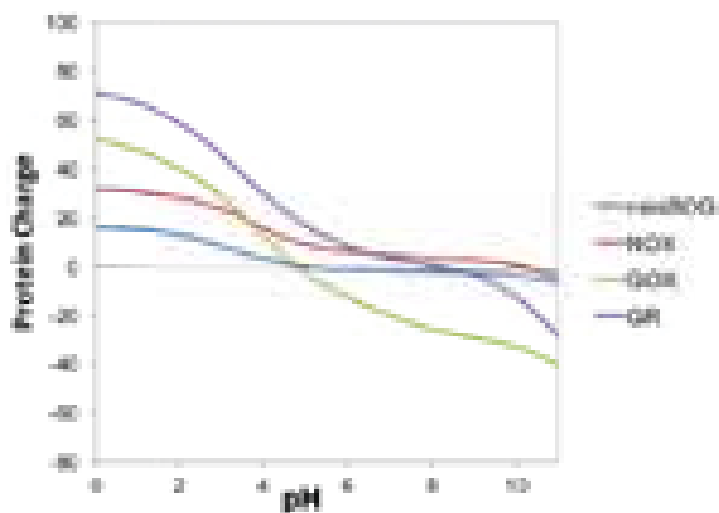


**Figure S39.** Net charge of miniSOG, NOX, GOX and GR at different pH. The values plotted in this map were calculated with Blues server.<sup>[3]</sup>

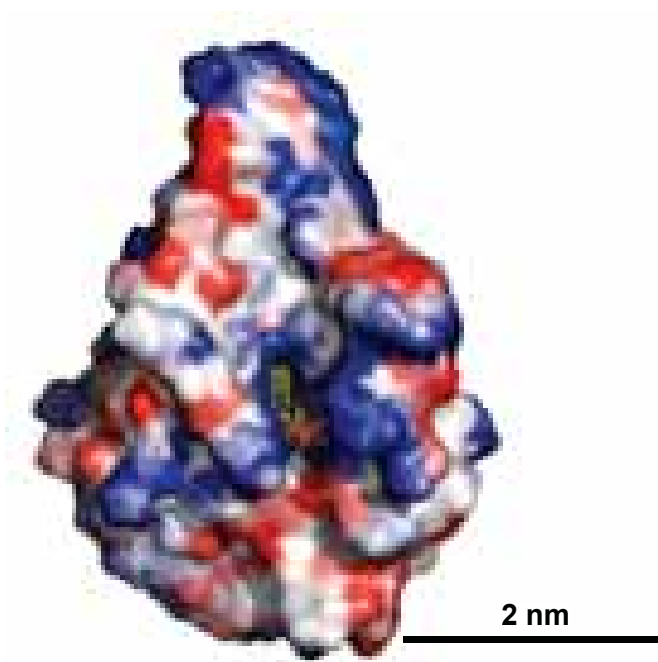


**Figure S40.** Electrostatic surface potential of miniSOG. The figure was created using pymol 0.99 (DeLano, USA) using a miniSOG molecular model based on the PDB ID: 4EET. The electrostatic potential was calculated using Blues server.<sup>[3]</sup> Color code: blue = positive and red = negative.

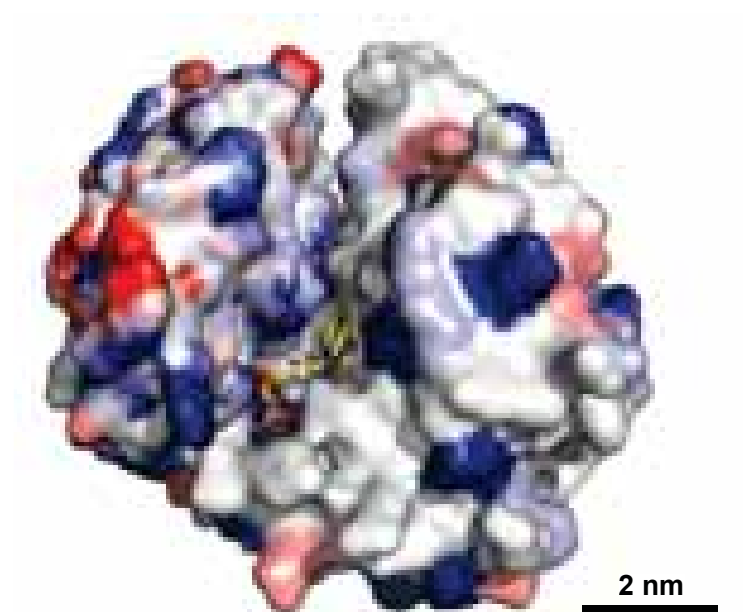


**Figure S41.** Electrostatic surface potential of NOX. The figure was created using pymol 0.99 (DeLano, USA) using the PDB ID 1NOX. The electrostatic potential was calculated using Blues server.<sup>[3]</sup> Color code: blue = positive and red = negative.

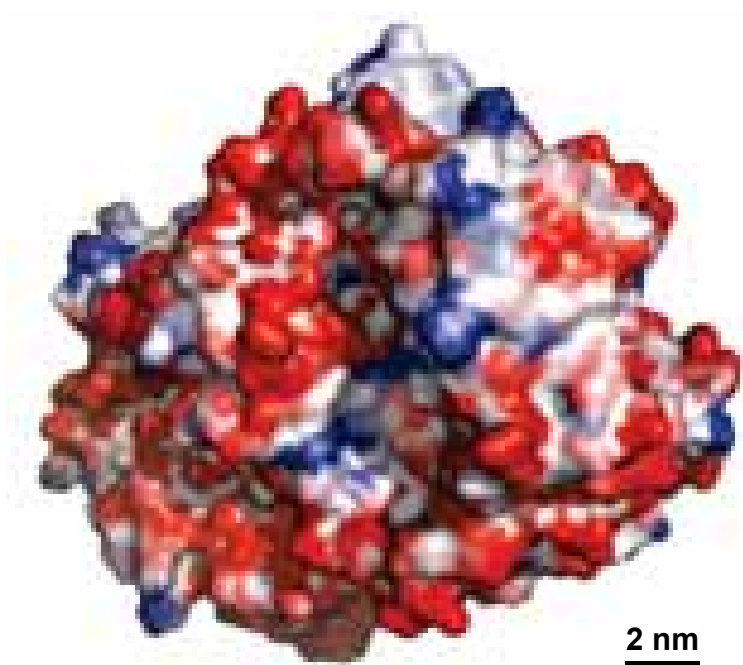


**Figure S42.** Electrostatic surface potential of GOX. The figure was created using pymol 0.99 (DeLano, USA) using the PDB ID 1CF3. The electrostatic potential was calculated using Blues server.<sup>[3]</sup> Color code: blue = positive and red = negative.

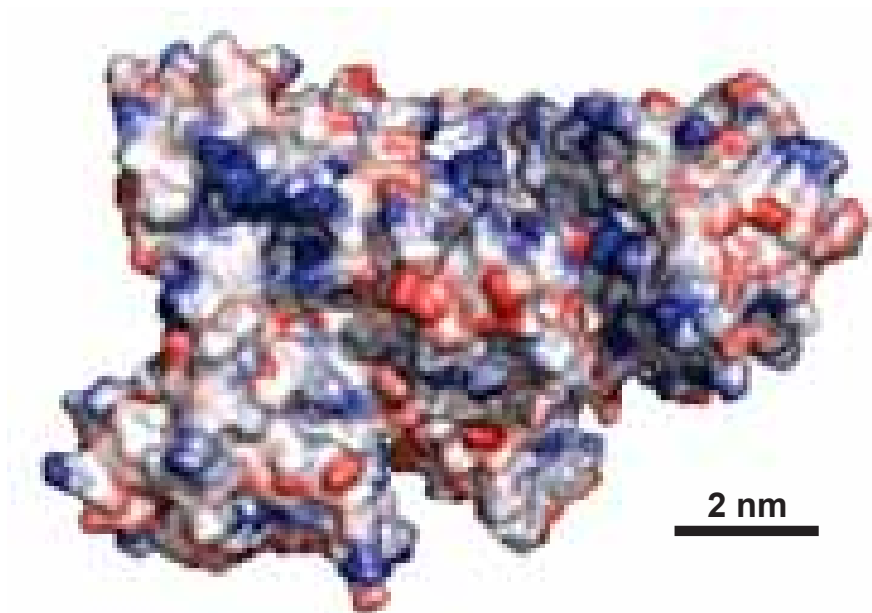


**Figure S43.** Electrostatic surface potential of GR. The figure was created using pymol 0.99 (DeLano, USA) using the PDB ID 2HQM. The electrostatic potential was calculated using Blues server.<sup>[3]</sup> Color code: blue = positive and red = negative.

## GOX

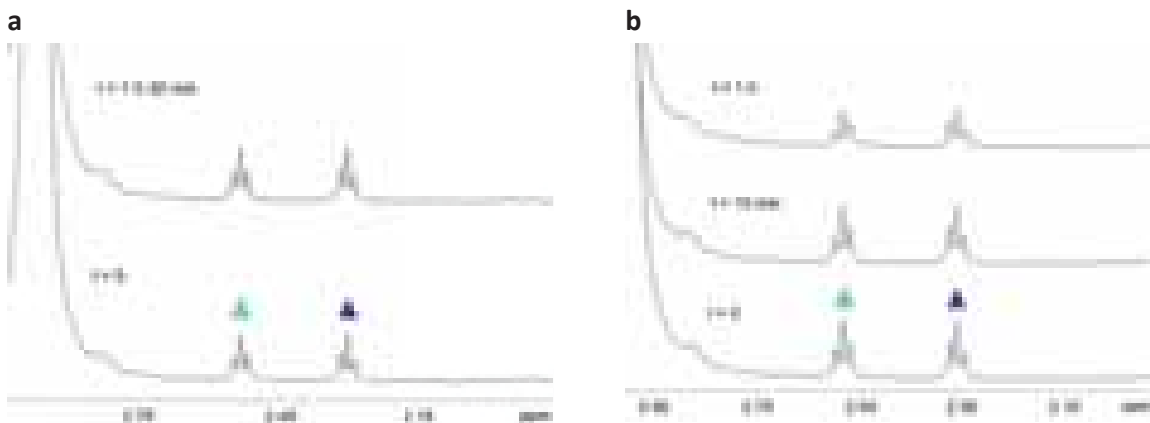


**Figure S44.** Stability in the dark (**a**) and under light irradiation (**b**) of 0.2 mM **1** in MES (pH 6, 20 mM, 10% D<sub>2</sub>O) and in the presence of 10 μM GOX over time. <sup>1</sup>H NMR signal labelling: ▲ Pt-OCOCH<sub>2</sub>CH<sub>2</sub>CO<sub>2</sub><sup>-</sup>, ▲ Pt-OCOCH<sub>2</sub>CH<sub>2</sub>CO<sub>2</sub><sup>-</sup>.

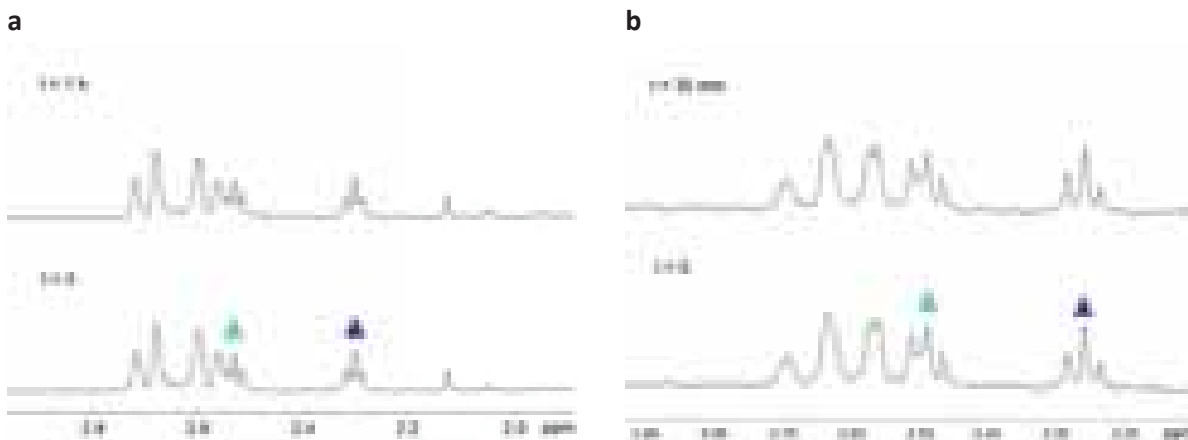


**Figure S45.** Stability in the dark (**a**) and under light irradiation (**b**) of 0.2 mM **1** in PB buffer (pH 7, 100 mM, 10% D<sub>2</sub>O) in the presence of 2 mM NADH and 10 μM GOX over time. <sup>1</sup>H NMR signal labelling: ▲ Pt-OCOCH<sub>2</sub>CH<sub>2</sub>CO<sub>2</sub><sup>-</sup>, ▲ Pt-OCOCH<sub>2</sub>CH<sub>2</sub>CO<sub>2</sub><sup>-</sup>.

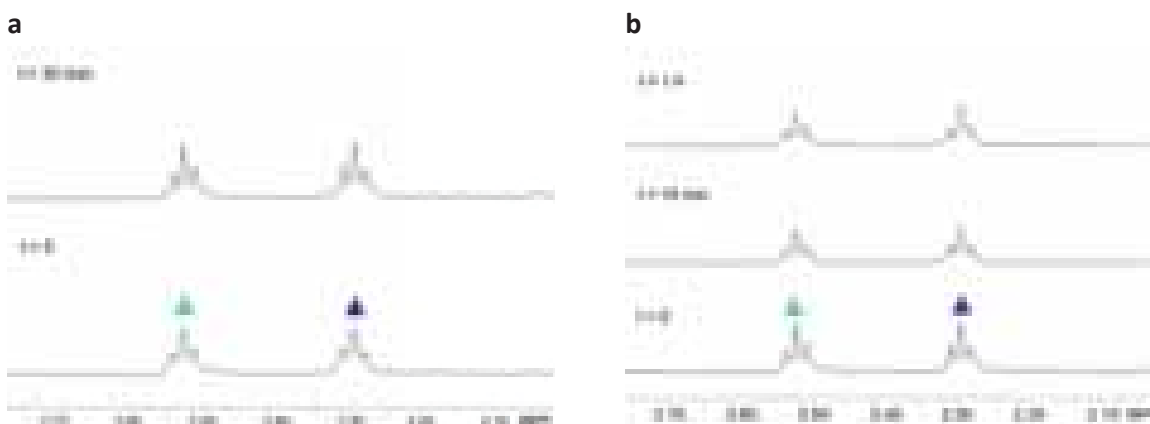


**Figure S46.** Stability in the dark (**a**) and under light irradiation (**b**) of 0.2 mM **1** in PB buffer (pH 7, 100 mM, 10% D<sub>2</sub>O) in the presence of 20 mM glucose and 10 μM GOX over time. <sup>1</sup>H NMR signal labelling: ▲ Pt-OCOCH<sub>2</sub>CH<sub>2</sub>CO<sub>2</sub><sup>-</sup>, ▲ Pt-OCOCH<sub>2</sub>CH<sub>2</sub>CO<sub>2</sub><sup>-</sup>.

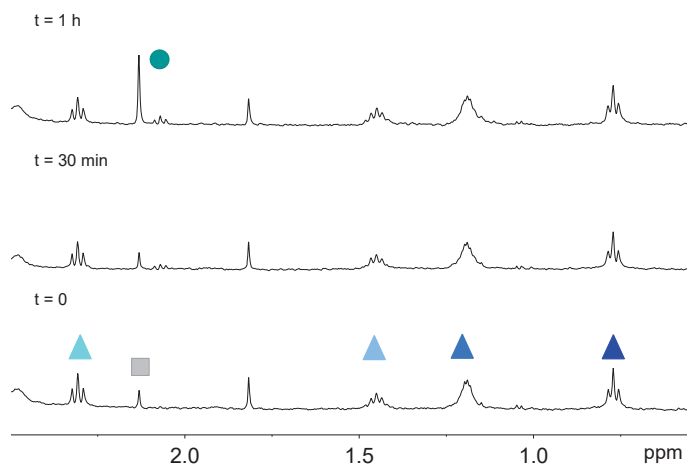


**Figure S47.** GOX-catalyzed photoreduction of **2** in MES buffer (pH 6, 20 mM) monitored by  $^1\text{H}$  NMR. Spectra were recorded for MES (10%  $\text{D}_2\text{O}$ , 1% dms $o$ - $d_6$ ) solutions of 200  $\mu\text{M}$  **2** and 10  $\mu\text{M}$  GOX upon  $t = 0, 30 \text{ min}$  and 1 h of 460-nm light irradiation ( $6 \text{ mW}\cdot\text{cm}^{-2}$ ).  $^1\text{H}$  NMR signal labelling:  $\blacktriangle$  Pt-OCOCH $_2$ CH $_2$ CH $_2$ CH $_2$ CH $_2$ CH $_3$ ,  $\blacktriangle$  Pt-OCOCH $_2$ CH $_2$ CH $_2$ CH $_2$ CH $_2$ CH $_3$ ,  $\blacktriangle$  Pt-OCOCH $_2$ CH $_2$ CH $_2$ CH $_2$ CH $_2$ CH $_3$ ,  $\blacktriangle$  Pt-OCOCH $_2$ CH $_2$ CH $_2$ CH $_2$ CH $_2$ CH $_3$ ,  $\bullet$  free  $^-$ OCOCH $_2$ CH $_2$ CH $_2$ CH $_2$ CH $_2$ CH $_3$ ,  $\blacksquare$  acetone impurity.

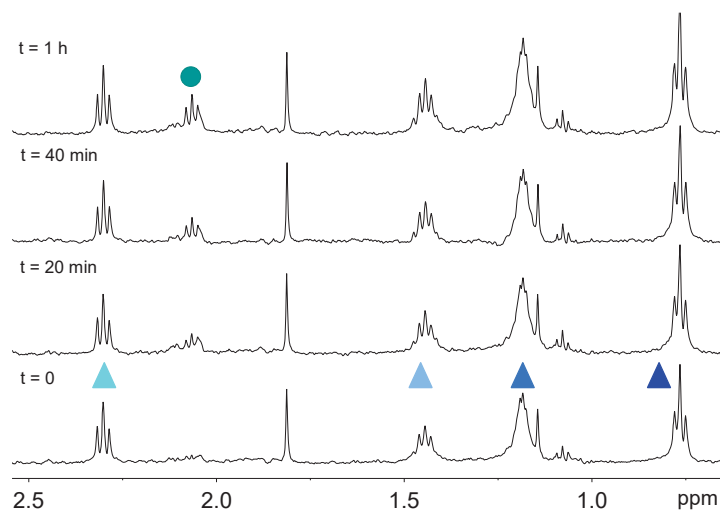


**Figure S48.** GOX-catalyzed photoreduction of **2** in PB buffer (pH 7, 100 mM) in the presence of NADH (2 mM) monitored by  $^1\text{H}$  NMR. Spectra were recorded for PB (10%  $\text{D}_2\text{O}$ , 1% dms $o$ - $d_6$ ) solutions of 200  $\mu\text{M}$  **2** and 10  $\mu\text{M}$  GOX upon  $t = 0, 20 \text{ min}, 40 \text{ min}$  and 1 h of 460-nm light irradiation ( $6 \text{ mW}\cdot\text{cm}^{-2}$ ).  $^1\text{H}$  NMR signal labelling:  $\blacktriangle$  Pt-OCOCH $_2$ CH $_2$ CH $_2$ CH $_2$ CH $_2$ CH $_3$ ,  $\blacktriangle$  Pt-OCOCH $_2$ CH $_2$ CH $_2$ CH $_2$ CH $_2$ CH $_3$ ,  $\blacktriangle$  Pt-OCOCH $_2$ CH $_2$ CH $_2$ CH $_2$ CH $_2$ CH $_3$ ,  $\blacktriangle$  Pt-OCOCH $_2$ CH $_2$ CH $_2$ CH $_2$ CH $_2$ CH $_3$ ,  $\bullet$  free  $^-$ OCOCH $_2$ CH $_2$ CH $_2$ CH $_2$ CH $_2$ CH $_3$ .



## miniSOG

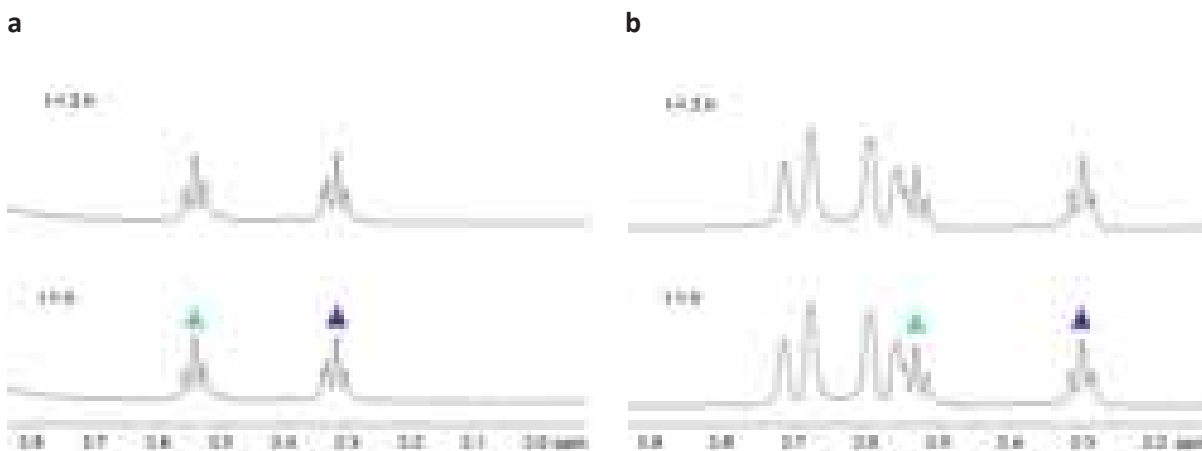


**Figure S49.** Dark stability of **1** in the presence of FMN in (a) MES buffer (pH 7, 20 mM, 10% D<sub>2</sub>O) and (b) PB buffer (pH 7, 100 mM, 10% D<sub>2</sub>O) over 2 h. NMR spectra were recorded for solutions of 200 μM **1** and 10 μM FMN and 2 mM NADH in the case of PB (b). <sup>1</sup>H NMR signal labelling: ▲ Pt-OCOCH<sub>2</sub>CH<sub>2</sub>CO<sub>2</sub><sup>-</sup>, ▲ Pt-OCOCH<sub>2</sub>CH<sub>2</sub>CO<sub>2</sub><sup>-</sup>.

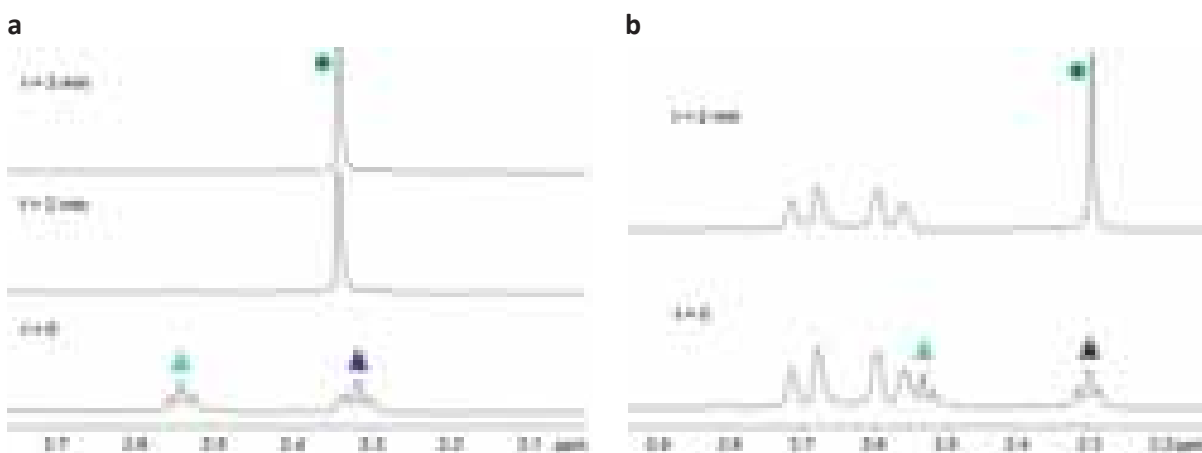


**Figure S50.** FMN-catalyzed photoreduction of **1** in (a) MES buffer (20 mM) and (b) PB buffer (pH 7, 100 mM) in the presence of NADH (2 mM). NMR spectra were recorded for solutions of 200 μM **1** and 10 μM FMN upon 460-nm light irradiation (6 mW·cm<sup>-2</sup>). <sup>1</sup>H NMR signal labelling: ▲ Pt-OCOCH<sub>2</sub>CH<sub>2</sub>CO<sub>2</sub><sup>-</sup>, ▲ Pt-OCOCH<sub>2</sub>CH<sub>2</sub>CO<sub>2</sub><sup>-</sup>, ● free <sup>-</sup>O<sub>2</sub>CCH<sub>2</sub>CH<sub>2</sub>CO<sub>2</sub><sup>-</sup>. The TOF of free FMN towards **1** was determined to be 3.9 ± 0.5 and 35.6 ± 4.3 min<sup>-1</sup> in MES and PB/NADH respectively.

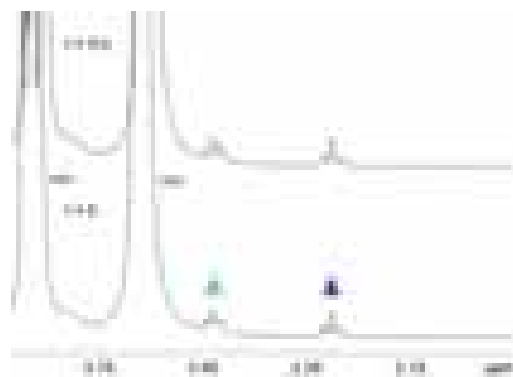


**Figure S51.** Dark stability of 0.2 mM **1** in MES (pH 6, 20 mM, 10% D<sub>2</sub>O) in the presence of 10 μM miniSOG over 3 h. <sup>1</sup>H NMR signal labelling: ▲ Pt-OCOCH<sub>2</sub>CH<sub>2</sub>CO<sub>2</sub><sup>-</sup>, ▲ Pt-OCOCH<sub>2</sub>CH<sub>2</sub>CO<sub>2</sub><sup>-</sup>.

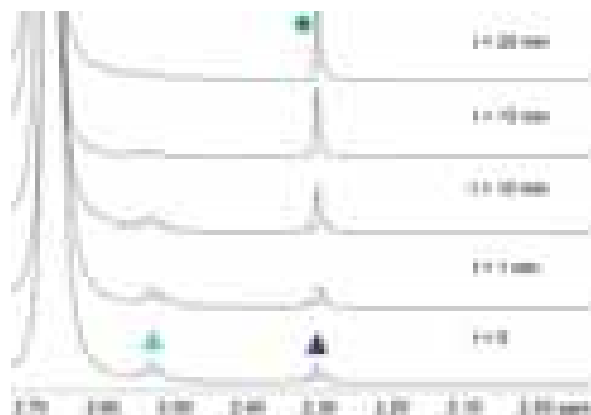


**Figure S52.** MiniSOG-catalyzed photoreduction of **1** in MES buffer (pH = 6, 20 mM). <sup>1</sup>H NMR spectra were recorded for MES (10% D<sub>2</sub>O) solutions of 200 μM **1** and 10 μM miniSOG upon t = 0, 1, 10, 15 and 20 min of 460-nm light irradiation (6 mW·cm<sup>-2</sup>). <sup>1</sup>H NMR signal labelling: ▲ Pt-OCOCH<sub>2</sub>CH<sub>2</sub>CO<sub>2</sub><sup>-</sup>, ▲ Pt-OCOCH<sub>2</sub>CH<sub>2</sub>CO<sub>2</sub><sup>-</sup>, ● free <sup>-</sup>O<sub>2</sub>CCH<sub>2</sub>CH<sub>2</sub>CO<sub>2</sub><sup>-</sup>.

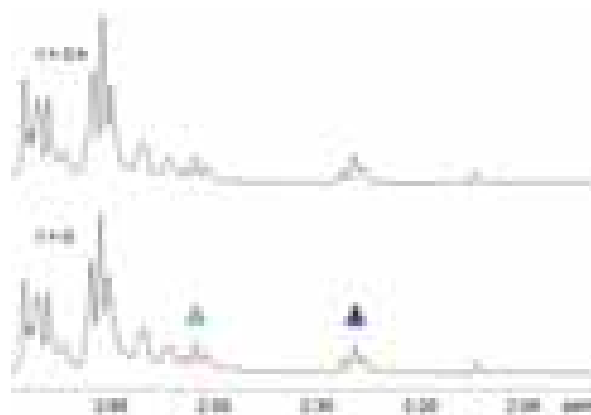


**Figure S53.** PB buffer (pH 7, 100 mM) stability of **1** in the dark and in the presence of NADH (2 mM). <sup>1</sup>H NMR spectra were recorded for PB (10% D<sub>2</sub>O) solutions of 200 μM **1** and 10 μM miniSOG. <sup>1</sup>H NMR signal labelling: ▲ Pt-OCOCH<sub>2</sub>CH<sub>2</sub>CO<sub>2</sub><sup>-</sup>, ▲ Pt-OCOCH<sub>2</sub>CH<sub>2</sub>CO<sub>2</sub><sup>-</sup>, ● free <sup>-</sup>O<sub>2</sub>CCH<sub>2</sub>CH<sub>2</sub>CO<sub>2</sub><sup>-</sup>. Signals above 2.65 correspond residual MES present in the protein stock solution.

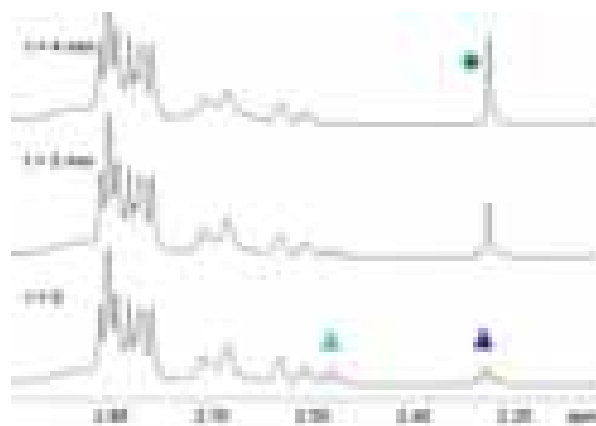


**Figure S54.** MiniSOG-catalyzed photoreduction of **1** in PB buffer (pH 7, 100 mM) and in the presence of NADH (2 mM).  $^1\text{H}$  NMR spectra were recorded for PB (10%  $\text{D}_2\text{O}$ ) solutions of 200  $\mu\text{M}$  **1** and 10  $\mu\text{M}$  miniSOG.  $^1\text{H}$  NMR signal labelling:  $\blacktriangle$   $\text{Pt-OCOCH}_2\text{CH}_2\text{CO}_2^-$ ,  $\blacktriangle$   $\text{Pt-OCOCH}_2\text{CH}_2\text{CO}_2^-$ ,  $\bullet$  free  $^- \text{O}_2\text{CCH}_2\text{CH}_2\text{CO}_2^-$ . Signals above 2.65 correspond residual MES present in the protein stock solution.

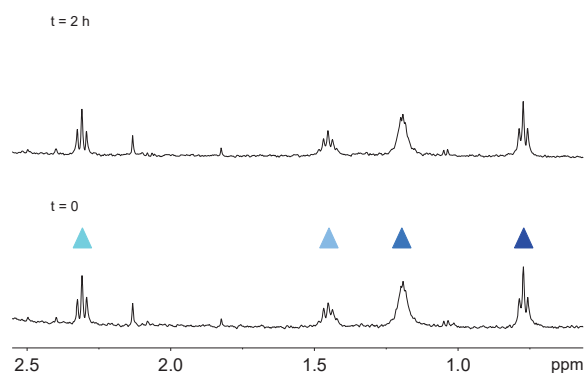


**Figure S55.** Dark stability of 0.2 mM **2** in MES (pH 6, 20 mM, 10%  $\text{D}_2\text{O}$ , 1%  $\text{dmsO-d}_6$ ) in the presence of 10  $\mu\text{M}$  FMN over 2 h.  $^1\text{H}$  NMR signal labelling:  $\blacktriangle$   $\text{Pt-OCOCH}_2\text{CH}_2\text{CH}_2\text{CH}_2\text{CH}_3$ ,  $\blacktriangle$   $\text{Pt-OCOCH}_2\text{CH}_2\text{CH}_2\text{CH}_2\text{CH}_3$ ,  $\blacktriangle$   $\text{Pt-OCOCH}_2\text{CH}_2\text{CH}_2\text{CH}_2\text{CH}_3$ ,  $\blacktriangle$   $\text{Pt-OCOCH}_2\text{CH}_2\text{CH}_2\text{CH}_2\text{CH}_3$ .

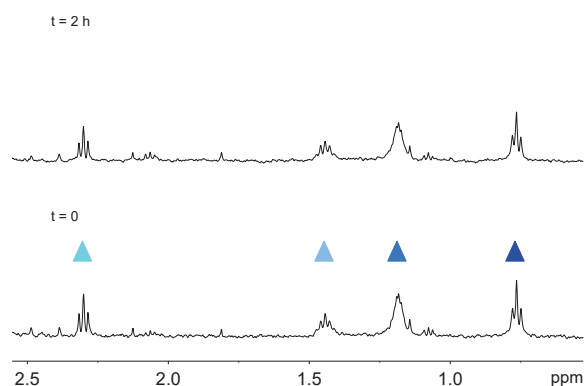


**Figure S56.** Dark stability of **2** in the dark and in PB buffer (pH 7, 100 mM) in the presence of NADH (2 mM) and FMN monitored by  $^1\text{H}$  NMR. Spectra were recorded for PB (10%  $\text{D}_2\text{O}$ , 1%  $\text{dmsO-d}_6$ ) solutions of 200  $\mu\text{M}$  **2** and 10  $\mu\text{M}$  FMN.  $^1\text{H}$  NMR signal labelling:  $\blacktriangle$   $\text{Pt-OCOCH}_2\text{CH}_2\text{CH}_2\text{CH}_2\text{CH}_3$ ,  $\blacktriangle$   $\text{Pt-OCOCH}_2\text{CH}_2\text{CH}_2\text{CH}_2\text{CH}_3$ ,  $\blacktriangle$   $\text{Pt-OCOCH}_2\text{CH}_2\text{CH}_2\text{CH}_2\text{CH}_3$ ,  $\blacktriangle$   $\text{Pt-OCOCH}_2\text{CH}_2\text{CH}_2\text{CH}_2\text{CH}_3$ .

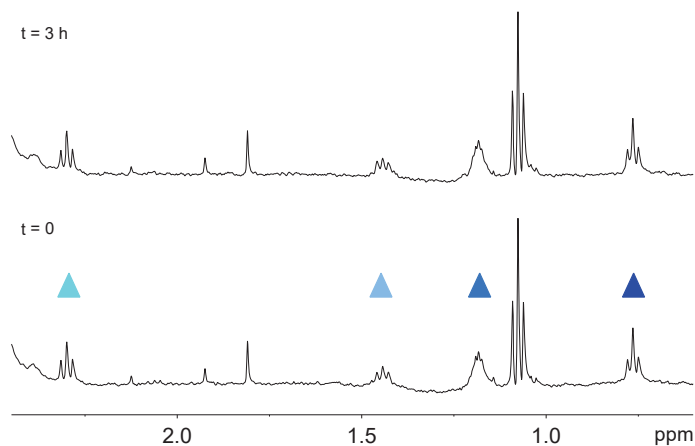


**Figure S57.** Dark stability of 0.2 mM **2** in MES (pH 6, 20 mM, 10% D<sub>2</sub>O, 1% dms<sub>o</sub>-d<sub>6</sub>) in the presence of 3 μM miniSOG over 3 h. <sup>1</sup>H NMR signal labelling: ▲ Pt-OCOCH<sub>2</sub>CH<sub>2</sub>CH<sub>2</sub>CH<sub>2</sub>CH<sub>3</sub>, ▲ Pt-OCOCH<sub>2</sub>CH<sub>2</sub>CH<sub>2</sub>CH<sub>2</sub>CH<sub>3</sub>, ▲ Pt-OCOCH<sub>2</sub>CH<sub>2</sub>CH<sub>2</sub>CH<sub>2</sub>CH<sub>3</sub>, ▲ Pt-OCOCH<sub>2</sub>CH<sub>2</sub>CH<sub>2</sub>CH<sub>2</sub>CH<sub>3</sub>.

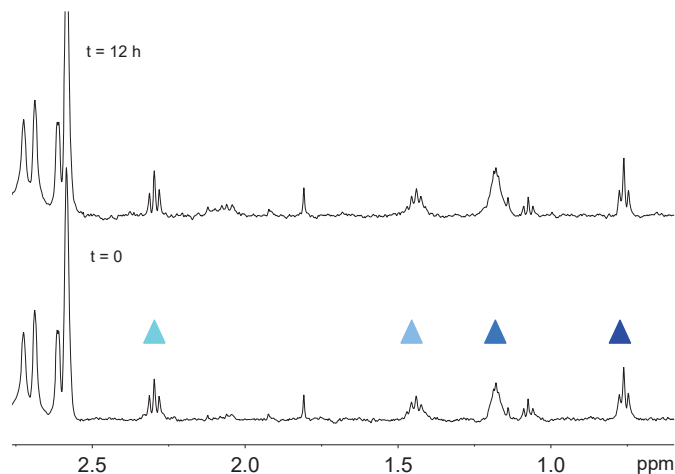


**Figure S58.** Dark stability of **2** in the dark and in PB buffer (pH 7, 100 mM) in the presence of NADH (2 mM) and miniSOG monitored by <sup>1</sup>H NMR. Spectra were recorded for PB (10% D<sub>2</sub>O, 1% dms<sub>o</sub>-d<sub>6</sub>) solutions of 200 μM **2** and 3 μM miniSOG. <sup>1</sup>H NMR signal labelling: ▲ Pt-OCOCH<sub>2</sub>CH<sub>2</sub>CH<sub>2</sub>CH<sub>2</sub>CH<sub>3</sub>, ▲ Pt-OCOCH<sub>2</sub>CH<sub>2</sub>CH<sub>2</sub>CH<sub>2</sub>CH<sub>3</sub>, ▲ Pt-OCOCH<sub>2</sub>CH<sub>2</sub>CH<sub>2</sub>CH<sub>2</sub>CH<sub>3</sub>, ▲ Pt-OCOCH<sub>2</sub>CH<sub>2</sub>CH<sub>2</sub>CH<sub>2</sub>CH<sub>3</sub>.

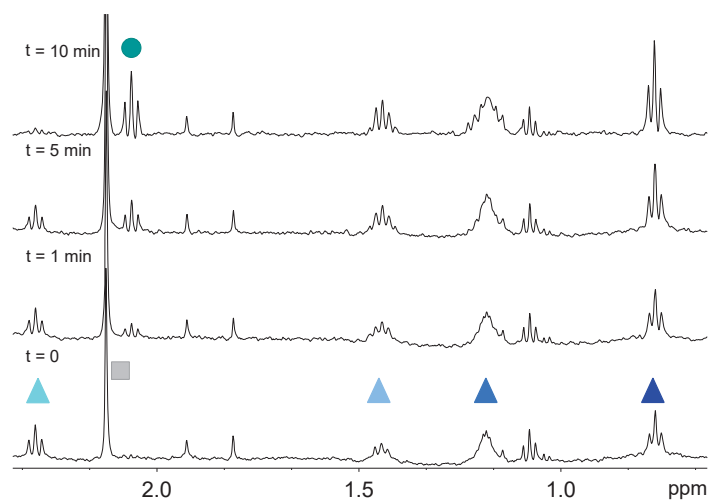


**Figure S59.** MiniSOG-catalyzed photoreduction of **2** in MES buffer (pH 6, 20 mM) monitored by  $^1\text{H}$  NMR. Spectra were recorded for MES (10%  $\text{D}_2\text{O}$ , 1%  $\text{dms}\text{-d}_6$ ) solutions of 200  $\mu\text{M}$  **2** and 10  $\mu\text{M}$  miniSOG upon  $t = 0, 1 \text{ min}, 5 \text{ min}$  and 10 min of 460-nm light irradiation ( $6 \text{ mW}\cdot\text{cm}^{-2}$ ).  $^1\text{H}$  NMR signal labelling:  $\blacktriangle$   $\text{Pt-OCOCH}_2\text{CH}_2\text{CH}_2\text{CH}_2\text{CH}_3$ ,  $\blacktriangle$   $\text{Pt-OCOCH}_2\text{CH}_2\text{CH}_2\text{CH}_2\text{CH}_3$ ,  $\blacktriangle$   $\text{Pt-OCOCH}_2\text{CH}_2\text{CH}_2\text{CH}_2\text{CH}_3$ ,  $\blacktriangle$   $\text{Pt-OCOCH}_2\text{CH}_2\text{CH}_2\text{CH}_2\text{CH}_3$ ,  $\bullet$  free  $^-\text{OCOCH}_2\text{CH}_2\text{CH}_2\text{CH}_2\text{CH}_3$ ,  $\blacksquare$  acetone impurity.

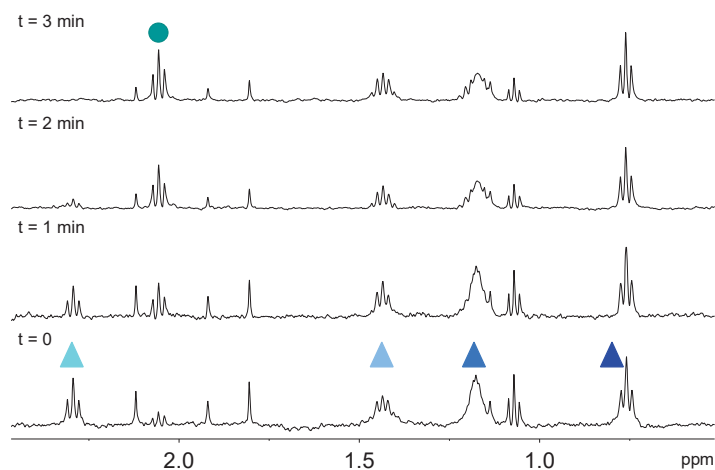


**Figure S60.** MiniSOG-catalyzed photoreduction of **2** in PB buffer (pH 7, 100 mM) in the presence of NADH (2 mM) monitored by  $^1\text{H}$  NMR. Spectra were recorded for PB (10%  $\text{D}_2\text{O}$ , 1%  $\text{dms}\text{-d}_6$ ) solutions of 200  $\mu\text{M}$  **2** and 10  $\mu\text{M}$  miniSOG upon  $t = 0, 1 \text{ min}, 2 \text{ min}$  and 3 min of 460-nm light irradiation ( $6 \text{ mW}\cdot\text{cm}^{-2}$ ).  $^1\text{H}$  NMR signal labelling:  $\blacktriangle$   $\text{Pt-OCOCH}_2\text{CH}_2\text{CH}_2\text{CH}_2\text{CH}_3$ ,  $\blacktriangle$   $\text{Pt-OCOCH}_2\text{CH}_2\text{CH}_2\text{CH}_2\text{CH}_3$ ,  $\blacktriangle$   $\text{Pt-OCOCH}_2\text{CH}_2\text{CH}_2\text{CH}_2\text{CH}_3$ ,  $\blacktriangle$   $\text{Pt-OCOCH}_2\text{CH}_2\text{CH}_2\text{CH}_2\text{CH}_3$ ,  $\bullet$  free  $^-\text{OCOCH}_2\text{CH}_2\text{CH}_2\text{CH}_2\text{CH}_3$ .

**Table S1.** H<sub>2</sub>O<sub>2</sub> production during the photoreduction of **1** by miniSOG in MES buffer. The H<sub>2</sub>O<sub>2</sub> content was spectrophotometrically determined by mixing a 50 μL of a solution containing 200 μM **1** and 10 μM miniSOG with 50 μL of a solution of containing horseradish peroxidase (HRP, 60 μg/mL) and 2 mM ABTS (20 mM MES, pH 6). The solution of **1** and miniSOG was irradiated for 5 min at 460 nm before mixing with HRP and ABTS.

	mini SOG + 1	mini SOG
[H <sub>2</sub> O <sub>2</sub> ] / μM	28 ± 4	27 ± 2

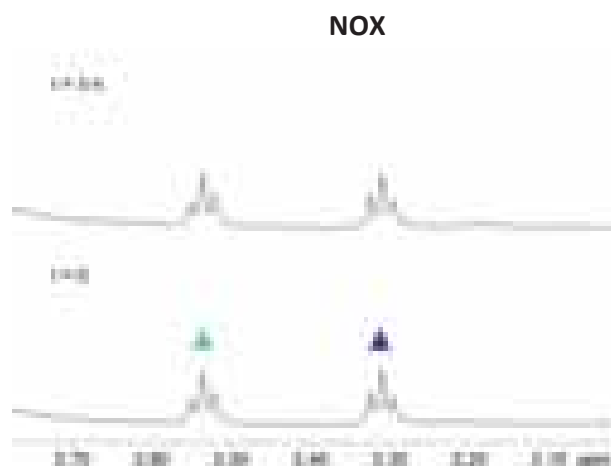


**Figure S61.** Dark stability of 0.2 mM **1** in MES (pH 6, 20 mM, 10% D<sub>2</sub>O) in the presence of 10 μM NOX over 3 h. <sup>1</sup>H NMR signal labelling: ▲ Pt-OCOCH<sub>2</sub>CH<sub>2</sub>CO<sub>2</sub><sup>-</sup>, ▲ Pt-OCOCH<sub>2</sub>CH<sub>2</sub>CO<sub>2</sub><sup>-</sup>.

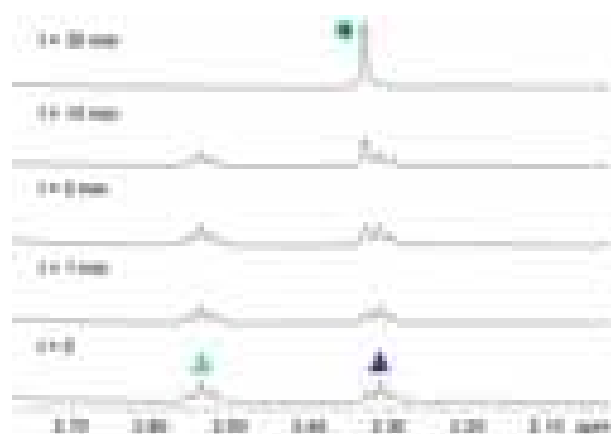


**Figure S62.** NOX-catalyzed photoreduction of **1** in MES buffer (pH = 6, 20 mM). <sup>1</sup>H NMR spectra were recorded for MES (10% D<sub>2</sub>O) solutions of 200 μM **1** and 10 μM NOX upon t = 0, 1, 5, 15 and 30 min of 460-nm light irradiation (6 mW·cm<sup>-2</sup>). <sup>1</sup>H NMR signal labelling: ▲ Pt-OCOCH<sub>2</sub>CH<sub>2</sub>CO<sub>2</sub><sup>-</sup>, ▲ Pt-OCOCH<sub>2</sub>CH<sub>2</sub>CO<sub>2</sub><sup>-</sup>, ● free <sup>-</sup>O<sub>2</sub>CCH<sub>2</sub>CH<sub>2</sub>CO<sub>2</sub><sup>-</sup>.

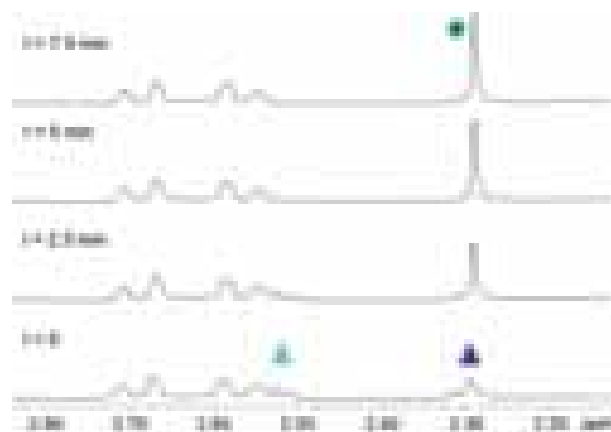


**Figure S63.** NOX-catalyzed reduction of **1** in PB buffer (pH 7, 100 mM) in the dark and in the presence of NADH (2 mM). <sup>1</sup>H NMR spectra were recorded for PB (10% D<sub>2</sub>O) solutions of 200 μM **1** and 10 μM NOX at t = 0, 2.5, 5 and 7.5 min. <sup>1</sup>H NMR signal labelling: ▲ Pt-OCOCH<sub>2</sub>CH<sub>2</sub>CO<sub>2</sub><sup>-</sup>, ▲ Pt-OCOCH<sub>2</sub>CH<sub>2</sub>CO<sub>2</sub><sup>-</sup>, ● free <sup>-</sup>O<sub>2</sub>CCH<sub>2</sub>CH<sub>2</sub>CO<sub>2</sub><sup>-</sup>.

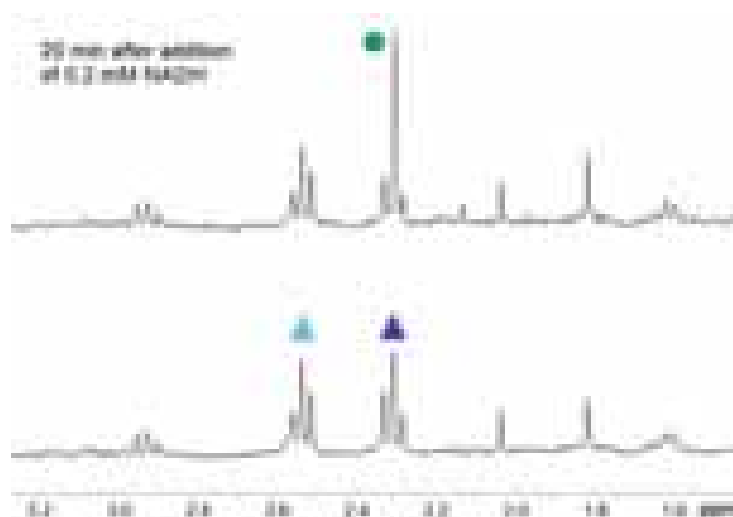


**Figure S64.** NOX-catalyzed reduction of **1** in O<sub>2</sub>-free PB buffer (pH 7, 100 mM) in the dark and in the presence of NADH (0.2 mM). <sup>1</sup>H NMR spectra were recorded for PB (10% D<sub>2</sub>O) solutions of 200 μM **1** and 10 μM NOX. <sup>1</sup>H NMR signal labelling: ▲ Pt-OCOCH<sub>2</sub>CH<sub>2</sub>CO<sub>2</sub><sup>-</sup>, ▲ Pt-OCOCH<sub>2</sub>CH<sub>2</sub>CO<sub>2</sub><sup>-</sup>, ● free <sup>-</sup>O<sub>2</sub>CCH<sub>2</sub>CH<sub>2</sub>CO<sub>2</sub><sup>-</sup>.

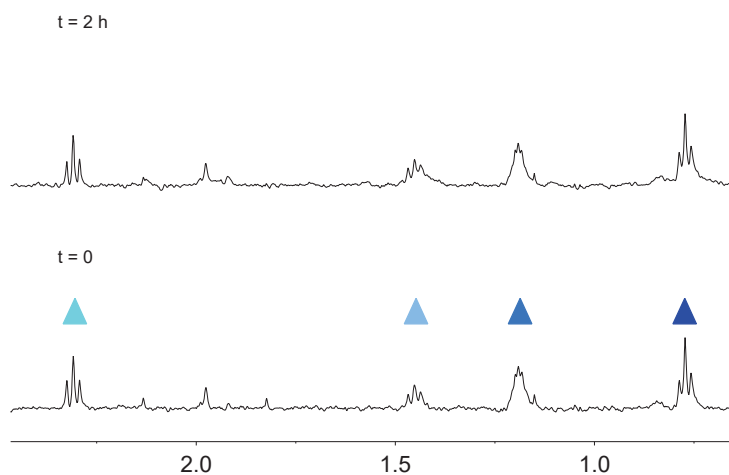


**Figure S65.** Dark stability of 0.2 mM **2** in MES (pH 6, 20 mM, 10% D<sub>2</sub>O, 1% dms<sup>-</sup><sub>o</sub>-d<sub>6</sub>) in the presence of 3 μM NOX over 2 h. <sup>1</sup>H NMR signal labelling: ▲ Pt-OCOCH<sub>2</sub>CH<sub>2</sub>CH<sub>2</sub>CH<sub>2</sub>CH<sub>3</sub>, ▲ Pt-OCOCH<sub>2</sub>CH<sub>2</sub>CH<sub>2</sub>CH<sub>2</sub>CH<sub>3</sub>, ▲ Pt-OCOCH<sub>2</sub>CH<sub>2</sub>CH<sub>2</sub>CH<sub>2</sub>CH<sub>3</sub>, ▲ Pt-OCOCH<sub>2</sub>CH<sub>2</sub>CH<sub>2</sub>CH<sub>2</sub>CH<sub>3</sub>.



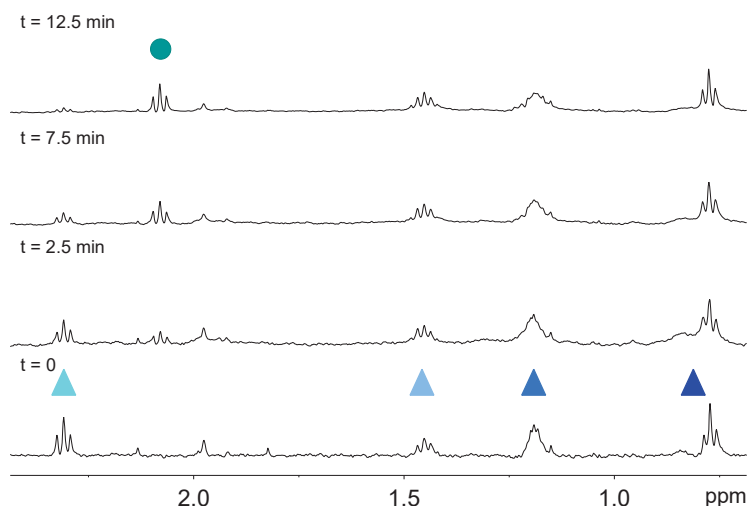


**Figure S66.** NOX-catalyzed photoreduction of **2** in MES buffer (pH 6, 20 mM) monitored by  $^1\text{H}$  NMR. Spectra were recorded for MES (10%  $\text{D}_2\text{O}$ , 1%  $\text{dms}\text{-d}_6$ ) solutions of  $200\ \mu\text{M}$  **2** and  $3\ \mu\text{M}$  NOX upon  $t = 0, 1\ \text{min}, 5\ \text{min}$  and  $10\ \text{min}$  of  $460\text{-nm}$  light irradiation ( $6\ \text{mW}\cdot\text{cm}^{-2}$ ).  $^1\text{H}$  NMR signal labelling:  $\blacktriangle$   $\text{Pt-OCOCH}_2\text{CH}_2\text{CH}_2\text{CH}_2\text{CH}_3$ ,  $\triangle$   $\text{Pt-OCOCH}_2\text{CH}_2\text{CH}_2\text{CH}_2\text{CH}_3$ ,  $\blacktriangle$   $\text{Pt-OCOCH}_2\text{CH}_2\text{CH}_2\text{CH}_2\text{CH}_3$ ,  $\blacktriangle$   $\text{Pt-OCOCH}_2\text{CH}_2\text{CH}_2\text{CH}_2\text{CH}_3$ ,  $\bullet$  free  $^-\text{OCOCH}_2\text{CH}_2\text{CH}_2\text{CH}_2\text{CH}_3$ .

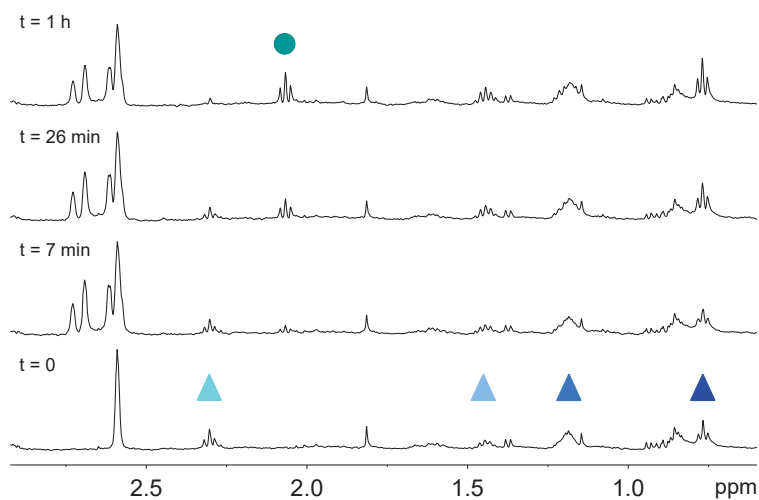


**Figure S67.** NOX-catalyzed reduction of **2** in PB buffer (pH 7, 100 mM) in the dark and in the presence of NADH (2 mM).  $^1\text{H}$  NMR spectra were recorded for PB (10%  $\text{D}_2\text{O}$ , 1%  $\text{dms}\text{-d}_6$ ) solutions of  $200\ \mu\text{M}$  **2** and  $1\ \mu\text{M}$  NOX at  $t = 0, 7\ \text{min}, 26\ \text{min}$  and  $1\ \text{h}$ .  $^1\text{H}$  NMR signal labelling:  $\blacktriangle$   $\text{Pt-OCOCH}_2\text{CH}_2\text{CH}_2\text{CH}_2\text{CH}_3$ ,  $\triangle$   $\text{Pt-OCOCH}_2\text{CH}_2\text{CH}_2\text{CH}_2\text{CH}_3$ ,  $\blacktriangle$   $\text{Pt-OCOCH}_2\text{CH}_2\text{CH}_2\text{CH}_2\text{CH}_3$ ,  $\blacktriangle$   $\text{Pt-OCOCH}_2\text{CH}_2\text{CH}_2\text{CH}_2\text{CH}_3$ ,  $\bullet$  free  $^-\text{OCOCH}_2\text{CH}_2\text{CH}_2\text{CH}_2\text{CH}_3$ .

## GR

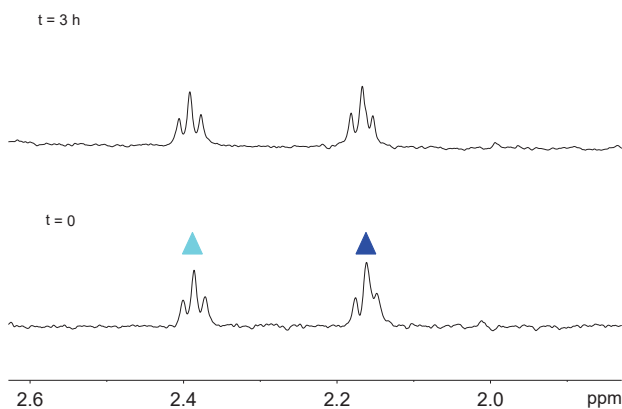


**Figure S68.** Dark stability of 0.2 mM **1** in MES (pH 6, 20 mM, 10% D<sub>2</sub>O) in the presence of 10 μM GR over 3 h. <sup>1</sup>H NMR signal labelling: ▲ Pt-OCOCH<sub>2</sub>CH<sub>2</sub>CO<sub>2</sub><sup>-</sup>, ▲ Pt-OCOCH<sub>2</sub>CH<sub>2</sub>CO<sub>2</sub><sup>-</sup>.

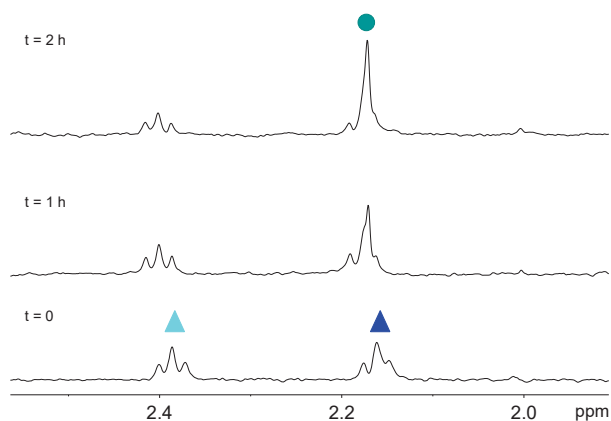


**Figure S69.** GR-catalyzed photoreduction of **1** in MES buffer (pH 6, 20 mM) monitored by <sup>1</sup>H NMR. Spectra were recorded for MES (10% D<sub>2</sub>O) solutions of 200 μM **1** and 10 μM GR upon t = 0, 1 h and 2 h of 460-nm light irradiation (6 mW·cm<sup>-2</sup>). <sup>1</sup>H NMR signal labelling: ▲ Pt-OCOCH<sub>2</sub>CH<sub>2</sub>CO<sub>2</sub><sup>-</sup>, ▲ Pt-OCOCH<sub>2</sub>CH<sub>2</sub>CO<sub>2</sub><sup>-</sup>, ● free <sup>-</sup>O<sub>2</sub>CCH<sub>2</sub>CH<sub>2</sub>CO<sub>2</sub><sup>-</sup>.

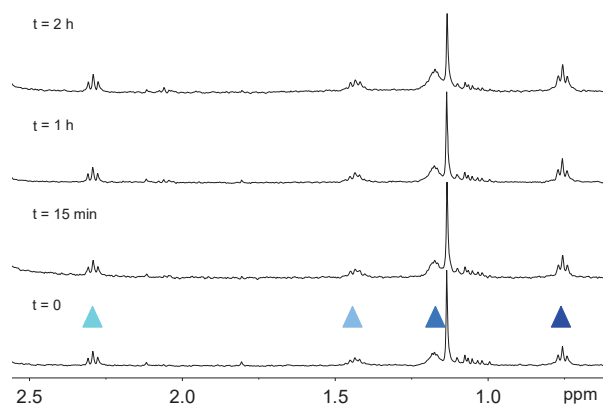


**Figure S70.** Photostability of 0.2 mM **2** in MES (pH 6, 20 mM, 10% D<sub>2</sub>O, 1% dmsO-d<sub>6</sub>) in the presence of 10 μM GR over 2 h (460 nm, 6 mW·cm<sup>-2</sup>). <sup>1</sup>H NMR signal labelling: ▲ Pt-OCOCH<sub>2</sub>CH<sub>2</sub>CO<sub>2</sub><sup>-</sup>, ▲ Pt-OCOCH<sub>2</sub>CH<sub>2</sub>CO<sub>2</sub><sup>-</sup>.

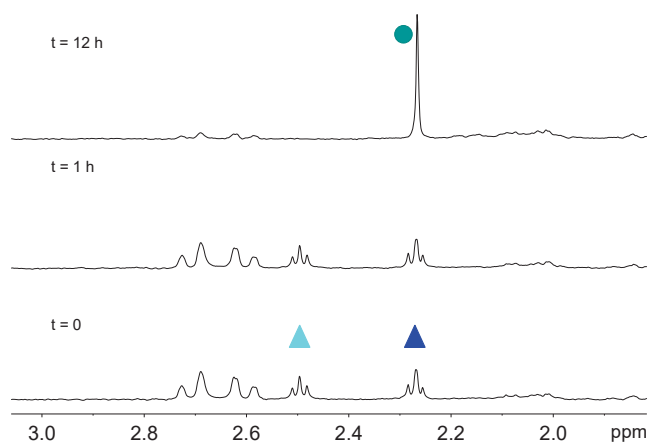


**Figure S71.** Dark stability of **1** in the dark and in PB buffer (pH 7, 100 mM) in the presence of NADPH (2 mM) and GR monitored by  $^1\text{H}$  NMR. Spectra were recorded for PB (10%  $\text{D}_2\text{O}$ ) solutions of 200  $\mu\text{M}$  **1** and 10  $\mu\text{M}$  GR.  $^1\text{H}$  NMR signal labelling:  $\blacktriangle$   $\text{Pt-OCOCH}_2\text{CH}_2\text{CO}_2^-$ ,  $\blacktriangle$   $\text{Pt-OCOCH}_2\text{CH}_2\text{CO}_2^-$ ,  $\bullet$  free  $^- \text{O}_2\text{CCH}_2\text{CH}_2\text{CO}_2^-$ .

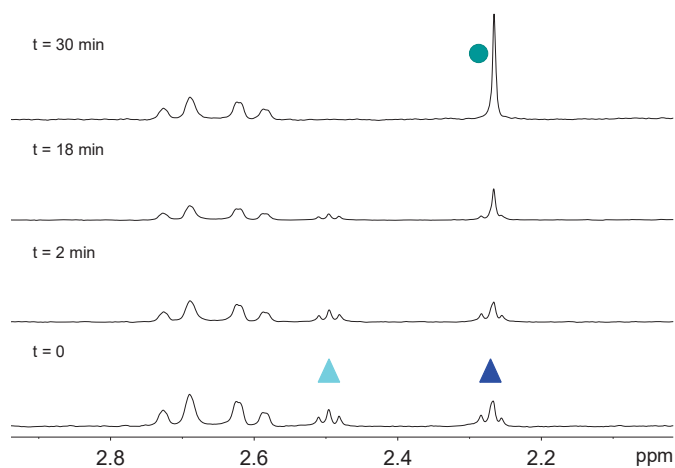


**Figure S72.** GR-catalyzed photoreduction of **1** in PB buffer (pH 7, 100 mM) in the presence of NADPH (2 mM) monitored by  $^1\text{H}$  NMR. Spectra were recorded for PB (10%  $\text{D}_2\text{O}$ ) solutions of 200  $\mu\text{M}$  **1** and 10  $\mu\text{M}$  GR upon  $t = 0, 1 \text{ min}, 2 \text{ min}, 18 \text{ min}$  and 30 min of 460-nm light irradiation ( $6 \text{ mW}\cdot\text{cm}^{-2}$ ).  $^1\text{H}$  NMR signal labelling:  $\blacktriangle$   $\text{Pt-OCOCH}_2\text{CH}_2\text{CO}_2^-$ ,  $\blacktriangle$   $\text{Pt-OCOCH}_2\text{CH}_2\text{CO}_2^-$ ,  $\bullet$  free  $^- \text{O}_2\text{CCH}_2\text{CH}_2\text{CO}_2^-$ .

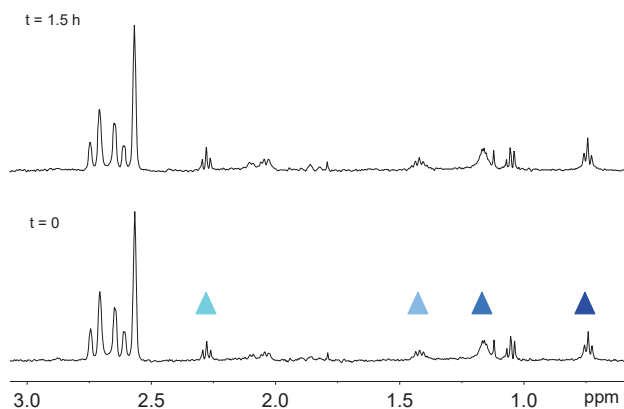


**Figure S73.** Dark stability of **2** in the dark and in PB buffer (pH 7, 100 mM, 1% dms<sub>o</sub>-d<sub>6</sub>) in the presence of NADPH (2 mM) and GR monitored by <sup>1</sup>H NMR. Spectra were recorded for PB (10% D<sub>2</sub>O) solutions of 200 μM **2** and 10 μM GR. <sup>1</sup>H NMR signal labelling: ▲ Pt-OCOCH<sub>2</sub>CH<sub>2</sub>CH<sub>2</sub>CH<sub>2</sub>CH<sub>2</sub>CH<sub>3</sub>, ▲ Pt-OCOCH<sub>2</sub>CH<sub>2</sub>CH<sub>2</sub>CH<sub>2</sub>CH<sub>2</sub>CH<sub>3</sub>, ▲ Pt-OCOCH<sub>2</sub>CH<sub>2</sub>CH<sub>2</sub>CH<sub>2</sub>CH<sub>2</sub>CH<sub>3</sub>, ▲ Pt-OCOCH<sub>2</sub>CH<sub>2</sub>CH<sub>2</sub>CH<sub>2</sub>CH<sub>2</sub>CH<sub>3</sub>.

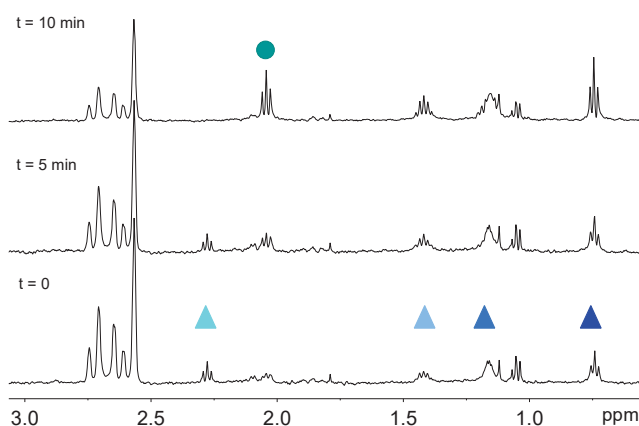


**Figure S74.** GR-catalyzed photoreduction of **2** in PB buffer (pH 7, 100 mM, 1% dms<sub>o</sub>-d<sub>6</sub>) in the presence of NADPH (2 mM) monitored by <sup>1</sup>H NMR. Spectra were recorded for PB (10% D<sub>2</sub>O) solutions of 200 μM **2** and 10 μM GR upon t = 0, 5 min and 10 min of 460-nm light irradiation (6 mW·cm<sup>-2</sup>). <sup>1</sup>H NMR signal labelling: ▲ Pt-OCOCH<sub>2</sub>CH<sub>2</sub>CH<sub>2</sub>CH<sub>2</sub>CH<sub>2</sub>CH<sub>3</sub>, ▲ Pt-OCOCH<sub>2</sub>CH<sub>2</sub>CH<sub>2</sub>CH<sub>2</sub>CH<sub>2</sub>CH<sub>3</sub>, ▲ Pt-OCOCH<sub>2</sub>CH<sub>2</sub>CH<sub>2</sub>CH<sub>2</sub>CH<sub>2</sub>CH<sub>3</sub>, ▲ Pt-OCOCH<sub>2</sub>CH<sub>2</sub>CH<sub>2</sub>CH<sub>2</sub>CH<sub>2</sub>CH<sub>3</sub>, ● free <sup>-</sup>OCOCH<sub>2</sub>CH<sub>2</sub>CH<sub>2</sub>CH<sub>2</sub>CH<sub>2</sub>CH<sub>3</sub>.

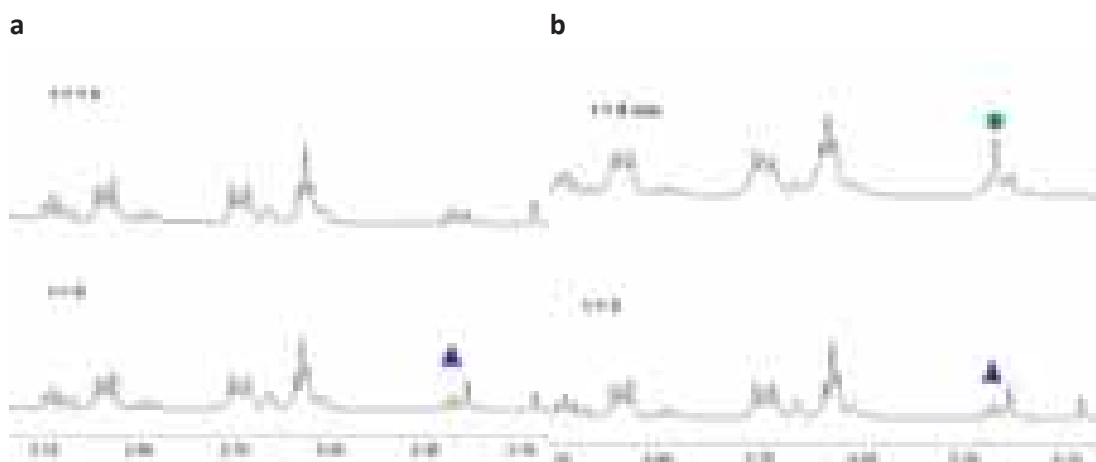


**Figure S75.** (a) Dark stability and (b) photocatalytic activity of miniSOG in cell culture medium (pH 7, f12k integrated with FBS) in the presence of NADH over time. Spectra were recorded for solutions of 200  $\mu\text{M}$  **1** and 10  $\mu\text{M}$  miniSOG and 2 mM NADH. Light irradiation was performed with an LED light source (460 nm, 6  $\text{mW}\cdot\text{cm}^{-2}$ ). Signals above 2.75 correspond residual MES present in the protein stock solution.  $^1\text{H}$  NMR signal labelling:  $\blacktriangle$  Pt-OCOCH<sub>2</sub>CH<sub>2</sub>CO<sub>2</sub><sup>-</sup>,  $\blacktriangle$  Pt-OCOCH<sub>2</sub>CH<sub>2</sub>CO<sub>2</sub><sup>-</sup>,  $\bullet$  free <sup>-</sup>O<sub>2</sub>CCH<sub>2</sub>CH<sub>2</sub>CO<sub>2</sub><sup>-</sup>.

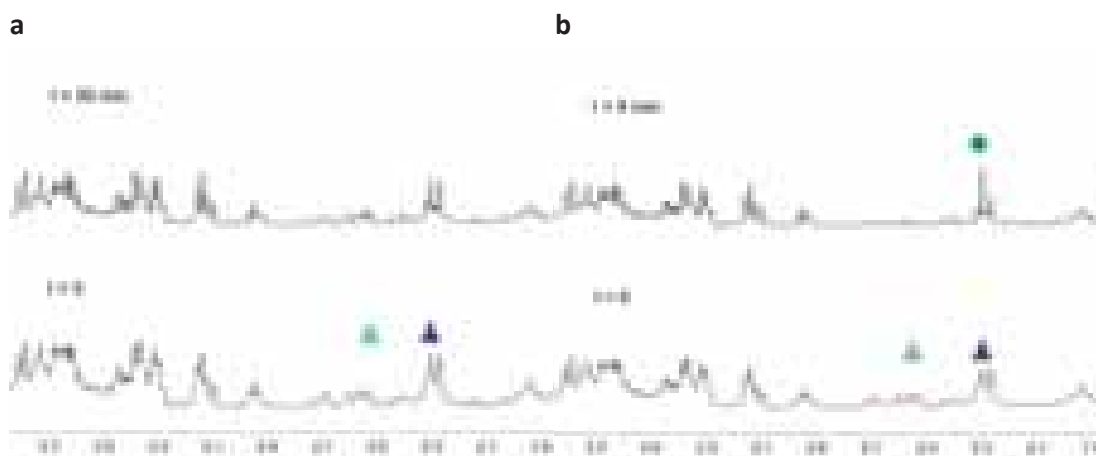


**Figure S76.** (a) Dark stability and (b) photocatalytic activity of FAD in cell culture medium (pH 7, f12k integrated with FBS) in the presence of NADH over time. Spectra were recorded for solutions of 200  $\mu\text{M}$  **1** and 10  $\mu\text{M}$  FAD and 2 mM NADH. Light irradiation was performed with an LED light source (460 nm, 6  $\text{mW}\cdot\text{cm}^{-2}$ ).  $^1\text{H}$  NMR signal labelling:  $\blacktriangle$  Pt-OCOCH<sub>2</sub>CH<sub>2</sub>CO<sub>2</sub><sup>-</sup>,  $\blacktriangle$  Pt-OCOCH<sub>2</sub>CH<sub>2</sub>CO<sub>2</sub><sup>-</sup>,  $\bullet$  free <sup>-</sup>O<sub>2</sub>CCH<sub>2</sub>CH<sub>2</sub>CO<sub>2</sub><sup>-</sup>.

**Table S2. Activity of GOX in presence of different concentrations of 1.** The enzyme activity was spectrophotometrically determined by using 30  $\mu\text{M}$  ABTS, 30 mM of glucose, 29  $\mu\text{g}/\text{mL}$  of horseradish peroxidase (HRP) and 0.05 mg/mL of GOX in 25 mM sodium phosphate at pH 7.

[1] / mM	Oxidation Rate (U/mg)
0	15.41 $\pm$ 0.50
2	15.98 $\pm$ 3.20

### References

- [1] S. Betanzos-Lara, A. Habtemariam, P. J. Sadler, *J. Mex. Chem. Soc.* 2013, **57**, 160–168.
- [2] S. Betanzos-Lara, Z. Liu, A. Habtemariam, A. M. Pizarro, B. Qamar, P. J. Sadler, *Angew. Chem. Int. Ed.* 2012, **51**, 3897–3900.
- [3] I. Walsh, G. Minervini, A. Corazza, G. Esposito, S. C. E. Tosatto, F. Fogolari, *Bioinformatics* 2012, **28**, 2189–2190.

## ***Acknowledgements***

First of all, I would like to thank Dr. Luca Salassa for providing me the opportunity to develop this Ph.D. thesis under his supervision. Thanks for guiding and helping me during these four years.

I would also like to thank Dr. Isabel Goñi for his assistance as University tutor of my Ph.D.

I wish also to thank Prof. Juan Carlos Mareque Rivas for giving the possibility to develop my experimental work in his laboratory at CIC biomaGUNE.

I thank all my past and present colleagues for all the support that I received in the lab during these years.

Thanks to all biomaGUNE and DIPIC/EHU people that helped me during my thesis.

In the end, I want to thank all the funding for their essential economic support: the Spanish Ministry of Economy and Competitiveness (grant CTQ2012-39315, CTQ2016-80844-R and BES-2013-065642) and the European COST Actions CM1105 and CM1403. Moreover, the EEBB-I-17-12445 fellowship funded my stay in the laboratory of Prof. Walter Berger at the Medical University of Vienna (Austria).

# Curriculum Vitae

silviaalonsodc@gmail.com  
0034 696 190931

## Academic Profile

---

### **Chemistry PhD (ongoing) in *Metal-based photochemotherapy*. (2014 - present)**

Research Group: Inorganic Photochemistry Lab

Supervisor: Dr. Luca Salassa

DIPC, San Sebastián, Spain

### **PhD research stay (3 months 2017)**

Research Group: Applied and Experimental Oncology

Supervisor: Dr. Walter Berger

Institute of Cancer Research and Comprehensive Cancer Center, Medical University of Vienna,  
(Austria)

### **Experimental Stage (3 days- 2015)**

European Synchrotron Radiation Facility (ESRF), Grenoble, France.

Experimental project: "*Nanoparticle-mediated photoreduction of Pt(IV) anticancer agents*", ESRF,  
BM23, 3-7 Feb. 2015 (CH4217).

### **Master of Science in Applied and Pharmaceutical Chemistry (2013)**

- Master thesis: *Tetrapeptidic Lysine Derivative Hydrogelators: Synthesis, Characterization and Coaggregation studies*.

Research Group: Organic Molecular Nanomaterials with Biomedical Applications

Supervisor: Dr. Juan F. Miravet

Universitat Jaume I, Castellón de la Plana, Spain

- External research (1 month): *Molecular Biology*.

Supervisor: Dr. Antonio Pineda-Lucena

Centro de Investigación Príncipe Felipe, Valencia.



### **Erasmus internship programme (6 months-2009)**

Research project: *Photo-Activation of cell penetrating peptides on a polymersome surface with Pharmacological Application*

Research Group: Physical-Organic & Supramolecular Chemistry

Supervisor: Dr. Stijn van Dongen/ Prof. dr. Jan van Hest and Prof. dr. Roeland J.M. Nolte  
Radboud University Nijmegen, The Netherlands.

### **Bachelor of Science in Chemistry (2011)**

Universitat Jaume I, Castellón de la Plana, Spain.

## **Work Experience**

---

### July 2013 – May 2014:

**Research collaboration with P&G**, developing the project: “Designing, Synthesizing and Testing Novel Non-Aminoacid Based Molecules Able to Structure Liquid P&G Consumer Goods”.

Universitat Jaume I, Castellón de la Plana (Spain).

Main duties:

- Synthesis and methods of gelation.
- Rheology study of gels obtained from the molecules in the *P&G* liquid matrix.

### January 2012 - May 2012:

**R&D** support in Perfume Delivery Technologies IP, granted by Leonardo da Vinci Programme.

**Procter & Gamble (P&G)**, Brussels, Belgium, in *Strategic Innovation & Technology* department.

Where I designed and implemented the plan to generate experimental data for the grant of the **patent US8278230 Procter & Gamble**.

Main duties:

- Intellectual Property Strategy development.
- Performance assessment of Perfume Delivery Technologies.
- Patent Publication searches and analysis (use of software, Orbit.com).

- IP mapping for white spaces identification.

## Techniques and Practical skills

---

**Language skills:** Spanish and Catalan (Mother tongues), English (good) and French (basic user).

**Technical skills:**

- Spectroscopy: UV-Vis, Fluorescence, Nuclear Magnetic Resonance (**NMR**), Infra-Red (**IR**) and Circular Dichroism (**CD**).
- Microscopy: Transmission Electron Microscopy (**TEM**), Scanning Electron Microscopy (**SEM**), cell observer Microscopy.
- Software: Microsoft Office™ tools such as Word™, Excel™ and PowerPoint™, ChemDraw™ and MestreNova™.

## Publications

---

**7.** “Bioorthogonal Catalytic Activation of Platinum and Ruthenium Anticancer Complexes by FAD and Flavoproteins”

Alonso-de Castro, S.; L. Cortajarena, A.; López-Gallego, F. and Salassa, L.

*Angew. Chem. Int. Ed.* **2018**, 57, 3143–3147 (VIP, Very Important Paper)

Inside cover: *Angew. Chem. Int. Ed.* 12/2018

Highlighted in *Chemistry Views*:

([https://www.chemistryviews.org/details/ezone/10902484/Activation\\_of\\_Platinum\\_and\\_Ruthenium\\_Anticancer\\_Prodrugs.html](https://www.chemistryviews.org/details/ezone/10902484/Activation_of_Platinum_and_Ruthenium_Anticancer_Prodrugs.html))

**6.** “Riboflavin As Bioorthogonal Photocatalyst For The Activation Of A Pt<sup>IV</sup> Prodrug”

S. Alonso-de Castro, E. Ruggiero, A. Ruiz-de-Angulo, E. Rezabal, J.C. Mareque-Rivas, X. Lopez, F.

López-Gallego and L. Salassa, *Chem. Sci.*, **2017**, 8, 4619

5. "Polyurethane Based Organic Macromolecular Contrast Agent (PU-ORCA) For Magnetic Resonance Imaging"

S. Garmendia, D. Mantione, S. Alonso-de Castro, C. Jehanno, L. Lezama, J. L. Hedrick, D. Mecerreyes, L. Salassa and H. Sardon, *Polym. Chem.*, **2017**, 8, 2693-2701

4. "Upconverting Nanoparticles For The Near Infrared Photoactivation Of Transition Metal Complexes: New Opportunities And Challenges In Medicinal Inorganic Photochemistry",

E. Ruggiero, S. Alonso-de Castro, A. Habtemariam and L. Salassa, *Dalton Trans.*, **2016**, 45, 13012-13020.

3. "Photorelease of Pyridyl Esters in Organometallic Ru(II) Arene Complexes"

A. Habtemariam, C. Garino , E. Ruggiero, S. Alonso-de Castro, J.C. Mareque-Rivas and L. Salassa, *Molecules*, **2015**, 20, 7276-7291.

2. "The Photochemistry of Transition Metal Complexes and Its Application in Biology and Medicine"

E. Ruggiero, S. Alonso-de Castro, A. Habtemariam and L. Salassa, *Struct. Bond.*, **2014**, 165, 69-108.

1. "Co-assembly of tetrapeptides into complex pH-responsive molecular hydrogel networks"

M. Tena-Solsona, S. Alonso-de Castro, J.F. Miravet and B. Escuder, *J. Mater. Chem. B*, **2014**, 2, 6192-6197.

---

### Oral Presentations

---

6. "Phosphonate-Functionalized Upconverting Nanoparticles As Multimodal Imaging Probes"

Spectral Shaping for Biomedical and Energy Applications (SHIFT2017), Tenerife, Canary Islands, November 2017.

5. "Efficient and bioorthogonal photoactivation of anticancer prodrugs using flavins"

BioBilbao 2017, X Scientific meeting of bioinorganic, Bilbao, from 9<sup>th</sup>-12<sup>th</sup> July 2017.

**4. “Bioorthogonal photocatalytic activation of Pt<sup>IV</sup> anticancer prodrugs”**

Applications of Photoactive Coordination Compounds: a preconference of the 22<sup>nd</sup> ISPPCC, in University of St Andrews, Scotland, from 5<sup>th</sup>-7<sup>th</sup> July 2017.

**3. “Towards bone-targeting using upconverting nanoparticles decorated with bisphosphonates”**  
251st ACS National Meeting in San Diego, California, from 13<sup>th</sup> to 17<sup>th</sup> March 2016.

**2. “Hybrid Upconverting Nanosystems for NIR Photoactivation and Theranostics”**

9<sup>th</sup> International Conference on the f-elements, Keble College in University of Oxford from 6<sup>th</sup>-9<sup>th</sup> September 2015.

**1. “Hybrid Upconverting Nanosystems for NIR Photoactivation and Theranostics”**

Joined Meeting WG1-WG5 COST CM1105, Belgrade from 10<sup>th</sup>-12<sup>th</sup> September 2015.

---

### Poster Presentations

---

**4. Alonso-de Castro, S.; Salassa, L.; “Hybrid Upconverting Nanosystems for Theranostics”**

Molecular Imaging Workshop 2015, 10-12 Noviembre 2015, CIC BiomaGUNE, San Sebastián.

**3. Alonso-de Castro, S.; Salassa, L.; “Gadolinium based Upconverting Nanoparticles for Theranostics”** 1st Young Researchers Workshop on Biomaterials and Bioapplications (*BIOMAPP 15*), 19-20 Octubre 2015 CIC BiomaGUNE, San Sebastián.

**2. Alonso-de Castro, S.; Ruggiero E.; Salassa, L.; “Hybrid upconverting nanosystems for theranostics”** 5th Early Stage Researchers Workshop, 17-18 June 2014, IMDEA, Madrid, Spain.

**1. Alonso-de Castro, S.; Salassa, L.; “Development of novel theranostic agents based on transition metal complexes and upconversion nanoparticles”** 4th Early Stage Researchers Workshop, 25-26 June 2014, IMDEA, Madrid, Spain.

## Courses / Workshops

---

Training School in cytotoxicity COST Action CM1403, Central for Medical Research, Graz from 19<sup>th</sup>-22<sup>th</sup> October 2015.

“Year of Light 2015 – The chemical point of view” Department of Chemistry and Industrial Chemistry of the University of Pisa, Italy (9 – 10 Feb 2015).

COST Action CM1105: Functional metal complexes that bind to biomolecules. WG5 Prodrugs with novel activation strategies, “Where the activation of metallodrugs takes research”, Universidad Autonoma de Madrid, April 2014.

Postgraduate course: **SMARNET** *Workshop on Characterization of gels*, Universitat Jaume I, Castellón de la Plana (Spain), 26<sup>th</sup>-28<sup>th</sup> Nov 2013.

Trainings at **P&G**: *Finance for R&D* (3h), *Scanning Electron Microscope* (1h), *Encapsulation* (2h), *Designing Compact Liquid Detergents* (4h), *Basic Statistics using JMP* (8h), *Patent Search and Analysis Using Questel’s Orbit.com* (2h), *Microbiology and Clean Design Basics for R&D* (2h), *Rheology* (6h), *Enzyme technology and stabilization in liquid detergents* (8h), and *People & Communication skills* (10h), Jan – May 2012.

**P&G** *Technical Training for Detergency* (28 hours) in March 2012

## Other Contributions to Conference

---

Alonso-de Castro, S.; Gurruchaga-Pereda J., Salassa, L. “*Unconventional modes of photoactivation for anticancer metal-based prodrugs*”, Theobio17, 26-30 June 2017, Donostia, Spain.

Ruggiero, E.; Alonso-de Castro, S.; Salassa, L. *“Upconverting Nanomaterials For The NIR Photoactivation Of Anticancer Metal Complexes”*, SACS – International Conference on Self Assembly in Confined Spaces, 25-27 October 2016, San Sebastian, Spain.

Alonso-de Castro, S.; Ruggiero, E.; Salassa, L. *“Upconverting nanoparticles: a tool for near infrared photochemotherapy and multimodal imaging”*, 13th European Biological Inorganic Chemistry Conference (EuroBIC-13), 28 Aug. – 1 Sept. 2016, Budapest (Hungary).

Ruggiero, E.; Alonso-de Castro, S.; Salassa, L. *“Near Infrared Photoactivation of Anticancer Metal Complexes”*, Computation of Electronic Excited States School (CEES), Donostia, 1-4 Sept. 2015.

Ruggiero E., Alonso-de Castro S., Salassa L.; *“Near infrared photoactivation of metal-based anticancer agents by upconverting nanoparticles”*  
Cancer Nanotechnology Gordon Research Conference, 28 June-3 July 2015, Boston, USA.

Ruggiero, E.; Alonso-de Castro, S.; Salassa, L.; *“Towards Theranostic Upconversion Nanomaterials”*  
2nd International Symposium on Functional Metal Complexes that Bind to Biomolecules, 22-23 August 2014, Zurich (Switzerland).

Ruggiero, E.; Alonso-de Castro, S.; Salassa, L.; *“Near infrared light activation of anticancer metal complexes using upconversion nanoparticles”* IWSN 2014, The International Jointed School-Workshop on Smart Nanomaterials and X-ray Optics 2014, 22-25 Sept. 2014, Kaliningrad (Russia).

Tena-Solsona, M.; Alonso-de Castro, S.; Escuder, B. Poster: *“Amyloid Peptidic Supramolecular Hydrogels”* Annual Scientific Meeting of Cost Action Supramolecular Chemistry in Water. 2011|2015 – COST action, Nov 2013 (Malta).